UNIVERSITÀ
DEGLI STUDI
DI PADOVA

Sede Amministrativa: Università degli Studi di Padova

Dipartimento di Geoscienze

CORSO DI DOTTORATO DI RICERCA IN SCIENZE DELLA TERRA

CICLO XXX

STRUCTURAL EVOLUTION OF PERIADRIATIC PLUTONS AND ITS IMPLICATIONS ON SOLID-STATE DEFORMATION OF GRANITOID ROCKS

Coordinatore: Ch.mo Prof. Fabrizio Nestola

Supervisore: Ch.mo Prof. Giorgio Pennacchioni

Dottorando: Alberto Ceccato

Riassunto

I plutoni granitoidi esumati sono un target di ricerca ideale per la caratterizzazione dei processi di nucleazione e sviluppo delle strutture deformative sia duttili che fragili. I plutoni granitoidi sono corpi magmatici che per definizione, sono privi della moltitudine di strutture pervasive derivanti dagli intensi processi tettono-metamorfici che caratterizzano le rocce metamorfiche in generale. Per cui, le strutture deformative sviluppate durante il raffreddamento dei plutoni da condizioni magmatiche alle temperature della roccia incassante, sono preservate nei loro stadi incipienti. Tali strutture possono essere prese come esempio per lo sviluppo di strutture deformative a differenti livelli strutturali della crosta continentale. Il principale soggetto di ricerca trattato in questa tesi di dottorato è l'analisi delle strutture deformative del plutone di Vedrette di Ries – Rieserferner – una delle più importanti intrusioni Periadriatiche. Gli obbiettivi dell'analisi sono molteplici: (i) ricostruzione del contesto tettonico durante lo sviluppo dei diversi *stage* dell'evoluzione strutturale del plutone, e (ii) definizione dei processi alla base della localizzazione della deformazione duttile a varie scale e definizione delle condizioni alle quali questi processi avvengono.

L'evoluzione strutturale durante il raffreddamento e successiva esumazione del plutone delle Vedrette di Ries comprende 5 fasi principali di deformazione: (i) joint, filoni leucocratici e vene a quarzo-feldspato ad alto angolo e zone di taglio associate; (ii) joint a basso angolo e associate vene a quarzo e vene a epidoto e associate zone di taglio duttili; (iii)faglie duttili-fragili ad alto angolo, associate a mineralizzazione a calcite e mica bianca e all'intrusione di filoni mafici; (iv) faglie cataclastiche e pseudotachylyti ad alto angolo; (v) faglie cataclastiche a zeoliti. Tali fasi sono state vincolate in termini di temperature e cronologia assoluta in questo lavoro tramite la comparazione di analisi microstrutturali, dati di letteratura e dati di rilevamento geologico. Tale vincolo ci ha permesso di collegare l’evoluzione descritta con la tettonica del Terziario delle Alpi Orientali. I principali risultati del nostro lavoro possono essere così riassunti: (i) Tre fasi principali di deformazione duttile sono avvenute durante il raffreddamento del plutone nell’Oligocene; in seguito, due fasi fragili si sono sviluppate durante l’esumazione regionale nel Miocene; (ii) l'analisi della cinematica delle strutture

e l'inversione del paleostress suggeriscono una variazione complessa del campo di sforzi, principalmente legato alla variazione delle intensità relative delle componenti principali di sforzo; (iii) l'evoluzione del paleostress riflette la sequenza di processi tettonici avvenuti durante l'Oligocene ed il Miocene alla scala delle Alpi Orientali, dai processi legati allo slab break-off, alla tettonica di indentazione e di estrusione laterale.

Le indagini microstrutturali sono state principalmente indirizzate all'analisi delle zone di taglio derivanti da vene a quarzo ed epidoto. I processi di *softening* e localizzazione nelle vene a quarzo sono principalmente controllati da processi di *grain-size reduction* per ricristallizzazione dinamica. Le analisi dei campioni raccolti tramite *electron-backscattered diffraction* (EBSD) ed analisi di immagine hanno mostrato che l'orientazione cristallografica dei cristalli di quarzo della vena hanno controllato l'evoluzione microstrutturale e dell'orientazione cristallografica preferenziale (CPO) durante la deformazione di taglio semplice parallela alla vena fino ad elevate deformazione ($\gamma>10$). La ricristallizzazione tramite *subgrain rotation* (SGR) ha portato allo sviluppo di vene di quarzo ultramilonitiche a grana fine, nelle quali, la struttura a bande della CPO è stata ereditata della orientazione cristallografica originale dei cristalli di vena. La localizzazione della deformazione duttile su zone di taglio eterogenee nucleate sulle vene a epidoto, invece, è stata principalmente ottenuta tramite lo sviluppo di myrmekiti e successiva deformazione. Analisi EBSD suggeriscono che lo sviluppo di myrmekiti ha indotto uno scambio nei processi di deformazione dominanti, dalla ricristallizzazione dinamica per mezzo di *dislocation creep*, a processi di *diffusion-assisted grain boundary sliding* durante la deformazione degli aggregati di plagioclasio + quarzo derivanti dalle myrmekiti.

La modellizzazione termodinamica ha permesso di definire le condizioni di pressione-temperatura-fluidi alle quali questi processi furono attivi. Le risultanti pseudosezioni calcolate per i sistemi chimici NaCaKFMASHO e MnNaCaKFMASHO suggeriscono che: la formazione delle vene ad epidoto avviene a temperature comprese tra 520°C e 490°C in condizioni di saturazione della fase fluida; (ii) la fase di deformazione principale probabilmente avviene a 460 ± 40 °C e 0.35 ± 0.05 GPa, perdurando durante il raffreddamento del plutone probabilmente fino a 350°C in condizioni di quasi-saturazione della fase fluida.

Abstract

Exhumed granitoid plutons are an ideal natural research target for studying the processes of nucleation and evolution of ductile and brittle deformation structures. Granitoid plutons, unaffected by later tectono-metamorphic cycles, preserve pristine deformation structures developed during cooling from magmatic to host rock ambient temperatures, that can be assumed as representatives of structures that at different structural levels of the continental crust. The main focus of this Ph.D. project is the analysis of deformation structures of the Rieserferner pluton – one of the major Periadriatic intrusions. The aim of the study is two-fold: (i) reconstruct the tectonic framework during the different stages of the pluton structural evolution, and (ii) determine the processes controlling localized ductile strain at different scales and the environmental conditions at which they occurred.

The structural evolution during pluton cooling consists of 5 main deformation stages, that have been bracketed in time and thermal conditions according to microstructural and textural analysis, literature and field data: (i) steeply dipping joints, leucocratic dykes and quartz-feldspar veins and associated ductile shear zones; (ii) shallowly dipping joints with associated epidote and quartz veins and ductile shear zones; (iii) steeply dipping mafic dykes and calcite-white mica-bearing brittle-ductile faults; (iv) steeply dipping pseudotachylyte-bearing cataclastic faults; and (v) zeolite-bearing faults. Integrating new field, microstructural and geothermo-chronological data with published data we have related the deformation sequence to the Tertiary tectonics of the Eastern Alps. (i) three main ductile deformation stages developed during Oligocene, followed by two brittle deformation stages during Miocene; (ii) paleostress inversion from kinematic analyses suggest a complex stress field variation during the structural evolution mainly due to switch in relative magnitudes of principal stress components; (iii) the described paleostress evolution reflect the sequence of tectonic processes occurred during Oligocene and Miocene at the scale of the Eastern Alps, from slab break-off to indentation and lateral escape tectonics.

Microstructural investigations were mainly focused on the analysis of ductile shear zones exploiting epidote- and quartz-rich veins. Softening and localization in quartz veins was mainly controlled by grain size reduction by recrystallization. EBSD mapping and image analyses have shown that different crystallographic orientations of quartz vein crystals controlled the evolution of microstructures and crystallographic preferred orientations (CPO) during vein-parallel simple shear up to high shear strains ($\gamma \approx 10$). Recrystallization by Subgrain Rotation (SGR) lead to the development of fine-grained ultramylonitic quartz veins, in which, the observed CPO banding have been inherited from the original crystallographic orientation of the vein crystals. Localization of ductile strain within heterogeneous shear zones exploiting epidote veins was mainly obtained through myrmekite development and following shearing. EBSD investigations suggest that myrmekite induced a switch in the dominant deformation mechanism, from dynamic recrystallization by SGR to diffusion-assisted grain boundary sliding (GBS) during shearing of plagioclase + quartz aggregates. Thermodynamic modelling was aimed to define the temperature-pressure-fluid conditions under which deformation these processes occurred. Pseudosections computed for the chemical systems NaCaKFMASHO and MnNaCaKFMASHO suggest that: (i) the epidote-veining event in the RFP likely occurred at temperatures between 520°C and 490°C at water-saturated conditions; (ii) the main deformation phase likely occurred at 460±40°C and 0.35 ± 0.05 GPa, lasting probably during pluton cooling down to 350°C at slightly under-saturated water-conditions.

Structural evolution of Periadriatic Plutons and its implication on solid-state deformation of granitoid rocks

Introduction and Aims

The main focus of this thesis is the study of the processes controlling localization of ductile deformation. In the lithosphere, the outer shell of the Earth, only the very-uppermost layer (usually 10 km) behaves in a brittle manner, whereas, most of the deformation caused by plate tectonics is ductile in a general sense. Most of this deformation is localized along plate boundaries, along which, seismicity, volcanic activity and mountain building can occur. Localized deformation structures, under both ductile and brittle deformation regimes, control fluid fluxes into the lithosphere, from magmas to hydrothermal fluids. Therefore, the complete understanding of processes that cause deformation localization may help to disentangle the complex mechanisms at the base of tectonic stress transmission and seismicity, formation of mineral ore deposits, magma fluxes and volcanic eruptions.

Localized ductile deformation is usually shown by the development of mylonitic shear zones, a common feature of deformed and metamorphic rocks at all scales, from the plate boundary to the thin section.

We are going to characterize the processes controlling localized ductile deformation in granitoid rocks. Granitoid rocks are the ideal research target for this topic for several characteristics: (i) granitoid rocks are relatively homogeneous rock bodies, without pervasive discontinuities or heterogeneities, that are, conversely, very common feature of almost all metamorphic rocks; (ii) granitoid rocks have a chemical and mineralogical composition similar to that of the middle/upper crust, they actually form more than one third of the continental crust, and therefore they best represent the upper part of the lithosphere. In addition, we are going to talk about ductile deformation and localized mylonitic shear zones in plutonic granitoids (i.e. igneous plutons). Granitoid plutons are the results of the solidification of magma at depth. Depending on the depth of intrusion, the geothermal gradient and the pluton composition, granitoid plutons usually crystallize and cool down to the host rock temperature in very short times from the geological point of view, usually in less than 2-3 Myr. Ductile deformation usually occurs at temperatures above the brittle-ductile transition (at 250-300 °C). Therefore, there is a limited time span during which ductile deformation can occur inside undeformed plutonic granitoids; i.e. the time that the pluton takes to cools down from solidus temperatures down to the brittle-ductile transition. This bring us a third and important reason to study localized ductile deformation in granitoid plutons: (iii) given the short time span in which ductile deformation can occur and the (relative small) amount of strain accommodated, usually ductile structures developed in granitoid plutons are preserved at their pristine stages, frozen-in by the decreasing temperature and changing environmental conditions.

We will focus on the structural evolution of Periadriatic Plutons, a series of magmatic intrusion and plutonic bodies of Oligocene age that occurs along the Periadriatic lineament, one of the major tectonic lineament of the Alpine orogen. Periadriatic magmatism occurred at different crustal levels and tectonic settings, including plenty of different magmatic bodies from subvulcanics to batholiths with dioritic to granitic compositions. Major igneous plutons includes the Adamello, Bergell Rieserferner, Rensen, Traversella, Biella, Pohorje plutons and a series of minor bodies (Rosenberg, 2004). Emplacement occurred at different crustal levels, from 5 km of the Adamello pluton (Rosenberg, 2004), down to the 15-20 km of Rieserferner (Tajčmanová et al., 2009) and Rensen plutons (Trepmann et al., 2004). The Oligocene bimodal Periadriatic magmatism is usually attributed to the break-off of the subducting European lithosphere and following rise of the hot asthenosphere (von Blanckenburg, 1995).

In particular, we have focused our attention on the Rieserferner pluton, one of the major plutonic bodies outcropping in the Eastern Alps (Bellieni et al., 1978).

The aim of this thesis is two-fold:

(1) analyses of the structural evolution of a cooling pluton in order to define the tectonic events at the

regional scale that caused the deformation sequence. Cooling plutons act as a blank recording tape on which tectonic events may leave their fingerprint. Metamorphic units and nappe systems are subjected to tectonic events too, but the (poly)metamorphic history and the overprinting pervasive polyphase deformation make more difficult to decipher the tectonic history they underwent. Magmatic plutons, instead, do not show any pre-existent pervasive fabric due to metamorphism and deformation, therefore tectonic event might be reflected in the development of “discrete” (both in time and space) structures, allowing us to infer the tectonic history in detail.

(2) characterization of the deformation mechanisms that lead to grain size reduction, softening and localization of ductile strain in the continental crust. As already said, ductile structures in cooling plutons develop during a short time span, therefore recording the pristine stages of deformation and allowing us to decipher the mechanisms controlling the localization of ductile strain, i.e. the nucleation of mylonitic shear zones and incipient strain accommodation.

This thesis is the result of three years of research during which the two-fold aims have been chased with a multi-disciplinary approach. The structural evolution of the Rieserferner pluton have been firstly defined by field survey, with more than 350 stations of structural analysis mainly concentrated in the central portion of the pluton, where structures are better exposed on glacially-polished outcrops. Structural data have been organised in a GIS database and then integrated with the interpretation of aerial images, DTMs and published maps of the area. Selected representative outcrops have been recreated digitally by photogrammetrical techniques (orthorectification of 3D images obtained from photomosaics) and detailed quantitative mapping of the structures have been carried out on orthophotos of the outcrop.

Oriented samples of selected structures have been collected on the field, from which oriented thin section have been cut for further microstructural investigations. Microstructural investigation have been carried out by means of optical microscopy, Computer-Integrated Polarization (CIP) microscopy, Scanning Electron Microscopy (SEM) and Electron MicroProbe (EMP). In particular, SEM-based techinques, such as Secondary Electron (SE) imaging, BackScattered Electron (BSE) imaging, Cathodoluminescence (CL) imaging and Electron BackScattered Diffraction (EBSD), were adopted to investigate microstructures in detail. Microstructural quantification have been carried out by means of image analyses techniques.

In addition selected samples were prepared for X-Ray Fluorescence (XRF) and X-Ray Powder Diffraction (XRPD) analyses in order to quantify the chemical and mineralogical compositions. Thermodynamic modelling with Perple_X (Connolly, 2005) have been carried out to define the temperature and fluid conditions at which selected deformation structures develop during the deformation sequence of the pluton.

Structure of the thesis

This thesis is subdivided into four main chapters.

In **Chapter 1**, the structural evolution of the Rieserferner pluton is described, interpreted and compared to the known Tertiary tectonic evolution of the Eastern Alps. The ductile-to-brittle evolution occurred in a period of complex and changing geodynamic processes, therefore its analysis and the paleostress inversion from structures may help us to decipher the evolving regional tectonics.

In **Chapter 2**, the microstructural and textural evolution of mylonitic quartz veins occurring in the Rieserferner pluton is described, the microstructural mechanisms that lead to grain size reduction and localization are discussed and compared to other natural cases and experimental results. This chapter is published in a modified form in Lithos (Ceccato et al., 2017).

In **Chapter 3**, the results of EBSD analysis on myrmekites (plagioclase + quartz symplectites) are presented and discussed in terms of grain size reduction processes and deformation mechanisms. Myrmekites are the most common metamorphic reaction that consumes K-feldspar, usually the strongest phase during deformation of granitoid rocks at middle-upper crustal conditions. The transformation of K-feldspar into a fine grained plagioclase + quartz aggregates lead to softening of the rock.

In **Chapter 4**, phase diagram sections computed through thermodynamic modelling with Perple_X are presented. Pressure-temperature-fluid conditions during deformation of granitoid ultramylonites developed during *stage 3* are discussed and compared to the observed microstructure.

At the end, a brief summary of the thesis and a general discussion about strain localization in the RFP are presented.

Chapter 1

Structural evolution of the Rieserferner Pluton in the framework of the Tertiary tectonics of the eastern Alps

Alberto Ceccato[1], Giorgio Pennacchioni[1]

[1] Department of Geosciences, University of Padova, Via Gradenigo 6, I-35131 Padova, Italy

Abstract

The central portion of the Oligocene Rieserferner pluton (RFP) consist of dominant tonalites and granodiorites that show a sequence of solid-state deformation stages developed during pluton cooling and exhumation. The ductile-to-brittle deformation sequence includes: (i) steeply dipping joints, leucocratic dykes and quartz-feldspar veins and associated ductile shear zones; (ii) shallowly dipping joints with associated epidote and quartz veins and ductile shear zones; (iii) steeply dipping mafic dykes and calcite-white mica-bearing brittle-ductile faults; (iv) steeply dipping pseudotachylyte-bearing cataclastic faults; and (v) zeolite-bearing faults. Integrating new field, microstructural and geothermo-chronological data with published data we have related the deformation sequence to the Tertiary tectonics of the Eastern Alps. (i) three main ductile deformation stages developed during Oligocene, followed by two brittle deformation stages during Miocene; (ii) Kinematics analyses suggest that a switch in shortening direction from N290° to N350° occurred between Early Oligocene and Late Miocene; (iii) this stress field variation can be related to regional scale tectonic processes such as the occurrence of slab break-off and isostatic rebound, exhumation and lateral escape tectonics and, in the end, indentation tectonics from the middle Miocene onward.

As observed in other plutons, the network of deformation structures within the RFP is controlled by the development and later reactivation in shear of precursor joint sets. These joints were either exploited as faults or localized ductile shear zones. Shear zone geometry and type depend on the composition and geometry of the precursor.

1.1. Introduction

The emplacement of igneous plutons in the middle to upper continental crust during syntectonic magmatism is strictly related to the tectonic regime and usually controlled by major deformation structures (e.g. Hutton, 1988). Depending on the exact spatial and temporal relation between pluton emplacement and tectonic deformation, igneous intrusions may show different degree of internal deformation (Gapais, 1989). Plutons behave as a blank recording tape on which tectonic processes are recorded and deformation structures can develop without the influence of pre-existing structures and pervasive heterogeneities typical of metamorphic rocks (e.g. Gapais, 1989).

During syntectonic emplacement, if tectonic strain is relatively small, pervasive homogeneous deformation structures does not develop, and does not influence the development of following structures. Therefore, the analysis and interpretation of deformation structures developed within relatively "undeformed" igneous pluton may be an useful tool to disentangle the complex tectonic events occurred during pluton cooling and further exhumation to the surface (e.g. Rosenberg, 2004; Ciancaleoni and Marquer, 2006, 2008).

The tectonic evolution of the Eastern Alps during Oligocene and Miocene is characterized by a varied sequence of different and interacting tectonic processes, including: slab break-off triggering magmatism (von Blanckenburg and Davies, 1995; Rosenberg, 2004), switch in regional dominant kinematics (Mancktelow et al., 2001), indentation and lateral escape tectonics (Ratschbacher et al., 1991), and orogen-parallel extensional tectonics leading to the formation of tectonic windows and exhumation of deep-seated units (Frisch et al., 2000; Scharf et al., 2014).

Syntectonic magmatism occurred during the Oligocene all along the inner portion of the Alpine orogen, along the Periadriatic lineament (PL) (Martin et al., 1993; Stipp et al., 2004; Rosenberg, 2004; Ciancaleoni et al., 2006; Pomella et al., 2011). Larger plutonic intrusions emplaced in the surrounding units bounded by the PL have mainly escaped strong tectonic deformations, that instead characterizes smaller, sheeted plutonic bodies outcropping directly along the PL (Martin et al., 1993).

In particular, the Rieserferner pluton is one of the major Periadriatic plutons occurring in the Eastern Alps (Bellieni, 1978). Previous works were mainly focused on the analysis of the bulk deformation structures of the pluton in order to define the emplacement mechanisms and syn-emplacement tectonic framework (Steenken et al., 2000; Wagner et al., 2006). The sub-solidus deformation internal to the pluton have always been poorly and briefly described (e.g. Mancktelow et al., 2001; Scheuvens and Mann, 2004).

In this work we show that during post-magmatic cooling the intrusive rocks were deformed along discrete ductile shear zones and cataclastic faults that overprinted sub-magmatic and solid-state foliations. The deformation sequence reflects the tectonic evolution during Oligocene-Miocene cooling and exhumation of the pluton. Integrating new data from meso- and microstructural analyses, geochronology and geothermobarometry focused on deformation structures with the existent literature, we have defined: (i) the deformation sequence characterizing the Rieserferner pluton during its cooling and exhumation history; (ii) the stress field evolution and (iii) the tectonic regime under which deformation occurred.

In addition, some initial constraints on the definition of the mechanisms controlling the development of localized ductile shear zone in the RFP treated in following chapters have been analysed. The discrete ductile shear zones exploited precursor joints and joint-filling veins, as it is commonly observed in other granitoid plutons (e.g. Adamello: Pennacchioni, 2005; Sierra Nevada: Pennacchioni and Zucchi, 2013) and in meta-granitoid units (Pennacchioni and Mancktelow, 2007; Menegon and Pennacchioni, 2010). Given the very short time span during which ductile deformation occurs and small amount of strain accommodated, pristine stages of localization and shear zone nucleation may be easily investigated.

1.2. Geological background

The Rieserferner pluton (RFP, Eastern Alps) belongs to a series of intrusions emplaced along the Periadriatic Lineament in the Eocene-Oligocene (referred to as Periadriatic magmatism: Rosenberg, 2004). The RFP emplaced at 32 ± 0.2 Ma (Romer and Siegesmund, 2003) in the polymetamorphic Austroalpine unit during the main Alpine "Tauern" metamorphism, at 15 km depth (0.25-0.375 GPa, Cesare, 1994; 0.3 GPa, 10.5-13.5 km Schultz et al., 2008; 0.4-0.41 GPa, Tajčmanová et al., 2009; Cesare et al., 2010).

The RFP consists of calc-alkaline magmatic rocks belonging to 4 main intrusions: (1) small batches of quartz-diorites; (2) coarse grained garnet-bearing tonalites, (3) fine grained hornblende-bearing granodiorites, and (4) fine grained leuco-granodiorite to granites (Fig. 1; Bellieni, 1978; Bellieni et al., 1981; Steenken et al., 2000). This magmatic association resulted from a complex two-stage process of fractionation of a tonalitic/dioritic magma in an "andean-type" continental margin (Bellieni et al., 1981). The less differentiated tonalites and quartz-diorites are preserved as a rim around the predominant, more evolved granodioritic to granitic core (Fig. 1). The contacts between magmatic intrusions are transitional and consist of mixing zones of hundreds of meters (Steenken et al., 2000). Mutual crosscutting relationships show that differently evolved magmas were coeval (Wagner et al., 2006). These intrusives were crosscut by different sets of aplite-pegmatite dykes ranging in age between 29 and 26 Ma (white mica and biotite K-Ar cooling ages: Prochaska, 1981). The latest magmatic event, although not related to the Periadriatic magmatic cycle, is represented by the lamprophyre dykes (26.3 + 0.7 Ma biotite K-Ar ages: Steenken et al., 2000).

Emplacement of the RFP occurred during a period of intense geodynamic activity and related complex tectonics for the region. Periadriatic magmatism have been related to slab-break off processes during continental collision between Adria microplate and Eurasia (von Blanckenburg and Davies, 1995). Europe-Adria convergence in the Eastern Alps shows an evolving direction from Eoalpine crustal stacking to Miocene Neoalpine tectonics (Platt et al., 1989; Ratschbacher et al., 1989). Indentation of Adria microplate into the Eoalpine Austroalpine orogen occurred during

Miocene leading to the onset of dominant lateral escape and exhumation processes in the Eastern Alps (Ratschbacher et al., 1991). Tertiary Alpine deformation and metamorphism affected the Austroalpine units surrounding the future RFP, resulting in a complex pattern of heterogeneous ductile mylonites developed at lower Greenschists facies conditions (350±50°C, Cesare and Hollister, 1995) (e.g. Defereggen-Antolz-Vals line, Mancktelow et al. 2001; Kalkstein-Vallarga line, Cima Dura – Durreck phyllonites, Mazzoli et al. 1993).

The DAV is the major sinistral strike-slip tectonic lineament, striking mainly ENE-WSW, representing the southern limit of the Alpine greenschists facies metamorphism (Mancktelow et al., 2001; Schulz et al., 2008; Linner et al., 2008). In addition, DAV controlled the emplacement of all the Periadriatic intrusives (Rieserferner, Zinsnock, Rensen and Monte Alto plutons) during Oligocene magmatism in the region (e.g. Rosenberg, 2004; Handy et al., 2005). Regional kinematics (and DAV kinematics too) switched from sinistral- to dextral dominated during the solidification of the RFP (Mancktelow et al., 2001).

Emplacement mechanisms for the RFP are still a matter of debate, and proposed models include: (i) infilling of a pull-apart structure between two E-W striking sinistral strike-slip shear zones bounding the pluton along its northern and southern borders (Steenken et al., 2000); (ii) subhorizontal hydrofracturation of the host Austroalpine units, with sill emplacement and following doming (Wagner et al., 2006). Both models agree on the fact that the feeder channels/dykes reside along the DAV fault system. As a consequence of pluton emplacement, an extensive metamorphic contact aureole developed in the Austroalpine host units (600-620°C at the contact with RFP; Cesare, 1994).

Oligocene transpression led to sinistral and north-side-up movement along the DAV (Steenken et al., 2002; Schulz et al., 1994, 2008). The Austroalpine units north of DAV were affected by a sinistral wrench corridor, dominated by sinistral stike-slip shear zones (DAV, KV, CD), S-vergent folds and back-thrusts (Ahrntal shear zone, Schneider et al., 2009; Lappach structure and Speikboden shear zone; Wölfler et al., 2008; Mancktelow et al., 2001). Austroalpine units south of the DAV were involved in a series of ductile-to-brittle structures, that includes in chronological order (Linner et al., 2008): (i) SW-directed thrust faults; (ii) steep WSW-ENE-striking transpressive faults with dominant strike-slip kinematics, and later (iii) NW- and SE-directed normal faulting. During pluton emplacement, the regional kinematics switched from sinistral- to dextral-dominated, as the result of the onset of the influence of the Periadriatic lineament around 29-30 Ma (Mancktelow et al. 2001, Muller et al., 2002).

The main regional phase of exhumation was coeval with the uplift of the Tauern Window through the activity of Brenner to the west, and Katschberg normal fault zones to the east (23-17 Ma; Genser and Neubauer 1989, Mancktelow et al., 2001). After exhumation across the brittle-ductile transition, the region was affected by sets of brittle faults coherent with a N-S to NNW-SSE regional shortening (Mancktelow et al., 2001; Pennacchioni and Mancktelow, 2007, 2013). These sets of faults include: (i) top-to-S or SE steep reverse faults; (ii) top-to-E or ENE steep normal faults with minor dextral component; (iii) NE- to NNE-striking sinistral strike-slip faults.

Differential exhumation, increasing from east to west, affected the Austroalpine units hosting the RFP, due to differential N-S shortening and lateral escape during Southern Alps indentation (Steenken et al., 2002; Trepmann et al., 2004; Luth and Willingshofer, 2008). This regional tilting affected the RFP causing a post-intrusive eastward tilting of about 5° around an N-S striking axis (2.2 km of differential exhumation between eastern RFP tail and westernmost tonalitic body; Steenken et al., 2002). This tilting occurred soon after the pluton emplacement, after the development of a stable paragenesis in the metamorphic aureole (that suggests at most 0.1 GPa of pressure difference between the western and eastern portion of the Rieserferner; Wagner et al., 2006); and before the system cooled down below the PAZ for apatite fission tracks (Steenken et al., 2002). Following exhumation is homogeneous over the surrounding area through closure temperature of apatite fission track (110°C) during Miocene (Luth and Willingshofer, 2008).

Even though the tectonic activity was very intense during emplacement of the pluton, previous workers have always reported a lack of pervasive deformation features inside the pluton, as a consequence of fast cooling between submagmatic and greenschist facies conditions (e.g. Steenken

2000; Scheuvens and Mann, 2004). The estimated cooling time of the pluton to equilibrate to the host rock temperature varies from 2 to 1.5 Ma, depending on the cooling model and the reference host rock temperature (350 °C: Steenken et al., 2002; 425 °C: Wagner et al., 2006). During this fast cooling, however, the RFP have recorded several deformation features. Early sub-magmatic to solid-state foliation commonly observed in the RFP is associated with both the emplacement-related doming process and the prolonged sinistral activity of the bounding shear zones (Henry, 1975; Steenken et al., 2000; Wagner et al., 2006). The transition from high-temperatures distributed to low-temperature localized deformation structures occurred during the first 100 kyr of cooling, according to the models of Wagner et al. (2006). High-temperature solid-state deformation microstructures (such as "chessboard" subgrains in quartz, grain boundary migration microstructures and biotite recrystallization, Steenken et al. 2000) are weakly developed and mainly preserved in the inner and western portion of the RFP. Low greenschist facies mylonitic zones along the northern (Scheuvens and Mann, 2004, Wagner et al., 2006) and southern contacts (Mancktelow et al., 2001; Wagner et al., 2006) are the main low-temperature deformation features reported for the RFP. A likely ductile reactivation of aplitic dykes was first reported by Scheuvens and Mann (2004) close to the northern mylonitic zone. A set of transitional narrow low-grade shear zones (localized along pre-existing quartz veins) to discrete brittle faults related to the Periadriatic lineament have been described inside the pluton by Mancktelow et al. (2001). Other mesoscale deformation structures (such as brittle-ductile faults and folded granitoids) have been reported by few authors but never described in detail (e.g. Dal Piaz, 1934; Visonà and Bellieni - personal communication, 1973; Henry, 1975; Mager, 1985).

Therefore, a more detailed description of the deformation structures recorded inside the RFP will help us to better understand and characterize both the structural evolution of this region of the Eastern Alps during Oligocene.

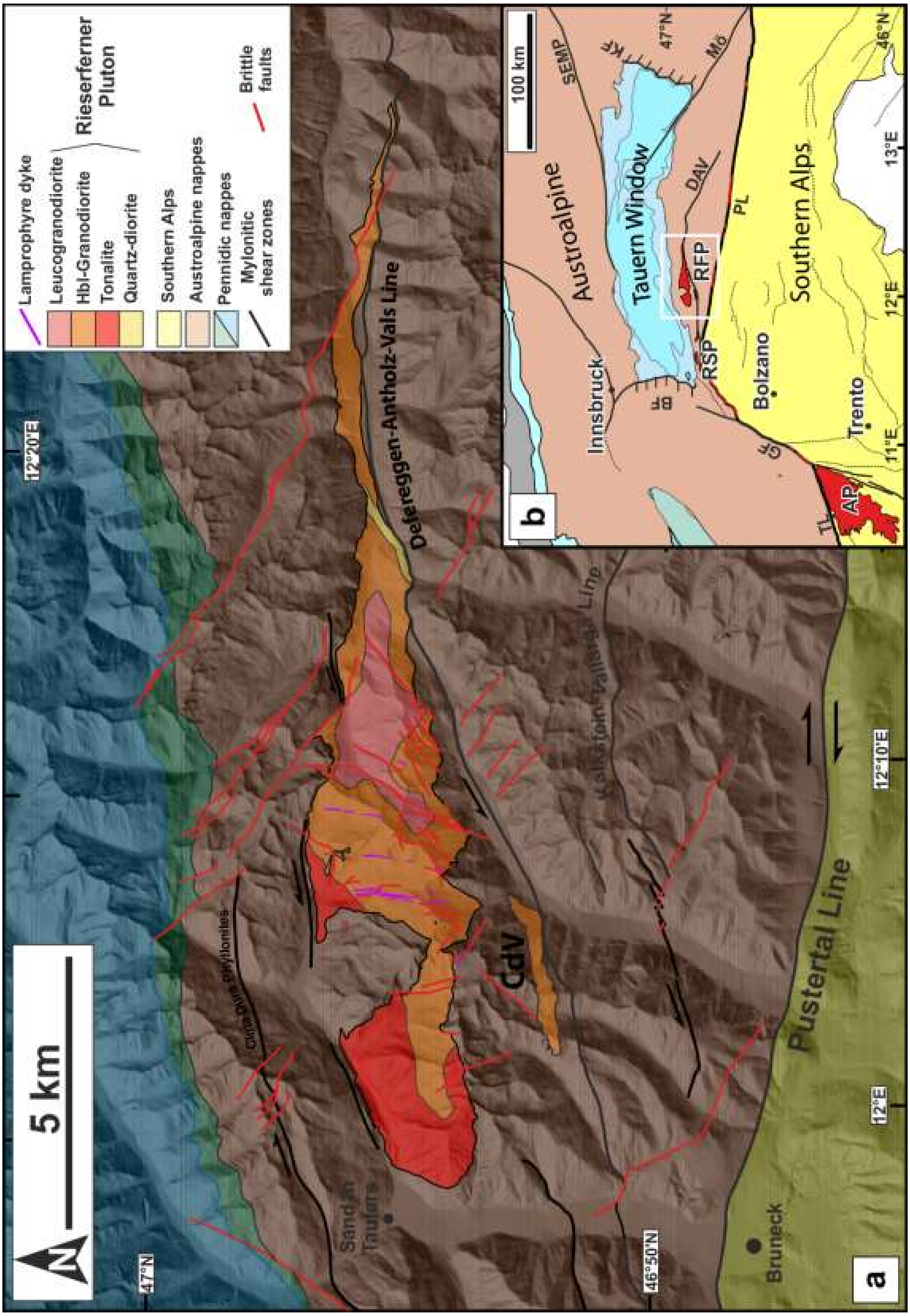

Figure 1: Geological sketch of the Rieserferner Pluton and Eastern Alps showing the main tectonic features. (a) Geological sketch of the Rieserferner pluton and surrounding Austroalpine and Pennidic units. CdV/ZNP: Cima di Vila/Zinsnock pluton. (b) Tectonic sketch of the central Eastern Alps. Acronyms as follow: **AP** Adamello pluton; **BF** Brenner Normal Fault; **DAV** Defereggen-Antholz-Vals lineament; **GF**: Giudicarie fault system; **KF** Katschberg Normal Fault; **Mö** Möltal fault; **PL** Periadriatic Lineament; **RFP** Rieserferner Plutonic Complex; **RSP** Rensen pluton; **SEMP** Salzach-Ennstell-Mariazell-Puchberg fault; **TL** Tonale Line.

1.3. Field observation and structural evolution

The field study was conducted in the central Rieserferner pluton, between the Geltal (Valfredda, Rein in Taufers, Italy) to the west, and the Staller Sattel area (Antholz, Italy; St. Jacob in Defereggen, Austria) to the east (Fig. 1). The studied area consists of, from west to east: (i) biotite tonalite with local magmatic garnet; (ii) medium- to fine-grained hornblende-bearing granodiorite commonly including fine-grained mafic microgranular enclaves (MME); (iii) fine grained leuco-granodiorite. This area provides excellent exposures on glacier-polished outcrops ideal for field study. The determined sequence of late- to post-magmatic intrusive and deformation structures includes (from oldest to youngest): (i) magmatic to submagmatic foliation (*stage 1*); (ii) steeply dipping joints, leucocratic dykes, quartz (±feldspar) veins and associated ductile shear zones (*stage 2*); (iii) shallowly dipping joints, filled with epidote and quartz veins, and associated ductile shear zones (*stage 3*); (iv) steeply dipping mafic dykes and calcite-white mica-bearing brittle-ductile faults (*stage 4*); (v) steeply dipping pseudotachylyte-bearing faults (*stage 5*); and (vi) zeolite-bearing faults (*stage 6*). The field characteritics of the different set of structures are described in the following sections and illustrated in the photographic plates of Figs. 2-8. The orientations of the structures are reported in the stereoplots of Fig. 9 and in the structural sketches of Figs. 10 and 11.

1.3.1 Stage 1 structures

The magmatic rocks of the studied area include a more or less well-developed, but pervasive foliation sub-parallel to the alignment of MME (Fig. 2a) and parallel to a local faint compositional layering due to the alternation of layers relatively richer in biotite and more leucocratic ones. The foliation is defined by alignment of biotite, hornblende and by the elongation of feldspars and quartz grain-scale domains. The trend of this “magmatic to submagmatic” foliation is described, at the scale of the whole RFP, by Steenken et al. (2000) and Wagner et al. (2006). In the studied area, the foliation shows a heterogeneous trend that apparently defines a S-C dextral structure in map view, with more strongly foliated “C” domains trending E-W (sub-parallel to the steeply dipping southern contact with the country rock) alternating with “S” domains with a weaker foliation trending from NW-SE to N-S

(Figs.9a and 10a). Similar dextral S-C structures are observed also at the outcrop scale (Fig. 2b).

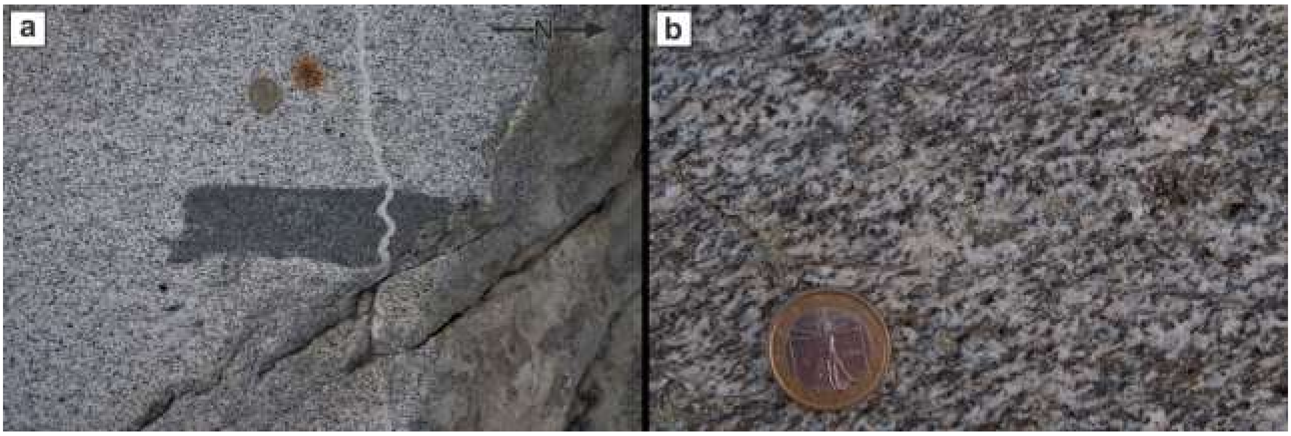

Figure 2: Magmatic/submagmatic structures. (a) Buckling of a thin aplitic dyke inside a mafic microgranular enclave (MME). The elongation of the MME tracks the local trending of bulk foliation (here, almost N-S trending). Flattening of MME and buckling of the aplitic dyke both suggest an E-W shortening direction. (b) Bulk homogeneous foliaton in the RFP showing S-C microstructure suggesting dextral strike-slip kinematics (sheared northern pluton margin). E-W trending C-planes are indicated by slightly deflection of the SW-NE trending S bulk foliation planes.

1.3.2. Stage 2 structures

Stage 2 structures are steeply dipping (>70°) and arranged in different crosscutting and conjugate sets (Figs. 9b-e). The leucocratic dykes, ranging in thickness between a few mm and several meters (up 7 m), include: garnet-bearing aplites, biotite-bearing aplites, and pegmatites. These dykes are locally zoned with a core of either biotite-rich aplite or quartz-feldspar vein and aplitic/pegmatitic margins. The main set of dykes strikes WNW-ESE (Figs. 9c and 10b) and is crosscut by biotite-bearing aplites arranged into two steeply-dipping conjugate sets striking WSW-ENE and NW-SE (Fig. 9d). Swarms of dykes with > 2-3 dyke/m (e.g. Figs. SM1-3) alternate with domains of low spatial density of dykes. The above described sets of leucocratic dykes crosscut rare N-S and NE-SW to NNE-SSW-striking aplites referred to earlier magmatic stages.

Joints and associated quartz (±feldspar) veins are mainly arranged in conjugate sets striking E-W and WNW-ESE, therefore sub-parallel to the main dyke set (e.g. Fig. 3e). Undeformed veins, discontinuously filling the joints, consist of massive milky quartz and minor feldspar. These veins show thin stripes of the host rock arranged sub-parallel to the boundary suggestive of episodes of crack-seal (Fig. 3a). The quartz vein filling is commonly developed at extensional domains related to a shear reactivation of the parent joint (Fig. 3b) (see below). Joints and veins are segmented and arranged en-echelon showing local stepovers at 1-10s cm scale. Joints, veins and biotite-bearing aplites localized strike-slip ductile shear (Figs. 3c-e), whereas the main set of aplite-pegmatite dykes did not (Figs. 3e). Shear strain within aplites and veins is commonly homogeneously distributed (Fig. 3c,d) with the accommodated shear strain γ, determined from the foliation inclination to the boundary, being commonly larger in quartz veins (locally >10) than in aplite ($\gamma < 5$).

Joints sharply localized ductile slip and accommodated displacements of as much as a few 10s cm. In the host rock of sheared joints an associated solid-state foliation is commonly only developed at contractional bends and step-over domains between en-echelon joint terminations (Fig. 3f) (e.g. Pennacchioni, 2005; Pennacchioni and Zucchi, 2013). The quartz vein filling of the sheared joints is preferentially developed at extensional bends, pull-aparts and wing-cracks consistently with the sense of ductile slip (Fig. 3b). Many of these extensional vein fillings are undeformed and, therefore, quartz deposition was coeval with shearing. Mutually intersecting sheared joints, quartz veins and aplites with opposite sense of shear locally develop foliated thinning zones (Fig. 3g) (Pennacchioni and Mancktelow, 2007) also indicative of the coeval ductile slip along the different shear zones. The spatial distribution and arrangement of exploited structures led to the development of a shear zone lozenge- to parallelogram-shaped network delimiting low-strain the undeformed domains at various scales (Fig. Supplementary Material SM1-4).

The sense of shear is opposite for the conjugate WSW-ENE- and the NW-SE-striking sets of aplite, and for E-W-and WNW-ESE-striking joints and quartz veins (dextral and sinistral, respectively: Figs. 9d-e, 10c, 11a). In the areas characterized by a stage 1 foliation trending about N-S, small (cm) lens-shaped, sub-vertical quartz veins also locally developed as filling of boudinaged necks of the faint more leucocratic layers within the granodiorite (Fig. 3h, 9b).

Figure 3: Deformation Stage 2 structures. Image orientation, where not differently reported, is looking down southward. (a) Non-sheared quartz-feldspar vein showing a banded structure composed by alternating layers of quartz-feldspar and host rock fragments. This banded structure likely reflect the crack-seal process during vein opening. (b) Quartz-feldspar vein croscutting MMEs. Pull-apart structures (right MME) and sinistral offset (left MME) across the quartz-feldspar vein suggest its shear reactivation. Quartz-feldspar infilling of pull-apart structure suggest the synkinematic emplacement of the vein. (c) Quartz-feldspar vein showing sinistral strike-slip reactivation as inferred from the development of homogeneous internal foliation, defined by the alternation of fine-grained feldspar layers and coarse sugary quartz. (d) Composite leucocratic dyke crosscutting a MME. The dyke is composed of pegmatitic rims and biotite-rich aplitic core. Shear reactivation with dextral strike-slip kinematics is inferred from dextral marker offset and the occurrence of a internal homogeneous foliation in the dyke, defined by iso-riented biotite grains in a fine-grained quartz-feldspar matrix. (e) Sub-parallel aplite dyke and quartz-feldspar vein crosscutting a MME. Quartz-feldspar vein is reactivated in shear as suggested by the dextral strike-slip offset of magmatic marker. (f) Sheared E-W trending joints crosscutting a leucocratic layer (N-S-striking). Joint segments are reactivated in shear as inferred from leucocratic layer dextral strike-slip offset and the development of a foliated contractional jog in between overstepping joint segments. Note the synkynematic quartz infilling at overstepping joint terminations. (g) Quartz-feldspar vein (E-W trending) crosscutting aplitic dyke (NE-SW trending). Both structures are reactivated in shear as inferred from the mutual strike-slip displacement (sinistral across the quartz-feldspar vein; dextral across aplitic dyke) and the development of a foliated thinning zone at the intersection between the two structures. (h) Leucocratic layers showing a set of diamond-shaped quartz veins. Their development is limited to the thickness of the layer. It is worth noting that, homogeneous bulk foliation (almost parallel to the layer) is lacking inside the leucocratic layer. Looking down eastward.

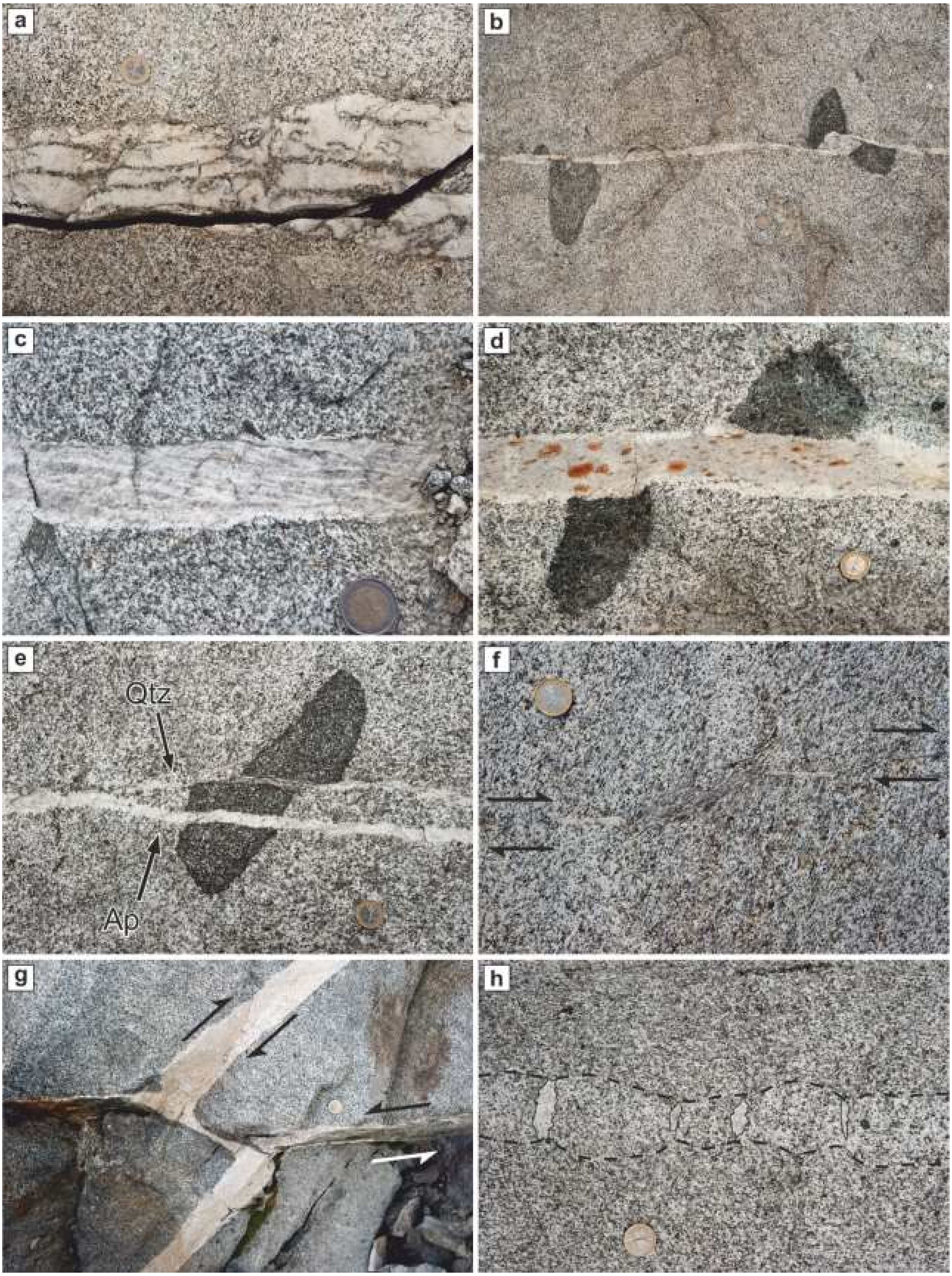
a
b
c
d
e
Qtz
Ap
f
g
h

1.3.3. Stage 3 structures

The studied area is characterized by a pervasive set of shallowly (15-25° on average) ESE-dipping joints (Figs. 4a, 9f, 10d), locally filled with either quartz or, more rarely, epidote veins (Fig. 4b-c). The spacing between these joints is rather regular and ranges between 2 and 5 m (cf. Fig. SM1). Other associated, but less expressed, joint sets shallowly dip toward WNW-NW, N-NNE and SSW-S (Fig. 9f). These joints commonly represent the surface of many outcrops of the area. The joints are segmented at several scales and locally arranged in en-echelon geometries (cf. Fig. SM1). In most cases, epidote and quartz veins are planar structures continuous over 10s of meters. The vein thickness is of as much as a few mm, for epidote veins, and 30 cm, for quartz veins (e.g. cfr. Figs. 4b and 4cSM4).

The *stage 3* structures systematically cut the *stage 2* ones and are commonly exploited as localized ductile shear zones (Fig. 4c-f). Similar to the *stage 2* structures: (i) joints were commonly sharply exploited without any major development of a foliation except at their tip and contractional stepovers; and (ii) quartz veins strongly localized ductile shearing. In contrast, the epidote veins (and only to a lesser extent the joints and the quartz veins) developed granitoid mylonites to ultramylonites at their boundary typically a few mm to few cm in thickness (Fig. 4d-e). The mineral stretching lineation of shear zones strikes WNW-ESE and kinematic indicators indicate a top-to-east sense of shear for all sets of stage 2 joints and veins, corresponding to a normal dip-slip lineation for the main joint set in its dominant present orientation (e.g. Figs. 4d, 11b). Looking down-dip, the main set of shear zones exploiting the main set there is a systematic sinistral offset of crosscut markers, consistent with the occurrence of right-stepping contractional stepovers (Fig. 4f) (e.g. Figs. SM1-3), that does not fit with the inferred general top-to-east kinematics. In many cases, slip planes are gently folded around a N-S-trending rotation axis (e.g. joint set in Fig. 4a). Thus, W-dipping planes are transformed into E-dipping planes and vice versa (e.g. model presented by Henry, 1975). In other outcrops instead, slip planes with different orientation are observed to mutually cross cut.

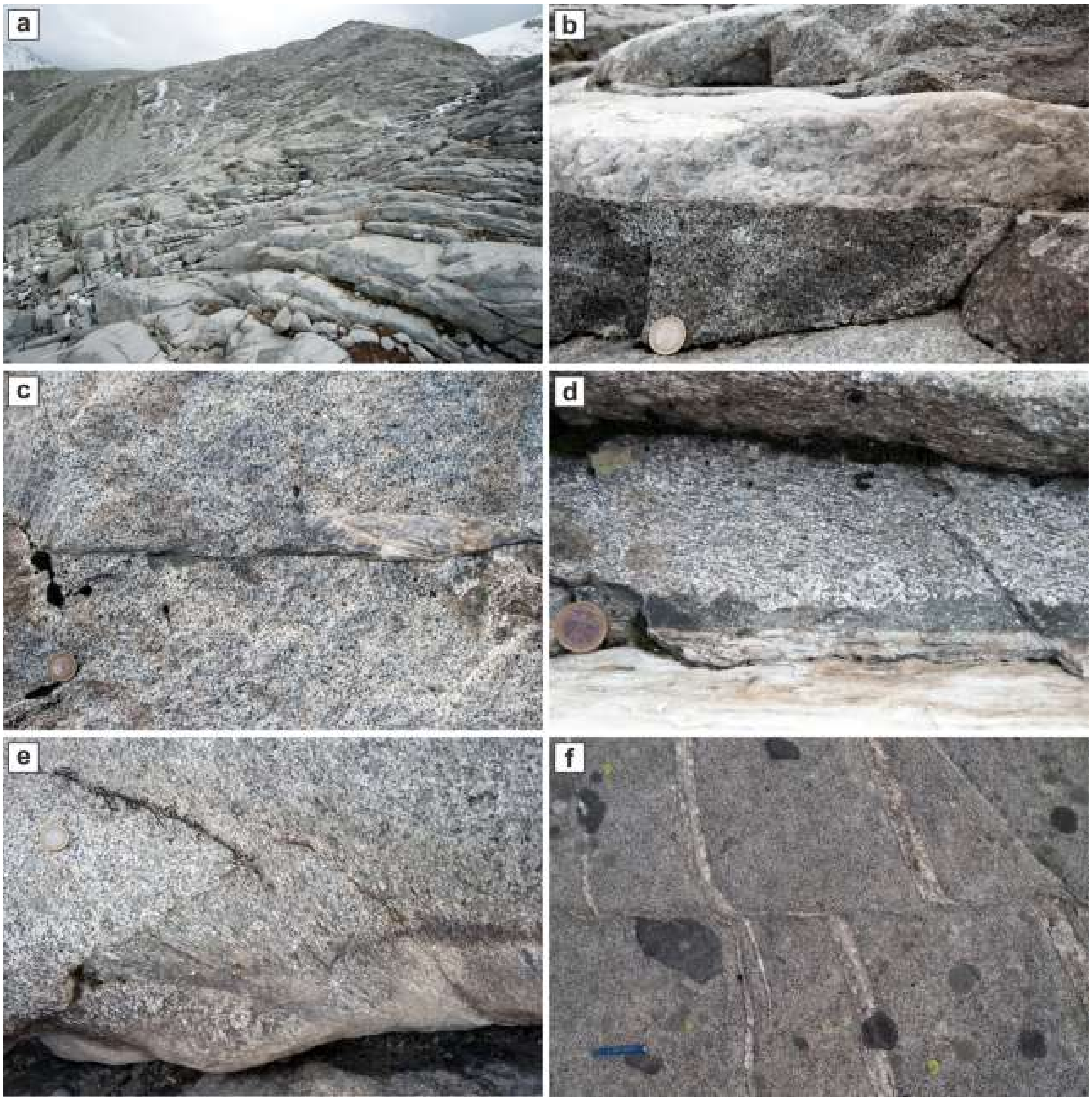

Figure. 4: Stage 3 ductile shear zones exploiting quartz- and epidote-rich veins. Image orientation, where not differently reported, is looking southward. (a) Pervasive set of shallowly E-dipping joints. Note the slight bending of joint planes around a N-S trending axis. Looking SE. (b) Thck coarse grained shallowly W-dipping quartz vein. (c) Tonalite ultramylonite developed exploiting quartz and epidote-rich veins, occurring along the same plane. Top-to-east shear sense can be inferred from the development of homogeneous foliation inside quartz mylonite and heterogeneous foliation in the host tonalite along the epidote vein/ultramylonite. (d) Quartz and tonalite ultramylonites developed along a former quartz vein showing east-dipping dip-slip lineation (black arrow). Top-to-east kinematic is inferred from sigmoidal foliation developed in the host granodiorite. (e) Sigmoidal foliation developed in the host granodiorite along a sheared epidote vein. (f) Tonalite ultramylonite nucleated epidote vein crosscutting E-W trending aplitic dykes. Dyke offset suggests the occurrence of a sinistral strike-slip kinematics during epidote vein shear reactivation. Looking east.

The quartz vein filling of *stage 3* joints is coarse (cm) grained and the progressive shearing of veins has been described in detail by Ceccato et al. (2017) and in Chapter 2. Quartz veins (Fig. 4b-c) that show incipient shear reactivation ($\gamma < 2$) are coarse grained and characterized by a more or less homogeneous internal foliation, at high angle to the shear plane, given by stretched quartz vein crystals. With increasing strain ($\gamma > 3$), a mylonitic homogeneous foliation is developed and the grain size is much finer, giving to the sheared quartz vein a flinty aspect. Along epidote-rich veins, a sigmoidal foliation is developed in the surrounding granitoid (Figs. 4c,d,e). With increasing strain, a cm-thick ultramylonitic fine grained band is developed along the vein selvages, and the former epidote-rich vein (and occasionally also quartz vein) is stretched and boudinaged along the shearing plane.

Along the shear plane (vein surface) sub-vertical quartz veins striking NNE-SSW are common interpreted as tensional T fractures (Fig. 9f).

1.3.4. Stage 4 structures

Stage 4 includes moderately-steeply dipping, N-S-striking fracture clusters, brittle-ductile shear zones and mafic dykes (Figs. 9g-k). The fracture clusters are approximately tabular zones (of as much as a few meters wide) of closely spaced (commonly at the cm scale), dominantly sub-parallel to anastomosing, mm-thick joints and slip surfaces/fractures (Fig. 5a) similar to the tabular fracture custers described by Riley and Tikoff (2010) in the Sierra Nevada pluton. Individual clusters may consist of a few 10s of fractures. These clusters alternate with non-fractured domains of as much as 100s m wide. More in detail, the 3D geometry of the fracture network is complex and includes shallowly dipping and folded surfaces (see below) as well as interference with previous shallowly dipping stage 3 structures (Fig. 5b); along strike (over distances ranging from few meters to 10-100 m), the shear zones change in thickness, in the spatial density of fractures and show a stepped geometry. The spatial density of fractures is also locally dependent on the host rock and abruptly increases within aplitic dykes. On vertical sections, the fracture clusters either crosscut the shallowly E-dipping set of *stage 3* structures or, more commonly, interact with them changing

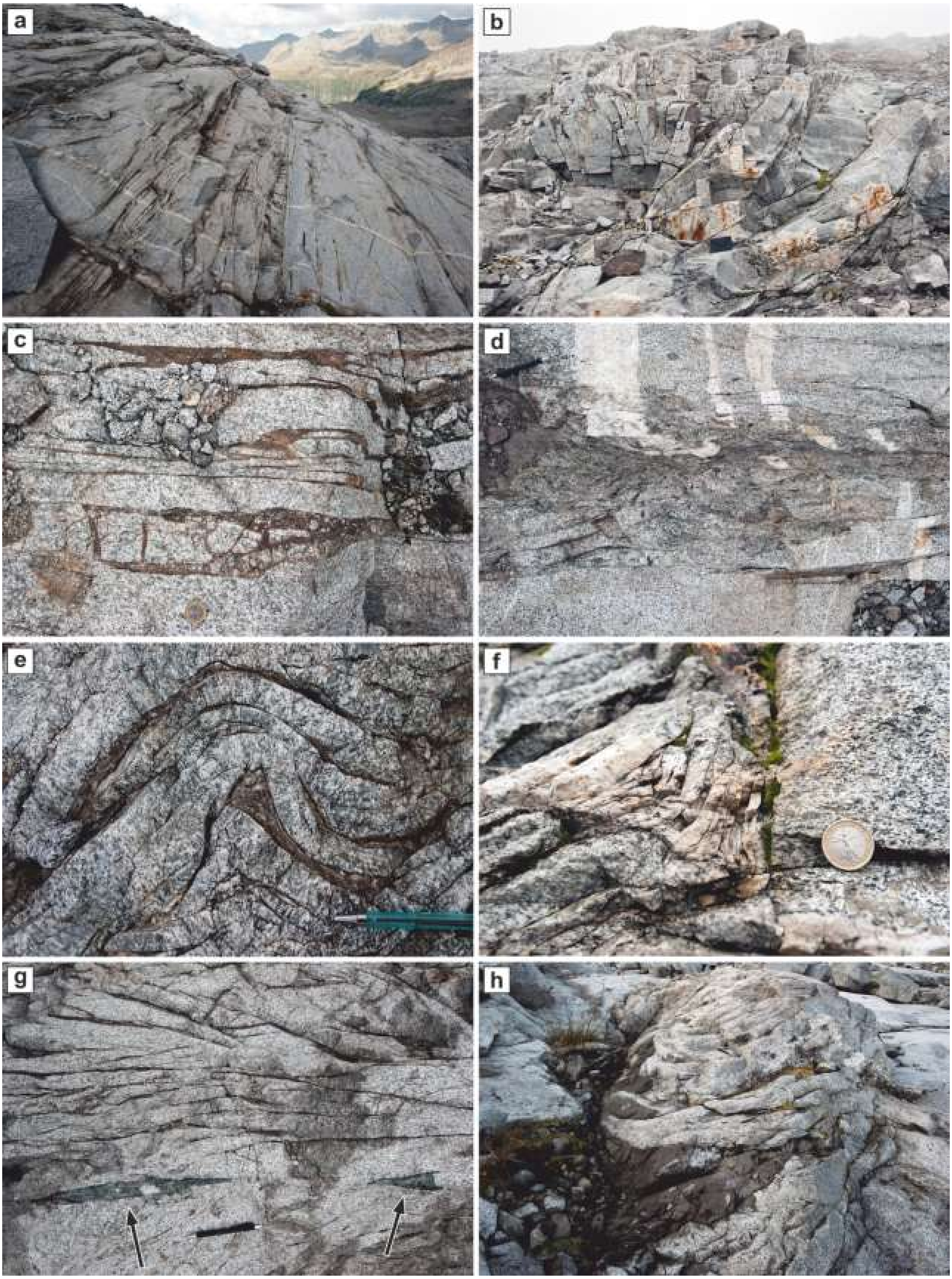
a
b
c
d
e
f
g
h

Figure 5 (previous page): Stage 3 brittle-ductile faults, fracture clusters and folded granitoids. (a) Outcrop of N-S trending joint cluster developed in the central RFP, showing the spatial organization of fractures in planar view. Fracture clusters are characterized by high fracture density areas of the pluton separated by un-fractured rock. Note the minimum offset of aplitic dykes crosscut by oints of the fracture cluster. Looking north. (b) Vertical outcrop of a fracture cluster showing the complex geometry of joints in depth. Vertical joints are crosscut, and in turn transect, E-dipping brittle-ductile shear planes. Looking south (c) White mica + calcite veins and fractures. Brecciated granodiorite in between two fracture sets is cemented by calcite. Looking down eastward. (d) Brittle-ductile mylonitic layer localized on precursor fracture cluster. Note the significant difference in (sinistral) strike-slip offset of aplitic dykes across knife-sharp joint of the fracture cluster and the mylonitic central layer. Looking down westward. (e) Detachment folds developed during strike-slip shear reactivation of a fracture cluster, showing vertical fold axis. Fold geometry changes from chevron-like completely detached folds in the inner portion to parallel continuous symmetrical folds in the outer and thicker granodiroite lithons. Granodiorite lithos are separated by white mica + calcite veins, on which flexural shear is completely localized. Folding is also shown by the rotation of bulk homogeneous foliation of the host granodiorite (here steeply-dipping and E-W trending). This fold outcrop were found in the eastern RFP. Looking down eastward. (f) Folding of small-scale fracture cluster developed close to a subvertical (shallowly W-dipping) brittle-ductile shear plane. Fracture density increases in aplitic dyke, and therefore, folding is preferentially developed inside aplitic dyke. Looking north. (g) Fracture cluster showing small pods of shredded lamprophyre dyke (indicated by black arrows). (h) Lamprophyre dyke apophyses intruding folded fractures, that are in turn slightly involved in folding and shearing along brittle-ductile shear planes (see Fig. 9f).

abruptly geometry across these shallow planes that are reactivated during the stage 4 deformation. Fractures are commonly filled with discontinuous calcite + white mica veins (Fig. 5c) and an alteration of the host rock occurs commonly resulting in change to a greenish colour of the granodiorites. Calcite veins are as much as a few cm thick and locally calcite forms the supporting cement of breccias.

The fracture patterns show a local ductile component of deformation indicated by (i) the local incipient development of a foliation aside or at the tip of fractures and, in the most advanced stages, of rare mylonitic mica-rich packages reaching up to a few 10s cm in thickness (Fig. 5d); and (ii) folding of the fractures and intervening granodiorite lithons. The foliated slips planes and mylonites show a mineral lineation and/or slickenfibers marked by white mica + calcite + quartz (± chlorite), which are preferentially dispersed on a E-W trending great-circle (Fig. 9g) and, only locally shallowly plunging lineations are observed (concentrated in the north-eastern area, Figs. 9i, 11c).

The structural sub-parallel fractures and joints of the fracture clusters are locally involved in folding as already reported by Dal Piaz (1934), Henry (1975) and Mager (1985). Folds are highly non-coaxial detachment folds, affecting discrete volumes of the fracture cluster, with a parallel fold geometry and are associated with flexural slip along the joint-fractures (Figs. 5e, f). Saddle-reefs at fold hinges are filled with calcite (Fig. 5e) and a radial “axial plane” foliation or rotation of the pre-existing rock foliation is locally observed. The folds have 2 main orientations (Fig. 9h, j): (i) sub-horizontal N-S axis and N-S striking axial plane dipping 45-60° toward E; and (ii) sub-vertical axis and axial plane with variable strike. The folds with sub-horizontal axes are dominant across the study area and are associated with the the E-W- striking mineral lineations and slickenlines of slip planes and brittle-ductile shear zones. The folds with sub-vertical axis are mainly found in the north-eastern part of the area and are associated with N-S striking and shallowly plunging lineations (Fig. 11c).

Four thick (as much as several meters wide) and few minor (< 1 m thick) mafic dykes are present in the study area. These dykes are steeply dipping and strike N-S (Figs. 9i - 10f) and correspond to those described and dated at 26.3 + 0.7 Ma (biotite K-Ar) by Steenken et al. (2000). Individual dykes are segmented and arranged en-echelon, but the thick dykes can be followed along strike across the whole pluton thickness. They largely preserve their magmatic fabric. Thin dykes are very-fine grained and show aphanitic fabric. Thicker dykes are usually porphyritic (biotite and amphibole phenocrysts) and composite, with re-ignition and mingling structures with a more acidic magma as the result of multiple magma pulses (Steenken et al., 2000). Locally, shreds of mafic dykes are present inside the brittle-ductile shear zones along the fractures (Fig. 5g) and dyke apophyses injected the fractures of the brittle-ductile shear zones and were involved in folding (Fig. 5h).

1.3.5. Stage 5 structures

Steeply-dipping, N-S-striking strike-slip faults and epidote-chlorite veins are common across the area. *stage 5* structures include: (i) heterogeneously distributed but pervasive incipient thin (mm-thick) segmented fractures locally arranged in swarms, and chlorite veins (Fig. outcrop map); (ii) sharp faults (e.g. Fig. 6a); and (iii) thicker cataclastic faults (Fig. 6b). The sharp faults are arranged in conjugate sets with a small (<60°) intersecting angle and associated chlorite veins are typically oriented parallel to the N-S-trending bisector (Fig. 9l). Epidote filling is more typically associated with shear fractures. Both epidote and chlorite veins are commonly surrounded by mm-cm thick, bleached alteration haloes (e.g. Fig 6a). The fault rocks of major faults consist of a layered assemblage of proto-cataclasite (darker green in colour), cataclasite (light green), ultra-cataclasite (whitish) and pseudotachylytes (Figs. 6b), very similar to the fault rock assemblage described by Di Toro and Pennacchioni (2005) for the Periadriatic Adamello tonalite-granodiorite pluton. The cataclastic rocks are massive and the matrix is very fine grained that makes it difficult in many cases to clearly identify a slickenline lineation. Most identified lineations are shallowly plunging and indicate a strike-slip fault kinematics (Fig. 9l, consistently with the vertical orientation of the pseudotachylyte injection veins (Fig. 6c). There are however also oblique lineations on the fault planes that may indicate a more complex kinematics or just reflect that the cataclastic faults in many cases exploited previous stage 4 faults and were in turn reactivated as stage 6 fault. Epidote veins are NNE-SSW striking with a sub-horizontal-to-oblique lineation (Fig. 9n). Throws range between few mm along incipient fault planes and epidote veins, to tens of meters (cumulative slip) along major fault zones (e.g., fault zone at the base of western Rieserferner Glacier).

1.3.6. Stage 6 structures

Zeolite-bearing faults and zeolite vein-fillings commonly exploited the pre-existing structural planes associated with the earlier deformation stages. Characteristic structures developed during this event are: (i) E-W striking zeolite-filled joints, locally exploiting pre-existing E-W *stage 1* joints (Fig. 6d); (ii) E-W striking cohesive zeolite-bearing cataclasites (Figs. 6e); (iii) whitish ultra-cataclasites, loose gouges and mirror-like surfaces (Fig. 6f) developed exploiting pre-existing structures, such as *stage 3* E-dipping brittle-ductile and Stage 4 N-S cataclastic faults (Figs. 9o). Therefore, these structures have variable orientation, but kinematic indicators are coherent all over the observed structures. Cohesive E-W zeolite-bearing cataclasites show a horizontal strike-slip E-W trending lineation, with significant dextral throw (up to 3.3 m). Slip planes are well polished and show impressive black mineral lineation and grooves, characterized by the occurrence of biotite. On reactivated fault planes, the main lineation is dip-slip with normal shear sense, both on W- and E-dipping planes; inferred from slickenfibers and mirror plane asperities. As previously described for cataclastic faults, a certain variability in structural data is due to the occurrence of overprinting lineations on the same reactivated fault plane.

Zeolite-bearing E-W striking joints are widespread all over the surveyed area, showing symmetric growth of acicular-prismatic crystals from joint wall. They commonly exploit E-W *stage 1* sheared joints, but given the preservation of the crystal growth structure we can infer that no additional offset has been produced during this deformation stage along sheared joints. Zeolite-bearing faults and joints commonly show cm-wide whitish-reddish alteration haloes in their surroundings.

Figure 6 (next page): Deformation Stage 5 and Stage 6 brittle structures. (a) N-S trending thin localized cataclastic layer showing an evident alteration halo in its surrounding due to fluid rock interaction during brittle deformation. The reddish outer halo may be due to later reactivation during zeolite-bearing brittle stage. (b) Composite layered cataclasite developed along major cataclastic faults. Looking west. (c) Major pseudotacylyte injection vein suggesting dominant dextral strik-slip kinematics on the main fault plane. Looking down westward. (d) E-W trending non-sheared zeolite-bearing joint showing syntaxial symmetrical microstructure. Looking down southward. (e) Zeolite-bearing fracture network developed close to the knife-sharp slip plane of zeolite-bearing cataclasite overprinting previous Stage 5 greenish fault zone (same structure of (b)). Looking west. (f) Zeolite-bearing mirror-like surface developed during Stage 6. Slikenlines and fault plane asperities suggest dip-slip normal kinematics. Looking east.

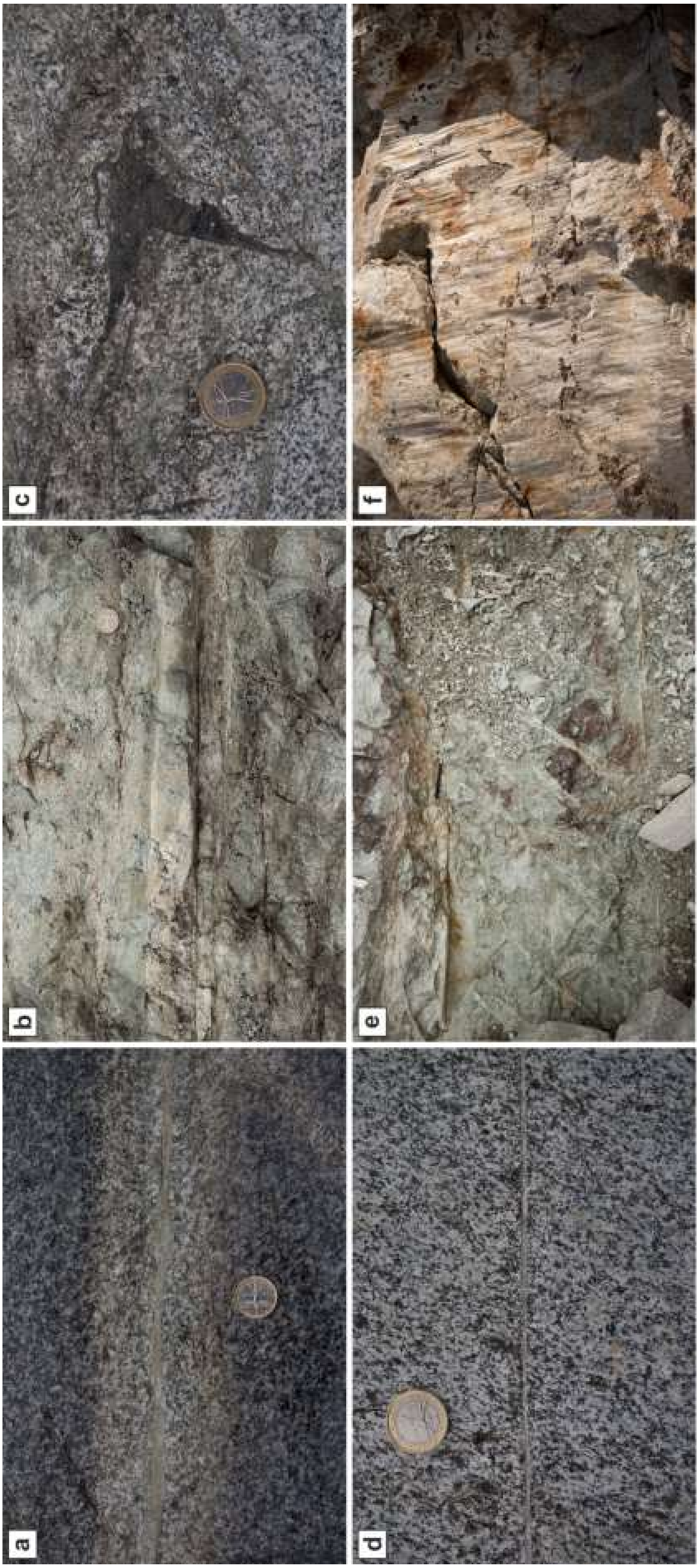

Figure 6

1.4. Microstructure of deformation features

In the following sections, optical microstructures of the various deformation stage structures are described in order to: (i) characterise the main deformation mechanisms acting during the deformation phases; (ii) providing the elements to further discussions on temperature and “fluid” conditions during the evolution of the RFP.

1.4.1. Bulk foliation and Stage 1 structures

Field surveys and sample collection have mainly interested the central portion of the RFP is a fine-grained horneblende-bearing granodiorite. The magmatic paragenesis of the host Hbl-bearing granodiorite includes: quartz + plagioclase + K-feldspar + biotite + allanite/epidote + horneblende + apatite + sphene; chlorite, calcite, white mica are common alteration products. Microstructural features of the RFP granitoids have been already described in Steenken et al. (2000), Scheuvens and Mann (2004) and Wagner et al. (2006). The detailed chemical and mineralogical analyses of the magmatic protolith are reported in Chapter 4.

Quartz grains show low internal deformation and undulose extinction, high-sutured boundaries and “island grains” (e.g. Pennacchioni et al., 2010). Plagioclase are usually found in glomerocrysts enveloped by anhedral K-feldspar mantles defining a synneusis microstructure (Scheuvens and Mann, 2004). Anorthitic cores (up to An_{60}) of plagioclase are sometimes replaced by coarse white mica + epidote aggregates. K-feldspar is usually found as interstitial or secondary phase.

All the analysed granodiorite thin sections show a more or less well-developed bulk foliation. This bulk foliation is defined by the alternation of elongated quartz aggregates (relatively coarse grained and unrecrystallized), biotite fish-foliae of recrystallized biotite and elongated/dismembered feldspar aggregates.

Different sets of intragrain fractures are commonly observed in feldspars and allanite grains: (i) syn-magmatic fractures filled with magmatic quartz and K-feldspar (Steenken et al., 2000); (ii) healed fractures and fluid inclusion planes in both magmatic plagioclase and allanite. These fracture sets are commonly perpendicular to the local weak bulk foliation or, in aplitic dykes, perpendicular to dyke boundaries.

Brown Ti-rich magmatic biotite is coarse grained, poorly oriented and partially recrystallized along the bulk foliation. Actinolite after horneblende and the development of white mica are reported by Bellieni (1978) to commonly occur in the magamtic protolith of the RFP.

1.4.2. Stage 2 sheared aplites and quartz-feldspars veins

The host granitoid surrounding the first generation of ductile structures preserves the magmatic microstructure and paragenesis.

Sheared Aplite: Undeformed biotite-rich aplites are mainly composed of quartz + K-feldspar + plagioclase + biotite ± allanite/epidote ± garnet ± sphene; chlorite is a common alteration product. An internal weak foliation defined by the alignment of elongated coarse-grained (mm-sized) quartz, feldspar laths and mm-sized biotite fishes have been observed also in the non-sheared samples.

Shearing and deformation lead to the development of a fine-grained (100-200 μm) homogeneous recrystallized matrix composed mainly by elongated and flattened quartz and feldspar grains in which scattered K-feldspar (and rare plagioclase) porphyroclasts are embedded (Figs. 7a-b). The elongation of recrystallized grains defines an homogeneous internal foliation. Quartz shows clear evidence of grain boundary migration (GBM) recrystallization (such as pinning and windowing microstructures, Passchier and Trouw, 2005). Plagioclase recrystallizes in coarse grained (~200μm?) polygonal aggregates. K-feldspars porphyroclasts are overprinted by myrmekite. Grain size refinement and myrmekite formation led to an increase in plagioclase content at the expense of K-feldspar (see Table 1, Chapter 4). Recrystallized biotite is very-fine grained (<100 μm?) and is dispersed inside the fine-grained matrix.

Sheared quartz-feldspar veins: Close to the sheared vein, the sub-magmatic solid-state foliation is weakly dragged into the shear zone according to the shear sense, preserving the magmatic mineral paragenesis.

Veins are mainly composed of quartz + K-feldspar; minor amounts of biotite + plagioclase ± allanite/epidote ± sphene are observed, usually organized in thin layers defining the macroscopic oblique foliation (Figs. 7c-d). Quartz grains are coarse (>>500 µm), slightly elongated and preferentially oriented oblique to the main slip plane, defining a shape preferred orientation (SPO) coherent with the sense of shear. The oblique foliation defined by quartz SPO is inclined at higher angle with respect to the shear plane than the foliation defined by feldspars + biotite layers. Quartz shows “chessboard” subgrains, deformation lamellae and patchy undulose extinction. Larger quartz grains show interfingered and strongly lobated grain boundaries that lead to the formation of the so called “island grains” and “mosaic-like” patters (e.g. Gapais and Barbarin, 1986; Pennacchioni et al., 2010). Quartz grain size drastically decrease along biotite-feldspar layers (<100µm).

Perthitic K-feldspar is coarsely (>200 µm) dynamically recrystallized and are usually concentrated along layers of polygonal grains that define the foliation plane. Elongated euhedral and fish-like K-feldspars are also observed scattered in the quartz matrix. Weak undulose extinction and flame perthites are common characteristics of deformed K-feldspars. K-feldspar is statically overprinted by myrmekite, especially when porphyroclasts are close to biotite-rich layer/foliation. Oblique feldspar layers are crosscut by fluid inclusion planes and fractures normal to the vein boundary, filled with quartz (Fig. 7d).

Biotite is preferentially found along fine-grained feldspar layers, but it is also dispersed inside quartz grains and along quartz grain boundaries, as small (~100 µm) recrystallized flakes obliquely oriented to form a weak dispersed foliation (Fig. 7c). Along biotite-feldspar layers, quartz shows evident GBM recrystallization microstructures (Fig. 7c).

1.4.3. Stage 3 quartz- and epidote-rich mylonitic veins

Detailed microstructural, textural and chemical analyses on deformation *stage 3* structures are reported in Chapters 2, 3 and 4.

Mylonitic quartz veins shows a characteristic microstructural and textural evolution with increasing strain, analysed and deeply discussed in Chapter 2 and therefore it will be only briefly described here. Quartz veins with incipient shear ($\gamma<2$; Fig. 7e) show a coarse grained (mm-cm size) protomylonitic microstructure characterized by elongated single quartz crystals (ribbons) that form a coarse oblique foliation at high angle to the shear plane. Recrystallization to fine grained mylonites and ultramylonites occurs with increasing strain ($\gamma>3$) (Fig. 7f). Quartz c-axis texture shows an evolution from a distribution similar to Type-I single girdle at the protomylonitic stage, toward an inclined partial girdle at mylonitic and ultramylonitic stages with increasing strength of maxima close to the centre of the pole figure (see Chapter 2). Epidote-rich veins are mainly composed by a granular aggregate of epidote + biotite + allanite (central brown epidote aggregate in Fig. 7g). Accessory phases are interstitial quartz + feldspars (probably related to mechanical mixing after shearing).

Ultramylonites developed along epidote-rich veins are characterized by a fine-grained (about 30 μm) homogeneous matrix (Fig. 7g), whose mineral composition is: quartz + plagioclase + biotite + epidote + K-feldspar + sphene + apatite. In some cases, white mica and garnet are observed in significant amounts in the ultramylonitic matrix. The former epidote-rich vein is still observed along the ultramylonitic layer, in the form of large boudins and foliated lenses with S-C fabric (Figs. 7g-h).

1.4.4. Stage 4 structures and lamprophyres

Brittle-ductile faults mineral paragenesis includes: quartz + chlorite + white mica + calcite ± plagioclase ± K-feldspar.

The former solid-state foliation given by elongated sites of quartz, elongated plagioclase glomerocrysts and biotite is either gradually deflected into the main shear plane according to the shear sense (Fig. 8a) or rotated to form a radial “axial plane” foliation in folded granitoid lithons (e.g. Fig. 5e). Former magmatic coarse quartz is gradually stretched to form ribbons. Pervasive fluid-rock interaction related to Stage 4 structures led to the alteration of the surrounding host granitoid. Progressive destabilization of plagioclase into a fine aggregate of white mica + calcite occurs primarily along microfractures and cleavage planes (e.g. Fig. 8a). Destabilization increases getting closer to the slip planes. Biotite is completely destabilized into chlorite showing high amount of fine-grained inclusions (sphene and opaques). Discrete mylonitic layers are composed by a fine-grained matrix of white mica + calcite + recrystallized quartz showing a strong foliation with S-C' microstructure that wraps around quartz and allanite/epidote porphyroclasts. C' shear planes, and later anastomotic slip planes, are defined by sheared aggregates of late stage calcite + white mica (Fig. 8b). Calcite + quartz veins cross cut the main foliation and are then buckled and sheared along with the main foliated slip zone. Calcite and/or calcite + quartz fibres are observed sometimes along slip planes.

Folded granodioritic lithons are interested by a pervasive network of localized brittle-ductile shear planes, along which quartz recrystallizes in fine-grained aggregates along micro-shear zones (µSZ) showing low-temperature plasticity features (e.g. Derez et al., 2014), whereas feldspars are substituted by white mica (Fig. 8c-d). Very fine recrystallization of quartz is widespread at hinge zones. Folding is principally aided by shearing between lithons, and is completely localized into white mica + calcite veins that are then transformed into phyllonitic-like layers (Fig. 8e). Oxide seals parallel to fold axial plane in the hinge zone, and along grain boundaries parallel to fold axial plane may suggest the occurrence of some dissolution-precipitation process. Different fluid inclusion trails are observed, in both quartz and feldspar, both normal and at high angle to the fold axial plane.

Lamprophyres

Undeformed lamprophyres preserve their magmatic porphyric microstructure with chilled margins. The magmatic paragenesis includes: amphibole + plagioclase + biotite + quartz + sphene + rutile + oxides. Acicular to prismatic brown amphiboles show strong shape preferred orientation (SPO). The aphanitic matrix is mainly composed by randomly oriented amphiboles, interstitial plagioclase and (microcrystalline aggregates of?) biotite. Quartz is commonly observed as scattered few phenocrysts, as single crystal or stretched aggregates. Quartz shows very weak internal deformation (ondulose extinction). In the aphanitic matrix, a second generation of colourless acicular to fibrous amphibole is observed.

Lamprophyres are involved in the deformation during the activity of both brittle-ductile faults and cataclasites. The associated alterations due to fluid-rock interaction lead in both cases to the destabilization of plagioclase, chloritization of amphiboles (colourless chlorite with dark-green/greyish interference colours) and deposition of calcite veins.

Lamprophyre apophyses intruded in folded fractures of Fig. 5h have been sampled and analysed to verify the involvement of lamprophyres during brittle-ductile deformation of the Rieserferner pluton. The lamprophyre apophysis shows a solid-state foliation localized close to the dyke margins and a pervasive S-C structure in the inner portions (Fig. 8f). Calcite + quartz veins cross cut the foliation and are in turn dislocated by localized shear planes. These shear planes sometimes are decorated by fine-grained aggregates of mylonitic calcite.

1.4.5. Stage 5 Cataclasites and pseudotachylytes

All the collected cataclasite samples show a pervasive alteration of the host rock. Biotite is mainly destabilized to chlorite + sphene and opaques; whereas plagioclase show an increasing destabilization to a fine-grained aggregate of white mica + calcite (?).

Thick coherent cataclasites are characterized by a mm-cm layered structure. Each layer consists of a crypto-crystalline ultracataclastic matrix, turbid and un-resolvable under the optical microscope, in which angular clasts and fragments of quartz and feldspar are embedded. The mineral paragenesis (obtained from X-Ray Powder Diffraction – XRPD – analyses) includes quartz, K-feldspar, albite, chlorite and epidote (± calcite). Each cataclastic layer differs in grain size, amount of angular clasts and relative amount of mineral phases.

Brown-to-orange homogeneous pseudotachylytic layers occur discontinuously along fault planes. Horn-shaped injection veins in the surrounding cataclasites are commonly observed (Fig. 8g). Thick pseudotachylytes are symmetrically banded, with each layer showing different textures and clast-matrix ratio. The outer layers are mainly composed of a finer grained matrix (probably given by microliths) and small amount of quartz clasts. The inner core of the pseudotachylyte is defined by a coarser matrix, with larger clast/matrix ratio, and characterized by the occurrence of spherulites. The former glass matrix seems to have recrystallized in a cross-hatched aggregate of phyllosilicates.

1.4.6. Stage 6 zeolite cataclasites

During *stage 6* brittle faulting, the mineral paragenesis of the host rock is partially preserved at incipient deformation stage. Zeolite-bearing faults and joints show microstructures similar to those described by Dempsey et al. (2014) in the Adamello pluton. The mineral paragenesis (obtained from XRPD analyses) includes: chabazite, stilbite, quartz, plagioclase, K-feldspar, biotite, actinolite, chlorite. E-W striking cohesive zeolite-bearing cataclasites show a complex microstructure, characterized by a cataclasite with coarse quartz and feldspar clasts, cemented by a crosshatched aggregate of zeolites and cross cut by discrete anastomotic planes (Fig. 8h). Quartz and K-feldspar are shuttered and show low internal plastic deformation (such as ondulose extinction). Biotite is partially transformed into chlorite, that shows kinks and fractures and decorates major discrete slip planes. Plagioclase are instead completely transformed into a coarse aggregate of second generation phase (Ca-stilbite and chabazite) with a lower optical relief and low interference colours. In these aggregates, a skeleton of corroded plagioclase is still preserved, and with parallel nichols the former feldspar twinning or inclusion trails can be still observed. The phase that substitute plagioclase seems to be the same that forms the cataclastic aphanitic matrix. Amphiboles and allanite/epidote are fractured but they do not show any sign of destabilization.

Whitish ultracataclasite cataclasites and poorly consolidated gouges are characterized by the occurrence of clast-cortex aggregates, made of clasts of cataclasites with different grain size and mineral abundances, indicating several overprinting cataclastic events, floating in a fine-grained matrix, composed mainly of prismatic to acicular low-relief and low interference colours crystals of zeolites (+ white mica?). Homogeneous layers of whitish ultracataclasites are composed of a turbid and optically unresolvable crypto-crystalline matrix in which quartz and epidote clasts are dispersed.

Figure 7 (next page): Microstructure of deformation Stage 2 and 3 structures. (a) Optical micrograph (crossed nichols) of a sheared biotite-bearing aplite. Fine-granied feldspar and quartz grains of the recrystallized matrix show a well-developed SPO. K-feldspar and plagioclase porphyroclasts are observed. (b) Optical micrograph (crossed nichols + gypsum plate inserted) of the recrystallized matrix of a sheared biotite-bearing aplite. Note the occurrence of small (<100µm) flakes of recrystallized biotite. (c) Optical micrograph (crossed nichols) of a sheared quartz-feldspar vein. Coarse grained quartz shows lobate grain boundaries and a shape preferred orientation defining an oblique foliation. The quartz matrix is crosscut by recrystallized feldspar – biotite – quartz layers defining the macroscopic oblique foliation. Note the strong grain size reduction of both feldspar and quartz along feldspar – quartz – biotite layers. Note the occurrence of dragging and windowing microstructures (Passchier and Trouw, 2005) in quartz grains close to this layers. (d) Recrystallized aggregate of K-feldspar in a sheared quartz-feldspar vein. Note the occurrence of iso-oriented quartz-filled fractures and fluid inclusion planes. (e) Protomylonitic quartz vein ($\gamma<2$) characterized by the occurrence of elongated quartz ribbons and incipient recrystallization localized along conjugate sets of micro-shear zones. (f) Ultramylonitic quartz vein ($\gamma>10$) completely recrystallized, showing some quartz porphyroclasts embedded in a very-fine grained (~10µm) martix. (g) Granodiorite ultramylonite developed along an epidote-rich vein. Mylonitic granodiorite (lower part) is separated by boudinged epidote vein (central portion) from the ultramylonitc layer (upper portion). (h) Optical micrograph (crossed nichols + gypsum plate inserted) of a sheared quartz + epidote vein showing the simultaneous deformation of quartz and epidote.

Figure 8 (second next page): Microstructures of deformation Stages 4, 5 and 6 structures. (a) Optical micrograph of the homogeneous foliation developed along the main brittle-ductile slip plane. Quartz is homogeneously stretched to form ribbons; plagioclase is completely destabilized into white mica + calcite fine aggregates. White mica + Calcite later C' planes cut across the mylonitic foliation. (b) White mica + calcite S-C' mylonite. The S main foliation is given by the alternation of quartz ribbons (as in (a)) and sheared aggregates of white mica + calcite. C' planes are outlined by mylonitic calcite layers. (c) Fine recrystallization of quartz and sheared white mica + calcite layer developed in a folded granodiorite lithon. (d) Anastomotic shear planes in a folded lithon that show fine recrystallization of quartz (typical of low temperature plasticity). When shear planes cut across feldspars grains, they are filled with sheared white mica (+ calcite?) aggregates. (d) White mica (+calcite) phyllonitic layer developed during flexural slip shearing between two granodiorite lithons. (f) Sheared lamprophyre apophysis sampled in the folded dyke of Fig. 5h. Note the pervasive foliation and the S-C' geometries locally developed. Microstructures of deformation Stage 5 and 6 brittle faults. (g) Stage 5 pseudotachylyte-bearing faults. Optical micrograph (crossed nichols) of a thick zoned pseudotachylyte with injection vein. (h) Stage 5 zeolite-bearing cataclasitc faults. Optical micrograph that show the complex microstructure of zeolite-bearing faults characteristic of Stage 6 deformation (e.g. Dempsey et al., 2014).

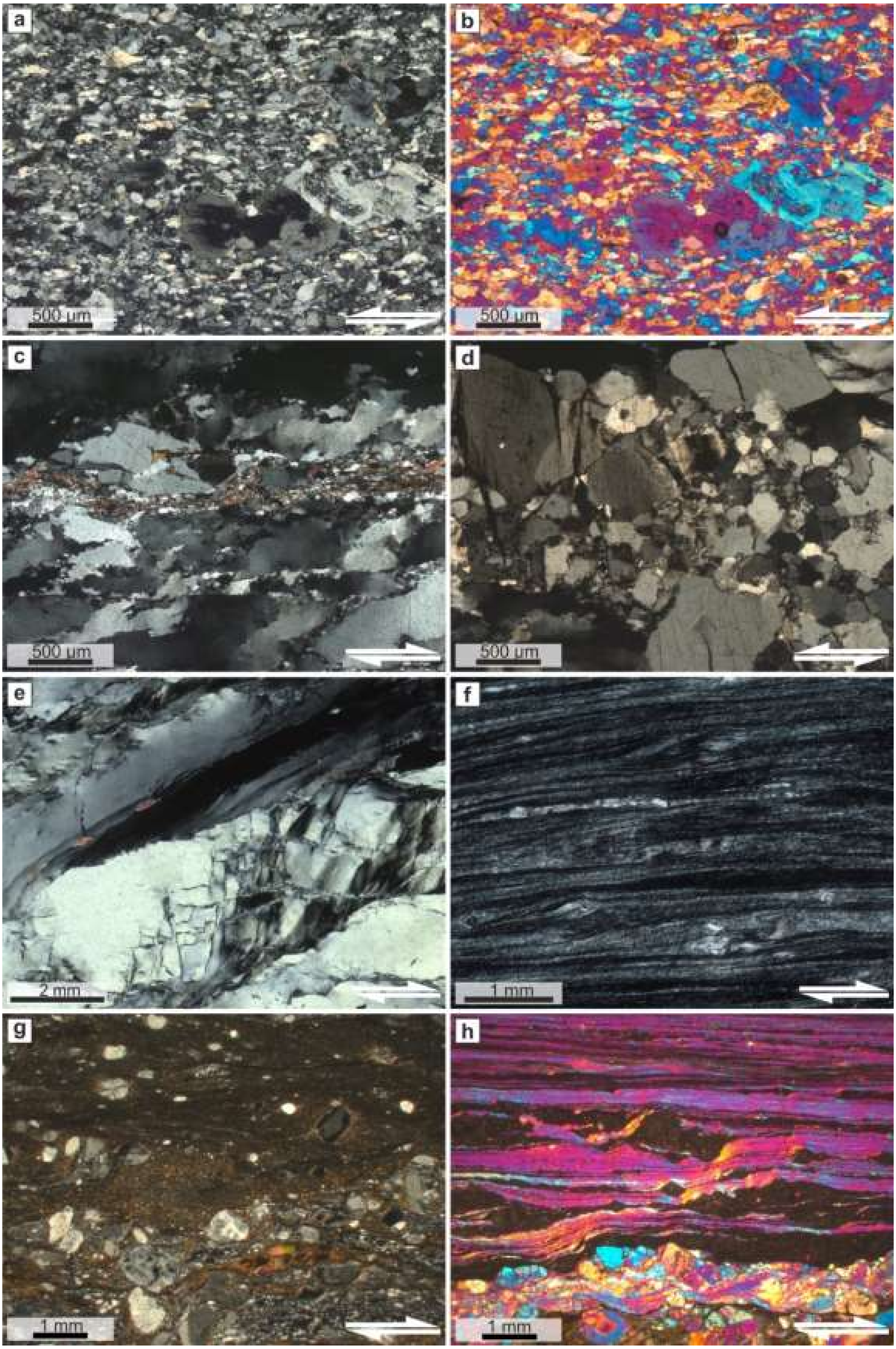

Figure 7

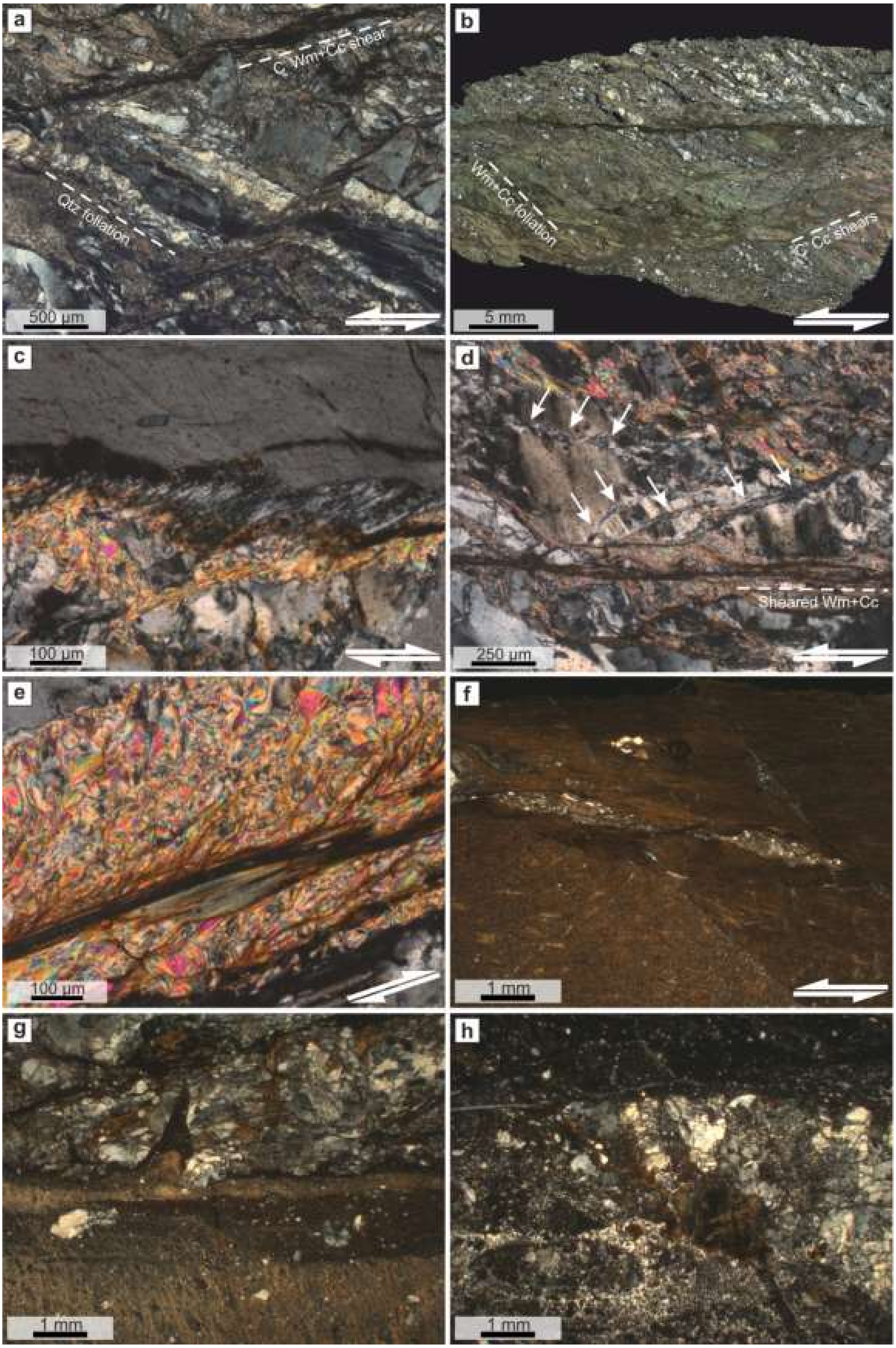
a
C Wm+Cc shear
Qtz foliation
500 µm
b
Wm+Cc foliation
C Cc shears
5 mm
c
100 µm
d
Sheared Wm+Cc
250 µm
e
100 µm
f
1 mm
g
1 mm
h
1 mm

Figure 8

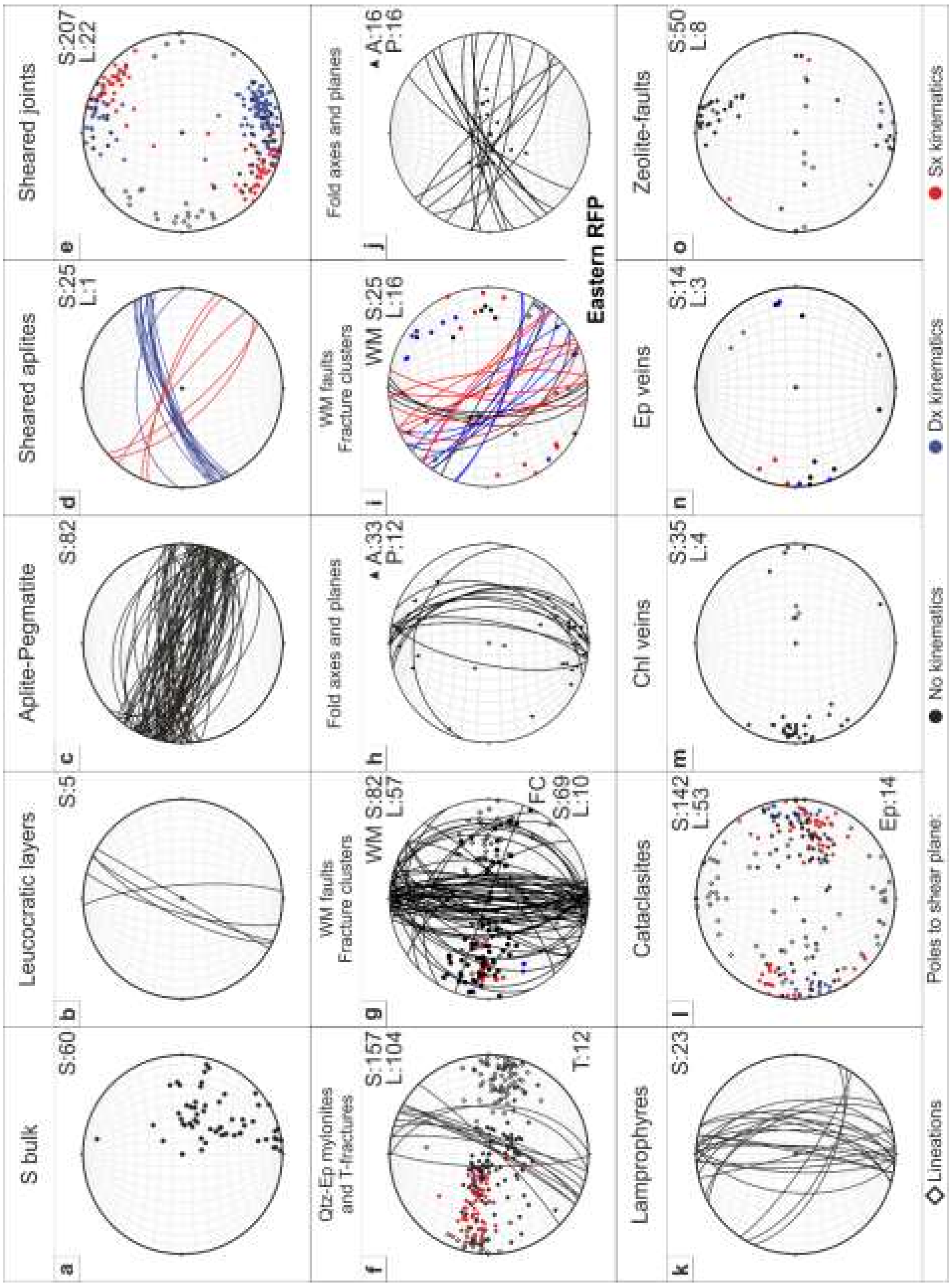

Figure 9: Stereographic projection of poles, planes and lineation of the observed deformation structures. Lower hemisphere, Equal area projection. S: Foliation/Planes; L: Lineations; T: tensional fractures; A: fold axes; P: fold axial planes. Poles to planes are colour-coded according to the strike-slip component of the shear plane kinematics: red for sinistral, blue for dextral, black for no kinematics. (a) Poles to Sbulk foliation planes; (b) projection of boudinaged leucocratic layer planes; (c) projection of main sets of aplitic-pegmatitic dykes; (d) projection of Stage 2 sheared biotite-bearing aplite; (e) projection of poles and lineations relative to Stage 2 sheared joints and quartz-feldspar veins; (f) projection of poles and lineations relative to Stage 3 mylonitic quartz- and epidote-rich veins. Planes of tensional fractures are projected (in black); (g) projection of Stage 4 brittle-ductile faults and fracture clusters cropping out in the central RFP; (h) projection of Stage 4 fold geometrical elements cropping out in the central RFP; (i) projection of Stage 3 brittle-ductile faults and fracture clusters cropping out in the eastern RFP; (j) projection of Stage 4 fold geometrical elements cropping out in the eastern RFP; (k) projection of lamprophyres/mafic dykes; (l) polse to Stage 5 cataclastic faults; (m) poles to chlorite-veins related to Stage 5; (n) poles to epidote veins related to Stage 5-veins; (o) poles to Stage 6 zeolite-bearing faults and joints.

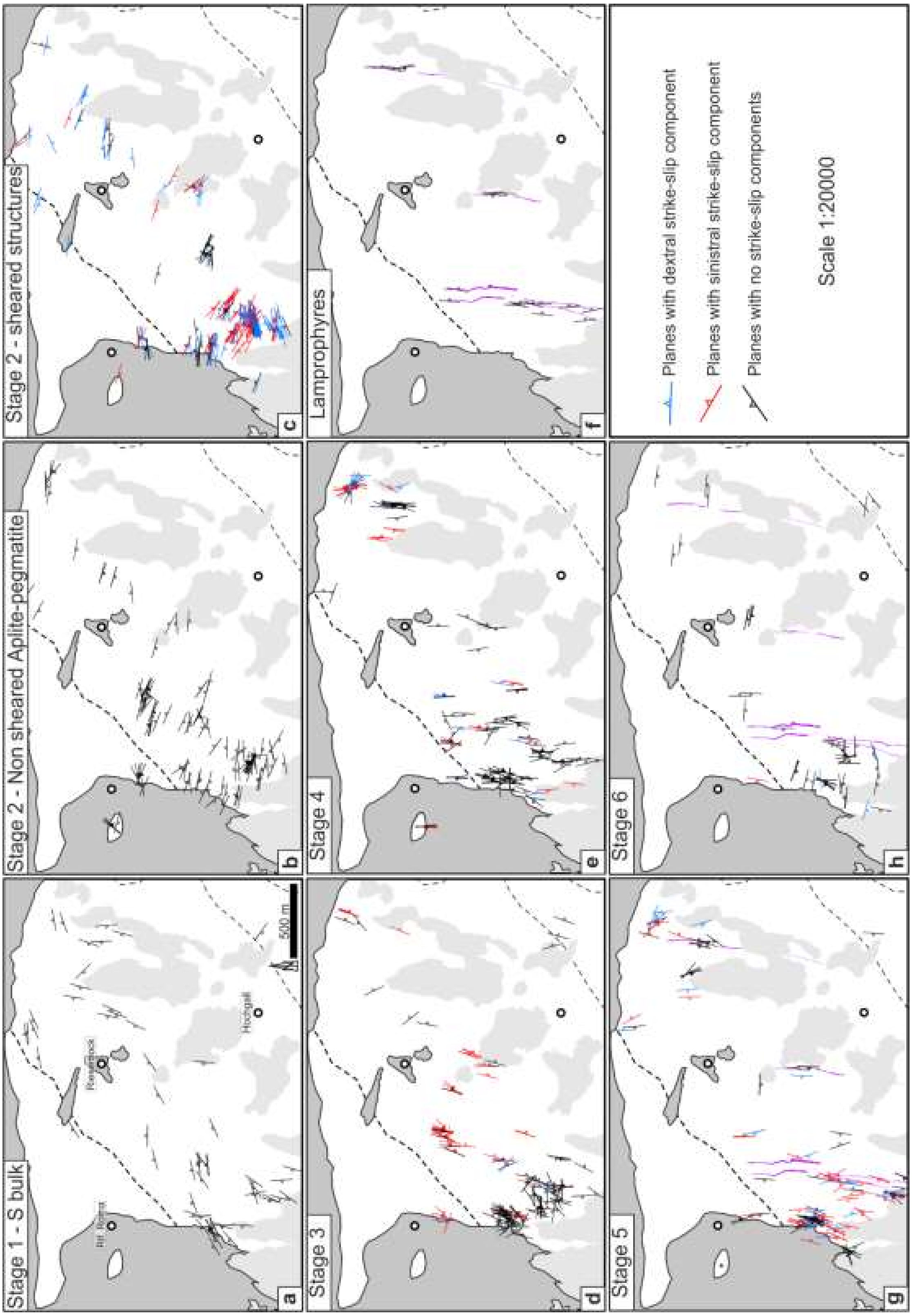

Figure 10: Small geological sketches of the central RFP reporting strike and kinematics of the structural features. Each symbol represent the strike of one single structure. Dashed curves represent the lithological contact between magmatic sub-units of the RFP. (a) Foliation pattern in the central portion of the RFP. (b) Stage 2 non-sheared aplite-pegmatite dykes; (c) Stage 2 sheared joint and biotite-bearing aplite; (d) Stage 3 mylonitic quartz- and epidote-rich veins; (e) Stage 4 brittle-ductile faults and fracture clusters; (f) Lamprophyres and mafic dykes related to Stage 4; (g) Stage 5 cataclasite and pseudotachylyte-bearing faults; (h) Stage 6 zeolite-bearing faults and joints.

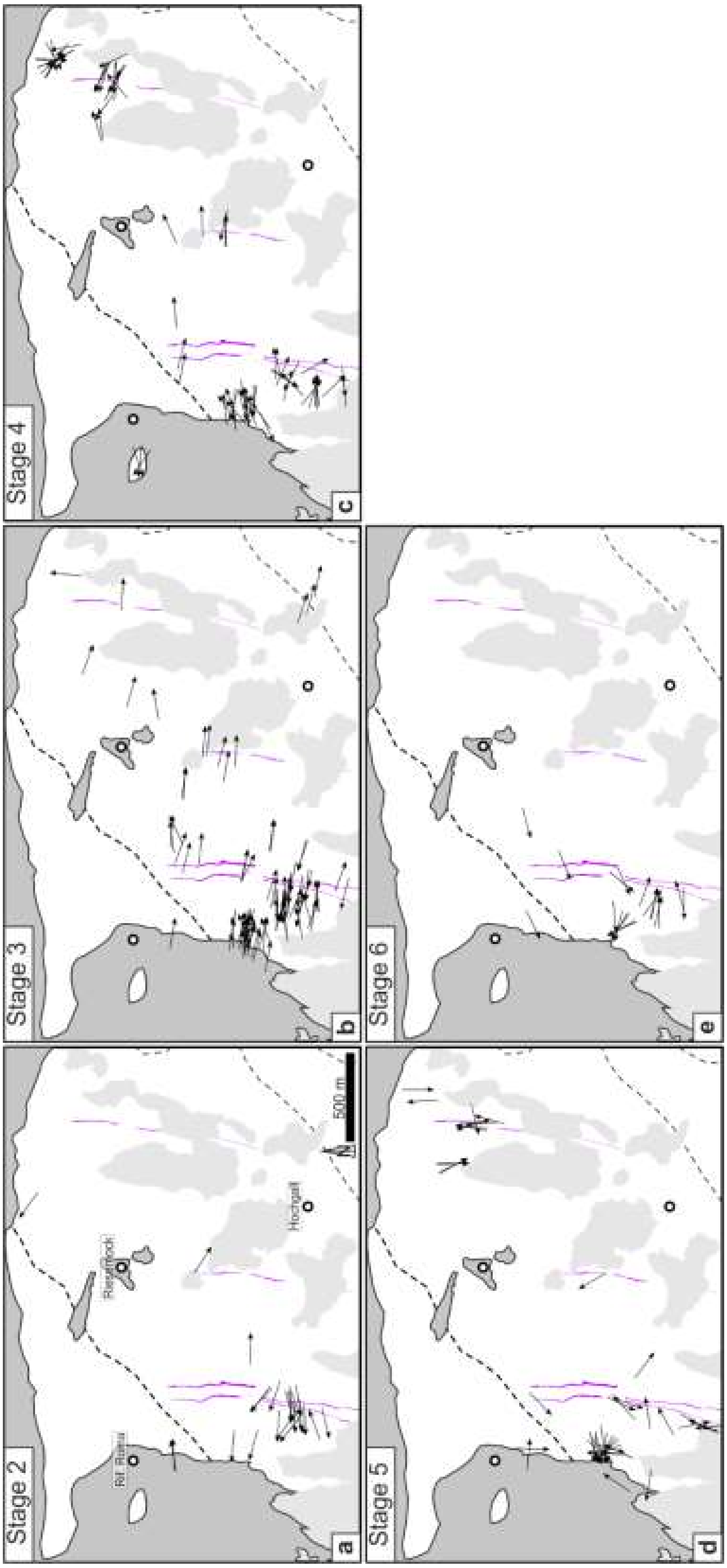

Figure 11: Small geological sketches of the central RFP reporting lineation trend of the structural features. Each symbol represent the strike of one single structure. (a) Stage 2 sheared joint and biotite-bearing aplite; (b) Stage 3 mylonitic quartz- and epidote-rich veins; (c) Stage 4 brittle-ductile faults and fracture clusters; (d) Stage 5 cataclasite and pseudotachylyte-bearing faults; (e) Stage 6 zeolite-bearing faults and joints.

1.5. Discussion

1.5.1. Temperature-time evolution

In this section, we use the microstructures and mineral assemblages observed in the deformed rocks produced during the different deformation stages, and the available geochronological data, to reconstruct a temperature-time curve for the Rieserferner pluton (Fig. 12).

This T-t solid-state evolution includes (i) 2 main stages (*2*-*3*) associated with crystal-plastic deformation and formation of mylonitic rocks; (ii) a deformation stage (*3*) developed at the transition to brittle behaviour of quartz; and (iii) 2 stages (*4*-*5*) of brittle deformation. The whole history records an almost continuous decrease of temperature from the magmatic stages (700 °C) to temperatures as low as ca. 100 °C during pluton cooling and exhumation, with the brittle/crystal plastic transition of quartz assumed to occur at 300 °C (Pennacchioni and Zucchi, 2013; and reference therein).

Stage 2 is characterized by a coarse grain size, fast grain boundary migration recrystallization of quartz and chessboard coarse polygonization, typical of upper amphibolite facies metamorphic conditions, and by recrystallization of biotite and feldspar along the shear zone foliation. The chessboard subgrain pattern, interpreted as a combination of basal <a> and prism [c] (Mainprice et al., 1986), has been suggested to occur at the quartz α-β transition at around 630 °C (Kruhl, 1996; Stipp et al., 2002). The fine subgrains and recrystallization at the boundary of the coarse grains and the patchy extinction are referred to a later overprint during stage 3 deformation. Based on these observation, a temperature of around 600 °C is assigned to Stage 2 deformation.

Stage 3 mylonitization is characterized by (i) predominant subgrain rotation recrystallization of quartz: (ii) the dominant activity of prism <a> slip during quartz crystal-plastic deformation; and (iii) the development of a syn-kinematic assemblage of Qz + Pl (Ab_{75}) + Bt + Ep (Ps_{20}) + Kfs + Tit + Ap. These features are rather characteristic of ductile shear zones developed during cooling of several granodioritic-tonalitic plutons (e.g. Avio granodiorite, Adamello: Pennacchioni, 2005; Lake Edison granodiorite, Sierra Nevada, California: Pennacchioni and Zucchi, 2013). Preliminary thermodynamic modelling (see Chapter 4) constrains the deformation temperatures in the range between 420 and 460 °C.

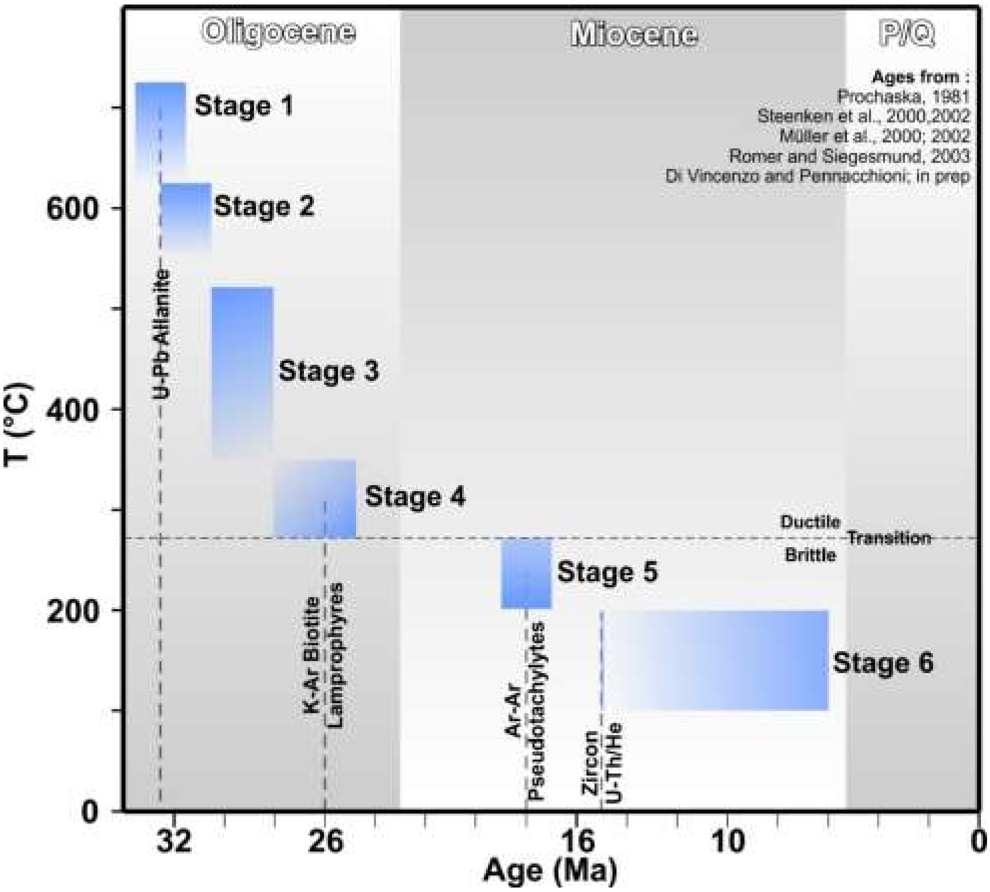

Figure 12: Temperature-time cooling curve for the Rieserferner pluton. Background colours indicate the geological epoch. Blue semi-transparent boxes suggest the inferred temperature conditions and period of time during which deformation stages most likely developed. References are reported in the text.

Stage 4 deformation occurred at the brittle-ductile transition conditions with very incipient low temperature crystal plasticity of quartz and bulging recrystallization. This stage of deformation includes the association of fracturing and faulting with the mylonitic deformation induced by the strong fluid rock interaction along the precursor brittle fractures. We attribute the classically assumed temperature of 300 °C for brittle/crystal-plastic transition for quartz for *stage 3*.

Regarding the age of *stage 2-3* deformations, the cooling models of Wagner et al. (2006) indicate that the RFP took 100 kyr to cool down from 700 °C (solidus) to 550 °C, and 2 Myr to equilibrate to the host rock temperatures of 400 °C. (Wagner et al., 2006). This would date the development of *stage*

2-3 deformation to a short time span between 32 (intrusion age) and 30 Ma. The age of *stage 3* is constrained by the younger age obtaine from lamprophyre K-Ar dating on biotite at 26 Ma (Müller et al., 1992; Steenken et al., 2000), since these dykes intruded along the fracture network associated with the brittle–ductile shear zones and were involved in mylonitization and folding (Fig. 4h).

Stage 5 consist of cataclasite-pseudotachylyte association similar to that described for the Periadriatic Adamello intrusion and other granitoid intrusion and constrained to have developed at the base of the seismogenic crust. In addition, the stable mineral paragenesis includes chlorite + albite + epidote, typical of the lower Greenschists facies, therefore suggesting temperatures slightly lower than 300 °C (Pennacchioni et al., 2006). *stage 5* is dated by Ar-Ar dating of the pseudotachylytes to 17 Ma (Di Vincenzo et al., submitted).

The *stage 6* of exploitation of former structures (especially *stage 5* faults) and diffuse fracturing by zeolite-bearing faults and veins is also identical to late stage fracturing in many plutons (e.g. Adamello: Dempsey et al., 2014). The observed mineralization and associated alteration of the tonalite wall rocks requires the nflow and throughput of significant volumes of aqueous, low temperature (< 200 °C) alkaline fluids (see Weisenberger and Bucher, 2010 and references therein). The maximum age of *stage* 6 deformation event can be assumed at 15 Ma, i.e. the oldest age obtained by U-Th/He dating of zircons (data not reported in this thesis).

1.5.2. Kinematics analysis, stress field and regional interpretation

In this section, we first use the orientation and kinematics of the field structures of the different deformation stages to reconstruct the evolution of the stress field at the local scale of the RFP. Secondly, an attempt is made to correlate this evolution to regional tectonics and meso-structure of the pluton, kinematics of mesostructures are analysed at the scale of the Eastern Alps. The local scale stress field evolution is schematized in the block diagrams of Fig. 13.

1.5.2.1. Local stress field within the RFP

Stage 2. *Stage 2* shear zones are steeply-dipping, strike slip structures with different sense of shear. The sheared biotite-rich aplitic dykes, quartz-feldspar veins and joints are generally organized in two strike-slip conjugate sets with opposite kinematics. The switch between dextral and sinistral strike-slip structures kinematics occurs at around an WNW-ESE N290° direction (Fig. 10d and 10e). This implies that σ_1 was sub-horizontal, oriented N290°, and σ_2 vertical. This direction can be assumed as the shortening direction (i.e. subhorizontal principal stress σ_1) during this deformation event (Fig. 13a).

Stage 3. We distinguish 2 events during *stage 3* deformation. The first event (*stage 3a*) includes the development of the pervasive sets of shallowly dipping joints (Fig. 3a) filled with epidote and, more commonly, with quartz veins. This *stage 3a* event is interpreted to have occurred under a similar orientation of the principal stress axes as during *stage 2*, but with σ_2 and σ_3 switched, and σ_1 still sub-horizontal and oriented N290° (Fig. 13b). The σ_2-σ_3 switch could be explained by progressive exhumation during cooling. *Stage 3b* represents the event of localized shear exploitation with top-to-E kinematics of the *stage 3a* structures under the same stress field, but reflecting the clockwise rotation (look north) of the structural planes as consequence of pluton tilting (Steenken et al., 2000; Wagner et al., 2006). The differential uplift of the western side of the pluton would induced a domino-like reactivation of the planes with a kinematics consistent with the observed top-to-E sense of shear (Fig. 13b).

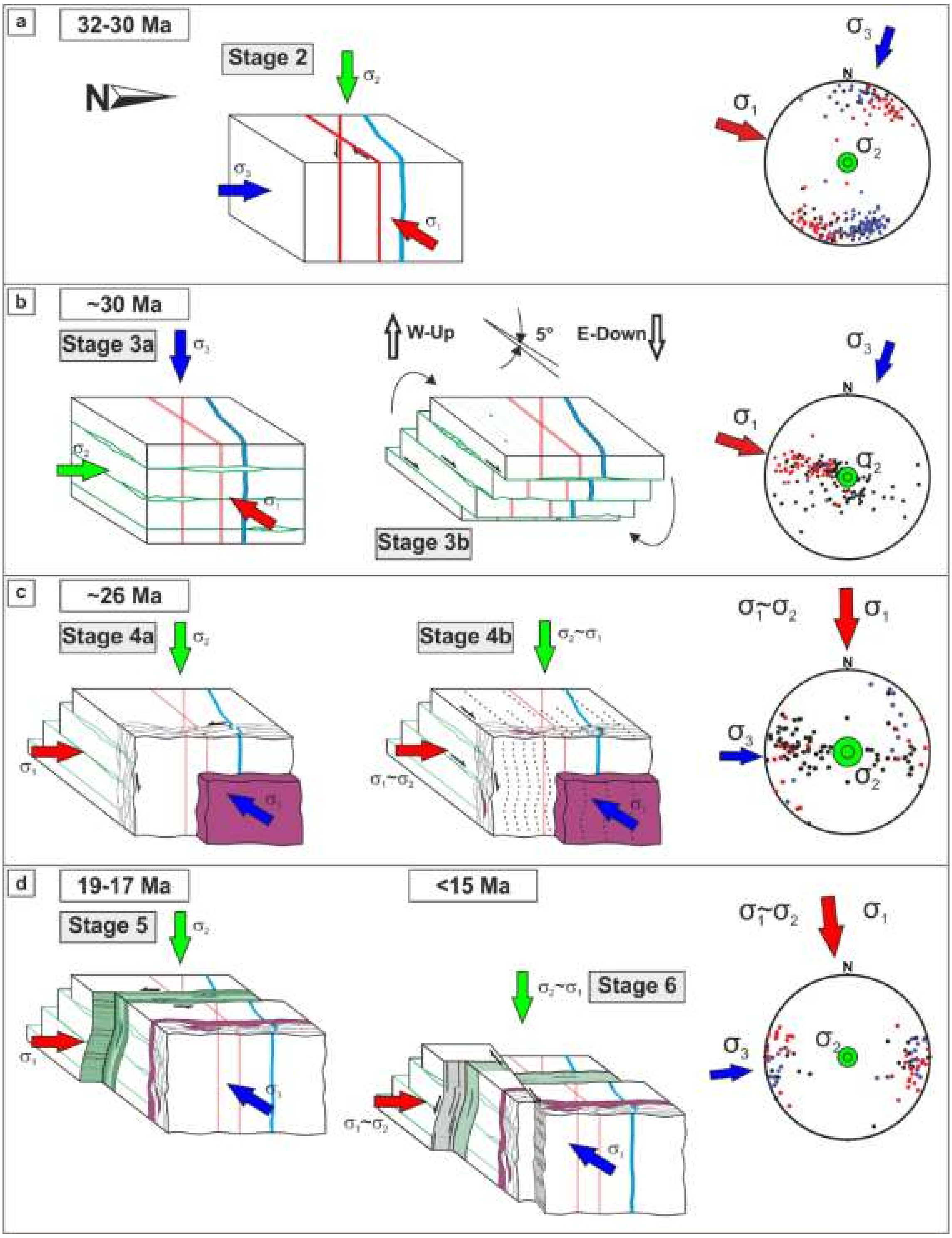

Figure 13: Black diagram showing the inferred structural evolution ad relative switch in stress field orientation retrieved from kinematic analyses. See text for explanation.

Stage 4. *Stage 4a* is interpreted to correspond to switch from WNW-ESE (N290°) to NNW-SSE (N350°) shortening consistent with the development of N-S-trending fractures and emplacement of the mafic dykes (Fig. 13c). The ductile reactivation of the fractures to brittle-ductile shear zone (*stage 4b*) produced a characteristic lineation on the differently oriented planes dispersed along an E-W great circle.

Stage 5. Stage 5 cataclasites are steeply-dipping strike-slip fault, whose kinematics switches from dextral to sinistral around N350°. This direction is interpreted to be the dominant shortening direction, i.e. $\sigma1$, during deformation stage 5, with $\sigma2$ vertical (Fig. 13d).

Stage 6. The few kinematics data of stage 6 strike-slip faults, even though they do not allow a reliable reconstruction of the shortening direction, are consistent with the N350° shortening direction inferred from stage 5 structures (Figs. 9o-13d).

1.5.2.2 Regional interpretation

We attempt here to upscale the local dynamic evolution inferred in the investigated area of the RFP to the regional tectonic framework of the Eastern Alps. A main inference of the local study is the occurrence of a switch in the main shortening direction from “E-W” (N290°) to “N-S” (N350°) direction, dated between 29 and 26 Ma. A local change in shear zone kinematics, likely consistent with this switch in shortening direction, has been recorded by Mancktelow et al. (2001) from the the northern country rocks of the Rieserferner the occurred just before the emplacement of the main plutonic RFP bodies (32 Ma, Romer and Siegesmund, 2003). Similarly, Pennacchioni and Mancktelow (2007) describe an earlier stage of “inverse” shear zone kinematics with respect to the main shearing event during the peak metamorphic stage in the Pennidic Tauren Window (occurring at 30 Ma or slightly after) that reflects a shortening direction oriented N345°.

Two possible different and mutually non-exclusive tectonic scenarios may explain the above described change in shortening direction:

(i) The shortening direction directly reflect the vector of relative motion between converging plates.

The switch from E-W shortening during Early Oligocene to N-S shortening during Miocene likely occurred consequently to the end of ESE-dipping subduction of the European oceanic lithosphere beneath Adria, its detachment from continental lithosphere following Europe-Adria continental collision and initial indentation. Continental indentation led to coupling between Alps and Adria-Austroalpine nappe stack leaving to Africa-Europe relative motion to control the (N-S) convergence direction (Handy et al., 2010). Analogous interpretations have been discussed by previous authors to explain similar two-stage convergence patterns inferred from deformation fabrics along the former NE-SW-striking Alpine orogen (Eastern Alps, Platt et al., 1989; Handy et al., 2010; Ligurian Alps: Capponi et al., 2001; Western Alps: Lacassin, 1989; Betic Cordillera: Aarden and Sayab, 2008). A slight counterclockwise rotation (<30°) of the shortening direction occurred during Miocene since the onset of N-S convergence.

(ii) Slab break-off modified the regional low-differential stress field imposed by N-S convergence between African and European plates in terms of relative magnitudes of principal stress components. Slab breakoff of the subducted oceanic lithosphere following continent-continent collision have induced uplift of the orogenic core and plate rebound, triggering also the Periadriatic magmatism itself (von Blanckenburg and Davies, 1995; Davies and von Blanckenburg, 1995; Buitier et al., 2002; Rosenberg, 2004; Magni et al., 2017). In this scenario, the E-W “shortening” direction during Oligocene deformation *stages 2 and 3a* does not reflect a real shortening direction it does likely reflect, instead, the reduction of vertical and horizontal N-S directed tectonic loadings during the fading stages of the slab breakoff process at regional scale. In this scenario, both the pluton emplacement and the development of *stage 1* and *2* structures occurred during a transient “orogen-perpendicular extension” (von Blanckenburg and Davies, 1995). This interpretation, however, suffer from the lack of knowledge about the exact age of slab break-off and the persistence in time of its effect on the regional stress field.

Possible interpretations of stage 3 and 4 top-to-east extensional shear zones. Geometry and kinematics of *stage 3* and *4* structures may be explained in different ways.

(i) Following the interpretation described in the above section (*Local stress field within the RFP*), *stage 3a* jointing and veining can be interpreted as (sub)horizontal tensional fractures responding to vertical unloading. Once N-S-directed shortening was reactivated after the cessation of post-slab break-off rebound influence, protracted uplift occurred simultaneously to shortening. The occurrence of both processes resulted in a W-up differential and eastward migrating uplift of the Austroalpine units hosting the RFP during the Oligocene (Trepmann et al., 2004; Bertrand et al., 2015). This W-up uplift is interpreted to have induced pluton tilting and top-to-east shear reactivation of *stage 3a* structures during deformation *stage 3b*. In addition, differential uplift may have also triggered the initiation of lateral escape tectonics (Ratschbacher et al., 1989).

(ii) Regional uplift lead to gravitational collapse of the orogen uppermost structural levels (i.e., above the brittle-ductile transition; Handy et al., 2005) resulting in the exhumation of deep seated units through lateral escape tectonics and the development of extensional shear zones, such as the Miocenic Brenner and Katschberg normal fault (since 23 Ma; Fügenschuh et al., 1997; Genser and Neubauer, 1989; Bertrand et al., 2015). Regional exhumation brought the RFP toward the brittle-ductile transition conditions of the host rock, when the temperatures within the pluton were still higher than the brittle-ductile transition (T>300°C). The onset of extensional tectonics was reflected by the development of *stage 3* and *4* normal ductile shear zones within the pluton. The transition from top-to-east shallowly-dipping ductile *stage 3* structures to *stage 4* steeply dipping brittle-ductile structures is interpreted to reflect the evolution of geometry and rheology of a low-angle normal fault system similar to the Katschberg normal fault during the exhumation of the footwall units (the RFP and hosting Austroalpine). Given the non-Andersonian geometry of low-angle normal fault systems, palaeostress inversion is not straightforward (Bistacchi et al, 2012). N-S-striking *stage 4b* joint clusters and mafic dykes are consistent with the N-S-directed shortening and E-W-directed extension. The possible occurrence of an oblate stress field (σ_1 and σ_2 almost equal) may explain in part the complex geometry and kinematics of s*tage 4* structures.

In any case, the development of *stage 3* and *4* structures implies the onset of regional uplift and exhumation processes earlier than usually reported for the Eastern Alps (Miocene age, 23 Ma; Frisch et al., 2000) as already suggested by recent structural analyses in the eastern Tauern Window (Favaro et al., 2017).

The onset of *stage* 5 strike-slip faulting occurred as a consequence of the eastward migration of exhumation tectonics (e.g. Bertrand et al., 2015), and symultaneous onset of paroxysmal strike-slip shearing along the Giudicarie fault system around 17 Ma (e.g. Viola et al. 2001, Müller et al., 2001, Favaro et al., 2017). Coheval structures developed in the surrounding Austroalpine and Pennidic Zentralgneise units are related to indentation tectonics, consistently to the N-S shortening direction (Mancktelow et al., 2001; Viola et al., 2001; Pennacchioni and Mancktelow, 2007, 2013; Bertrand et al., 2015). Stage 6 E-W trending strike-slip faults were already recognized by Mancktelow et al. (2001) and related to the Miocene N-S directed transpression along the dextral strike-slip Periadriatic lineament.

The interpreted local deformation sequence of the RFP reflects a complex regional tectonic evolution, during which, since N-S shortening was reactivated, principal stress directions remained almost (<30° counterclockwise rotation) constant, whereas magnitudes of the principal stress components have been modified by local scale and transient tectonic events.

1.5.3. Nucleation of shear zones and fluid rock interaction

The RFP is continuously interested by the cyclical development of high-temperature joints, from sub-magmatic stage down to solid-state conditions. The nucleation, geometry and orientation of *Stage 2, 3* and *4* deformation structures were controlled by the presence of 3 main sets of earlier brittle joints. *Stage 2* aplitic dykes, veins and joints were reactivated as strike-slip ductile shear zones (as indicated by marker offsets and by the geometry of foliated contractional jogs at joint stepovers) and filled with quartz veins in extensional bends. The mutual intersection between sheared structures and non-sheared precursors suggest the cyclical development of brittle structures and following shearing (e.g.

Pennacchioni and Mancktelow, 2007). Shearing along the conjugate joint and dyke sets developed a shear zone network bounding lozenge-shaped low-strain domains. Strain compatibility problems resulting from relative offset between lozenge-shaped low-strain domains were solved with the development of a weak mylonitic foliation at contractional jogs and thinning zones at structure intersections. Fractures and veins usually developed to weaken strain compatibility problems inside low-strain domains (Pennacchioni and Mancktelow, 2007) were not developed during deformation *stage 2*, probably as the consequence of either the small amount of strain accommodated or the lack of fluids enhancing brittle deformation. Limited amount of fluids during deformation is also suggested by the limited occurrence of bleaching haloes along *stage 2* structures. Discontinuous bleaching zones developed occasionally at dyke tips and, however they did not influenced the development of foliation or localization of deformation (similar to Pennacchioni, 2005).

Stage 3 ductile mylonites nucleated exploiting a set of E-dipping joints, epidote and quartz veins. Quartz veins sharply localized ductile shear and were commonly transformed to homogeneous quartz mylonites. Epidote-filled veins acted as nucleation structures for heterogeneous shear zones involving the host granitoid, as suggested by the development of a sigmoidal foliation in the host rock (Ramsay, 1980). The geometry of the ductile shear zone is controlled by the composition of the joint mineral infilling. Heterogeneous (continuous and asymmetric) shear zones with sigmoidal foliation involving the host tonalite are developed along epidote-veins, with a ultramylonitic core; homogeneous (discontinuous) quartz mylonites are developed where the joint is filled with quartz veins, with the development of a homogeneous oblique foliation inside the vein.

Stage 4 steeply dipping and N-S striking joints were exploited by transtensive brittle-ductile faults. Faulting was associated with extensive fluid infiltration. The occurrence of fracturing (joint formation and brittle-ductile shearing), intense fluid-rock interaction and low-T crystal plasticity for quartz lead to a macroscopic ductile behaviour of the fault zone as inferred from the occurrence of flexural-slip folding of the mechanical anisotropy formed by calcite-white mica veins and altered tonalite lithons. These fluids might be related directly to the emplacement of lamprophyre dykes, that are usually K-rich (K^+ for white mica) and releases significant amount of CO_2 (carbonates).

As reported from other plutons (e.g. Adamello: Pennacchioni, 2005; Sierra Nevada: Pennacchioni and Zucchi, 2013) and meta-granitoid units (Pennacchioni & Mancktelow, 2007), the ductile shear zones of the Rieserferner localized on brittle precursors (joints) and compositional heterogeneities (quartz and epidote veins). In contrast, the numerous mafic and felsic dikes did not localized ductile strain. Ductile folding associated with faulting is interpreted to have resulted from fluid-assisted deformation associated with the presence of a pervasive set of fractures.

The transition from homogeneous distributed to heterogeneous and localized deformation occurs after the emplacement of Stage 1 precursors (joints, dykes and veins). No localized deformation features (apart from the sheared northern border) are observed to postdate bulk foliation and predate dyke sets. Some minor homogeneous deformation may had outlasted dyke emplacement, as shown by the occurrence of buckled aplite dykes (Fig. 2a).

1.6. Conclusions

The structural evolution during pluton cooling consists of 5 main deformation stages, that have been bracketed in time and thermal conditions according to microstructural and textural analysis, literature and field data:

1. Stage 1: conjugate steeply-dipping E-W-trending joints, quartz veins and aplitic dikes, that were exploited as strike-slip ductile shear zones; submagmatic to high-T solid-state (>600°C) conditions; age: 32 Ma;
2. Stage 2: shallowly E-dipping joints filled with quartz- and epidote-veins, exploited as ductile shear zones with top-to-East kinematics; lower-amphibolite-facies conditions (400-450°C); age: 32-30 Ma;
3. Stage 3: N-S-trending steeply-dipping joints, exploited as brittle-ductile transtensive faults. Joints/faults were locally involved in folding; emplacement of steeply dipping N-S-striking mafic dikes (26.3±3 Ma, Steenken et al., 2000) are associated with this deformation stage;
4. Stage 4: steeply-dipping N-S-trending cataclasite- and psesudotachylytes-bearing strike-slip faults; associated with epidote veins; lower-greenshists-facies conditions (250-300°C); age: 17 Ma (Ar-Ar dating of pseudotachylyte);
5. Stage 5: steeply-dipping dip-slip N-S and strike-slip E-W-striking zeolite-bearing faults marked by whitish cataclasites and mirror-like surfaces, with a general E-W trending lineation; very-low temperature conditions (<200°C); <15 Ma.

The above described deformation stages and structures have been tentatively referred to trend and kinematics of regional structures and tectonic processes occurred during Oligocene and Miocene in the Eastern Alps. Kinematics analyses suggest that the observed switch in shortening direction from N290° during Early Oligocene to N350° during Late Miocene can be related to regional scale tectonic processes such as the occurrence of slab break-off and isostatic rebound. Once the N-S shortening direction was re-established, at around 29 Ma, exhumation and lateral escape tectonics controlled the local scale evolution and stress field, leaving the control to indentation tectonics from the middle

Miocene onward.

Acknowledgements

Silvia and Arnold Seeber, Gottfried Leitgeib are thanked for the warm hospitality in their alpine huts during fieldwork in the Rieserferner Group area. Simone Papa (UniPd) is thanked for the assistance and good company during fieldwork. Leonardo Tauro (UniPd) is warmly thanked for its work and assistance during sample and thin section preparation. Nei Mancktelow (ETH Zurich) and Bernardo Cesare (UniPd) are greatfully thanked for fruitful discussions. Dario Visonà (UnipPd) is thanked for the helpful hints about good field outcrops and discussions.

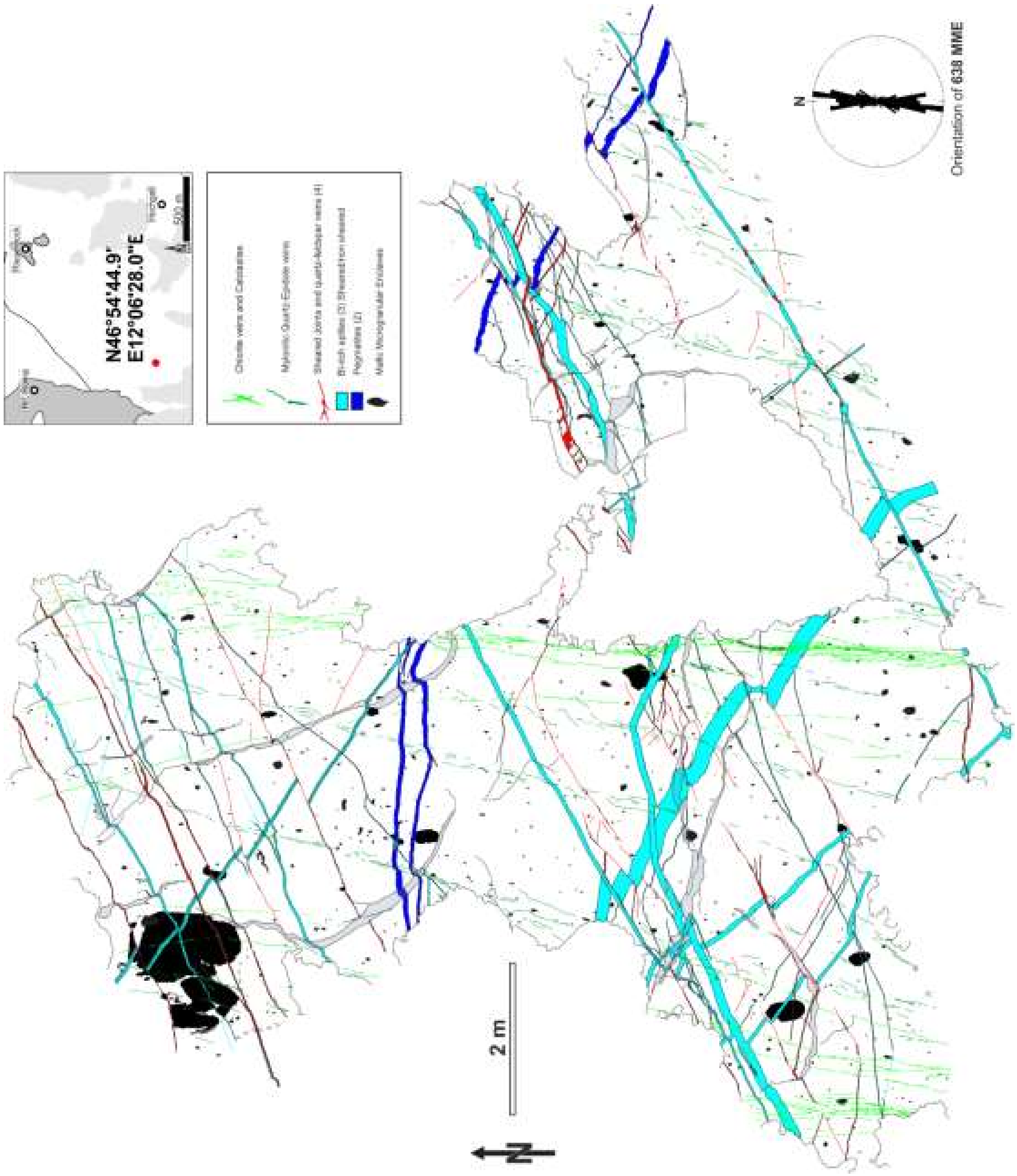

Figure Supplementary Material 1 : Surface map of the studied outcrop WP360, where aplite-pegmatite dykes, Stage 1 and 2 and Stage 4 brittle structures are perfectly exposed. The orientation of the elongation of mafic enclaves is reported in the rose diagram.

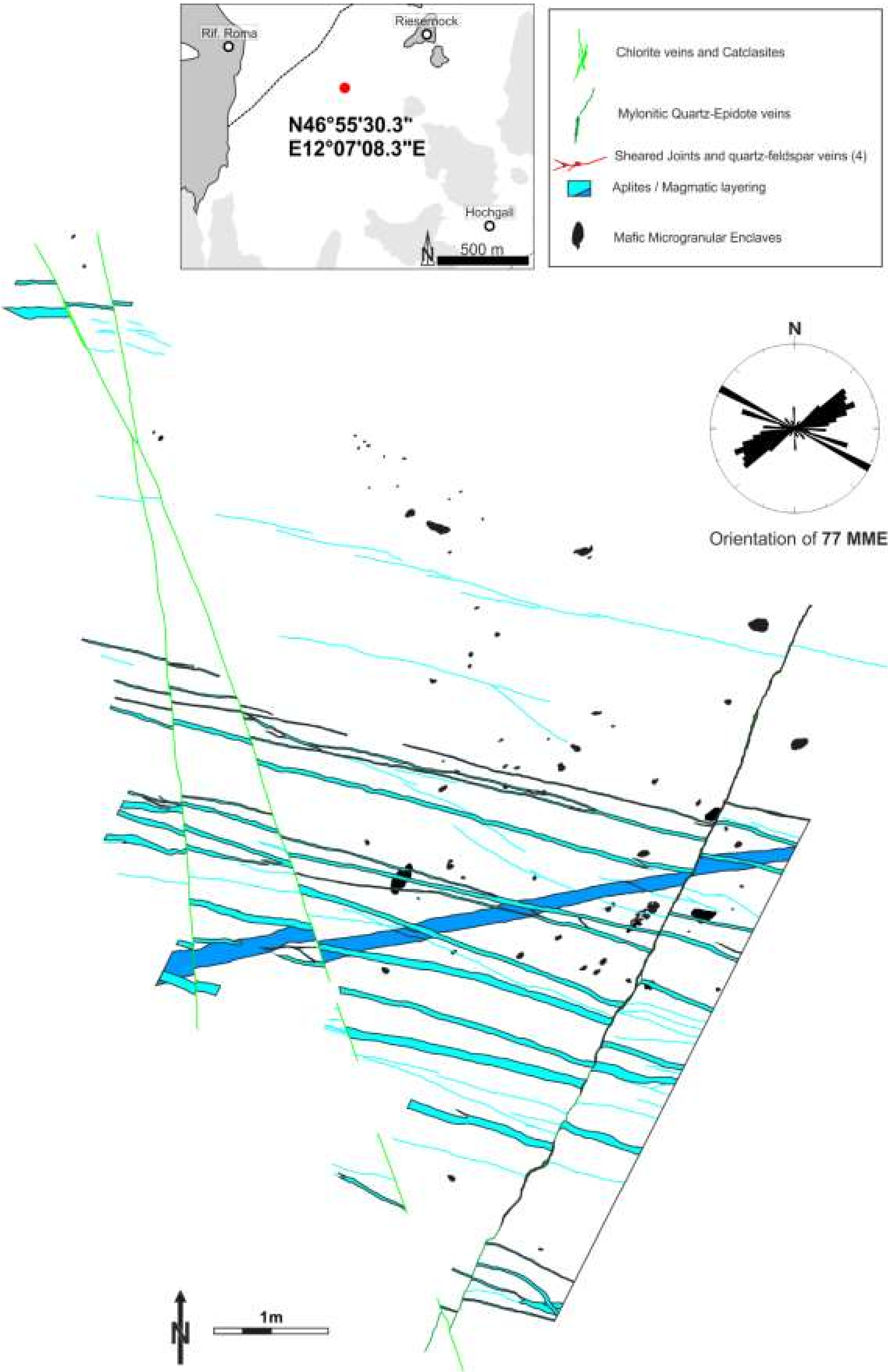

Figure Supplementary Material 2: Surface map of the studied outcrop WP036. Structures that can be identified here: aplite-pegmatite dykes, Stage 2 mylonitic veins, Stage 4 brittle faults. The orientation of the elongation of mafic enclaves is reported in the rose diagram.

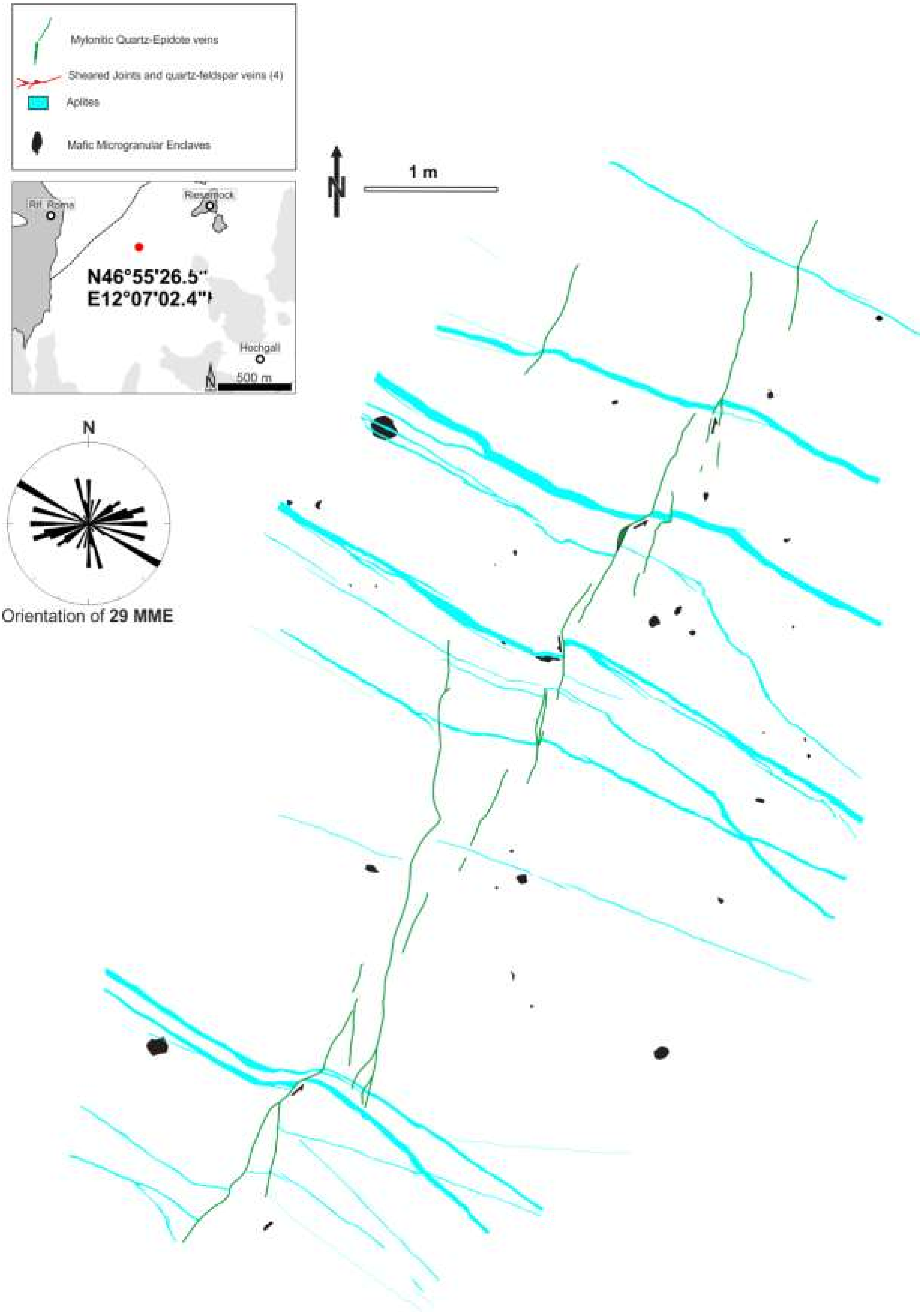

Figure Supplementary Material 3: Surface map of the studied outcrop WP039. Structures that can be identified here: aplite-pegmatite dykes, Stage 2 en-echelon mylonitic veins. The orientation of the elongation of mafic enclaves is reported in the rose diagram.

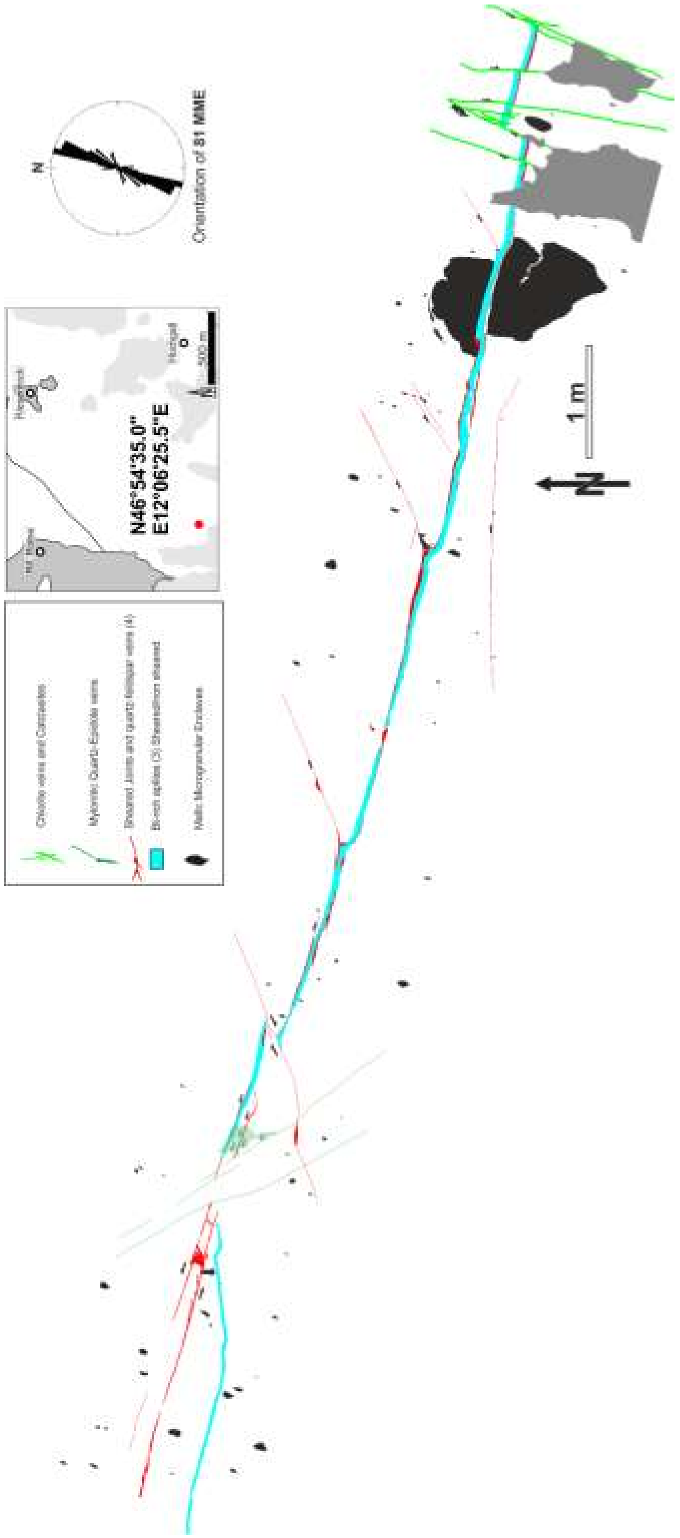

Figure Supplementary Material 4: Surface map of the studied outcrop WP230. Structures that can be identified here: aplite-pegmatite dykes, Stage 1 sheared joints and quartz-feldspar veins; Stage 2 (WSW-dippng) mylonitic epidote vein; Stage 4 localized cataclastic faults. The orientation of the elongation of mafic enclaves is reported in the rose diagram.

Chapter 2

Crystallographic control and texture inheritance during mylonitization of coarse grained quartz veins

Alberto Ceccato[1], Giorgio Pennacchioni[1], Luca Menegon[2], Michel Bestmann[3]

[1] Department of Geosciences, University of Padova, Via Gradenigo 6, I-35131 Padova, Italy

[2] School of Geography, Earth and Environmental Sciences, Plymouth University, United Kingdom

[3] GeoZentrum Nordbayern, Friedrich-Alexander-Universität Erlangen-Nürnberg (FAU), Germany

Abstract

Quartz veins within Rieserferner pluton underwent deformation during post-magmatic cooling at temperature close to 450 °C. Different crystallographic orientations of cm-sized quartz vein crystals conditioned the evolution of microstructures and crystallographic preferred orientations (CPO) during vein-parallel simple shear up to high shear strains ($\gamma \approx 10$). For $\gamma < 2$, crystals stretched to ribbons of variable aspect ratios. The highest aspect ratios resulted from {m}<a> glide in ribbons with c-axis sub-parallel to the shear zone vorticity Y-axis. Ribbons with c-axis orthogonal to Y (XZ-type ribbons) were stronger and hardened more quickly: they show lower aspect ratios and fine (grain size ~ 10-20 μm) recrystallization along sets of microshear zones (μSZs) exploiting crystallographic planes. Distortion of XZ-type ribbons and recrystallization exploit preferentially those slip systems with misorientation axis close to Y. New grains of μSZs initiated by subgrain rotation recrystallization (SGR) and thereupon achieved high angle misorientations by a concurrent process of heterogeneous rigid grain rotation around Y associated with the confined shear within the μSZ. Dauphiné twinning occurred pervasively, but did not played a dominant role on μSZ nucleation. Ribbon recrystallization

became widespread at $\gamma > 2$ and pervasive at $\gamma \approx 10$. Ultramylonitic quartz veins are fine grained (~ 10 μm, similar to new grains of μSZ) and show a CPO banding resulting in a bulk c-axis CPO with a Y-maximum, as part of a single girdle about orthogonal to the foliation, and orientations at the pole figure periphery at moderate to high angle to the foliation. This bulk CPO derives from steady-state SGR associated with preferential activity, in the different CPO bands, of slip systems generating subgrain boundaries with misorientation axes close to Y. The CPO of individual recrystallized bands is largely inherited from original crystallographic orientation of the ribbons (and therefore vein crystals) from which they derived. High strain and pervasive recrystallization were not enough to reset the initial crystallographic heterogeneity and this CPO memory is explained by a dominance of SGR. This contrast with experimental observation of a rapid erasure of a pristine CPO by cannibalism from grains with the most favourably oriented slip system under dominant grain boundary migration recrystallization.

2.1. Introduction

Quartz is one of the most representative minerals of continental crust rocks and has been commonly assumed to control the first-order rheology of large portions of the ductile crust (e.g. Ranalli, 2000). This explains the huge effort made in understanding quartz rheology during geological deformation. Physical deformation experiments have determined constitutive flow laws for quartz under different laboratory conditions (e.g., Luan and Paterson, 1992; Hirth and Tullis, 1992; Gleason and Tullis, 1995; Hirth et al., 2001). Application of these lab-determined flow laws to natural deformation implies extrapolation to over several orders of magnitude in strain rate (from $< 10^{-5}$ s^{-1} to values as high as 10^{-12}-10^{-16} s^{-1}) and the reliability of such extrapolation is legitimized by the similarity of microstructures, crystallographic preferred orientations (CPO) and inferred recrystallization mechanisms between the experimentally and naturally deformed quartz (e.g. Hirth et al., 2001; Mancktelow and Pennacchioni, 2010). With this aim numerous experimental studies have investigated the development and evolution of microstructures and CPO with strain (Tullis et al., 1973; Tullis, 1977; Dell'Angelo and Tullis, 1989; Gleason et al., 1993; Heilbronner and Tullis, 2006; Muto et al., 2011). Due to limitations of experimental apparatus, deformation experiments on quartz have been conducted on either single quartz crystals (Hobbs, 1968; Vernooij et al., 2006a, b; Muto et al., 2011) or on relatively fine-grained natural and synthetic quartz aggregates (e.g.: novaculite, Black Hill quartzite). The experiments on quartz single crystals are of particular relevance for the interpretation of many natural mylonitic quartz where recrystallized aggregates were derived from coarse original grains (several mm to tens of mm in grain size); either quartz grains of granitoid rocks and metamorphic rocks (Kilian et al., 2011; Bestmann and Pennacchioni, 2015) or quartz crystals from veins (Stipp et al., 2002; Pennacchioni et al, 2010; Price et al., 2016). The experiments of Muto et al. (2011) have evidenced a control of the initial quartz crystallographic orientation with respect to the imposed stress field on the crystal strength, recrystallization rate and developing CPO of recrystallized aggregates. However, Muto et al. (2011) observed that all crystals developed, during dynamic recrystallization, distinct domains with a CPO consistent with the favoured {m}<a> slip that rapidly cannibalized the aggregates with other unfavourable orientations with increasing shear. The memory of the original crystallographic orientations was totally erased after a relatively small amount of shear. This experimental result is not consistent with the observed evolution of some mylonitic quartz veins that shows a more long-lasting heredity of the original crystallographic orientations of parent grains in the CPO of recrystallized aggregates (Pennacchioni et al., 2010).

We present here the analysis of the microstructural and CPO evolution at increasing strain of quartz veins from a simple geological setting of a cooling pluton, similar to the context described in Pennacchioni et al. (2010). This analysis reveals a complex evolution over large strain determined by the initially different orientations of the vein crystals. This initial heterogeneity in crystal orientations is not dismantled by mylonitization up to stages of complete dynamic recrystallization.

2.2. Geological background and field description

During deformation *stage 3*, ductile shear zones develop exploiting quartz and epidote veins. Quartz veins of variable thickness (up to few decimetres thick) occurs along a shallowly ESE-dipping joint set (mean dip-direction/dip: N115°/20°), that almost invariably localized top-to-E normal ductile shearing at conditions close to 450°C and 0.3 GPa (Chapter 4). Deformed veins, ranging from protomylonites to ultramylonites, have been sampled for the study presented here (Figs. 1a-c). The protomylonites are coarse grained (reflecting the multi-millimetric grain size of the pristine quartz vein crystals) and show an oblique rough foliation forming an angle in the range between 20° and 30° to the vein boundary (Fig. 1a). The ultramylonites are fine grained, with a macroscopic flinty aspect, and show a pervasive foliation oriented at a very low angle to the vein boundary (Fig. 1c).

2.3. Microstructure of deformed quartz veins

In the kinematic reference system adopted here for the shear zones, the X axis is parallel to the stretching direction, the XY plane is parallel to the vein boundary, and the Z direction is orthogonal to the vein boundary. Thin sections were cut parallel to the XZ plane. The microstructure and the CPO of quartz in deformed quartz veins were analysed by: polarized light microscopy, computer integrated polarization microscopy (CIP) and electron backscattered diffraction (EBSD). CIP allowed the expeditious microstructure-linked analysis of the c-axis orientations of the coarse grained protomylonites over large thin section areas (mm^2 to cm^2). The details of the CIP and EBSD methods are given in the Appendix. Assuming simple shear within the tabular-shaped quartz veins, the shear strain γ localized into the vein was estimated from the angle θ between the internal oblique foliation and vein boundary according to the equation (Ramsay, 1980):

$$\tan 2\theta = -2/\gamma$$

2.3.1 Protomylonitic quartz veins

2.3.1.1. Ribbon grains

Weakly deformed quartz veins (Figs. 1a, 2a and, in supplementary online material, SOM1a) are characterized by largely predominant monocrystalline quartz ribbons, with different crystallographic orientation, which define a foliation inclined 20-30° to the vein boundary. Shear strains γ of 1.3 and 2.1 were estimated for the 2 analysed protomylonite samples.

The cumulative results of the microstructural analysis of 2 thin sections are shown in Fig. 2 (thin sections shown in Figs. 2a and SOM1a). In Figs. 2b and SOM1b, the different quartz ribbons are colour-coded, based on the CIP analysis, as a function of their dominant c-axis orientation according to the look-up-table of Figs. 2c and SOM1d. The cumulative c-axis CPO of the ribbons from the 2 thin sections shows a clustering (i) along a girdle approximately orthogonal to the ribbon elongation, and (ii) along the pole figure periphery, with a main clustering of the c-axes at a high angle to the ribbon elongation (Figs. 2c and SOM1d). We observe a difference in the ribbon

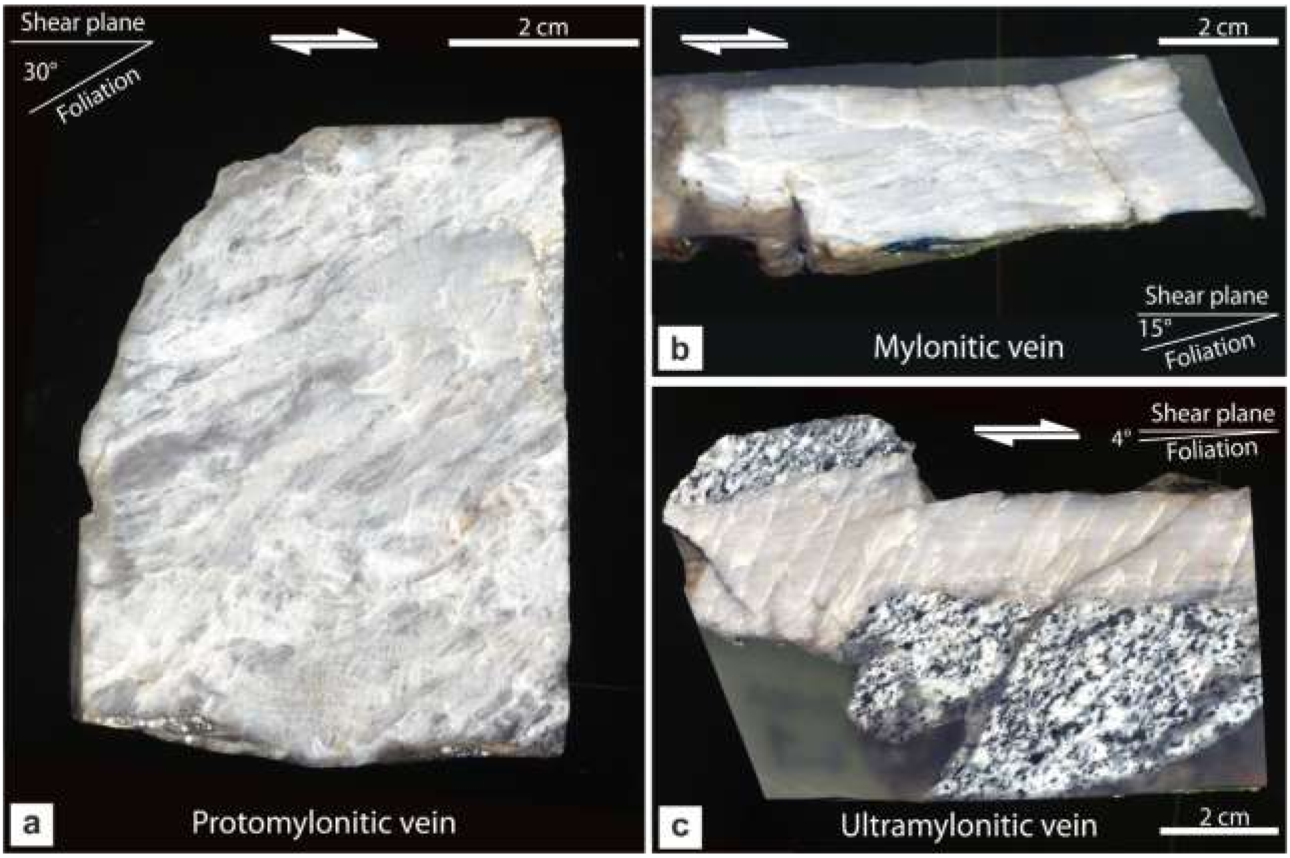

Fig. 1 - Polished slabs of sheared quartz veins of the Rieserferner pluton. The vein boundary is horizontal and the sense of shear is dextral (as can be inferred from the internal oblique foliation) for all samples. (a) Protomylonite showing a coarse, irregularly developed foliation defined by elongated to ribbon grains. The mean foliation inclination indicates a bulk shear strain $\gamma \simeq 1$. (b) Mylonitic vein with a more homogeneous oblique foliation corresponding to a bulk shear strain $\gamma \simeq 3.4$. (c) Ultramylonitic vein within a weakly deformed host tonalite localizing shear strain $\gamma > 10$.

microstructure depending on the c-axis orientation allowing the distinction of 3 end-member types: (1) Y-type ribbons, with c-axis close to Y (Fig. 3a); (2) Z-type ribbons, with c-axis close to Z (Fig. 3b); (3) XZ-type ribbons, with c-axis plotting along the pole figure periphery in intermediate position between X and Z. The XZ-type ribbons can be further distinguished in XZa- and XZb-types with the c-axis almost orthogonal and parallel to the ribbon elongation, respectively (Figs. 3c-f).

The aspect ratio of ribbons is shown, for the different ribbon c-axis orientations, in the pole figure of Fig. 2d. The measured aspect ratios are minimum values, given that most of the ribbons exceed in length the thin section width, but there is a clear relationship between the measured aspect ratios and the c-axis orientations (Fig. 2d): (i) the lowest aspect ratios (as low as about 2) belong to XZ-type ribbons, and especially to XZa-types; and (ii) most of the high aspect ratios (as high as 17.5) belong to Y-type ribbons.

2.3.1.2. Recrystallization of ribbons

The quartz ribbons of protomylonites show incipient recrystallization to fine-grained aggregates that are distinguished with a black colour in the microstructural sketches of Figs. 2b and SOM1b. On average over the whole thin section, the recrystallized aggregates form about 10% of the area. The new grains have an average grain size, determined from EBSD data (see Appendix for the methods), between 10 and 20 µm. Figure 2e shows the area fraction of recrystallized aggregates for to the different c-axis orientations of the host ribbons and indicates that recrystallization is larger (as much as 23% of ribbon area) in Z- and XZ-type ribbons. In Y-type ribbons, the recrystallization is very limited or absent. The different crystallographic orientations of the ribbons also translate into a difference of the internal deformation microstructures and of the geometry of the recrystallized aggregates:

1) Y-type ribbons show subgrains elongated parallel to the ribbon elongation, sweeping undulose extinction and limited recrystallization preferentially located at the ribbon boundaries (Fig. 3a).

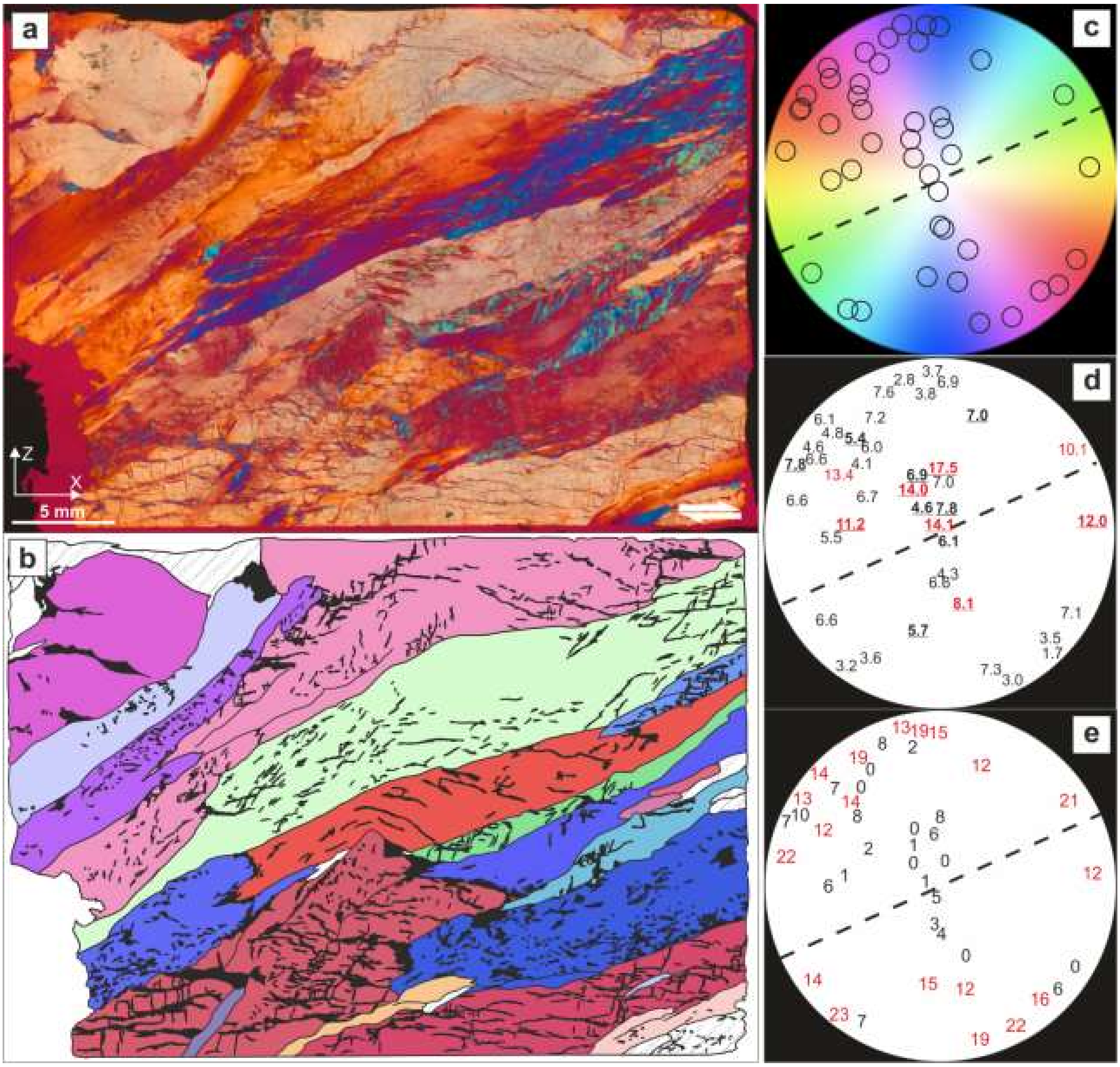

Fig. 2 - Microstructure and CPO of protomylonitic quartz vein. (a) Optical microphotograph (crossed polarizers and inserted gypsum plate) of a thin section from the protomylonite shown in Fig. 1a. (b) Sketch drawn from (a) showing the different ribbons (in different colours) and incipient recrystallization aggregates (in black colour). The ribbons are colour-coded as a function of the dominant c-axis orientation determined by CIP analysis, accordingly with the Look-Up Table (LUT) reported in (c). (c) Pole figure (with a coloured LUT background) of the c-axis orientations (small black circles) of the ribbons in the 2 analysed thin sections of protomylonite (see also Fig. SOM1). The dashed line represents the trace of the average ribbon elongation. (d) Aspect ratios for the different ribbon orientations. The aspect ratio values larger and lower than the mean value (6~7) are evidenced in black and red characters, respectively. Underlined bold values represent actual aspect ratios for ribbons completely included within the thin section. (e) Area fractions of recrystallized aggregates for to the different c-axis orientations of the host ribbons. The red and black values represent values larger and smaller than the bulk sample recrystallization (~10%), respectively. High values occur mostly along the periphery of the pole figure. Low values dominate close to the centre of the pole figure.

2) Z-type ribbons show weak undulose extinction, a single set of deformation lamellae (fine extinction bands, FEB: Derez et al., 2015) and recrystallized aggregates scattered across the ribbon or arranged along sharp discontinuities aligned sub-parallel to the ribbon elongation (Fig. 3b). In the most deformed ribbons (or portions of ribbons), recrystallized aggregates are clustered into elongated domains, inclined at variable angle with respect to the ribbon elongation, locally forming intersecting sets (lower ribbon portion in Fig. 3b). Coarse (100's of μm in size) polygonization and recrystallization resemble the blocky localized extinction bands described in Derez et al. (2015) (Fig. 3b).

3) XZ-type ribbons typically show bands of recrystallization arranged in two intersecting sets (Figs. 3c-f). These bands of recrystallization commonly correspond to micro-shear zones (μSZs) as inferred from the displacement of the orthogonal set of μSZs. The dominant set of μSZs is commonly oriented sub-parallel to the vein boundary. The other set is oriented at a high angle to the vein boundary, sub-parallel to Z or slightly rotated consistently with the shear sense (i.e. clockwise in all the images presented here showing dextral sense of shear: Figs. 4 and SOM1c). The direction of the μSZs are slightly different in different ribbons (Figs. 4 and SOM1c). The μSZs of each set have roughly a regular spacing (in the range between 10's of μm to 300 μm) on a local (sub-millimetric) scale, but the spacing and the spatial density are variable across the ribbon. On a local scale, the μSZs of both sets show a comparable thickness. The thickness of the μSZs correlates with the amount of accommodated slip (Fig. SOM2).

The XZa-type ribbons are almost free of an optically visible internal distortion (except for a weak undulose extinction) in between incipient μSZs (Fig. 3c). The domains cut by the μSZs preserve a roughly square-lozenge shape up to relatively high degree of ribbon recrystallization. The XZb-type ribbons commonly show a strong internal distortion manifested by undulose extinction and wide extinction bands (WEBs of Derez et al., 2015; e.g. outlined by white arrows in Fig. 3f) (Fig. 3d). The recrystallization aggregates of both XZa- and XZb-type have a strong CPO (evaluated with the gypsum plate) different from that of the host ribbon (e.g. Fig. 3c). In XZa-type ribbons, the position of c-axis of the recrystallized aggregates in pole plots is orthogonal to the boundary of the µSZs (Figs. 3c-e; “c-normal” shear bands of van Daalen et al., 1999). In XZb-type ribbons, the position of c-axis of the aggregates is almost parallel in pole plots, or slightly rotated with the sense of shear, to the boundary of the µSZs (Figs. 3d-3f; “c-parallel” shear bands of van Daalen et al., 1999). The CPO within the µSZs has been investigated in more detail by EBSD (see below).

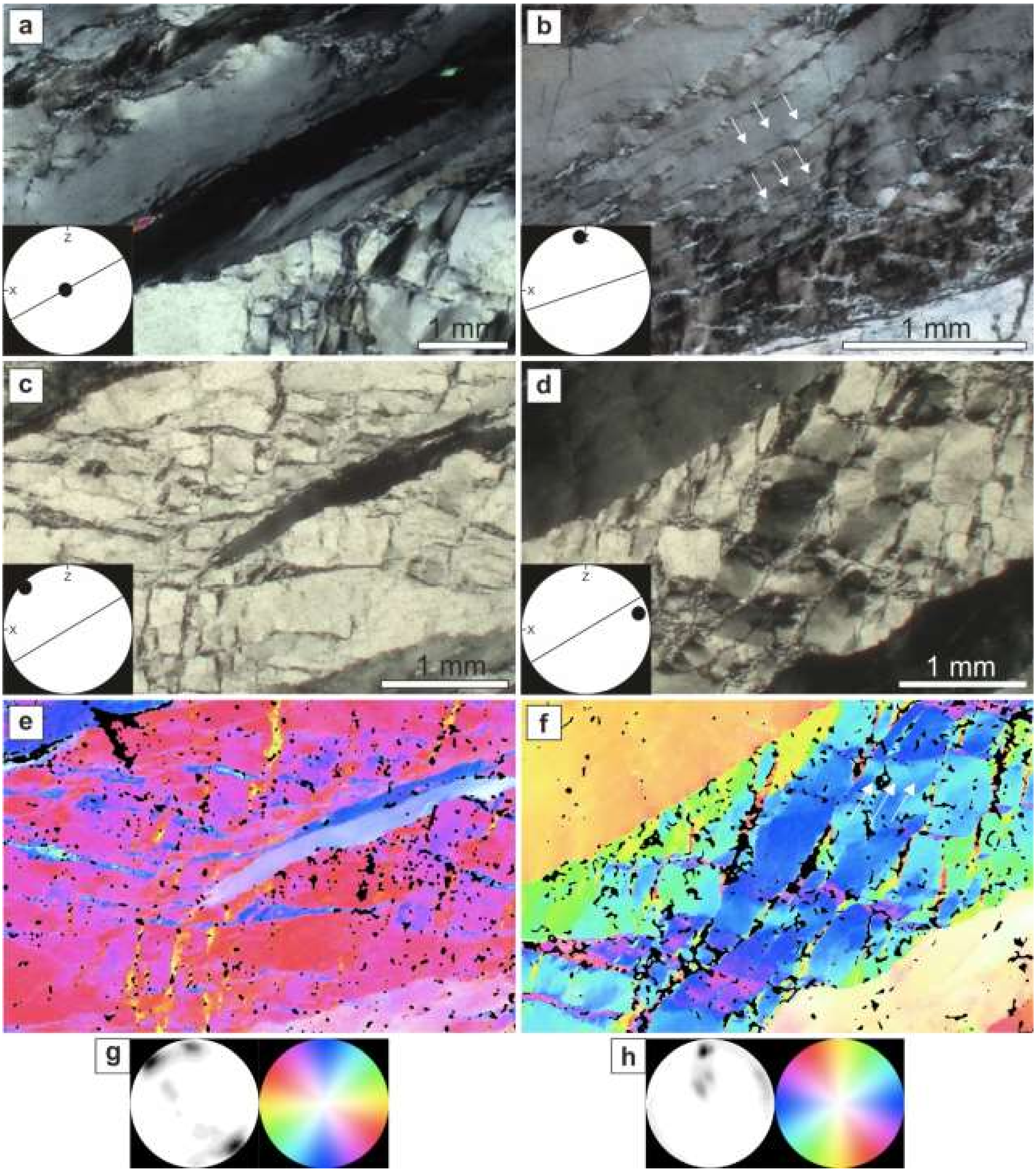

Fig. 3 – Optical microstructures of ribbons in the protomylonite with a schematic representation of the [c] axis orientation determined by CIP analysis (lower-left pole figures). (a) Cross-polarized microphotograph of a dark-gray to black Y-type ribbon almost free of recrystallization. (b) Cross-polarized microphotograph of a Z-type ribbon with sharp longitudinal discontinuities sub-parallel to the ribbon elongation and incipient recrystallization. Recrystallization occurred along the sharp discontinuities (some are indicated by white arrows) and, in the most strained part of the ribbon (down right), along conjugate microshear zones dominate by a synthetic Riedel-type set. (c) Microphotograph (crossed polarizers and inserted gypsum plate) of a XZa-type ribbon showing two sets of μSZs. (d) Cross-polarized microphotograph of XZb-type ribbon with two sets of μSZs. (e) CIP-derived c-axis orientation map of the microstructure in (c) coloured according the LUT (equal area, lower hemisphere). (f) CIP-derived c-axis orientation map of the microstructure in (d) coloured according the LUT. (g) c-axis CPO of the domain in (e) determined by CIP. (h) c-axis CPO of the domain in (f) determined by CIP.

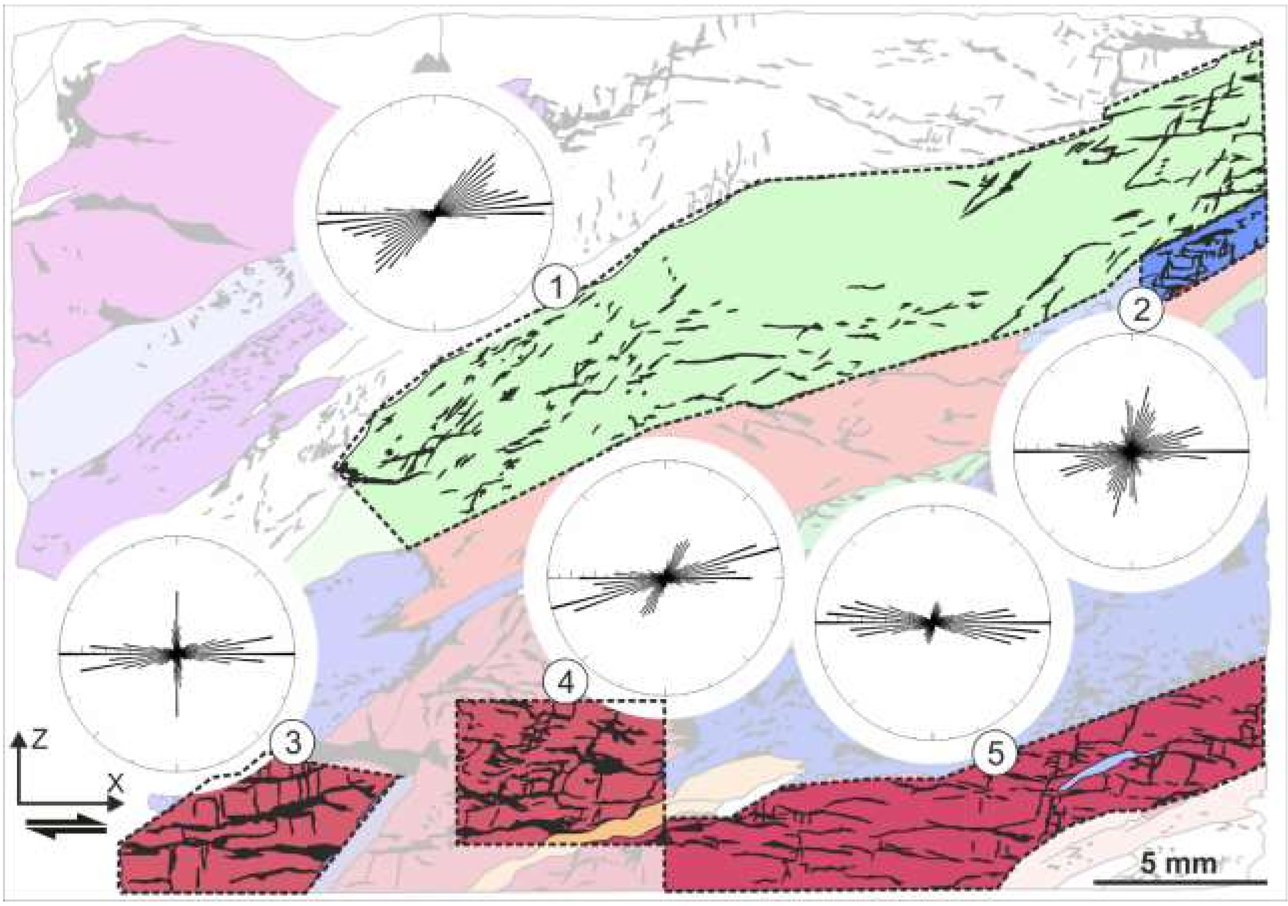

Fig. 4 –Analysis of the orientations of fine-grained recrystallized aggregates in some ribbons of the protomylonite of Fig. 2b. A similar analysis of the 2nd studied protomylonite sample is reported in Fig. SOM1c. The orientations of the µSZs in the selected areas (surrounded by the dashed line and showing un-blurred colour) are shown in the rose diagrams.

2.3.1.3 Distribution of fluid inclusions

In protomylonites, fluid inclusions are mainly present within recrystallized aggregates, along the μSZ selvages and associated with polygonized domains of ribbons. In the latter case, subgrains are locally outlined by fluid inclusions. In secondary electrons SEM images on broken surfaces (Figs. SOM3a-b), the grain boundaries of recrystallized grains commonly show regularly arranged pores with crystallographically-controlled etch-pit type shapes (Mancktelow and Pennacchioni, 2004). Within relatively undeformed portions of XZ- and Z-type ribbons, local fluid inclusions are scattered and not arranged in trails. Y-type ribbons are mainly free of fluid inclusions. Recrystallized aggregates next to the μSZs, commonly decorated with fluid inclusions, contain locally small mica flakes that are aligned to define an internal foliation (Figs. SOM 3c-d).

2.3.2. Mylonitic quartz veins

Mylonitic quartz veins show a layered microstructure (Fig. 5a) determined by the alternation of: (i) high aspect ratio (>7) monocrystalline ribbons; (ii) partially recrystallized ribbons; and (iii) completely recrystallized layers. The amount of bulk recrystallization is close to 50% of the area. The grain size of the recrystallized grains is comparable with the one along the µSZ within the ribbons of the protomylonites. Shear strains γ of 3.5 and 6.6 have been estimated for the mylonite samples.

The monocrystalline ribbons are coarsely polygonized with prevalent subgrain boundaries orthogonal to the ribbon elongation (Z-type ribbons). Ribbon recrystallization occurred at the boundaries and along sharp bands trending parallel to the ribbon elongation (especially in Z-type ribbons; e.g. Figs. 5a-b). The layers of partially recrystallized ribbons include lozenge-shaped to elliptical quartz ribbon porphyroclasts (mainly XZa-type) embedded in the aggregate of recrystallized grains (Fig. SOM3e). Completely recrystallized layers show an extinction banding parallel to the foliation.

The cumulative CIP-determined c-axis pole figure of the monocrystalline ribbons resembles a type-I girdle dominated by a concentration of c-axes in two small circles around the foliation pole (Fig. 5c). The bulk pole figure of the pervasively recrystallized domains consists of a short girdle (low density of c-axis poles at the pole figure periphery) oriented at a high angle to the foliation (Fig. 5d).

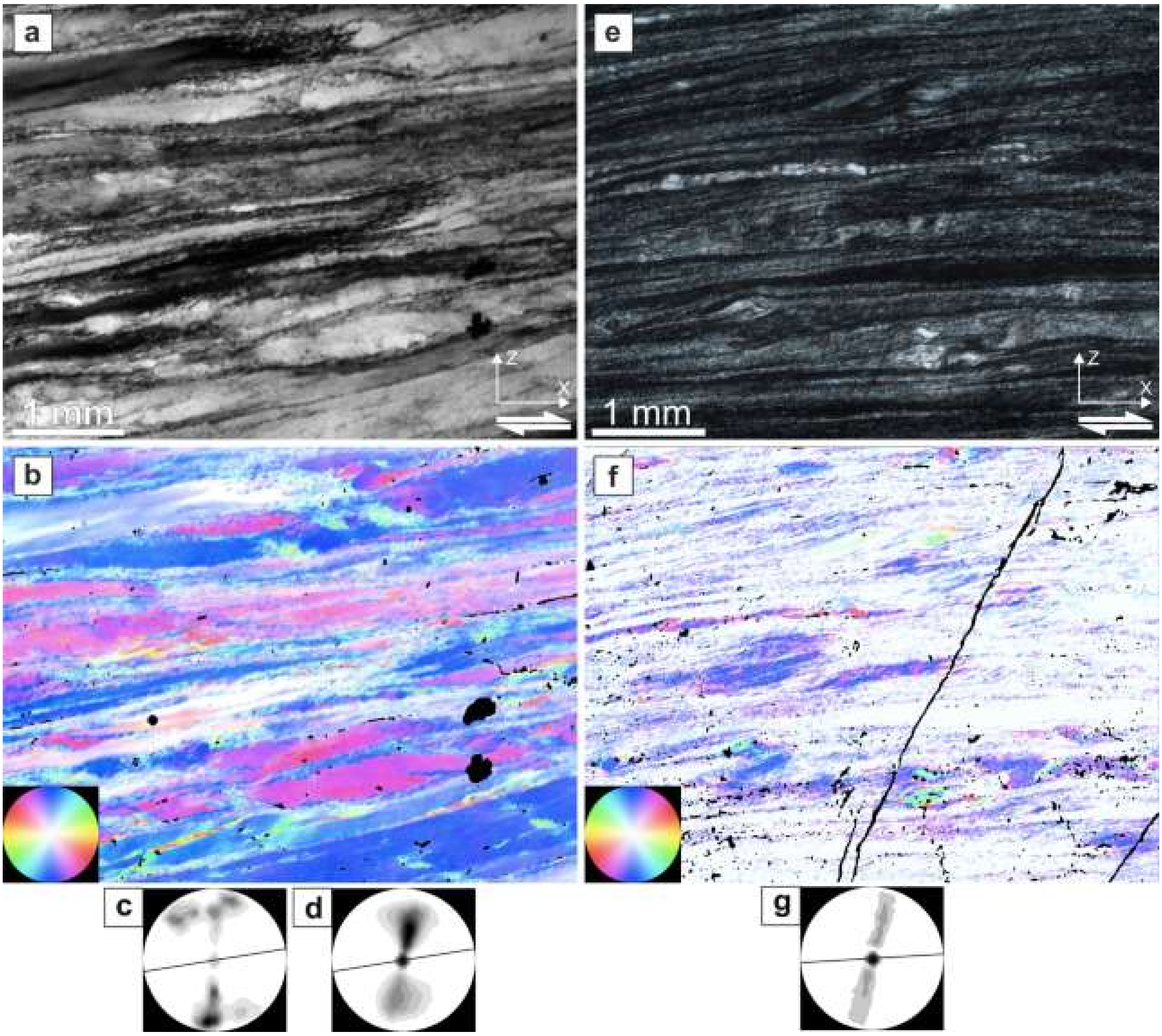

Fig. 5 – Optical microstructures and c-axis orientation map (from CIP) of a quartz mylonite and ultramylonite. (a) Circular polarization microphotograph of mylonite showing the alternation of un-recrystallized to partly recrystallized ribbons and lens-shaped domains, and completely recrystallized matrix. (b) c-axis orientation map (from CIP analysis) of the image in (a) showing the LUT in the lower left corner. (c) CIP-determined c-axis pole figures for non recrystallized ribbons of (b). (d) CIP-determined c-axis pole figure for recrystallized matrix of (b). (e) Cross-polarized microphotograph of a pervasively recrystallized quartz ultramylonite showing an extinction banding of the matrix, very elongated ribbons and small un-recrystallized ribbon porphyroclasts. (f) c-axis orientation map (from CIP analysis) of the image in (e) showing the LUT in the lower left corner. (c) CIP-determined c-axis pole figures of the ultramylonite in (f).

2.3.3 Ultramylonitic quartz veins

Ultramylonites consist of a dominant (> 90% area) matrix of fine-grained (10-15 µm determined by EBSD; see below) recrystallized grains that includes isolated quartz porphyroclasts (ribbon porphyroclasts) and high aspect ratio (> 50) monocrystalline ribbons (Fig. 5e). The extinction banding of the mylonitic aggregate and the ribbon grains define a foliation oriented at a low (~5°) angle to the vein boundary yielding a shear strain $\gamma > 10$. The recrystallized grains show a shape preferred orientation defining a foliation oblique to the extinction banding and inclined consistently with the shear sense (Figs. SOM3g-h).

The ribbon porphyroclasts range in shape from lozenge- to lenticular- and fish-shaped and have an asymmetry with stair-stepping geometry climbing against the sense of shear (Figs. SOM3f-g-h). As inferred from CIP and optical (gypsum-plate inserted: Fig. SOM3d) analysis, all the porphyroclasts have a similar c-axis orientation, about orthogonal to the mylonitic foliation.The CIP-determined bulk CPO of the ultramylonite shows a strong maximum close to Y, which is part of a single girdle inclined with respect to Z consistently with the sense of shear (Fig. 5g). This bulk CPO, derived from layers with different CPO, has been investigated in detail by EBSD (see below).

2.4. Cathodoluminescence investigations

The CL in quartz is a powerful tool for investigating microstructural complexity and possible signs of fluid-rock interaction (e.g. Bestmann and Pennacchioni, 2015). Two main observations come from CL investigation: (i) recrystallization in and polygonalization around µSZs are associated with a lower (darker) CL-signal that overprint the heterogeneous CL signal of protomylonitic quartz grains (Figs. SOM15a-f); (ii) ultramylonite textural domains are characterized by different CL signatures (Figs. SOM15g-h). Quartz luminescence is mainly related to the ~415 nm (blue) peak in panchromatic spectra that is strongly correlated with the trace concentration of Ti (Wark and Spear, 2005; Bestmann and Pennacchioni, 2015). Many studies have suggested that Ti resetting (and therefore resetting in CL patterns) in mylonitic rocks is enhanced by the occurrence of water-assisted deformation mechanisms and quartz precipitation (Grujic et al., 2011; Haertel et al., 2013; Bestmann and Pennacchioni, 2015). We performed a preliminary CL analysis of deformed Rieserferner quartz veins, with the purpose of detecting potential signatures for fluid-rock interaction during the different stages of shearing of the quartz veins.

We present CL images (Fig. SOM11) that provide evidence for the marked heterogeneity in the CL signal associated with the different microstructures. Protomylonites show complex and heterogeneous CL patterns (Fig. SOM11). The most strained parts of the XZ- and Z-type ribbons (that are less deformed than Y-type ribbons) have the lightest CL grey tones of the microstructure, which turn into dark tones in domains associated with crystal distortion, subgrain polygonization, incipient recrystallization and µSZs. The domains of homogeneous deformation of Y-type ribbons (Figs. SOM11a-b) show a pervasive regular array of bright CL linear features organized in 2 intersecting sets, forming a lozenge shaped grid, overprinting a dark grey CL background. In zones of distortion of the Y-type ribbons this array is dissected irregularly across a network of darker CL zones coinciding with aggregates of subgrains and new grains or highly distorted zones. The dark CL zones of incipient recrystallization have a granular appearance that is more clearly shown at the higher magnifications in CL images of the µSZs across XZ-type grains (Figs. SOM11c-f). A direct comparison between the

EBSD map of Fig. 7a and the corresponding CL image of Fig. SOM11f, clearly shows that the grains visible in the CL image perfectly match to subgrains and new grains along the µSZ. These grains visible in CL show a light grey core and a dark rim, which results in the grainy appearance of the zone of polygonization and recrystallization described above. Adjacent to µSZs there is commonly a very heterogeneous overprinting of the lighter CL tones of the less distorted portions of host ribbon by dark grey CL zones that are also associated with pervasive linear features subparallel to the main shortening direction. In general there is a coincidence between the CL darker tones with the most distorted parts of the ribbons. In ultramylonites, there is still heterogeneity in the CL patterns (Figs. SOM11g-h). The local ribbon leftovers have a lighter CL shade than the recrystallized matrix. This latter shows a CL banding, that partially matches the CPO banding, similar to that described by Bestmann and Pennacchioni (2015) for quartz in a mylonitic granodiorite.

2.5. EBSD analysis

The EBSD analysis (Figs. 6-10) was performed on selected microstructures of protomylonite and ultramylonite. Information of EBSD analytical conditions are reported in the Appendix A. In protomylonites, Y- and XZ-type ribbons, and the associated recrystallization aggregates along µSZs, were investigated as microstructural end-members of the ribbon evolution. In ultramylonite, we have investigated both the CPO banding of the pervasively recrystallized matrix and a ribbon porphyroclast that survived such high strains.

2.5.1 EBSD analysis of protomylonite

2.5.1.1. Y-type ribbon

The analysed Y-type ribbon (Fig. 6a) shows a c-axis distribution in pole figure forming a short girdle centred on the Y-axis and oriented orthogonal to the ribbon elongation (Fig. 6b). The subgrain boundaries are mostly straight and sub-parallel to the ribbon elongation with a spatial density increasing towards the zones of incipient recrystallization at the ribbon boundaries. The subgrains of highly polygonized domains and the few new grains have a similar grain size of about 15-20 µm. The misorientation angle distribution (MAD) (both correlated and uncorrelated) shows a strong maximum at low angle misorientations (< 20°) and, for correlated misorientations, at around 60° (Fig. 9a). In crystal coordinates, the low angle misorientation (< 15°) axes show higher density towards the c-axis and weakly around {m}; for high angle misorientations (close to 60°) there is a high density towards the c-axis (Fig. 6c). In sample coordinates, the low angle misorientation axes show high density close to the Y-axis (Fig. 6c) and at the pole figure periphery coinciding with {m} poles, and there is an overall distribution to define a girdle sub-parallel to the ribbon elongation. The high angle misorientations axes (mainly related to misorientations with angle ~ 60°: Fig. 10a) show high density around Y (i.e., sub-parallel to the c-axis) (Fig. 6c).

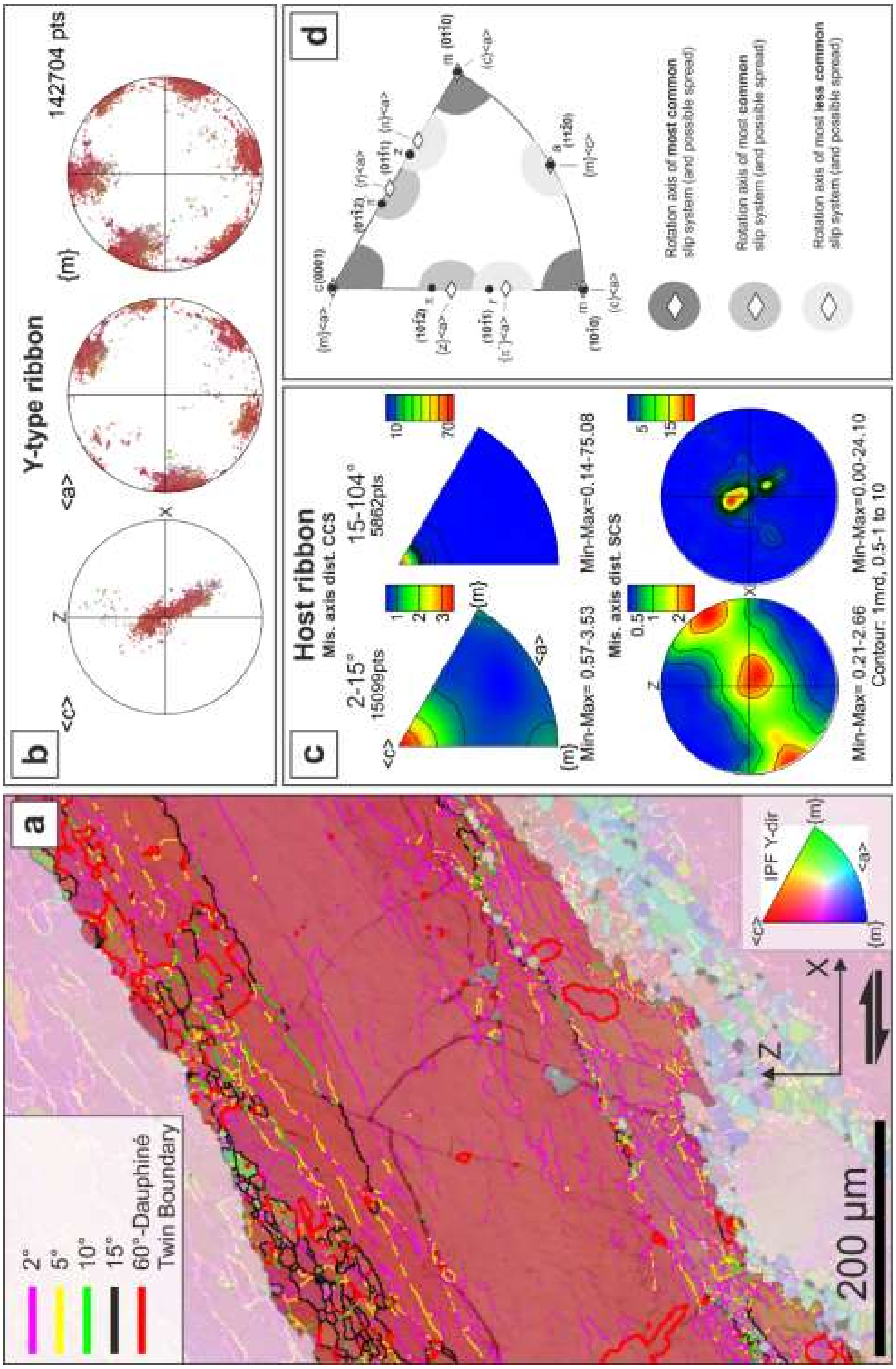

Fig. 6 - EBSD analysis of a Y-type ribbon. (a) Orientation map of the ribbon colour-coded according to the inverse pole figure in the lower right corner. Subgrain boundaries are colour-coded as a function of misorientations according to the legend in the upper left corner. (b) Pole figures for the orientations of [c], <a> and {m} crystallographic directions; (c) Misorientation axis distribution in crystal (upper row) and sample (lower row) coordinate system for both low (2-15°) and high angle misorientations (15-104°). ((d) Scheme of misorientation axis distribution in crystal coordinate system for hexagonal quartz showing the most common slip systems (edge dislocations) for the different misorientation axes (redrawn from Neumann, 2000). (e) Optical microphotographs (crossed polarizers) of the domain mapped in (a) (included in the white box).

2.5.1.2. XZa- and XZb-type ribbons

The EBSD analysis was conducted on both XZa- (Figs. 7 and SOM6) and XZb-type ribbons (Fig. 8) and on included µSZs with different degrees of evolution: incipient (one to few grains thick), evolved (in the range between few grains and 100s µm thick), and mature (several 100s µm thick). The µSZs of XZa- and XZb-type ribbons are similar in their microstructural evolution and are described together.

2.5.1.2.1 Internal distortion of the host ribbons

Both XZa-type and XZb-type ribbons show a heterogeneous internal distortion (Figs. 7b and 8b) consistent with rotation of crystallographic directions around an axis sub-parallel to Y. This results in a dispersion along the periphery to over 45° of the c-axis orientations (Figs. 7b and 8b). In the XZa-type ribbon, the low-angle low misorientation boundaries are heterogeneously distributed, wavy and poorly interconnected. In the XZb-type ribbon, low angle boundaries are straight with sets sub-parallel to the trace of rhombohedral planes (low angle boundaries of areas (1) and (2) of Fig. 8a). The MAD (Figs. 10b-c) for both types of ribbons show two maxima at low angle misorientations (< 15°) and at around 60°, similar to what observed for the Y-type ribbon. In crystal coordinates, all the analysed portions of XZa- and XZb-type ribbons show, as a bulk, a widely scattered distribution across the entire plot of low angle misorientation axes, but with increasing density towards the positive and negative rhombs (see scheme of Fig. 6e for reference) and especially towards the c-axis. It is of note that the distribution maxima are weak in all cases. This bulk distribution probably masks a rather more heterogeneous distribution of misorientation axes as indicated by the plots for the areas 1 and 2 in Fig. 8f showing more distinct clustering towards the c-axis (area 1) and along a girdle between rhombohedral crystallographic planes {r} and {z} (area 2) (see scheme of Fig. 6e for reference). The analysis of more strongly deformed portions of the XZ-b type ribbon adjacent to the incipient µSZs α and β also indicates distinct local patterns of low angle misorientation axis in comparison to the rest of the host ribbon (Figs. SOM4a-b).

In sample coordinates, the misorientation axes of XZa-type ribbon are clustered at the periphery of the pole figure close to the c-axis orientations of the host ribbon (Fig. 7e) for both low and high angle misorientations. For XZb-type ribbons the bulk misorientation axes are: (i) strongly clustered off-axis in the between Y and X in a region including the direction of {r} and the c-axis for low angle misorientations; and (ii) sub-parallel to the host c-axis for high angle misorientation (basically of 60°).

2.5.1.2.2 Incipient μSZs

Incipient μSZs are defined by discontinuous linear arrays of one-grain-thick recrystallization aggregates in alternation with, and flanked by, discontinuous subgrains rows (e.g. Fig. 8a). The new grains have the same size (about 10-20 μm) as the surrounding subgrains (Figs. 7a-b and SOM5a). The contact area between the host and the incipient μSZs is defined by one-subgrain-thick zone. The μSZ traces are sub-parallel to the trace of rhombohedral crystallographic planes of the host ribbon (Figs. 8b-c). The c-axes of the new grains are distributed, in a rotational sense consistent with the μSZ sense of shear (e.g., sinistral for the μSZs α and β that are inclined more than 45° to the shear plane: Fig. 8), along the pole figure periphery. The spreading of these c-axis orientations ranges from orientations close to that of the host grain to almost orthogonal orientations (Fig. 8c). The axis distributions of new grains, together with the lattice distortion of the host grain, are consistent with rotations around Y (anticlockwise for the sinistral μSZs α and β and clockwise for the dextral μSZ ϕ, ε and δ). The host ribbon can be in direct contact with highly misoriented new grains even in one-grain-thick μSZs.

The misorientation analysis of low angle boundaries (misorientations in the range of 2-15°) in the host grain adjacent to incipient μSZs α and β (enclosed in the black polygons marked in Fig. 8a) shows misorientation axes clustering parallel to primary (<r> and <z>) or secondary (<π> and <π'>) rhombohedral directions (inverse pole figure of Fig. SOM4). In sample coordinates, these axes show a clustering that is close to the Y-axis (Fig. SOM4). The small number of new grains of incipient μSZs (that show subgrain boundaries anyway) does not allow a statistically meaningful analysis of the misorientation axes.

2.5.1.2.3 Evolved µSZs

Evolved µSZs consist of recrystallized aggregates with a thickness of a few grains (µSZs δ of Fig. 7a, and ϕ of Fig. 8a). A transition zone (< 100 µm in thickness) between host crystal and the µSZ aggregate is discontinuously present and includes a high spatial density of low- and high-angle boundaries, and relatively high lattice distortion gradients (~ 0.25-0.5 °/µm, point-to-point smallest misorientation angle). These transition zones alternate with domains where recrystallized grains are in sharp contact with a weakly distorted portion of host grain (Fig. 7a: µSZ δ). High spatial density of subgrain boundaries is observed at intersections and stepover domains between µSZs. The subgrains next to µSZs and the new grains have comparable mean grain size of 10-20 µm (Figs. SOM5b and 7c). The 2 analysed µSZs are sub-parallel to the trace of either one of the positive {r} or negative {z} rhombohedral crystallographic planes (µSZ δ: Fig. 7b) and to the {m} crystallographic plane (µSZ ϕ: Fig. 8b).

As for incipient µSZs, the c-axis of new grains of evolved µSZs within both XZa- and XZb-type ribbons are distributed in a rotational sense from the host orientation with rotation axis sub-parallel to Y (Figs. 7c and 8d). Recrystallized grains are polygonal to sub-rectangular in shape, which results in common triple and four-grain junctions, and show a strong shape preferred orientation inclined consistently with the shear sense of the µSZs. The grain size is homogeneous within a single µSZ, but can be slightly different (of few µm) in different µSZs (Figs. SOM5c). Pores are observed both at triple junctions and along the grain boundaries (Figs. SOM3a-b).

In relatively coarse (grain size >15 µm) and high aspect ratio (>3) new grains, the boundaries of local subgrains are mostly oriented orthogonal to grain elongation (e.g. Figs. 7a and 8a). However, recrystallized grains are dominantly strain-free (lattice distortion gradient <0.2 °/µm, point-to-point smallest misorientation angle). Though the number of data is very small, the misorientations axis related to these subgrain boundaries plot close to either rhombohedral (<r> and <z>) or peripheral

(<m> and <a>) crystal axes when analysed individually. The MAD for the evolved μSZs is comparable to the MADs for the host ribbons, in the case of μSZ ϕ (Fig. 9g), but differs in μSZ δ (Fig. 9e) for the presence of a wide range of misorientation angles also including intermediate values between 10° and 60°. In sample coordinates the misorientation axis distribution for both low and high angle (15-45°) misorientations of both the evolved μSZ δ (Fig. 7f) and ϕ (Fig. 8g) shows a higher density spot eccentric to the Y-directions (in addition to the spot close to c-axis direction observed for high angle misorientations).

2.5.1.2.4 Mature μSZs

The 2 analysed mature μSZs belong to XZa-type ribbons (Figs. 7 and SOM6) and trend parallel to the trace of one {r} plane of the host ribbon (e.g., μSZ ε in Figs. 7a-b). An irregular, discontinuous contact zone (< 200 μm thick) is locally present between the host ribbon and the recrystallized aggregate of the μSZs that involves a higher distortion and spatial density of subgrains of the ribbon (Figs. 7a and SOM6a). The recrystallized aggregate of the μSZs includes, close to its boundaries, relatively coarse relics of the host ribbons that show a core-and-mantle transition to the recrystallized grains in the interior of the μSZs. The subgrains in the host transition zone and within clasts inside the μSZs have a comparable size (10-20 μm, e.g. Fig. SOM6d) as the new recrystallized grains of the μSZs.

Similar to incipient and evolved μSZs, the mature μSZs also show a CPO with crystallographic axes dispersed (with rotation axis parallel to Y) from the orientations of the host grain (Figs. 7d and SOM6e-g). In the thicker μSZs of Fig. SOM6a, there is still a dispersion of crystallographic axes around Y, but the c-axis maxima are also spread towards intermediate positions of the pole figure (3 columns on the left of Figs. SOM6e-g), that can be in part associated with the larger distortion (and therefore crystallographic dispersion) of the host grain (Fig. SOM6b). The different domains distinguished in the mature μSZ of Fig. SOM6a, show distinct CPO, though still mainly referable to different degrees of rotational spreading of crystallographic axes around Y from the host orientation.

These domains likely represent coherent portion of the host grain, dissected during the incipient stage of the µSZ evolution (as can be seen in the host grain of Fig. SOM6e), which underwent rigid rotation before extensively recrystallized in the µSZ.

The MADs of both the analysed mature µSZs is comparable with those of the evolved µSZ δ (Figs. 9f and 9h) .

In crystal coordinates, the low angle misorientation axis distributions have very low maxima for all domains, with concentrations along girdles between {r} and {z} poles (e.g. domains ω and ψ) and between {m} and <a> directions (e.g. domains ξ and ψ) (Figs. 7g; Figs. SOM6e-g). In sample coordinates there are stronger maxima of low angle misorientation axis towards the centre of the pole figure (Y-axis) in all domains with a tendency to distribute along a girdle in domain ξ (Fig. 7g; Figs. SOM6e-g).

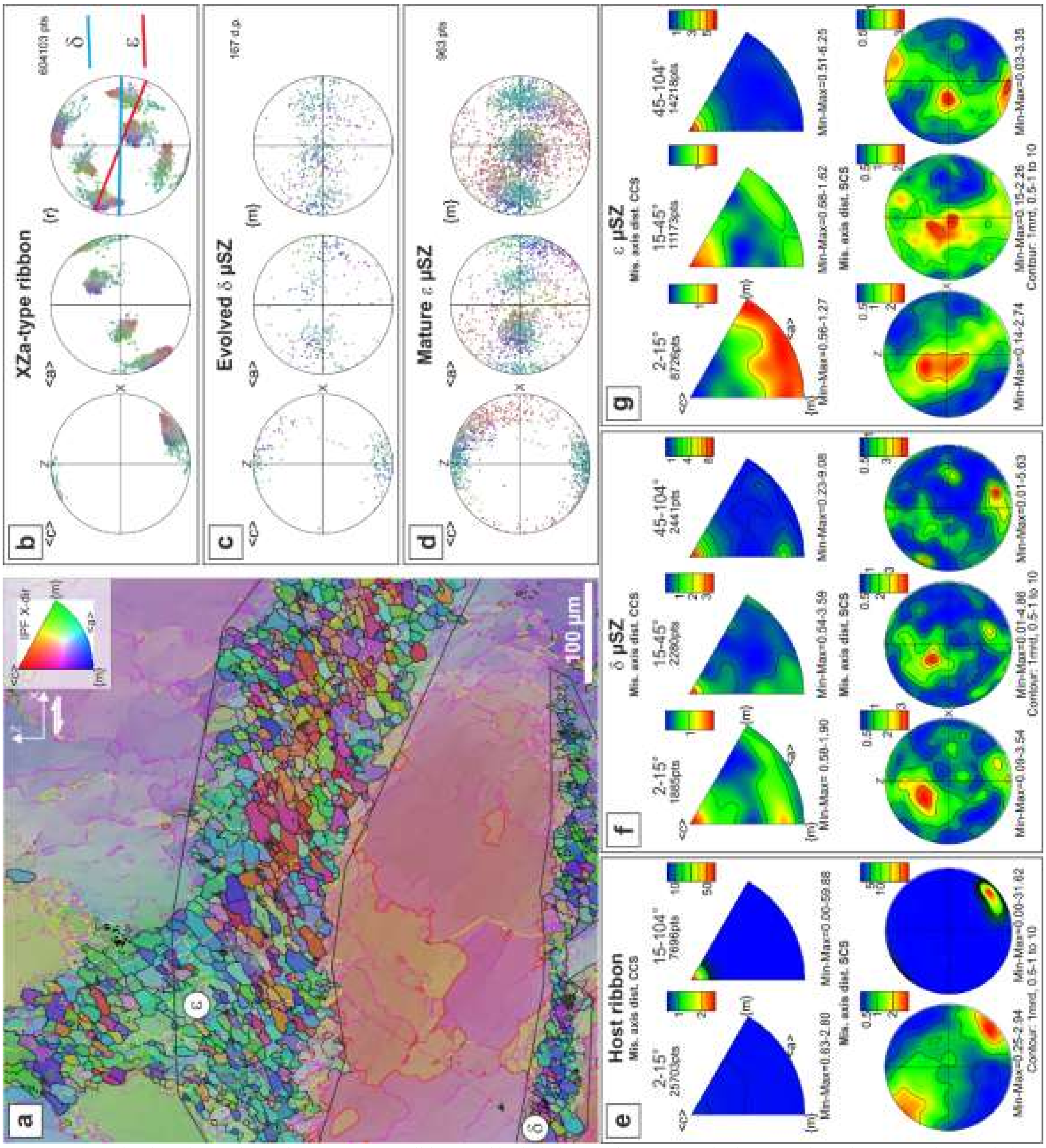

Fig. 7 - EBSD orientation imaging and data for an XZa-type ribbon, and included µSZs, in a protomylonite. (a) Orientation map colour-coded according to the inverse pole figure shown in the upper right corner. Boundaries are colour-coded as a function of misorientations according to the same legend in Fig. 6a. (b) Pole figures for the host ribbon showing the orientations of [c], <a> and {r} crystallographic directions. Note the parallelism between one of the {r} crystallographic plane and the µSZ trace (red line). (c) Pole figures ([c], <a> and {m} crystallographic directions) for the recrystallized aggregate along the evolved µSZ δ. (d) Pole figures ([c], <a> and {m} crystallographic directions) for the mature µSZ in the lower part of the map (a). (e) Misorientation axis distributions for low (2-15°) and high (15-104°) misorientation angles and in sample coordinates for the host ribbon. (f) Misorientation axis distributions for low (2-15°), intermediate (15-45°) and high (45-104°) misorientation angles in crystal and sample coordinates for the evolved µSZ δ. (g) Misorientation axis distributions for low (2-15°), intermediate (15-45°) and high (45-104°) misorientation angles in crystal and sample coordinates for the mature µSZ ε. (h) Optical microphotographs (crossed polarizers) of the domain mapped in (a) (included in the red box).

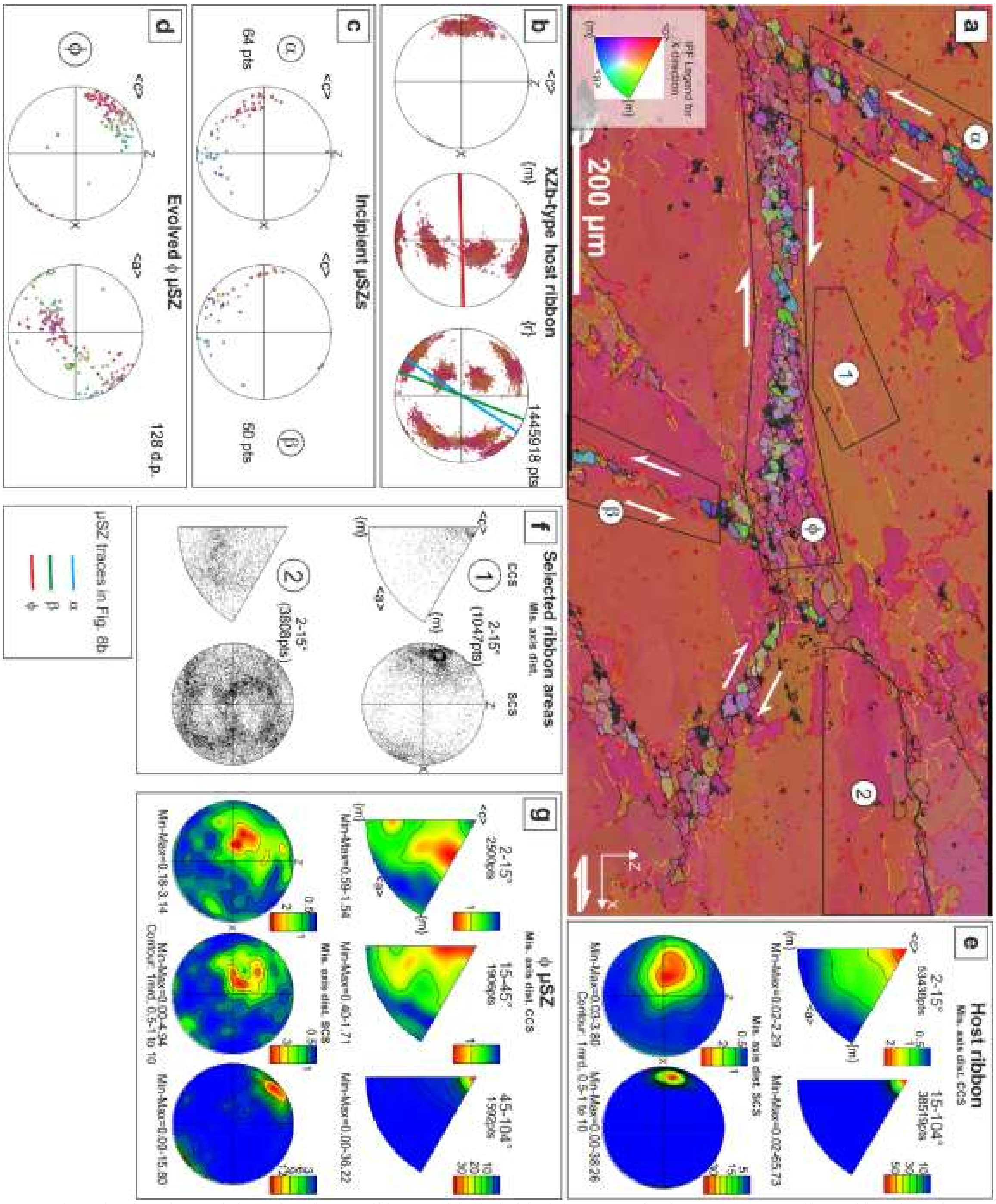

Fig. 8 - EBSD orientation imaging and data of XZb-type ribbon, and included incipient to evolved µSZs. (a) Crystallographic orientation map with inverse pole figure (IPF) for colour-coding (with respect to the X kinematic direction). The ribbon includes 2 incipient µSZs (α and β) with antithetic (left-lateral) sense of shear, and a main synthetic (right-lateral) evolved µSZ (ϕ). (b) Pole figures ([c], {m} and {r} crystallographic orientations) for the host ribbon including the orientations (bold lines) of the µSZs (blue: α; green: β; red: ϕ). (c) Pole figure of the c-axis orientations (one-point-per-grain) for recrystallized grains in the incipient µSZs α and β, (d) Pole figures of c- and a-axis orientations (one-point-per-grain) for recrystallized grains in the evolved µSZ ϕ. (e) Misorientation axis distributions for low (2-15°) and high (15-104°) misorientations in crystal and sample coordinates for the host ribbon. (f) Misorientation axis distributions (for the misorientation range 2-15°) in crystal and sample coordinates for two selected areas (1) and (2) shown in the orientation map (a). (g) Misorientation axis distributions for low (2-15°), intermediate (15-45°) and high (45-104°) misorientations in crystal and sample coordinates for the evolved µSZ δ. (h) Optical microphotographs (crossed polarizers) of the domain (included in the red box) shown in the EBSD map (a).

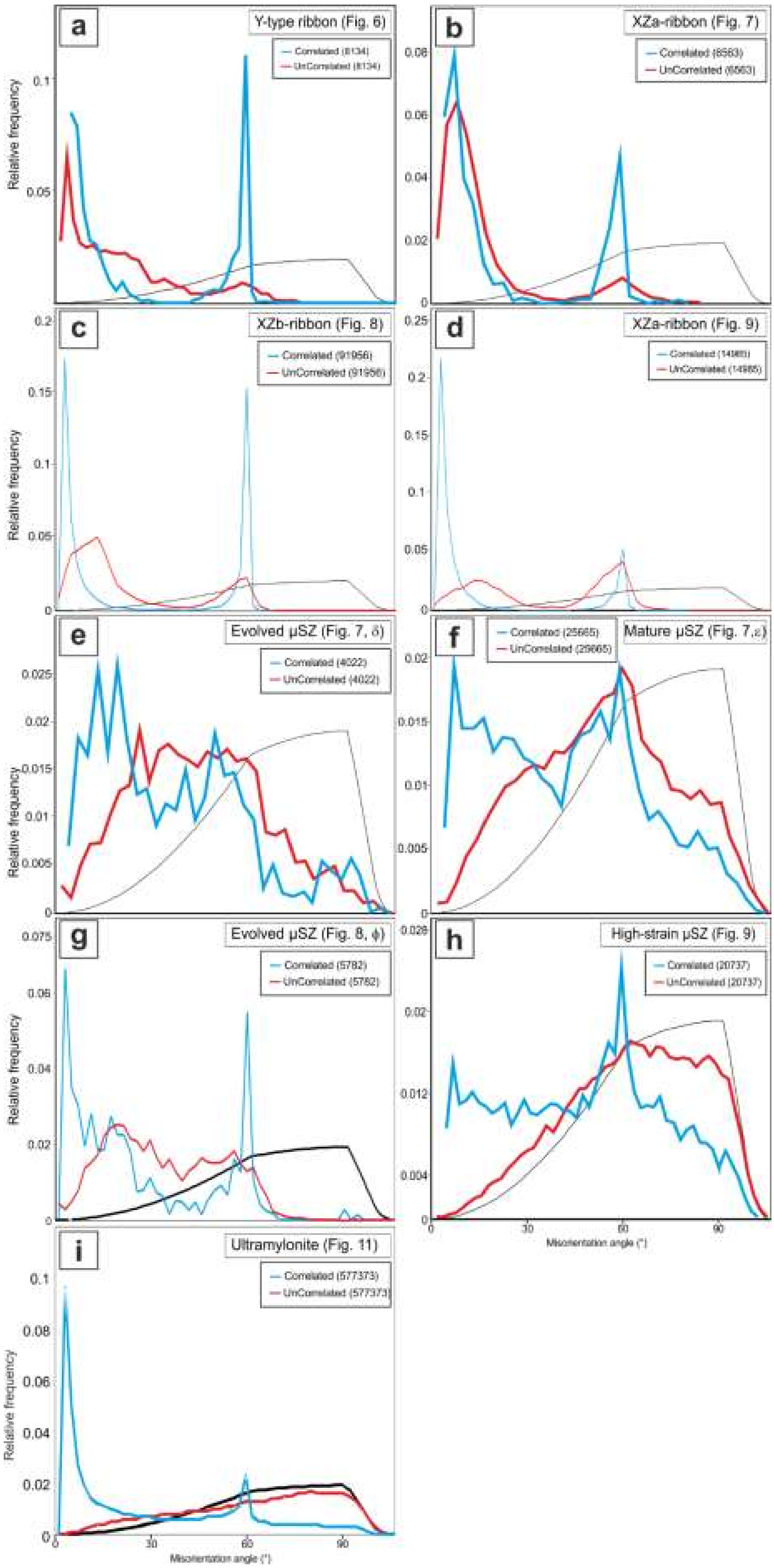
a
Y-type ribbon (Fig. 6)
Correlated (8134)
UnCorrelated (8134)
Relative frequency
0.1
0.05
b
XZa-ribbon (Fig. 7)
Correlated (6563)
UnCorrelated (6563)
0.08
0.06
0.04
0.02
0
c
XZb-ribbon (Fig. 8)
Correlated (91956)
UnCorrelated (91956)
Relative frequency
0.2
0.15
0.1
0.05
0
d
XZa-ribbon (Fig. 9)
Correlated (14985)
UnCorrelated (14985)
0.25
0.2
0.15
0.1
0.05
0
e
Evolved µSZ (Fig. 7, δ)
Correlated (4022)
UnCorrelated (4022)
Relative frequency
0.025
0.02
0.015
0.01
0.005
0
f
Correlated (25665)
UnCorrelated (25665)
Mature µSZ (Fig. 7, ε)
0.02
0.015
0.01
0.005
0
g
Evolved µSZ (Fig. 8, ϕ)
Correlated (5782)
UnCorrelated (5782)
Relative frequency
0.075
0.06
0.04
0.02
0
h
High-strain µSZ (Fig. 9)
Correlated (20737)
UnCorrelated (20737)
0.028
0.02
0.012
0.004
0
0
30
60
90
Misorientation angle (°)
i
Ultramylonite (Fig. 11)
Correlated (577373)
UnCorrelated (577373)
Relative frequency
0.1
0.08
0.06
0.04
0.02
0
0
30
60
90
Misorientation angle (°)

Fig. 9 - Misorientation angle distributions (MAD) for correlated (blue curve) and uncorrelated misorientations (red curve). The thin black curve represents the theoretical random distribution for any trigonal point group. M is the misorientation index. (a) Host Y-type ribbon of Fig. 6. (b) Host XZa-type ribbon of Fig. 7. (c) Host XZb-type ribbon of Fig. 8. (d) Host XZa-type ribbon of Fig. 7. (e) Evolved µSZ δ of Fig. 7. (f) Mature µSZ ε of Fig. 7. (g) Evolved µSZ ϕ of Fig. 8. (h) Mature µSZ of Fig. 9. (i) Ultramylonite of Fig. 10.

2.5.2 EBSD analysis of ultramylonite

2.5.2.1. Recrystallized matrix

The EBSD map of the ultramylonite in Fig. 10a includes a large portion of recrystallized matrix showing a CPO banding and a large ribbon porphyroclast.

The bulk c-axis pole figure (Fig. 10b) shows a girdle slightly inclined to the YZ plane, with the sense of shear, and a peripheral concentration fading progressively towards the foliation plane and therefore resembles the type of pole figure determined for the protomylonites and mylonites (Figs. 2c and 5c, respectively). This bulk pole figure results from the combination of distinct c-axis CPO characteristic of the different layers composing the ultramylonite microstructure and referable to 3 main types (Figs. 10c-f): (1) layers with a c-axis short girdle, orthogonal to foliation, centred on the Y-axis (Fig. 10e) and showing a dominant red colour in Fig. 10a (e.g. layer III); (2) layers with c-axis maxima concentrated, along the bulk girdle, at intermediate positions between Y and the pole figure periphery (referred to as “intermediate orientation”: Fig. 10f; layer IV) and showing violet and purple colour in Fig. 11a; (3) layers with c-axis maxima towards the pole figure periphery (referred to as “peripheral orientation”: Figs. 10c-d; layer I-II) and showing dominant blue and green colours in Fig. 10a (e.g. domain I-II). The layers with the dominant peripheral c-axis direction commonly contain grains with an intermediate orientation, but rarely grains with a Y-orientation. These layers also commonly include quartz porphyroclasts.

The MAD indicates the presence of a strong maximum for correlated misorientations at low angle misorientations (< 15°) and a weak one for misorientations around 60° (Fig. 9i) for the bulk microstructure and also for the individual layers with distinct CPO. The misorientation axis distributions in crystal coordinates are very similar for all the different layers except for those containing the ribbon porphyroclasts, and show high density towards the c-axis orientation for both low and high (~60°) misorientations (2nd-3rd plots of Figs. 10b-f). For low angle misorientations the distribution of axes is broad with the maximum intensity increasing from the layers with peripheral directions (max = 1.6 multiple of uniform distribution, mud) to the intermediate directions (max = 2.29 mud) and to the Y-directions (max = 3.68 mud). For high angle misorientation the axes strongly concentrate around the c-axis orientation. In sample coordinates, the misorientation axes plots are also very similar for the different layers with misorientation axes clustered around Y, for low angle misorientations, and around the dominant c-axis orientation of the layer for high angle misorientations.

The mean (geometric) grain size of recrystallized grains in ultramylonites is ~ 9 μm with negligible differences between the layers with different CPO (Fig. SOM8). The recrystallized aggregates show a strong oblique SPO. Grains belonging to layers with a Y- and intermediate c-axis orientations have a slightly larger aspect ratio (Y-orientation: R mean = 3.06; σ = 1.26; intermediate-orientation: R mean = 2.92; σ = 1.29) than those with peripheral maximum (R mean = 2.38; σ = 1.05).

2.5.2.2 Ribbon porphyroclasts

Asymmetric ribbon porphyroclasts are common within recrystallized layers with peripheral c-axis maxima. (Figs. 10a, 10g and 10i) As described above, the asymmetry of the ribbon porphyroclast is opposite to that commonly shown by mineral fishes in mylonite (e.g. Pennacchioni et al., 2001; ten Grotenhuis et al., 2002). This shape derives from dissection of ribbon grains along μSZs that are sub-parallel to a rhombohedral planes and suitably oriented for being activated as C' shear bands. The internal distortion of the porphyroclasts is manifested by undulose extinction and zones of high subgrain density especially close to the porphyroclast tips.

The c-axes of the ribbon porphyroclasts plot along the periphery of the pole figure dispersed over a range of ~80° from directions nearly orthogonal to the ultramylonitic foliation to directions at a low angle to foliation in the NW-SE pole figure quadrant for this “dextral” quartz mylonite (Fig. 10g).

The recrystallized aggregate surrounding the ribbon porphyroclasts show a c-axis preferred orientation distributed along the pole figure periphery (Fig. 10h) with two c-axis maxima: (i) close to the c-axis orientation of the ribbon porphyroclast; and (ii) close to the peripheral maxima at the end of the CPO girdle visible in the bulk

The MAD for both the porphyroclast and the surrounding aggregate show a strong peak at low (<15°) misorientations and a weaker one at about 60° (Figs. SOM7f-g). In crystal coordinates, the misorientation axes distributions of both porphyroclast and recrystallized aggregate show (2nd-3rd plots of Figs. 10g-h): (i) slightly higher density close to the periphery of the IPF along a {m} to <a> girdle and close to the c-axis for low angle misorientations; and (ii) high density around the c-axis for misorientations around 60°. In sample coordinates, the low angle misorientation axes cluster around Y, while the high angle misorientation axes overlap in orientation with the c-axis orientation (4th-5th plots of Figs. 10g-h).

Fig. 10 - EBSD orientation imaging and data for the quartz ultramylonite. (a) Orientation map colour-coded according to the inverse pole figure shown below. The white solid lines bound domains (I-IV) with a different CPO analysed individually. The dashed white lines encompass quartz ribbon porphyroclasts (b)-(h) c-axis pole figures (1st column), pole figures for low angle misorientations (2nd column) and high angle misorientations (3rd column), and misorientations axis plots in sample coordinates for low (4th column) and high angle misorientations (5th column). In the pole figures, data are reported as one-point-per-grain except for (g) ; (i) Crossed polarizer microphotograph of the ultramylonite (red box indicate the analysed area)

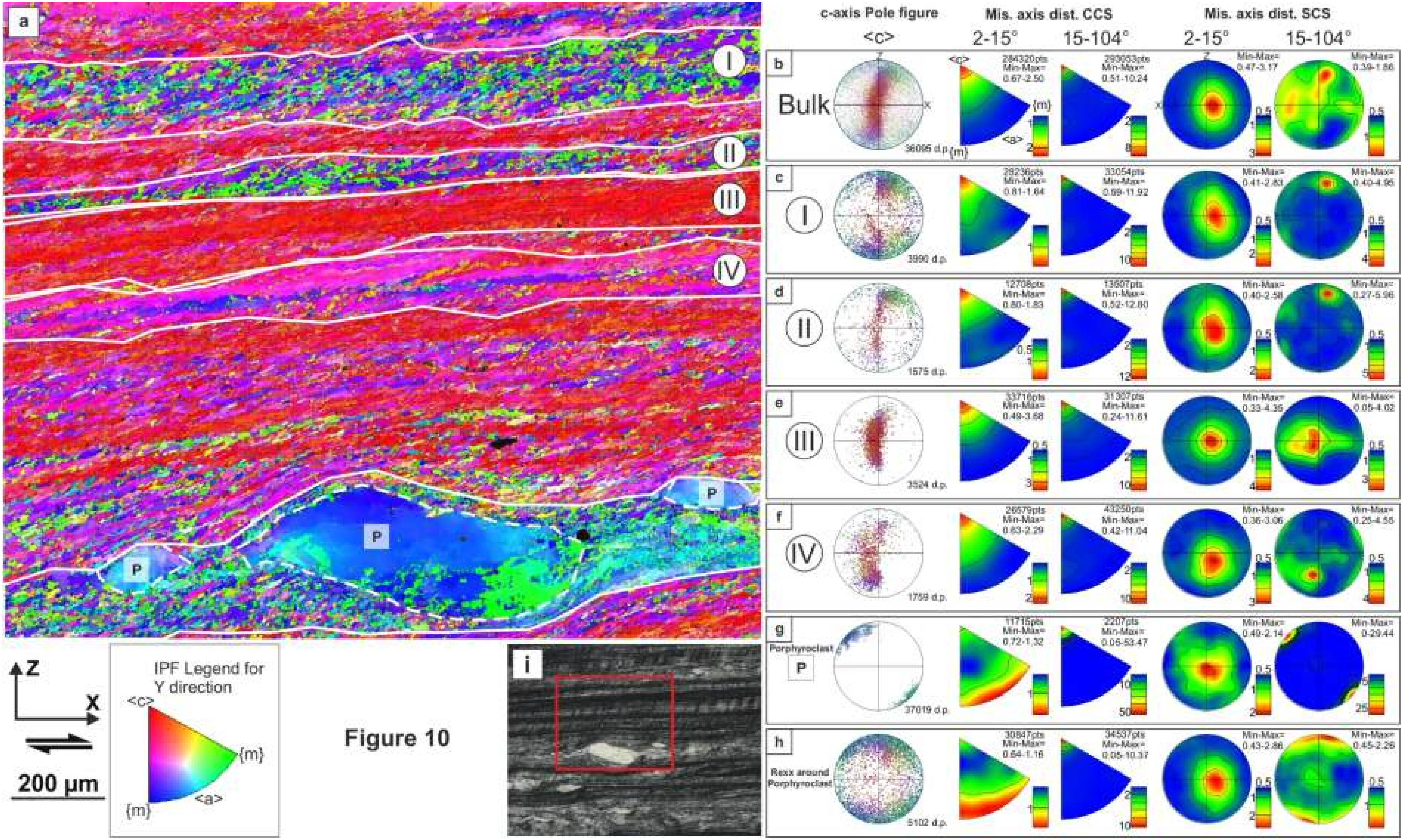
a
I
II
III
IV
P
P
P
Z
X
200 µm
IPF Legend for Y direction
<c>
{m}
{m}
<a>
i
c-axis Pole figure
<c>
Mis. axis dist. CCS
2-15°
15-104°
Mis. axis dist. SCS
2-15°
15-104°
b
Bulk
36095 d.p.
284320pts Min-Max= 0.67-2.50
293053pts Min-Max= 0.51-10.24
Min-Max= 0.47-3.17
Min-Max= 0.39-1.86
c
I
3990 d.p.
28236pts Min-Max= 0.81-1.64
33054pts Min-Max= 0.59-11.92
Min-Max= 0.41-2.83
Min-Max= 0.40-4.95
d
II
1575 d.p.
12708pts Min-Max= 0.80-1.83
13507pts Min-Max= 0.52-12.80
Min-Max= 0.40-2.58
Min-Max= 0.27-5.96
e
III
3524 d.p.
33716pts Min-Max= 0.49-3.68
31307pts Min-Max= 0.24-11.61
Min-Max= 0.33-4.35
Min-Max= 0.05-4.02
f
IV
1759 d.p.
26579pts Min-Max= 0.63-2.29
43250pts Min-Max= 0.42-11.04
Min-Max= 0.36-3.06
Min-Max= 0.25-4.55
g
Porphyroclast
P
37019 d.p.
11715pts Min-Max= 0.72-1.32
2207pts Min-Max= 0.05-53.47
Min-Max= 0.49-2.14
Min-Max= 0-29.44
h
Rexx around Porphyroclast
5102 d.p.
30847pts Min-Max= 0.64-1.16
34537pts Min-Max= 0.05-10.37
Min-Max= 0.43-2.86
Min-Max= 0.45-2.26

Figure 10

2.6. Discussion

From ribbons to dynamic recrystallization

To a first approximation, the deformed quartz veins of Rieserferner show 2 main stages of evolution with increasing strain: (i) formation of ribbon grains at low strain, with only subordinate recrystallization; and (ii) ribbon dismantling by localized to pervasive dynamic recrystallization. Ribbons dominate the microstructure at low bulk strain ($\gamma < 2$) and recrystallization became widespread, for shear strain in a range between 3 and 6, to pervasive at $\gamma > 10$, when > 90% of the vein volume was converted to an aggregate of small (10 μm mean grain size) dynamically recrystallized grains. A similar evolution, from ribbon to fine-grained mylonites, was described for deformed quartz veins within tonalites of Adamello pluton (Pennacchioni et al., 2010) that formed and deformed in a similar context of pluton cooling as Rieserferner quartz veins. In Adamello, Pennacchioni et al. (2010) determined that transition from non-recrystallized elongate-ribbon grains to pervasively recrystallized veins occurred abruptly at $\gamma = 3$, a value roughly coinciding with the threshold for widespread recrystallization estimated for Rieserferner veins. This γ value is also remarkably similar to the effective shear strain recalculated in Heilbronner and Kilian (2017) for pervasive recrystallization of Black Hill Quartzite during the general shear experiments described by Heilbronner and Tullis (2006).

Non-recrystallized ribbon portions

The pristine quartz veins were coarse grained and, in protomylonites, each ribbon represents a stretched non-recrystallized crystal. Different initial crystallographic orientations of the vein crystals caused different deformation behaviours during vein boundary-parallel simple shear (e.g Bouchez, 1977; Mancktelow, 1981). Y-type ribbons behaved as the most plastically compliant grains and stretched to high aspect ratios without significant recrystallization (Figs. 2d-e). This implies that {m}<a> was the easy (most efficient in accommodating strain, and/or slip system with low critical resolved shear stress) slip system at the conditions of deformation, as also supported by the low angle misorientation axis distribution showing a relatively strong maximum close to c-axis in crystal coordinates (Fig. 6c) and the resulting maximum parallel to the Y-direction in sample coordinates. Boundary trace analysis (Prior et al., 2002; Piazolo et al., 2008) of subgrains with misorientation axes either around [c] and <m> are consistent with the local occurrence of both {m}<a> and (c)<a> slip (Fig. SOM7). Misorientation around <m> (oriented NE-SW in the pole figure of Fig. 6b) could also explain the dispersion into a girdle (orthogonal to <m>) of the c-axis by a distortional “tilting” or “flexural slip” along the basal plane with slip along the <a> nearly orthogonal to the misorientation axis (and roughly parallel to the shortening direction). This c-axis dispersion and the absence of a dispersion around the c-axis reflect the different efficiency of the 2 slip systems, with the favoured {m}<a> slip effectively accommodating crystal elongation and inducing negligible internal distortion of the ribbon.

The XZ- and Z-type ribbons derived from vein crystals with c-axis orthogonal to the Y-direction that should disadvantage the activity of {m}<a> slip. These ribbons were less strain-compliant than Y-types as indicated by their lower aspect ratio; the higher internal distortion resulted in faster hardening and in a higher degree of recrystallization at the same bulk strain. This is consistent with the experimental results of Muto et al. (2011) on synthetic single quartz crystals with different initial orientations chosen to activate the 3 main slip systems of quartz ((c)<a>, {m}<a>, and {m}[c] under the same experimental conditions) even though there are remarkable differences in the microstructural and CPO evolution in the experiments compared with our natural samples as it will be discussed below.

XZ- and Z-type ribbons experienced lattice distortion, formation of subgrains, and incipient recrystallization, and show a widespread occurrence of Dauphiné twinning. In XZ-types ribbons the internal distortion is manifested by a dispersion of crystallographic axes around the Y-direction (similarly to the dispersion of c-axis observed for non recrystallized domains in Muto et al.,2011). Part of the internal distortion was accomplished through rotations around low angle misorientation axes as indicated by the MAD (Figs. 9a-d). In all XZ-type ribbons, we infer that {m}<a> slip system still partially assisted intracrystalline deformation despite the unfavorable crystal orientation. This is suggested by the clustering of low angle misorientation axes towards the c-axis in crystal coordinates (Figs. 7e, 8e and SOM6c) and by trace analysis of a few subgrains (Fig. SOM10-12). As discussed for Y-type ribbons, the efficiency of {m}<a> slip resulted in a very minor lattice distortion associated with the misorientation around c-axis and this would explain the absence of any major dispersion of crystallographic axes around [c] in all pole figures of Figs. 7-SOM6. This interpretation is also supported by the fact that, in sub-plots of low angle misorientation axis distributions in crystal coordinates considering smaller ranges of misorientations (2-5°, 5-10° and 10-15°), the c-axis maxima are stronger at very low angle misorientations (Fig. SOM13-14).

In XZb-type ribbons, the distribution of low angle misorientation axis towards [c] in crystal coordinates is close to uniform (Fig. 8e).I In sample coordinates, this distribution results in an eccentric maximum with respect to Y that does not coincide with the c-axis position in the pole figure. This maximum rather coincides with the position of {r-z} suggesting that available slip systems (or combinations of slip systems) with misorientation axis close to the Y-direction were preferentially activated (e.g. Neumann, 2000; Lloyd et al., 2004; Morales et al., 2011). The heterogeneity in the deformation and activation of specific slip systems is illustrated by the analysis of the areas 1 and 2 of the same ribbon that show different types of distribution of low angle misorientation axes towards the c-axis and towards {r-z}. In the XZa-type ribbon of Fig. 7a the low angle misorientation axes distribution in sample coordinatesshows a distribution along a girdle between the two peripheral c-axis directions suggesting the activation of slip systems with misorientation axis close to the Y-direction.

In general terms, this preferential activation of slip system with misorientation axis close to the kinematic vorticity axis may be aided also by the elsatic and plastic anisotropic properties of quartz. The most compliant directions in quartz are close to <m> and <r>, whereas the most stiff directions are close to <z> (McSkimin et al., 1965; Menegon et al., 2011). This elastic anisotropy may be also reflected in the differential activation of slip system (Menegon et al., 2011), activating preferentially those slip system that exploit {m} or {r} planes.

Recrystallization within μSZs of XZ-type ribbons

In XZ-type ribbons, incipient recrystallization occurred along μSZs. These recrystallization microstructures have been already described for quartz and their origin has been interpreted in different ways (e.g. van Daalen et al., 1999; Vernooij et al., 2005, 2006a, b; Trepmann et al., 2007, 2017; Stipp and Kunze, 2008; Menegon et al., 2008, 2011; Derez et al., 2015; Kjøll et al., 2015). Similar μSZs have also been described in feldspars (Stünitz et al., 2003; Menegon et al., 2013) and in calcite (Bestmann and Prior, 2003; Rogowitz et al., 2016). The main characteristics of the μSZs in the quartz ribbons of the Rieserferner veins are summarized and discussed below.

a) The CPO of recrystallized aggregates of μSZs show a dispersion of the crystallographic axes, from the crystallographic orientations of the host grain, consistent with the sense of shear of the μSZs and with a rotational axis roughly coinciding with the vorticity axis of the shear zone (Y-axis). The amount of dispersion does not scale with μSZs thickness (and accommodated slip). In fact, large rotations of crystallographic ([c]) axes (~ 90°) are also observed for the new grains within incipient μSZs. As discussed above, a smaller, but similar dispersion of crystallographic axes is observed within the distorted host ribbon grains.

b) The MAD for evolved and mature μSZs include a wide range of misorientation angles between 10° and 60° (except the evolved μSZ ϕ:□Fig. 9g).These MADs are significantly different from those of both the host ribbons and ultramylonites that show clear and strong peaks at low angle misorientations (< 15°) and around 60° (Figs. 9b-d and 9i).

c) The misorientation axis distributions for low angle misorientations include high density spots around different crystallographic orientations in the different μSZs (e.g. {m},{r-z}, and <a>

for μSZ ε: Fig. 7g), but in sample coordinates higher density systematically occurs close, though slightly eccentric, to the Y-axis. Along with minor clustering towards the orientation of the c-axis they tend to form a girdle. ; showing also some correlation with misorientation axis distributions ofof the host ribbon. The eccentricity of the maximum is interpreted to reflect either the deviation of the local vorticity vector with respect to the bulk vorticity vector of the sample (i.e., the Y-axis), or the difficulty to precisely place the sample coordinate frame in a protomylonite and exactly cut the sample parallel to the principal kinematic sections (or both factors). High density of the low angle misorientation axes "close to Y" therefore implies a main rotation parallel to the vorticity axis with some preferential activation of well-oriented slip systems. This rotation of subgrains, controlled by the vorticity axis, is supported by the fact that also high angle misorientations (15-45°) between new grains within the μSZs show very similar maxima close to Y (Fig. SOM6). This suggests the occurrence of a purely kinematic "rigid body" rotation of the new grains around Y (e.g. Bestmann and Prior, 2003; Trepmann et al., 2007; Stipp and Kunze, 2008). A feature less easy to interpret is the dispersion of the misorientation axes to form a girdle in sample coordinates nearly orthogonal to grain SPO especially in mature μSZs (e.g. μSZs ε, Fig. 7g, and ξ, Figs. SOM6e-h). In the μSZ ε (Fig. 7) the girdle is clearly subparallel to the trace of the subgrain and grain boundaries internal to the elongated grains .

d) Dauphiné twinning occurred pervasively within the host ribbons, but the orientation of μSZs is not systematically linked to Dauphiné twin boundaries in contrast to what was reported by Menegon et al. (2011).

e) There is crystallographic control on the orientation of the μSZs whose trend is subparallel to the trace of {r-z}, {m} or (c), as reported in van Daalen et al. (1999), Vernooij et al. (2006a, b) and Kjøll et al. (2015). Negative rhombs <z> are the least compliant crystallographic directions in quartz (in terms of its anisotropic elastic properties, McSkimin et al., 1965; Menegon et al., 2011) and they may act as site of accumulation of dislocation and defects promoting recovery processes and/or micro-fracturing along them.

f) The grain size of the new grains is in the range between 10 and 20 μm for the differently evolved μSZs and is similar to the mean (geometric) grain size of the ultramylonitic recrystallized matrix (10 μm). In the μSZs the grain size of new grains is similar to the size of the subgrains locally developed at the boundary of the μSZs (e.g. Bestmann and Prior, 2003; Trepmann et al., 2007). This supports the occurrence of a component of SGR recrystallization during incipient μSZ nucleation or at the moving μSZs boundary during progressive strain accumulation (e.g. Halfpenny et al., 2012). The size of the new recrystallized grains in the μSZs was determined by the occurrence of recovery processes in the parent grains and cannot therefore be completely ascribed to a cataclastic process which has been inferred to occur during initial stages of μSZ development by some authors (e.g. van Daalen et al., 1999; Vollbrecht et al., 1999; Kjøll et al., 2015)

g) The μSZs were preferentially infiltrated by fluids and formed the backbones for fluid redistribution into the host ribbons as indicated by (i) the clustering of fluid inclusions along the μSZs; and (ii) the pervasive resetting of the CL signature along and nearby μSZs (e.g. Fig. SOM15e). The presence of mica, precipitated along incipient μSZs and deformed within the aggregate of more evolved μSZs (Figs. SOM3c-d), suggests that part of the fluid infiltration did not just post-date shearing. There are not evident fluid-inclusion trails within the host ribbon subparallel to the μSZs that could support the hypothesis of an origin of the μSZs from nucleation on precursor, healed microcracks.

Strain hardening of XZ-type ribbons resulted in development of crystallographically-controlled μSZs. We infer that initial recrystallization along the μSZs is associated with SGR as indicated by: (i) the discontinuous presence of a zone of subgrain polygonization in the host ribbon flanking the μSZs (e.g. Bestmann and Prior, 2003); and (ii) by the similarity in size between the host ribbon subgrains and recrystallized new grains. The MADs of μSZs show a wide range of high misorientation angles that indicate the occurrence of a concurrent deformation mechanism together with the incipient SGR.

This concurrent mechanism must be at the base of the sudden change in orientation of new grains within μSZs to the host and neighbour grains since the incipient stages of recrystallization and is indicated by a rotation of crystallographic axes preferentially around the vorticity axis Y, but also around other directions (third column of Fig. SOM6). This mechanism apparently became inactive in mylonites/ultramylonites despite the similarity in grain size of recrystallized aggregates. We envisage that process of grains reorientation within the μSZs as a "rigid-body" rotation of grains, initiated as subgrains by SGR, related to the geometric roughness of the μSZs and to the confined slip along the μSZs (similarly to the model presented by Trepmann et al., 2017). This process is essentially an example of viscous grain boundary sliding which is in part kinematically-controlled by the orientation of the local vorticity axis. The roughness results from both the heterogeneous degree of subgrain/new grain evolution along the μSZs that is renewed by continuous formation of new subgrains at the μSZs. Thickening of the μSZs in fact occurred by progressive incorporation of the host ribbon selvages and in mature shear zones the aggregate at the core of the shear zone experienced higher degree of rotation, as shown by van Daalen et al. (1999) in similar μSZs in quartz (e.g. Fig. SOM6). Probably, thickening of the recrystallized aggregate decreased the influence of the geometric roughness during confined shear and the efficiency of "rigid body" rotation mechanisms, leaving the complete control on recrystallization process to SGR recrystallization in mature μSZs and in the following stages of mylonitization.

Our observation and interpretation are very similar to the results of Kjøll et al., (2015), who describe the development of localized recrystallization along crystallographycally-controlled features similar to μSZs in hardened quartz grains. Despite the similarities, we do not observe striking evidence for cyclical embrittlement induced by fluid pressure oscillation or the evidence for pressure-solution processes as suggested by Kjøll et al. Lack of (unexploited) fluid inclusion trails point to a different origin for μSZs. Initial brittle processes and micro-cataclasis locally induced by anisotropic rheological properties of quartz may explain some of the above described characteristics (e.g. high angle misorientation of new grains in incipient μSZs) but we do not observe any other evidence for it.

The observations from the Rieserferner deformed quartz veins are difficult to reconcile with many experimental results of Muto et al. (2011). We observe, as in their experiments, that the initial crystallographic orientation of the crystals resulted in a different strength of the grains that promoted recrystallization of XZ-type ribbons badly oriented for easy glide. However, Muto et al. (2011) observed the development of distinct domains of recrystallized grains with a Y-max CPO in all crystals independently of the starting crystallographic orientation, which is not found in the Rieserferner veins. In the experiments recrystallization within crystals with {m}[c] and (c)<a> orientations were not spatially organized into µSZs as in the Rieserferner XZ-type ribbons.

Unexploited vein crystals geometry, preferred orientation and strain estimation

Conversely to experimental samples, in which the geometry and fabric of the starting material can be characterized in detail. In many cases, when we deal with natural sample of deformed rock, any interpretation about fabric and texture evolution suffer from our lack of knowledge about the exact structure of the un-exploited starting natural rock. In particular, the initial texture of quartz crystals in the Rieserferner pluton veins may have some direct consequences on the interpretation of texture development during incipient stages of deformation and on foliation-geometry based strain estimations.

Unfortunately, we were not able to sample completely undeformed quartz veins from the Rieserferner pluton. We therefore assume that the geometry of the low-strain ($\gamma<2$) ribboned protomylonitic vein highly resemble that of the former un-exploited starting vein. Unexploited quartz veins might have resembled those described by Nishikawa and Takeshita (2000; their fig. 2b), which show similar deformation microstructures during shearing. Unexploited quartz veins might have shown a typical syntaxial structure (e.g. Passchier and Trouw, 2005), coherently with the interpretation of these structures as extensional type-I fractures (see *Chapter 1*). Under this assumption, strain estimation based on the “foliation” angle may be reliable, given that crystal might have behaved as “material lines” during shearing.

In this scenario, however, the assumption of a syntaxial structure of the vein may have some effect on the interpretation of the relationship between quartz crystal aspect ratios and crystallographic orientations. In the case of a homogeneous *ab initio* high aspect ratio disregarded to crystallographic orientation, we would not have been able to observe “low” aspect ratios for XZ grains. In general terms, quartz growth is usually anisotropic, promoting crystal growth along the prism plane and c-axis direction. The relationship between aspect ratio and CPO of quartz crystals is exactly the opposite to what we would expect for the usual anisotropic grain growth of euhedral quartz crystals. In the case of perfectly euhedral crystals in a syntaxial veins, with crystals growing with their c-axis perpendicular to vein boundaries, XZ-type crystals should display greater aspect ratios with respect to Y-type crystals, when the vein is observed along our “Y” reference direction. This relationship is exactly opposite to what we observe. Therefore, we have assumed that no initial relationship between crystallographic orientation of vein crystals and their aspect ratios existed.

We cannot exclude the occurrence of an *ab initio* crystallographic preferred orientation of quartz vein crystals, as already proposed by Pennacchioni et al. (2010) for the Adamello quartz mylonites. This initial CPO has been related to the fact that quartz veins formed as shear fractures and therefore only quartz vein crystals that had a suitable orientation for the activation of favoured slip system during deformation grew. This would not affect in any case our interpretation about the CPO evolution and the different recrystallization mechanisms observed in crystals with different orientations.

Ultramylonitic quartz veins

The quartz ultramylonites consist of a fine-grained aggregate of recrystallized grains. A typical feature of mylonite and ultramylonite is the presence of CPO banding that is interpreted to be inherited from the former vein quartz crystals and to derive from recrystallization of ribbons (and therefore of vein crystals) with different original crystallographic orientations (e.g. Pauli et al., 1996; Lloyd et al., 1992; Pennacchioni et al., 2010; Morales et al., 2011; Price et al., 2016) persisting up to very high strains ($\gamma > 10$). The bulk c-axis CPO of the pervasively recrystallized ultramylonites is comparable in type to the CPO of the ribbon protomylonites and shows a girdle at a high angle to the mylonitic foliation (slightly inclined to the foliation normal according with sense of shear) and a wide peripheral spreading becoming more rarefied close to the foliation. The mean (geometric) grain size of recrystallized grains (~ 10 μm), almost identical within the different layers (at the contrary of Heilbronner and Tullis, 2006), is comparable (albeit slightly smaller and more homogeneous) with the recrystallization grain size within the μSZs of XZ-type ribbons. This suggests that, throughout the whole deformation/recrystallization history and in all microstructures, the recrystallized grain size was controlled by subgrain formation and recrystallization by SGR (as also indicated by MAD; e.g. Halfpenny et al., 2012). Despite there was a clear difference in strength between the differently oriented ribbons in the protomylonites, there is not a consequent variation in subgrain and new grain sizes that should be expected according to grain size piezometry (Stipp and Tullis, 2003). The individual misorientation axes distribution in crystal coordinates for the layers with different CPO all show a more or less broad clustering towards the c-axis, that is however weaker for the layers with a dominance of peripheral orientations (e.g. layers I and II of Fig. 10). The misorientation axis distributions in sample coordinates shows, for all layers, that the slip systems with misorientation axes well aligned with the Y-axis of the shear zones were preferentially activated and indicate a control of the bulk shear zone kinematic framework on recrystallization.

In Rieserferner ultramylonites, despite the evidence that the favoured slip system was {m}<a>, there is no indication of any relevant strain partitioning between layers with different CPO in recrystallized aggregates and therefore of significant strength differences of recrystallized aggregates (as instead proposed by Heilbronner and Tullis, 2006; Toy et al., 2008; Muto et al., 2011). In Rieserferner ultramylonites there is no evidence of cannibalism of {m}<a> against the other slip systems, at least for the range of investigated strain and no significant reset of the CPO occurred. As recalled above, the microstructure appears homogeneous in terms of grain size and show only minor differences in the grain aspect ratios. These observations are not dissimilar from the conclusions of Pennacchioni et al. (2010), who also noted that (i) dynamic recrystallization, occurring rather abruptly in a range of γ between 2 and 3, did not significantly altered the CPO from weakly deformed ribbon mylonites to strongly deformed and pervasively recrystallized veins; and (ii) initial crystal orientations badly oriented for dominant {m}<a> persisted up to high strain.

In the experiments of Muto et al. (2011) on synthetic single crystals all the different starting orientations developed distinct domains of recrystallized grains with c-axis Y-maximum CPO and the area of these domains increased with increasing bulk shear strain and extent of dynamic recrystallization. They noted that there was a reset from the initial {m}[c] and (c)<a> orientations that was basically complete for 100% recrystallization and $\gamma < 3$. In practice, these experiments imply that a quartz vein with initial random orientation of crystals would end up at relatively low strain in a homogeneous quartz ultramylonite with strong Y-max CPO without any inheritance from the original microstructure. This is in stark contrast with the evolution derived for the Rieserferner sheared quartz veins and other natural examples (e.g. Pennacchioni et al., 2010; Rahl and Skemer, 2016). A main reason for such contrast could be the difference in recrystallization mechanism and/or fluid conditions in the experimental/natural case. As pointed out by Muto et al. (2011) replacement of the original crystal orientation by growth of more favourable (Y-maximum) orientations requires grain boundary migration, whereas the Rieserferner veins were deformed in a dominant SGR regime. At natural strain rates, the experimental conditions of Muto et al. (2011) likely extrapolate to temperatures slightly higher than those estimated for deformation in the Rieserferner quartz veins (i.e. ca. 450 °C). The dominance of SGR during shearing may also explain, in part, the presence of a CL banding in ultramylonites that we interpret as difference in Ti concentration between the different layers. As described by Bestmann and Pennacchioni (2015) dominant SGR is not efficient in completely resetting the Ti concentrations even at stages of pervasive deformation. The CL signature associated with the deformation microstructures of the Rieserferner veins are however suggestive of more water-rich conditions compared with the Sierra Nevada sample of Bestmann and Pennacchioni (2015).

2.7. Conclusions

Mylonitization of coarse grained quartz veins resulted in a complex evolution during deformation at temperature of ~ 450 °C, in large part derived by the initially different crystallographic orientations of the vein crystals. The following points summarize the main results of the study.

- Depending on the initial crystallographic orientations vein crystals manifested, in early stages of shearing, different strengths resulting in distinct aspect ratios and degree of incipient recrystallization of developing ribbon grains. The most favourably oriented crystals were Y-type ones, indicative that {m}<a> was the easy slip system. Ribbons with c-axis orthogonal to Y underwent early hardening and recrystallized along conjugate sets of crystallographically-controlled μSZs.
- Recrystallization in μSZs initiated most likely by SGR. Once formed, new grains rotated around Y (up to misorientations > 90°), accordingly with the μSZ shear sense, since the incipient μSZ slip. Distorted ribbons show a similar (but lower) rotational spreading of crystallographic axes. This rotational CPOs resulted from both the preferential activity of slip systems which formed subgrain boundaries with a misorientation axis coinciding with Y (especially in the host ribbon) and passive grain rotation.
- Grain rotation within the μSZs was associated with the confined shear.
- Pervasive recrystallization and high shear strains were not capable of resetting the initial texture to a c-axis Y-maximum CPO as it would be expected from the evidence of the preferential activity of {m}<a> slip. Quartz ultramylonites show a domainal texture inherited from deformation and recrystallization of original crystals with a different CPO.
- In ultramylonites the misorientation angle/axis plots indicate that recrystallization by dominant SGR was assisted by the preferential activity of slip systems which formed subgrain boundaries with a misorientation axis parallel to Y, though {m}<a> was still the most efficient slip system, and/or passive rotation around Y.

- Within the different domains, grains with c-axis parallel to Y did not grow "rapidly" with increasing strain at the expenses of other grains in contrast to what is observed in the experiments of Muto et al. (2011). If a selective replacement by Y-grains of other grains did effectively occur with strain accumulation, the process was sluggish.
- The grain size of recrystallized grains does not depend significantly on (i) the amount of strain and degree of recrystallization; (ii) the CPO of the parent ribbon grain (protomylonite) or of the recrystallized layers (ultramylonite). This contrasts with the observation the inferred strength between ribbons and with the evidence of preferential {m}<a> slip.

Acknowledgements

Rudiger Kilian and Reneé Heilbronner are thanked for the assistance and guidance with the CIP analysis. Giulia Degli Alessandrini, Anna Rogowitz are thanked for discussion. Financial support from the University of Padova ("Progetto di Ateneo" CPDA140255) and from the Foundation "Ing. Aldo Gini" is acknowledged. LM thanks FP7 Marie Curie Career Integration Grant «Evolution of Continental Strength from Rifting to Collision - A Journey through the Wilson Cycle" PCIG13-GA-2013-618289 and the help of the Electronic Microscopy Centre staff at University of Plymouth.

Appendix – Methods and Analytical techniques

CIP Microscopy / Image Analysis / Microstructural feature quantification

Computer-integrated polarization microscopy (CIP: Heilbronner and Pauli, 1993) was mainly aimed at evaluating the c-axis orientation of the coarse grained ribbon protomylonites. The CIP microphotographs were acquired on a Zeiss Axioplan, with attached a Basler Ace (acA1600-20gm) camera, at the Institute of Geology and Paleontology of Basel University (Switzerland). Areas of 20 mm^2 were imaged with a resolution of ~ 3µm/pixel with a magnification of 2.5x each. To obtain a bulk pole figure of representative areas of the thin section, microphotographs were stitched (with a consequent decrease in resolution) and then processed with the CIP software suite for texture analysis and orientation imaging. Crystallographic orientations are plotted on equal area, lower hemisphere pole figures.

Optical images and processed EBSD maps were analysed in some cases with Paror and Surfor (FABRIC software suite, Heilbronner and Barret, 2014) to estimate grain shapes, shape preferred orientations and the orientation of µSZs (reported in rose diagram in Fig.4 and SOM1C)

Several scan images of the same thin section (no polarizer, crossed polarized, gypsum-plate inserted and CIP images) have been compared and analysed by image analysis to define the areal extension of each ribbon, its bulk c-axis orientation and its microstructural features (Aspect Ratio; AR; Recrystallization amount: Rexx%, given as area fraction, Area%). These methods have some limitation: (1) image optical resolution and the possibility to discern localized recrystallization features. For example, Rexx% quantification (Fig. 2e) in those cases where the recrystallization is localized it represent a good approximation of the real value, whereas where the recrystallization is scattered and irregularly distributed all over the ribbon, this values represent a minimum estimation. (2) Thin section dimensions commonly are too small to contain mm-cm ribbons. The reported AR value (Fig. 2d) is therefore a minimum value of AR.

EBSD analysis

Electron backscattered diffraction analysis was carried out with: (i) FEG-SEM Zeiss 1540 EsB (Flamenco acquisition software, Oxford Instruments) at the Material Science Department – Geozentrum Nordbayern Erlangen; and (ii) JEOL 6610 LV SEM equipped with a NordLys Nano EBSD detector (AZTec acquisition software, Oxford Instruments); and (iii) JEOL 7001 FE SEM equipped with a NordLys Max EBSD detector (AZTec acquisition software, Oxford Instruments) at the Electron Microscope Centre of Plymouth University. Each thin section was SYTON-polished for at least 6 hours and carbon coated (about 3.5nm coating thickness). Analytical conditions, steps size, acquisition rates and other map characteristics are reported for each individual map in Table SOM1. All data have been processed (noise reduction following e.g. Bestmann and Prior, 2003) and analysed using CHANNEL5 software of HKL Technology, Oxford Instruments.

Monoclinic sample symmetry has been used. Quartz was the only mineral phase to be indexed, using trigonal symmetry (Laue group -3m). Critical misorientation for the distinction between low- and high-angle boundaries have been chosen at 15°, allowing grain boundary completion down to 0°. In addition, grain boundaries with 60°±5° of misorientation were disregarded from grain detection procedure, to avoid any contribution from Dauphiné twinning in the definition of grains.

The pole figures and the misorientation axis distributions in sample coordinates are equal area, lower hemisphere projections oriented with the general shear zone kinematics reference system (X = stretching lineation; Z = pole to general shear plane/vein boundary). The inverse pole figures for misorientation axis distribution in crystal coordinates are upper hemisphere projections.

Grain size analysis

Grain sizes are obtained from the grain detection routine in Channel5 Tango software. Equivalent grain diameters are obtained from grain area (μm^2). The minimum cut-off area below which grains are not considered have been set to 1 μm^2; therefore only grains composed of 4 to 9 pixels (according to map acquisition step-size) have been considered. Grain size data are then plotted as area-weighted distributions as frequency against square-root grain-size-equivalent grain diameters (as in Herweg and Berger 2004). The grain size distribution is close to a Gaussian distribution when plotted in this way, therefore it gives us a good estimation of the mean grain size. The geometric mean grain size is obtained graphically as the maximum frequency grain size of the distribution curve. The distribution curve is obtained interpolating distribution data with a 6th degree polynomial equation in Excel-MS Office. The arithmetic mean, instead, have been calculated directly from the equivalent grain diameter database without any area-weighting process.

Subgrain size have been determined in the same way but, setting the critical misorientation at 2° in Channel5 Tango grain detection routine. Then, only those subgrains useful for the analyses (those close to the µSZs) have been manually selected.

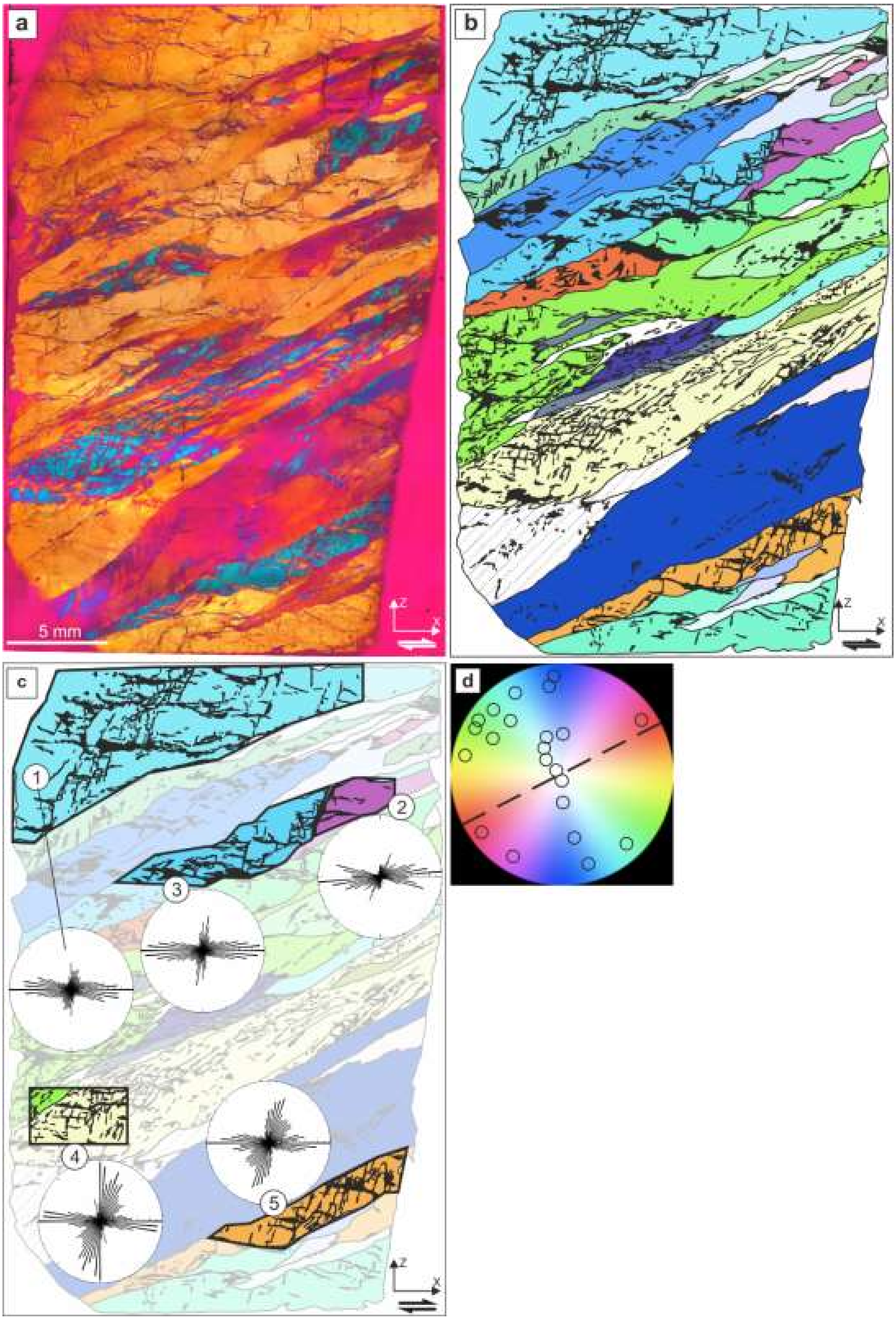

Fig. SOM1: Microstructure and CPO of protomylonitic quartz vein. (a) Optical microphotograph (crossed polars and inserted gypsum plate) of the 2nd thin section used with that shown in Fig. 2a for the analysis of the protomylonite. (b) Sketch drawn from (a) showing the different ribbons (in different colours) and incipient recrystallization aggregates (in black colour). The ribbons are colour-coded as a function of the mean c-axis orientation determined from CIP analysis, accordingly with the Look-Up Table (LUT) reported in (d); (c) Analysis of the orientations of fine-grained recrystallized aggregates (in black colour) in selected ribbon portions of the protomylonite shown in (a). The orientations of the μSZ in the selected areas are shown in the rose diagrams. (d) CIP LUT showing (empty dots) the c-axis orientations of the ribbons. The dashed line represents the trace of the mylonitic foliation.

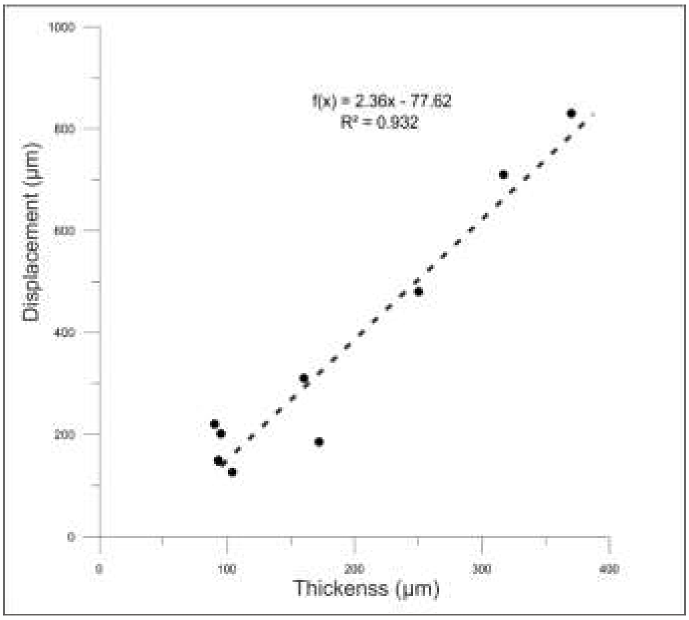

Fig. SOM2: Plot of the thickness versus displacement for µSZ within ribbon grains

Fig. SOM3: Microstructures of sheared quartz veins. (a) Thick (mature) µSZ including small white mica flakes defining the internal oblique foliation. Note the extensive formation subgrains within the ribbon at the lower contact with the µSZ. Crossed polars. (b) Same as in (a) with crossed polars and inserted gypsum plate. (c) Partially recrystallized ribbons in a mylonite. Note the incipient formation of a lozenge-shaped ribbon leftover derived from a XZ-type ribbon (central part of the microphotograph). (d) Ribbons dissected by pervasive C'-type µSZs leading to formation quartz porphyroclasts in the ultramylonite. Crossed polars and inserted gypsum plate. (e) Ultramylonite showing extinction banding and including a ribbon leftover with an asymmetry unusual for a dextral sense of shear. Crossed polars. (f) Same as (f), but showing a more strongly asymmetric shape of the porphyroclast. (g) Secondary Electron (SE) SEM images of the grain surface of recrystallized grains along a µSZ in mylonites showing pores with a crystallographically-controlled regular geometric shapes (etch pit type). (h) Same as (g). Sense of shear is dextral in all (a)-(f) microphotographs.

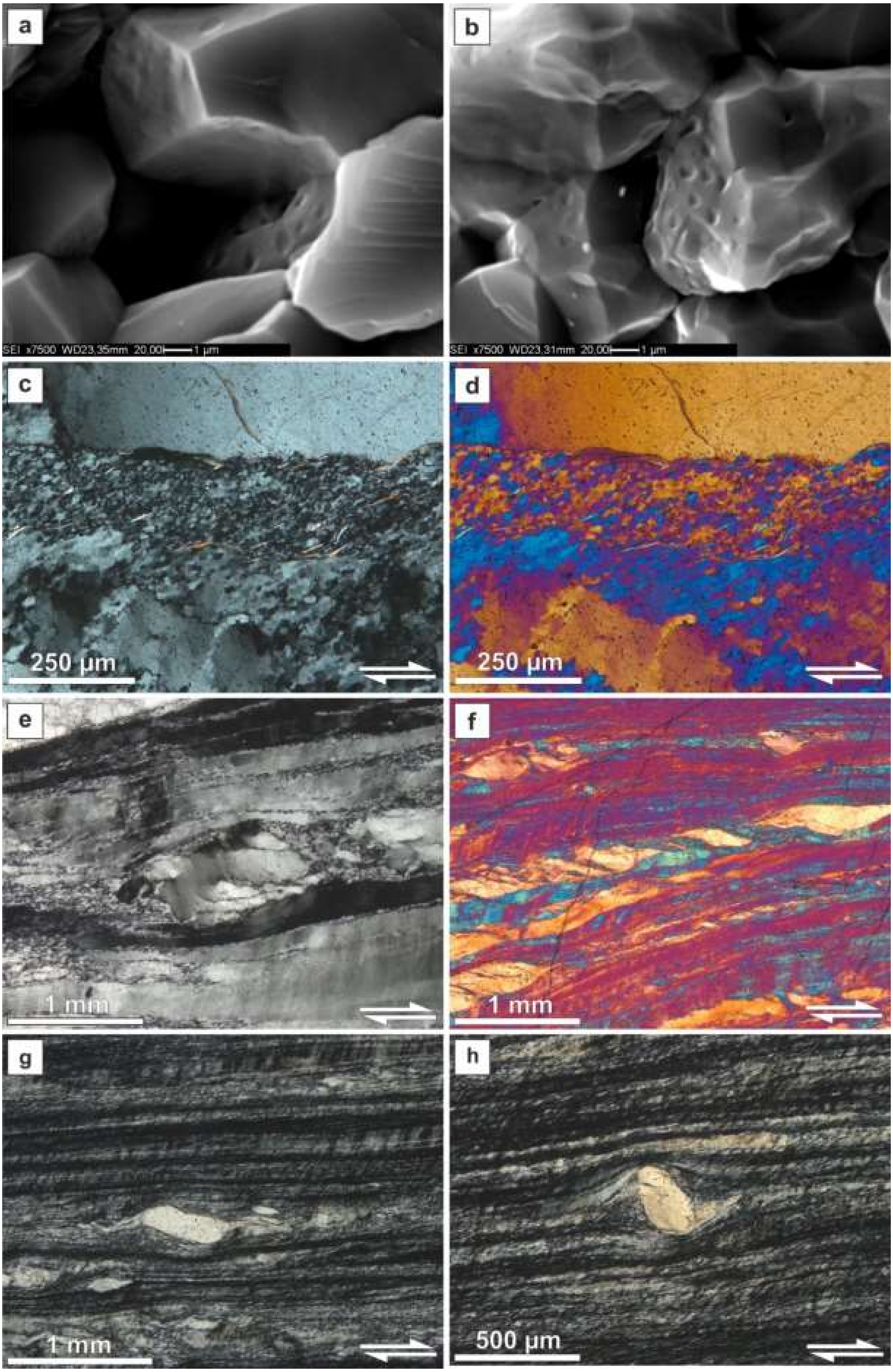
a
SEI x7500 WD23,35mm 20,00 1 µm
b
SEI x7500 WD23,31mm 20,00 1 µm
c
250 µm
d
250 µm
e
1 mm
f
1 mm
g
1 mm
h
500 µm

Figure SOM 3

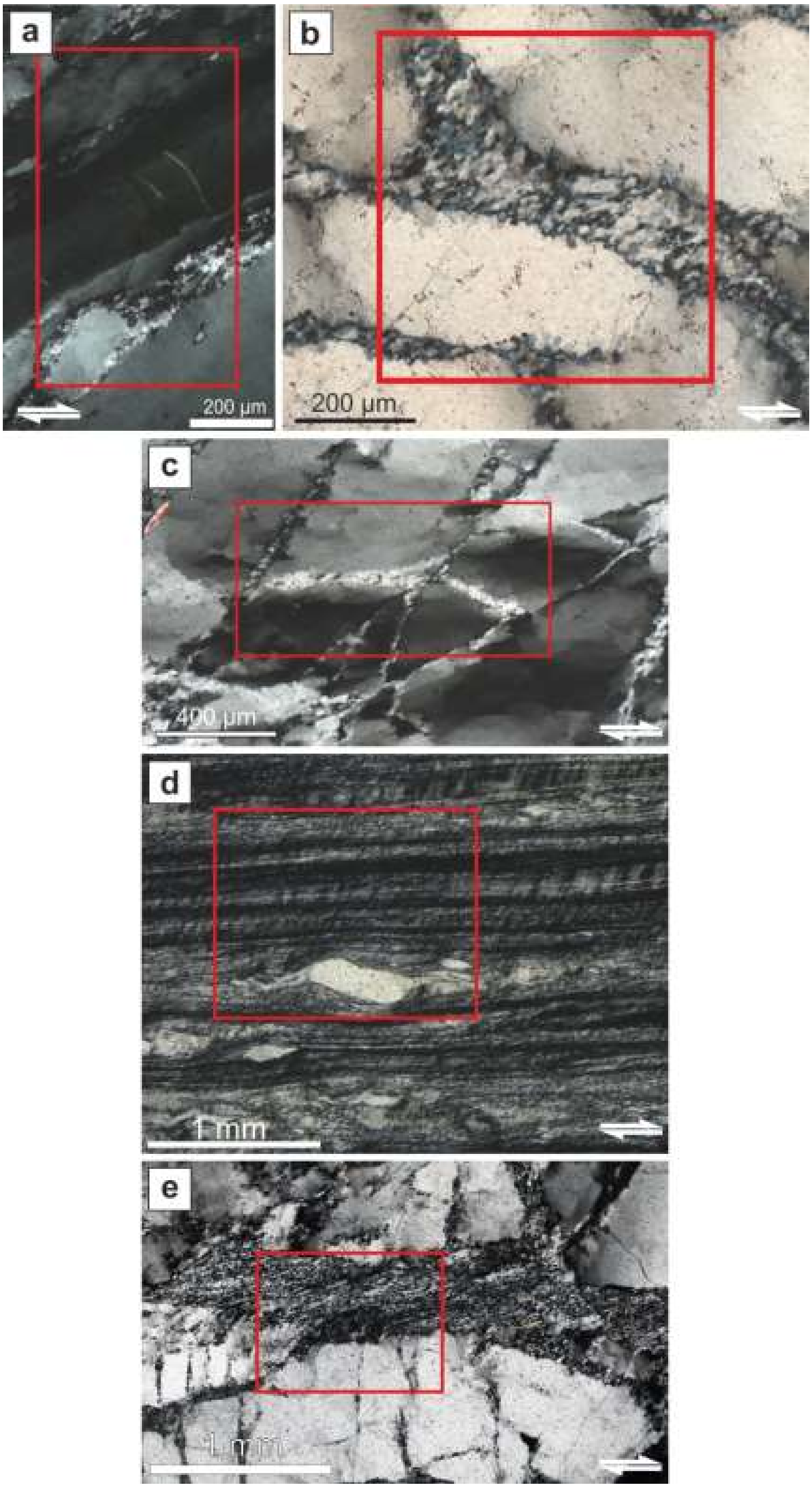

Fig. SOM4: optical micrographs (crossed polarizers) of ribbon areas (highlighted by the red rectangle) selected for the EBSD analyses. (a) Y-type ribbon of Fig. 6. (b) XZa-type ribbon of Fig. 7. (c) XZb-type ribbon of Fig. 8. (d) Ultramylonite (recrystallized matrix and porphyroclasts) of Fig. 10. (e) XZa-type ribbon with mature µSZ of Fig. SOM5.

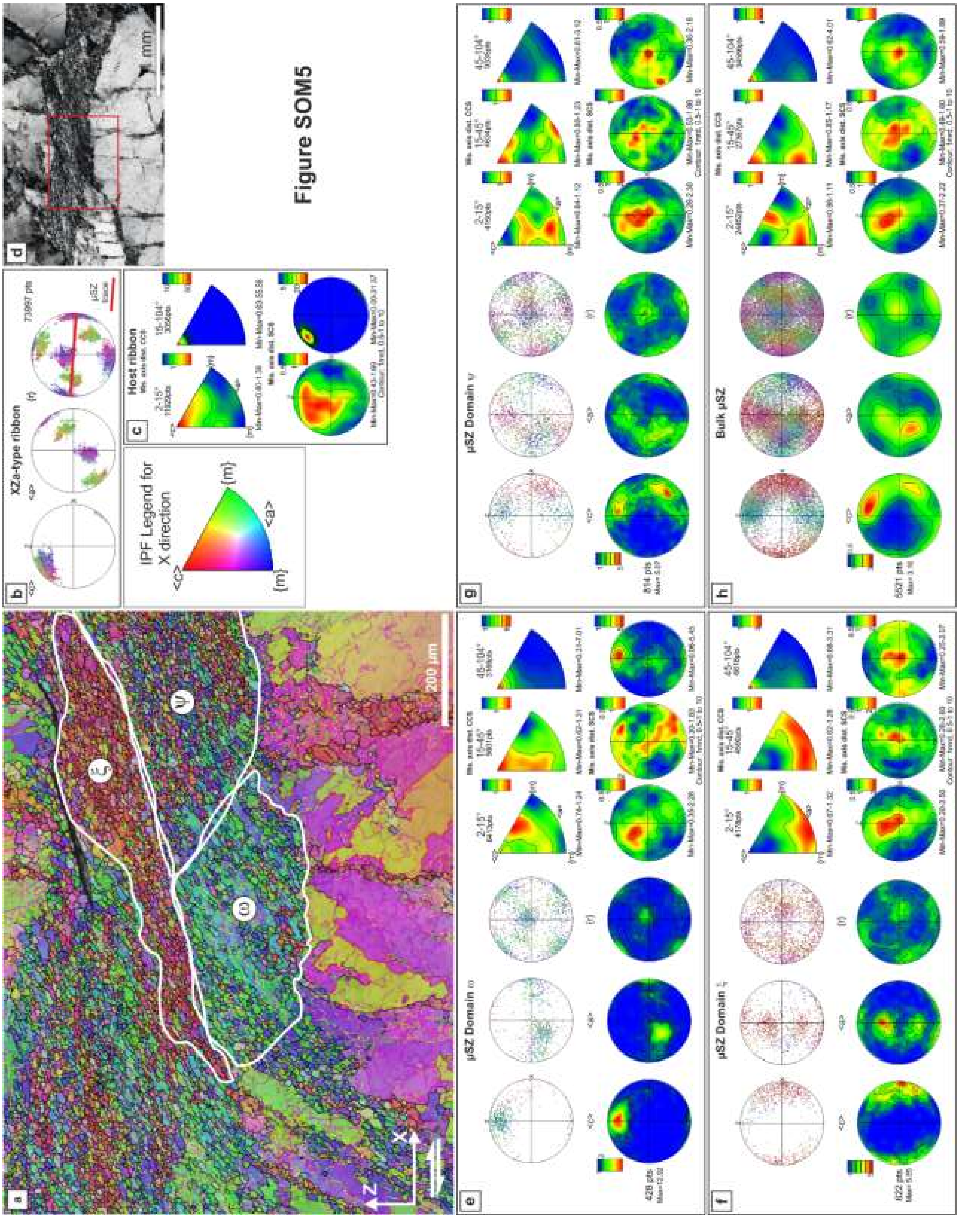
a
Z
X
ω
ξ
ψ
200 µm
b
XZa-type ribbon
<c>
<a>
{r}
73997 pts
µSZ trace
IPF Legend for X direction
<c>
{m}
<a>
c
Host ribbon
2-15°
15-104°
d
mm
e
µSZ Domain ω
428 pts
f
µSZ Domain ξ
622 pts
g
µSZ Domain ψ
814 pts
h
Bulk µSZ
5521 pts
2-15°
15-45°
45-104°

Figure SOM5

Fig. SOM5: EBSD orientation imaging and data for an XZa-type ribbon, and included mature µSZ w-y-x, in the protomylonite. (a) Orientation map colour-coded according to the inverse pole figure shown in the lower right corner. Boundaries are colour-coded as a function of misorientations according to the same legend in Fig. 6a. (b) Pole figures for the host ribbon showing the orientations of [c], <a> and {r} crystallographic directions. The trace of the µSZ is shown as a red line. (c) Misorientation axis distributions for low (2-15°) and high (15-104°) misorientations in crystal and sample coordinates for the host ribbon. (d) Optical microphotographs (crossed polarizers) of the domain (included in the red box) shown in the EBSD map (a). (e) Pole figures ([c], <a> and {r} crystallographic directions) and misorientation axis distributions for low (2-15°), intermediate (15-45°) and high (45-104°) misorientations in IPF and sample coordinates for the µSZ domain w. (f) Idem as (e) for the µSZ domain x. (g) Idem as (e) for the µSZ domain y. (h) Idem as (e) for the bulk µSZ (w+y+x).

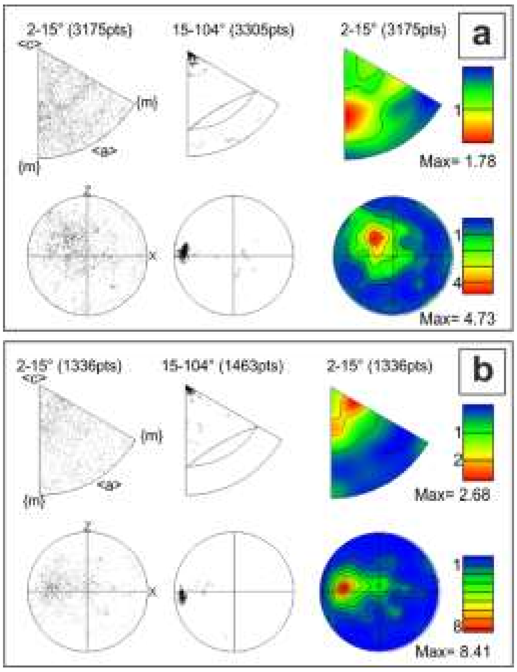

Fig. SOM6: Misorientation axis distributions for low (2-15°) and high (15-104°) misorientation in the host ribbons adjacent to incipient µSZ a (a) and b (b) of Fig. 8. Both (a) and (b) include the misorientation axes distribution in crystal coordinate (first row) and in samples coordinates (second row) in both raw and contoured format.

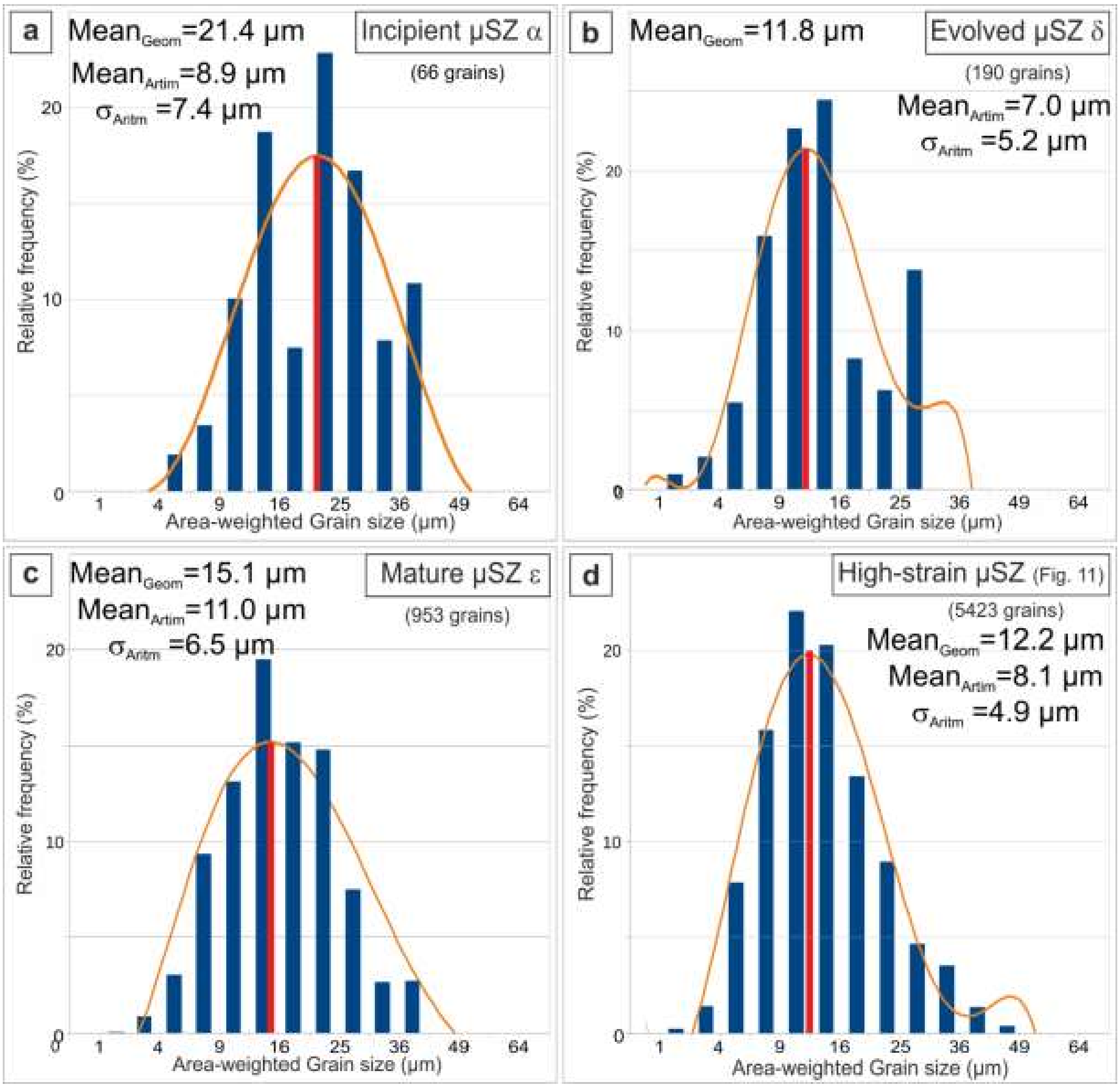

Fig. SOM7: Area-weighted grain size distributions (Herweg and Berger, 2004) for the recrystallized aggregates within µSZ zones: (a) incipient µSZ a (Fig. 8a); (b) evolved µSZ d (Fig. 7a); (c-d) mature µSZ e (Fig. 7a) and of Fig. 9a

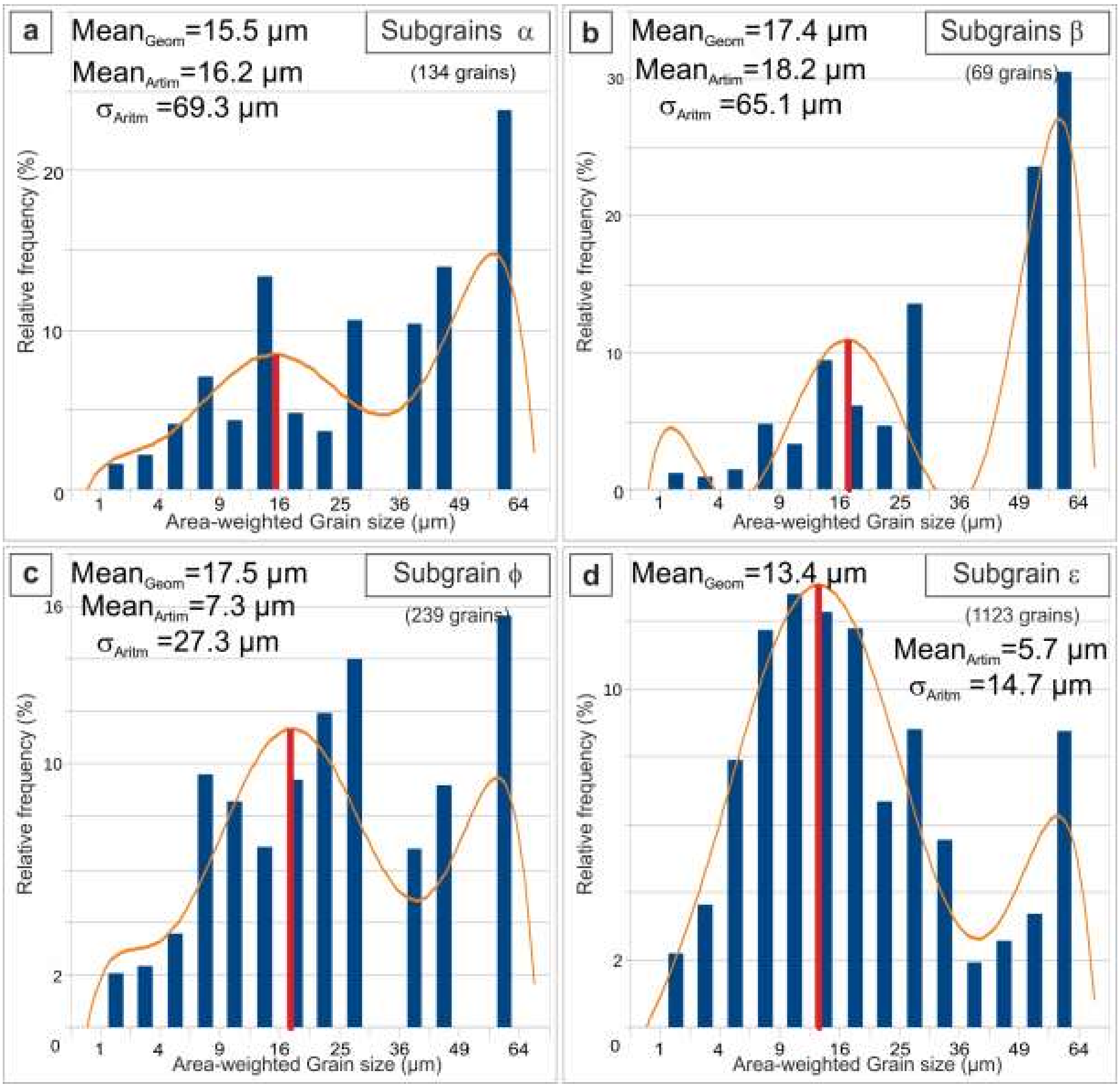

Fig. SOM8: Area-weighted subgrain size distributions (Herweg and Berger, 2004) for the host ribbon close to incipient µSZs a (a), b (b), and f (c) of Fig. 8.

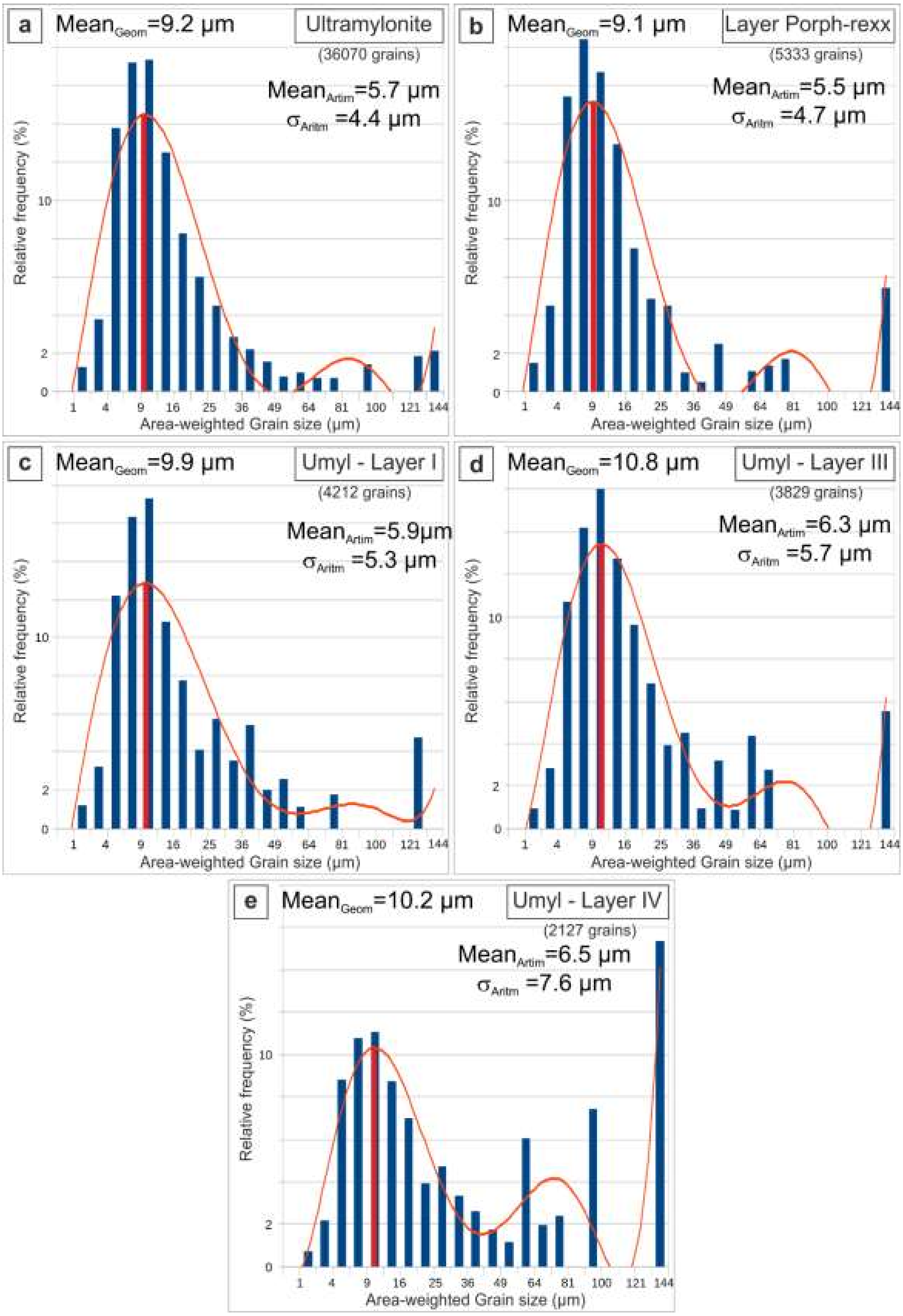

Fig. SOM9: Area-weighted grain size distributions (Herweg and Berger, 2004) for the recrystallized matrix aggregates of the ultramylonite of Fig. 11. (a) bulk ultramylonite (CPO in Fig. 11b); (b) recrystallized aggregate including the ribbon leftovers P (CPO in Fig. 10h); (c) layer I (CPO in Fig.10c); (d) layer II (CPO in Fig.10e); (e) layer IV (CPO in Fig.10f).

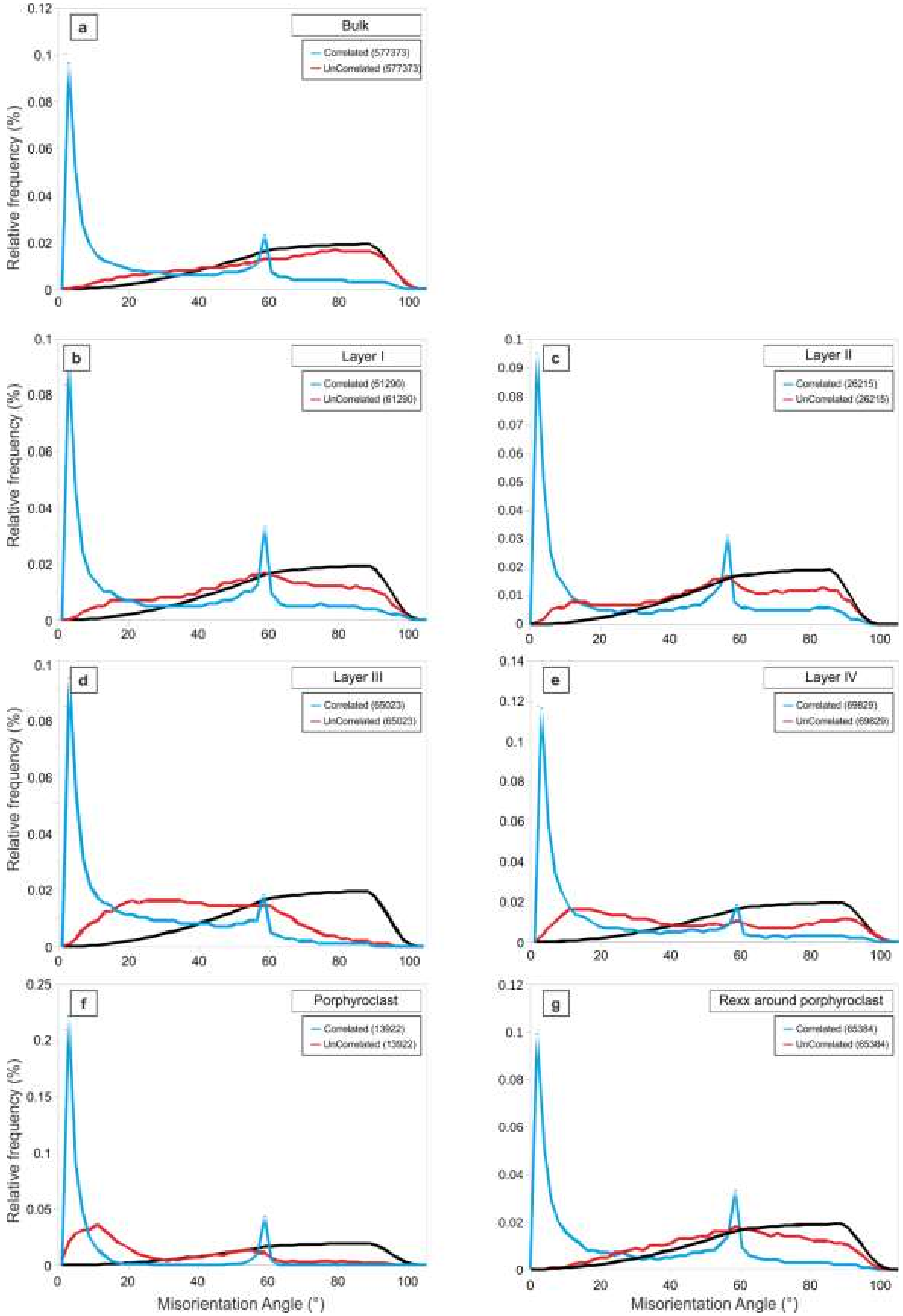

Fig. SOM10: Misorientation angle distribution for recrystallized aggregates of the ultramylonite of Fig. 10a. (a) bulk ultramylonite (CPO in Fig. 10b); (b) layer I (CPO in Fig.10c); (c) layer II (CPO in Fig.10d); (d) layer III (CPO in Fig.10e); (e) layer IV (CPO in Fig.10f); (f) ribbon leftover P (CPO in Fig.10g); (g) recrystallized aggregate around the ribbon leftovers P (CPO in Fig. 10h).

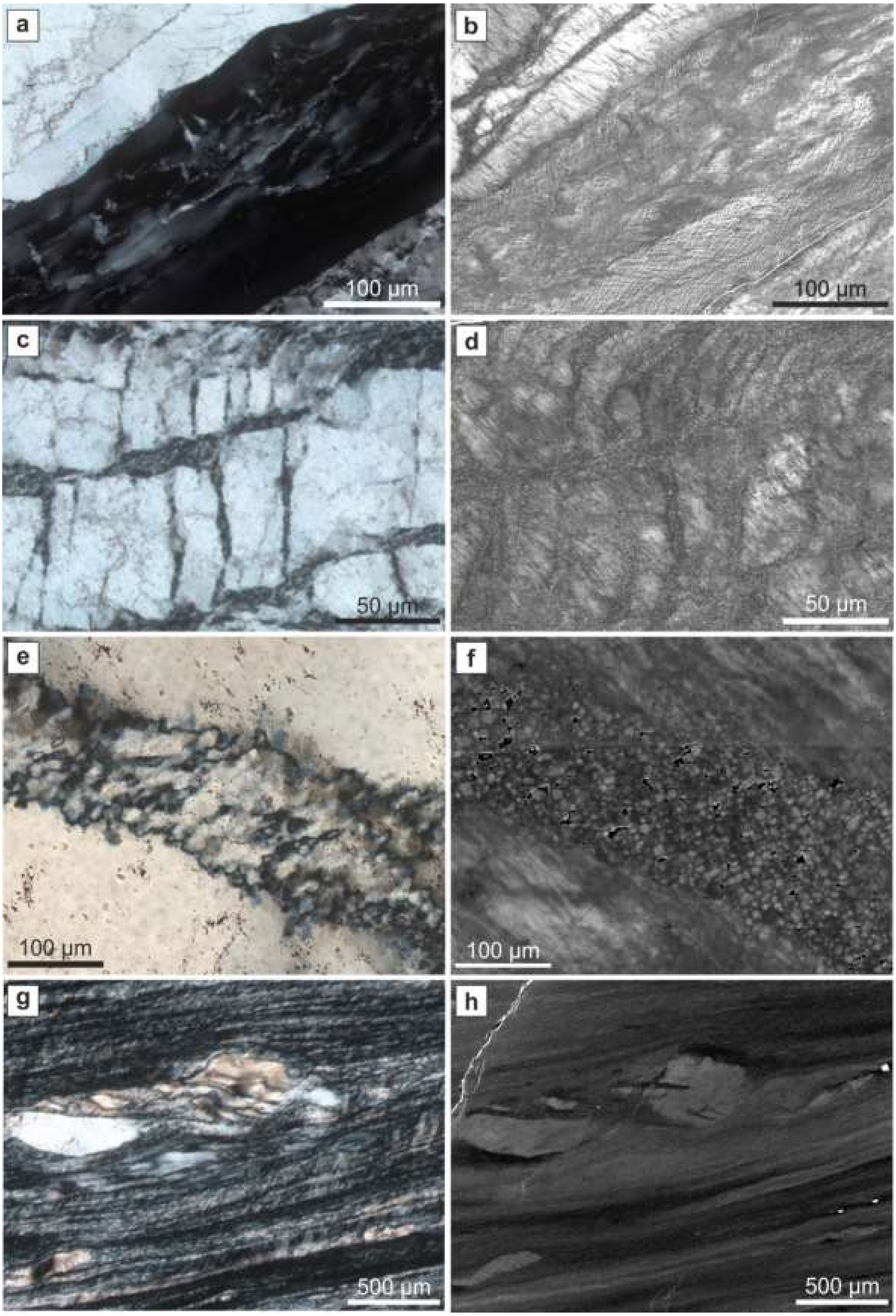

Fig. SOM11: Comparison between optical microstructure under crossed polarizers (right column) and SEM-CL images (left column). (a-b) Y-type ribbon. (c-d) Intersecting sets of recrystallized μSZs within a XZa-type ribbon; (e-f) Detail of a dextral μSZ within a XZa-type ribbon. (g-h) Ultramylonite showing a CPO banding and including a ribbon porphyroclast.

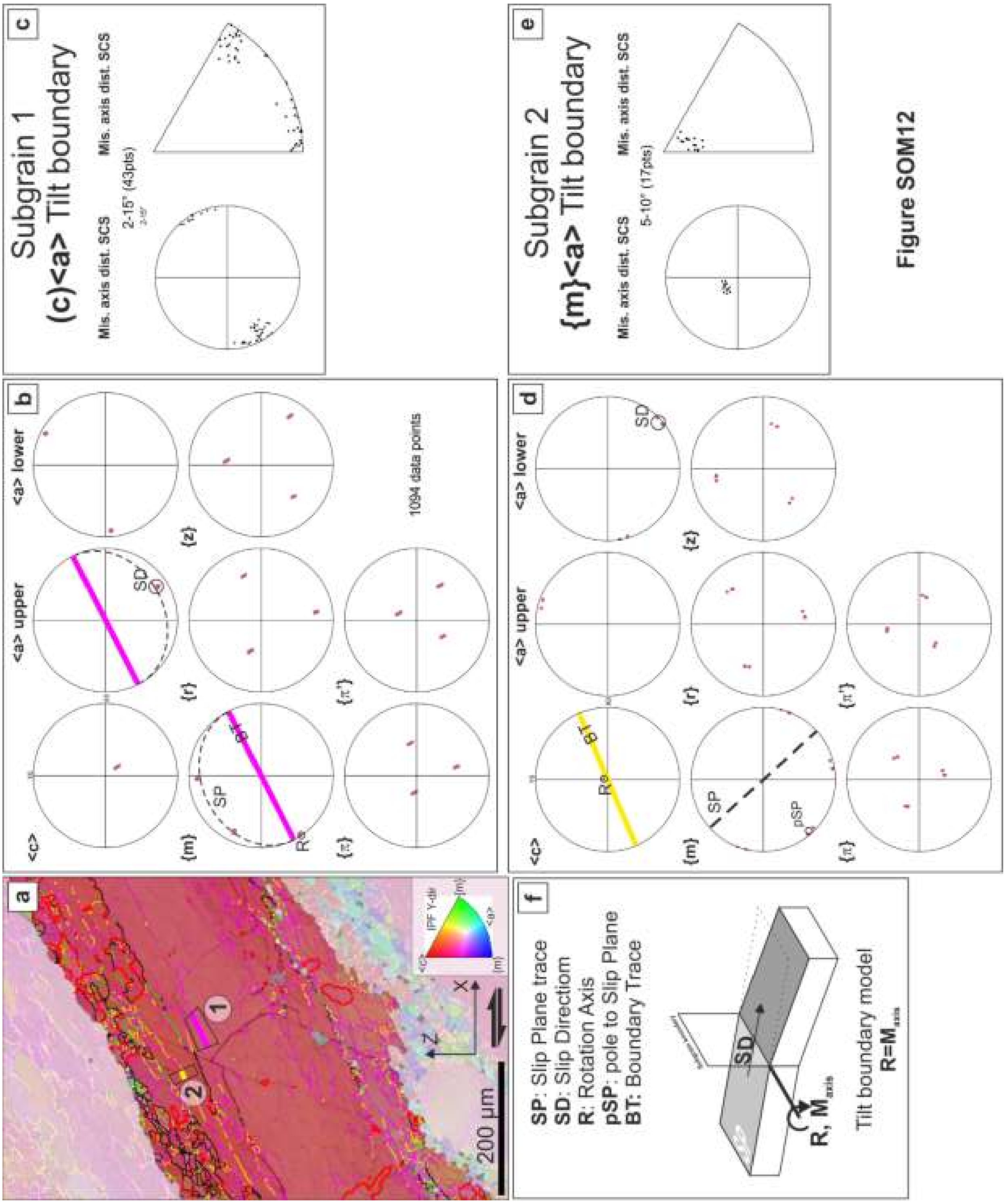

Figure SOM12

Fig. SOM12: Boundary trace analysis (Prior et al., 2002; Piazolo et al., 2008) of the Y-type ribbon of Fig. 6a. (a) EBSD color-coded map with location of the analysed subgrain boundaries 1 and 2. (b) Pole figures (<c>, <a>, {m}, {r}, {z}, {p} and {p'} crystallographic orientations) for EBSD data points around subgrain boundary 1; (c) Misorientation axis in sample and crystal coordinates across subgrain boundary 1; (d) Pole figures for EBSD data points around subgrain boundary 2; (e) Misorientation axis in sample and crystal coordinates across subgrain boundary 2. (f) Scheme of relationships between tilt boundaries and edge dislocations. In the pole figure sets (b, d), the possible geometrical elements are shown for a tilt boundary due to the activity of (c) <a> slip (subgrain boundary 1) and {m}<a> slip (subgrain boundary 2).

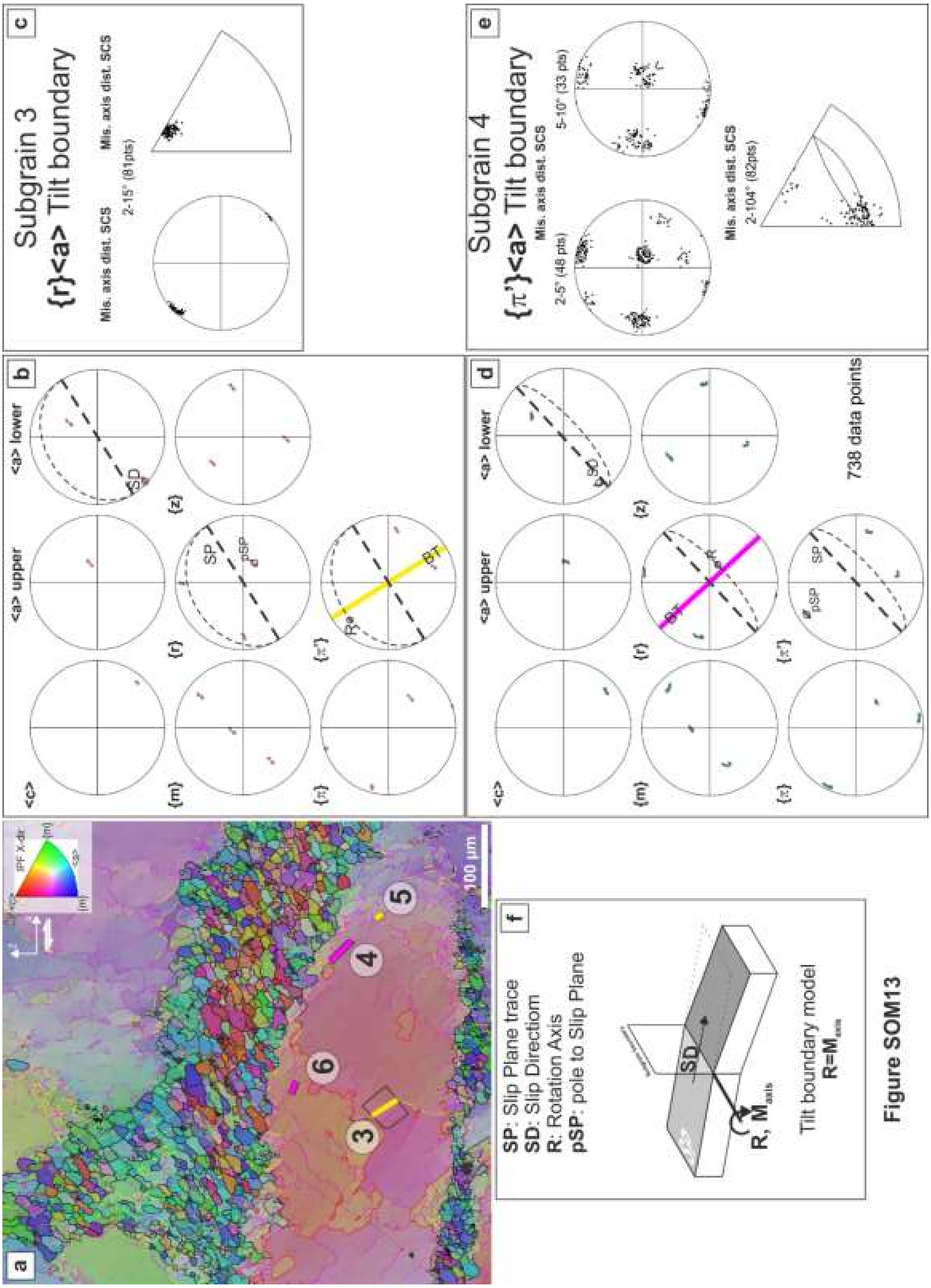

Fig. SOM13: Boundary trace analysis (Prior et al., 2002; Piazolo et al., 2008) of the XZa-type ribbon of Fig. 7a. (a) EBSD color-coded map with location of the analysed subgrain boundaries 3-6. (b-e) Pole figures for subgrain boundary 3; (c) Misorientation axis in sample and crystal coordinates across subgrain boundary 3; (d) Pole figures for subgrain boundary 4; (e) Misorientation axis in sample and crystal coordinates across subgrain boundary 4. (f) Scheme of relationships between tilt boundaries and edge dislocations. In the pole figure sets (b, d), the possible geometrical elements are shown for a tilt boundary due to the activity of {r}<a> slip (subgrain boundary 3) and {p'}<a> slip (subgrain boundary 4).

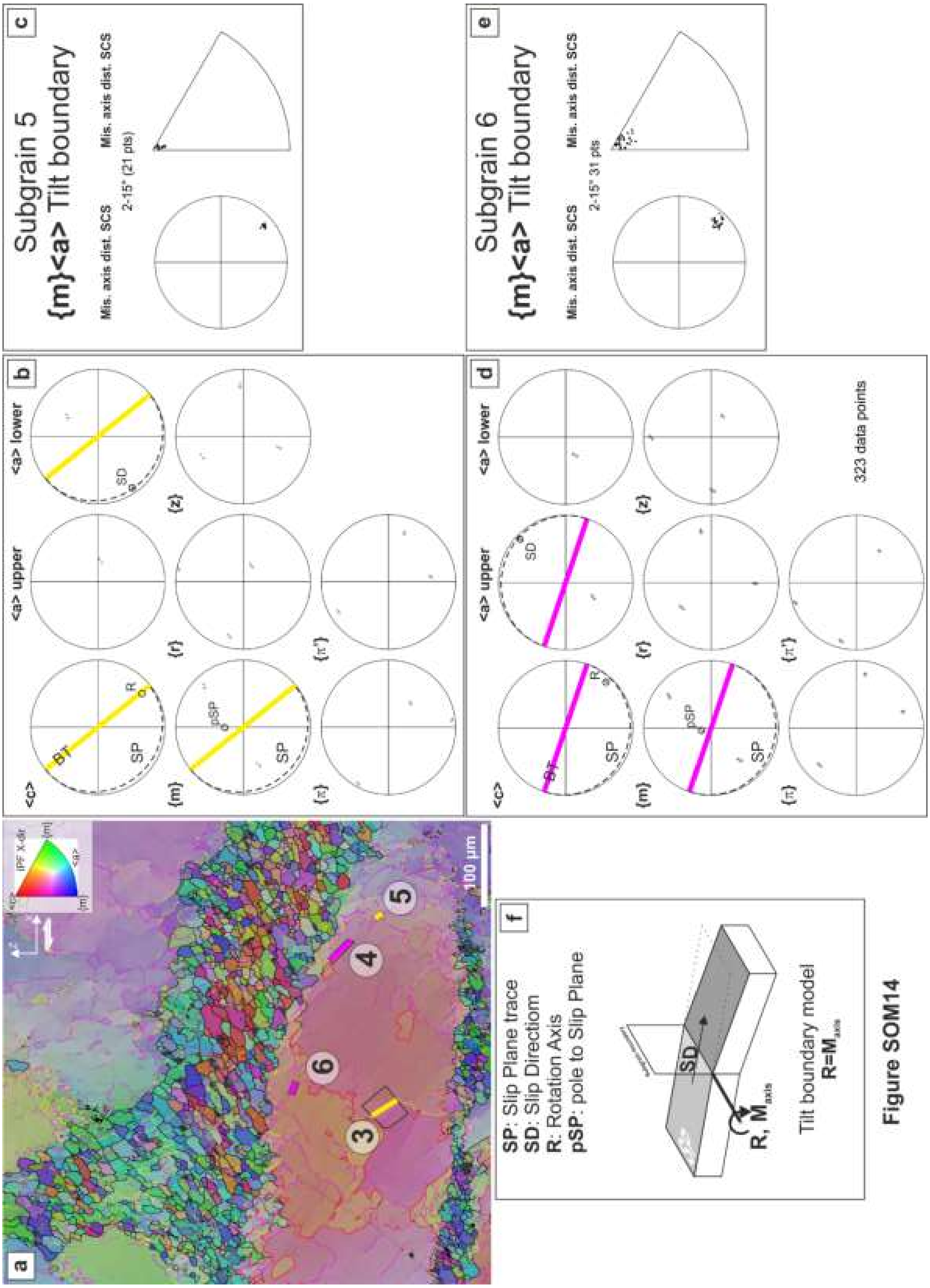

Fig. SOM14: Boundary trace analysis (Prior et al., 2002; Piazolo et al., 2008) of the XZa-type ribbon of Fig. 7a. (a) EBSD color-coded map with location of the analysed subgrain boundaries 3-6. (b-e) Pole figures for subgrain boundary 5; (c) Misorientation axis in sample and crystal coordinates across subgrain boundary 5; (d) Pole figures for subgrain boundary 6; (e) Misorientation axis in sample and crystal coordinates across subgrain boundary 6. (f) Scheme of relationships between tilt boundaries and edge dislocations. In the pole figure sets (b, d), the possible geometrical elements are shown for a tilt boundary due to the activity of {m}<a> slip for both subgrain boundaries 5 and 6.

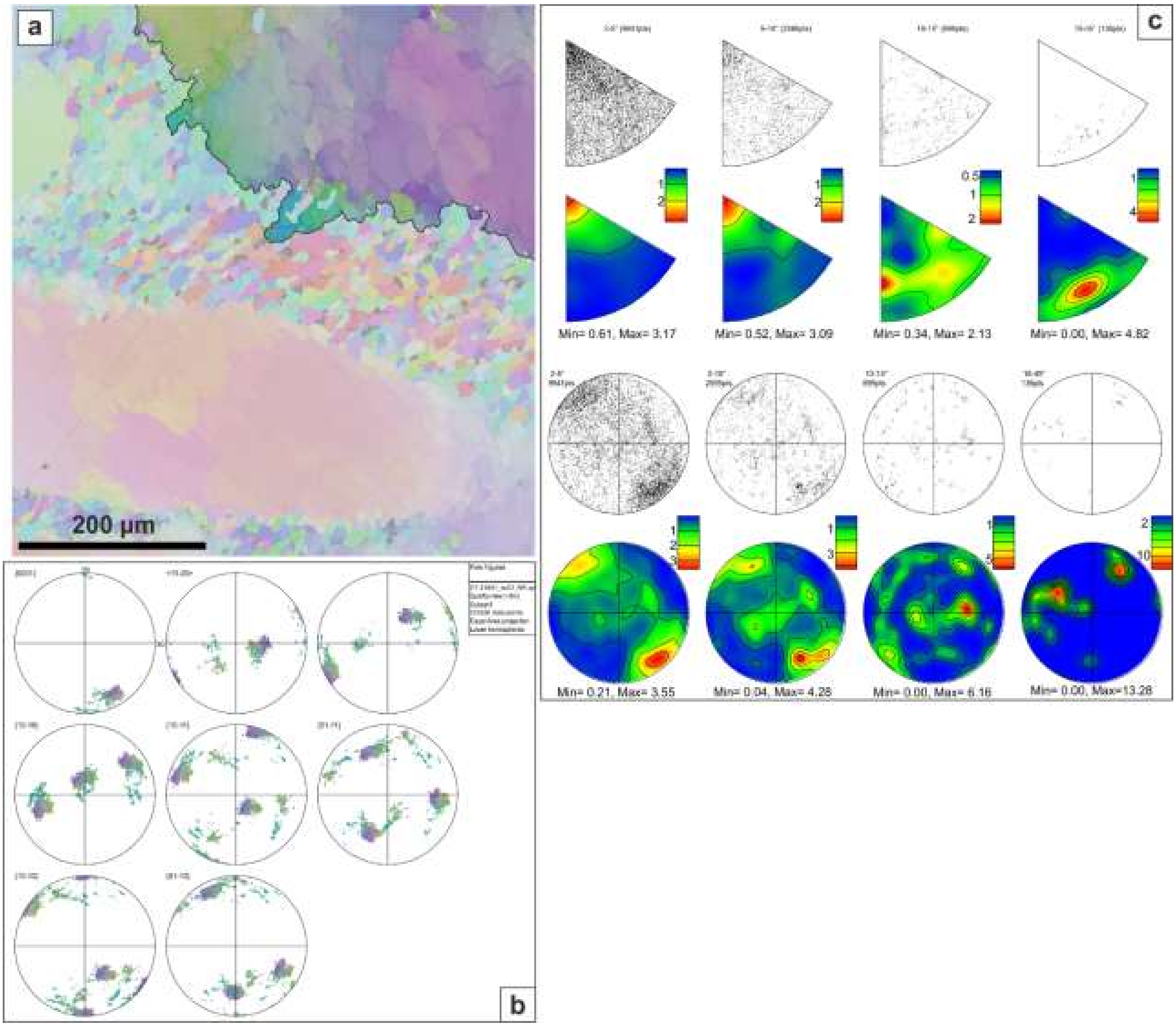

Fig. SOM15: Misorientation axis distribution for host ribbon of Fig. 7a (domain in the upper right side of the µSZ). (a) EBSD color-coded map (with semi-transparent colour for non-analysed areas). (b) Pole figures for <c>, <a>, {m}, {r}, {z}, {p} and {p'} crystallographic orientations. (c) Misorientation axis distribution diagrams (both inverse pole figures and in sample coordinates) for the misorientation ranges of 2-5°, 5-10°, 10-15° and 15-45°. See text for explanation.

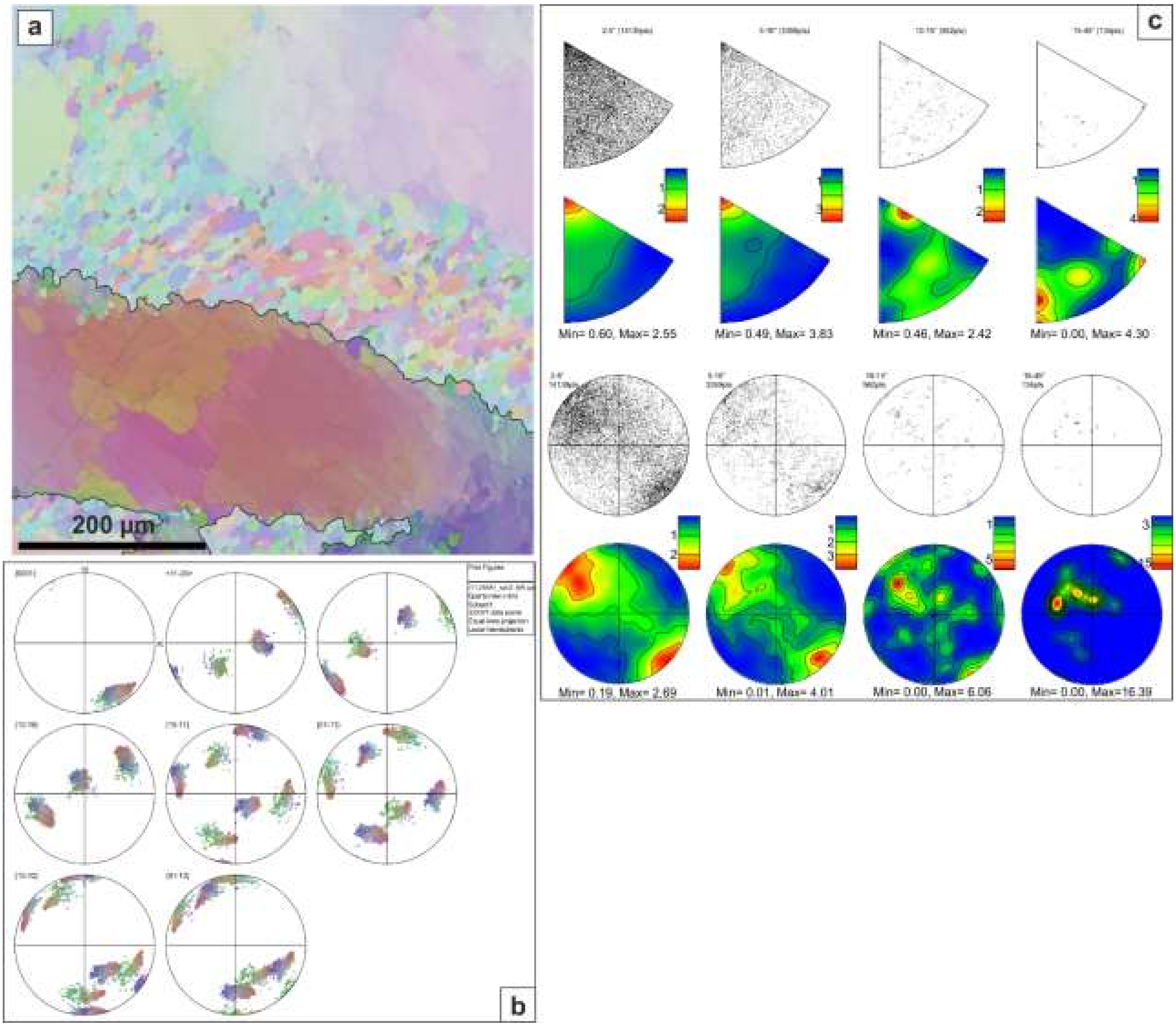

Fig. SOM16: Misorientation axis distribution for host ribbon of Fig. 7a (domain in the lower left side of the µSZ). (a) EBSD color-coded map (with semi-transparent colour for non-analysed areas). (b) Pole figures for <c>, <a>, {m}, {r}, {z}, {p} and {p'} crystallographic orientations. (c) Misorientation axis distribution diagrams (both inverse pole figures and in sample coordinates) for the misorientation angle ranges of 2-5°, 5-10°, 10-15° and 15-45°. See text for explanation.

SEM-EBSD detector	FEG-SEM Zeiss 1540 EsB		JEOL 6610 LV SEM – NordLys Nano		JEOL 7001 FE SEM NordLys Max
Figure	Fig. 7	Fig. 8	Fig. 9	Fig. 6	Fig. 11
Subject	XZa-type µSZ	XZb-type µSZ	XZa-type µSZ	Y-type ribbon	Ultramylonite
Magnification	130x	120x	120x	120x	90x
Step size (µm)	0.6	0.6	1.8	1.2	1.6
Size (µm)	560 x 590	520 x 600	1076 x 806	1076 x 484	1422 x 1195
Acquisition time (s/pxl)	0.074	0.074	0.178	0.040	0.34
Accelerating Voltage	20	20	20	20	20

Table SOM1: Scanning electron microscope typology and analytical conditions for EBSD maps reported in Figs. 6-7-8, Fig. 10 and Fig. SOM5.

Chapter 3

Deformation mechanisms during shearing of myrmekite in granitoid mylonites

Alberto Ceccato[1], Luca Menegon[2], Giorgio Pennacchioni[1]

[1] Department of Geosciences, University of Padova, Via Gradenigo 6, I-35131 Padova, Italy

[2] School of Geography, Earth and Environmental Sciences, Plymouth University, United Kingdom

Abstract

Localization of ductile strain within heterogeneous shear zones exploiting epidote veins developed during Stage 3 has been mediated by different grain-size reduction mechanisms. SEM-BSE observation has revealed a series of syn- to post-kinematic reaction microstructures: (i) recrystallization of quartz and biotite; (ii) plagioclase-muscovite-sphene symplectites that develop after plagioclase (andesine) and Ti-rich magmatic biotite; (iii) development of myrmekite on magmatic K-feldspar (albite-rich plagioclase + quartz intergrowths). We have investigated the processes of grain size reduction and the deformation mechanisms related to the formation and following shearing of myrmekite in K-feldspar, given their widespread occurrence and importance of myrmekite as grain-size reduction mechanisms in granitoid rocks (Menegon et al., 2006; Pennacchioni and Zucchi, 2013). Preliminary results indicate that: (i) myrmekite are strain-induced microstructures in K-feldspar that nucleate in site of stress concentrations (as already reported by Menegon et al., 2006), however K-feldspar is still stable and re-precipitate in stress/strain shadows; (ii) parent K-feldspar and myrmekitic plagioclase in some cases show perfect coincidence between crystallographic planes, mimicking a pseudomorphic relation; quartz does not show any

crystallographic relation with either of the feldspars; (iii) Shearing of myrmekite lead to the development of fine grained plagioclase + quartz aggregates (7 µm and 4 µm in grain size, respectively) that show an ordered (anticlustered) spatial distribution and well defined shape preferred orientation; quartz usually occurs at triple- and quadruple-junction between plagioclase grains; (iv) both plagioclase and quartz show weak CPOs and almost random misorientation angle distributions. All these microstructural and textural features point to grain-size sensitive deformation mechanisms, such as diffusion creep associated with grain boundary sliding mainly in plagioclase. In addition, EBSD investigation on pure quartz layers along the foliation and adjacent to sheared plagioclase + quartz aggregates have revealed that quartz deformed by crystal plasticity and recrystallized by SGR.

3.1. Introduction

In this Chapter, deformation mechanisms that lead to the development of localized Stage 3 ductile shear zones are analysed. Localization of ductile deformation usually occurs as a consequence of instabilities during homogeneous deformation of rocks (Hobbs et al., 1990). Instabilities in flowing ductile rocks may arise from weakening processes and variation in mechanical properties due to strain accumulation (Gueydan et al., 2014). Strain weakening/softening is usually associated to grain size reduction processes, such as dynamic recrystallization, metamorphic reactions and phase mixing (e.g. de Bresser et al., 2001 and reference therein). Switch in deformation mechanisms between grain-size-insensitive (GSI) and grains-size-sensitive (GSS) creep resulting from grain size reduction processes is one of the most effective mechanisms for strain weakening (e.g. Kruse and Stünitz, 1999; Kilian et al, 2011; Menegon et al., 2013).

Feldspars are the most common mineral phase in crustal rocks, and it usually build up the rock load-bearing framework during deformation (Handy, 1994). A common feature of feldspars is the development of fine-grained symplectic reaction at both magmatic and metamorphic conditions (Vernon, 1991). In particular, K-feldspar is usually replaced by the development of myrmekite, which are very fine-grained symplectic intergrowth of vermicular quartz and plagioclase (Becke, 1908). Therefore, myrmekite formation is one of the most common process of grain size reduction that may lead to softening and localization of ductile strain in granitoid rocks (reaction-softening) under mid- to lower-crustal conditions (Stünitz and Fitz Gerald, 1993a,b; Tsurumi et al., 2003; Menegon et al., 2006; Cesare et al., 2002; Simpson and Wintsch, 1989; Pennacchioni et al., 2005; Pennacchioni and Zucchi, 2013). Stress concentration and crystal strain have been demonstrated to trigger the development of myrmekite in deforming granitoid rocks (e.g. Simpson and Wintsch, 1989; Menegon et al., 2006). Deformation and shearing of myrmekite result into the development of fine-grained plagioclase + quartz layers, that are inherently weaker than the former K-feldspar grains (Tsurumi et al., 2003). In addition, myrmekite development is a fluid-assisted metamorphic process (e.g. Cesare et al., 2002; Menegon et al., 2006). The circulation of fluids may enhance the occurrence of dissolution-precipitation processes that promotes phase mixing and the development of ultramylonites (e.g. Vernon, 1991; Menegon et al., 2006; Kilian et al., 2011, Czaplińska et al., 2015). However, the exact deformation mechanisms of the fine-grained plagioclase + quartz layers that result from the recrystallization and shearing of myrmekite have never been investigated systematically and quantitatively yet. The mechanical behaviour and microstructural evolution of feldspar + quartz aggregates have been previously described from both experimental deformation at high temperature conditions (Dell'Angelo and Tullis, 1997; Xiao et al., 2002) and natural mylonites (e.g. Behrmann and Mainprice, 1987).

In the RFP deformation Stage 3 tonalitic mylonites, the microstructural evolution across the strain gradient from protomylonites to ultramylonites is characterized by increasing consumption of K-feldspar through myrmekite development, leading to the development of increasing volumes of plagioclase + quartz fine-grained layers. We have performed electron back-scattered diffraction (EBSD) analyses and mapping on selected areas including K-feldspar grains and sheared plagioclase + quartz aggregates along the strain gradient of the RFP Stage 3 mylonites in order to define: (i) possible crystallographic relationships between parent K-feldspar and plagioclase + quartz products during incipient stages of myrmekite formation; (ii) deformation mechanisms during myrmekite shearing and ultramylonitic matrix formation; (iii) recrystallization mechanisms and texture development in pure quartz layers.

3.2. Methods

Microstructural and chemical analyses were performed on polished thin section of tonalite mylonites cut parallel to the lineation (X) and perpendicular to the shearing plane. Optical microscopy and image analyses were performed at the University of Padua. Electron microprobe analyses were performed at the University of Padua (EM WDS Cameca SX50) and University of Milan (EM WDS Jeol 8200 SuperProbe).

EBSD analysis

Electron backscattered diffraction analysis was carried out on a JEOL 7001 FE SEM equipped with a NordLys Max EBSD detector (AZTec acquisition software, Oxford Instruments) at the Electron Microscope Centre of Plymouth University. The thin section was SYTON-polished for approximately 3 hours and carbon coated. All data have been processed and analysed using CHANNEL5 software of HKL Technology, Oxford Instruments. Resulting raw EBSD maps suffered from high rates of misindexing and non-indexed points: (i) noise reduction have been applied following Bestmann and Prior (2003); (ii) misindexing plagioclase and K-feldspar have been resolved nullifying the subset of selected grains with area $<1 \mu m^2$ in each map; (iii) Dauphiné twins smaller than 0.5 μm have been interpreted as an error from misindexing and were replaced by the average orientation of the neighbouring pixels.

Monoclinic sample symmetry has been used. The indexed phases and relative symmetry group used for the indexing are: quartz – Trigonal -3m; plagioclase – Anorthite Triclinic -1; orthoclase – Monoclinic 1/m; clinozoisite, biotite and garnet have been indexed where present, but orientation data have not been analysed. Critical misorientation for the distinction between low- and high-angle boundaries have been chosen at 10°, allowing grain boundary completion down to 1°. In addition, quartz grain boundaries with 60°±5° of misorientation were disregarded from grain detection procedure, to avoid any contribution from Dauphiné twinning.

The pole figures (one-point-per-grain, where not differently specified) and the misorientation axis distributions in sample coordinates are equal area, lower hemisphere projections oriented with the general shear zone kinematics reference system (X = stretching lineation; Z = pole to general shear plane/vein boundary). The inverse pole figures for misorientation axis distribution in crystal coordinates are upper hemisphere projections. Contoured projections have constant contouring parameters (Half width: 15°; Cluster size: 3°). Contouring lines are given only for the 0.5-10 m.u.d. range.

Local misorientation maps are calculated using a 3x3 pixel kernel with a maximum misorientation of 2° (minimum angle for a low misorientation angle boundary).

Grain size analysis

Grain sizes are obtained from the grain detection routine in Channel5 Tango software. Equivalent grain diameters are obtained from grain area (μm^2). The minimum cut-off area has been set to 1 μm^2; therefore, only grains composed of 4 to 9 pixels (according to map acquisition step-size) have been considered. Grain size data are then plotted as area-weighted distributions as frequency against square-root grain-size-equivalent grain diameters (as in Herweg and Berger, 2004). The grain size distribution is close to a Gaussian distribution when plotted in this way, therefore it gives us a good estimation of the mean grain size. The geometric mean grain size (red thick line in grain size distribution diagrams) is obtained graphically as the maximum frequency grain size of the distribution curve. The distribution curve (orange line in grain size distribution diagrams) is obtained interpolating distribution data with a 6th degree polynomial equation in Excel-MS Office. Relative frequencies are normalized to 1.

Image analyses

Image analysis of grain shape was performed on both SEM-BSE images and phase maps obtained from EBSD. Quantification of phase amount (vol%) has been performed through segmentation of SEM-BSE images of a whole thin section collected at the University of Plymouth (Electron Microscopy Centre). Image processing and thresholding have been done with ImageJ software and further processing and manual correction have been applied to improve data quality and to be sure of the correspondence between grayscale values and each phase.

Grain boundary images and phase distribution images have been obtained directly from EBSD phase maps and grain boundary maps elaborated by Channel5 (HKL technology). Before the analysis with ImageJ software, images were manually corrected to exclude misindexing and non-indexed orientation pixels. Grain boundaries and phase amount have been quantified by pixel counting.

3.3. Sample description and microstructure

Samples and microstructures described and analysed here come from heterogeneous shear zones developed in granodiorites and tonalites exploiting epidote-rich veins (Chapter 1).

The magmatic assemblage of fine-grained granodiorite of the RFP consist of: quartz + plagioclase + K-feldspar + biotite + allanite/epidote + Mg-hornblende + apatite + sphene. In the host granitoid, magmatic plagioclase is found in glomeroclasts enveloped by K-feldspar. Magmatic plagioclase is rhythmically zoned with a variable composition from An_{32} to An_{58}. Magmatic K-feldspar has an Ab rich composition ($Or_{93} – Ab_7$) on average. Magmatic biotite (Bt_I) is observed as either single mm-size crystals, or surrounding and embedding plagioclase glomeroclasts.

Foliation development in the host granitoid is aided by several grain-size reduction mechanisms: (i) recrystallization of magmatic quartz and biotite (white arrows in Figs. 1a-b); (ii) myrmekite formation at the expense of magmatic K-Feldspar (Fig. 1c) and (iii) synkinematic symplectite formation between biotite and plagioclase [plagioclase ($An_{29}Ab_{71}Or_{<1}$) + sphene + secondary muscovite; similar to Pennacchioni et al., 2006; Johnson et al., 2008; Fig. 1d].

Foliation is therefore defined by the alternation of (i) pure quartz layers; (ii) plagioclase ($An_{26}Ab_{74}Or_{<1}$) + quartz + K-feldspar layers and (iii) biotite – recrystallized biotite/plagioclase layers (Fig. 1a).

Feldspar aggregates (glomeroclasts) are dismembered along the strain gradient, flattened and plagioclase single crystal are isolated, rounded and grain size is reduced. With increasing strain, K-feldspar (Kfs_I – Or_{92}-Ab_8), which formerly enveloped plagioclase crystals, are progressively dismembered, rounded and replaced by myrmekite. Myrmekite mantle Kfs_I grains, even though they preferentially develop at stress concentration sites (e.g. Menegon et al., 2006), and these mantles are then sheared to form plagioclase + quartz aggregates originating from porphyroclasts tails (Fig. 1b). Close to the mylonitic portion, synkinematic K-feldspar is found in specific microstructural sites, such as strain shadows or dilatant sites close to plagioclase porphyroclasts (Fig. 2a). This newly formed K-feldspar is in turn replaced (at least locally) by myrmekite. Along the strain gradient, there is a net decrease in volume percentage of K-feldspar from 19vol% in the undeformed-protomylonitic rock portions, to 6-1% in the mylonite/ultramylonite layers (Figs. 3b-d). Accordingly, there is a net increase in volume percentage of fine-grained aggregates, mainly composed of plagioclase and quartz, from 3% in the undeformed-protomylonitic rock, up to 13% in the mylonite/ultramylonite (Figs. 3c-d).

Ultramylonites are characterized by a fine-grained (about 30 μm) homogeneous matrix, whose mineral paragenesis consists of quartz + plagioclase + biotite + epidote + K-feldspar + sphene + apatite ± garnet ± white mica. K-feldspar is usually observed in strain shadows and in dilatant triple junction in quartz layers (Figs. 2c-d; e.g. Menegon et al., 2006; Kilian et al., 2011).

Figure 1. Microstructures of Rieserferner tonalitic mylonites. **(a)** Photomicrograph (crossed polars) showing the layered structure of tonalite mylonites, composed of alternating layers of recrystallized quartz, recrystallized biotite + plagioclase + quartz layers and plagioclase + quartz layers. White arrows indicate layers of recrystallized quartz and biotite, respectively. **(b)** BSE image of the zone reported in (a). Here it is possible to perfectly distinguish K-feldspar porphyroclasts surrounded by myrmekites and sheared plagioclase + quartz aggregates. **(c)** BSE image of the Unexploited myrmekite invading an euhedral Kfeldspar. Close to the centre of the figure a small K-feldspar porphyroclast is embedded in plagioclase + quartz aggregate. Note the occurrence of plagioclase + sphene symplectite at the contact between sheared biotite and myrmekites. **(d)** BSE image of the Plagioclase + sphene symplectite after the reaction between magmatic plagioclase and biotite. **(e)** BSE image of a K-feldspar porphyroclast mantled by myrmekites and sheared plagioclase + quartz aggregate. **(f)** BSE image of a K-feldspar porphyroclast system linked by a sheared plagioclase + quartz aggregate. **(g)** BSE image of a K-feldspar porphyroclast mantled by myrmekites and sheared plagioclase + quartz aggregate along the foliation defined by recrystallized biotite (and sphene). **(h)** BSE image of a K-feldspar porphyroclast mantled by myrmekites and sheared plagioclase + quartz aggregate along the foliation defined by recrystallized biotite and plagioclase.

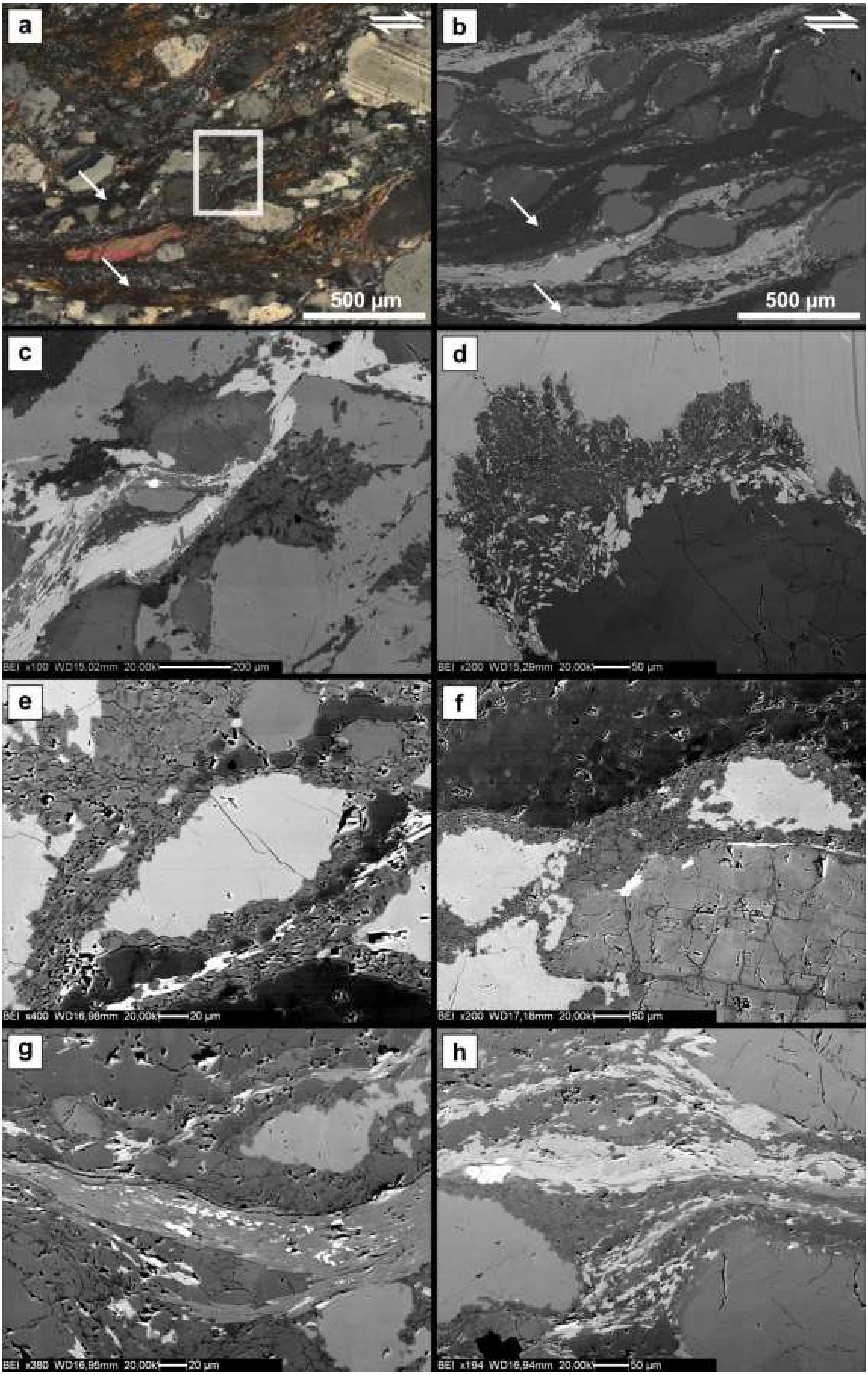
a
500 µm
b
500 µm
c
BEI x100 WD15,02mm 20,00kV 200 µm
d
BEI x200 WD15,29mm 20,00kV 50 µm
e
BEI x400 WD16,98mm 20,00kV 20 µm
f
BEI x200 WD17,18mm 20,00kV 50 µm
g
BEI x380 WD16,95mm 20,00kV 20 µm
h
BEI x194 WD16,94mm 20,00kV 50 µm

Figure 1

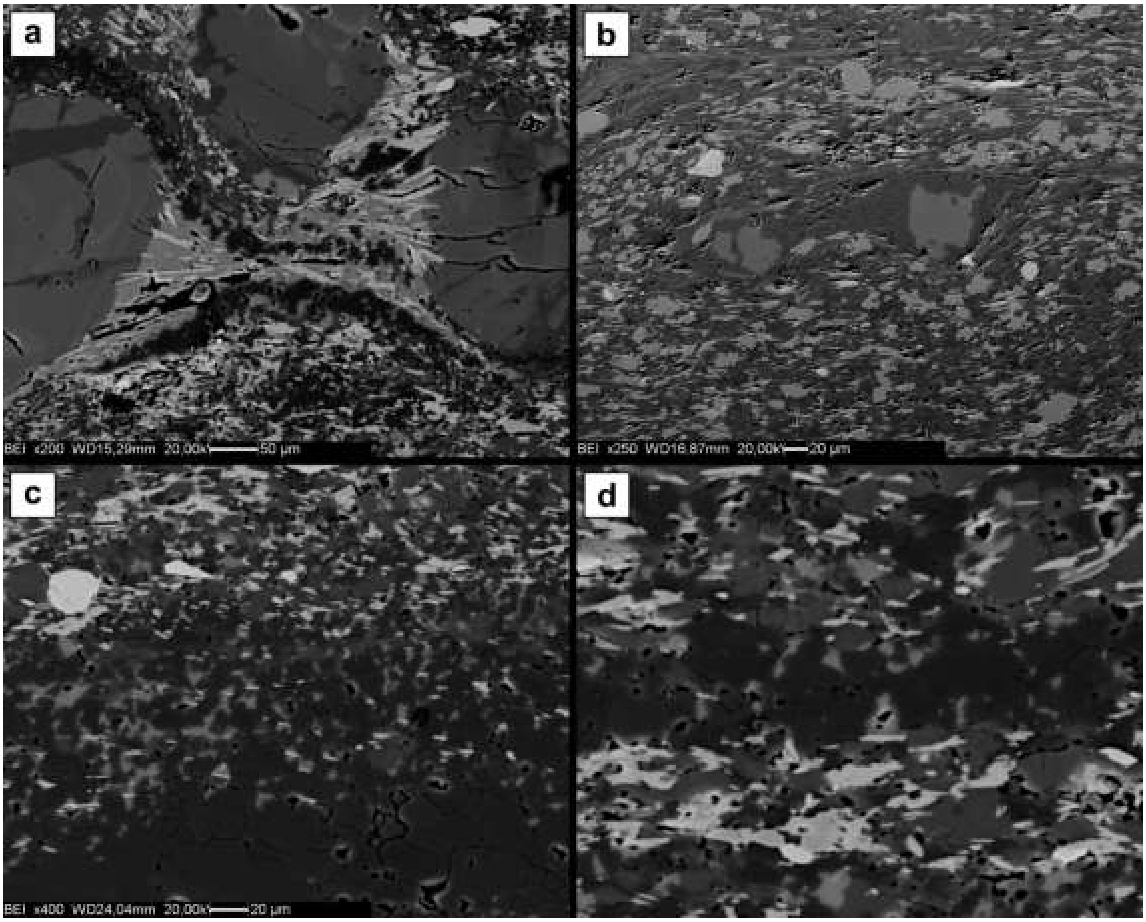

Figure 2. K-feldspar microstructures in tonalitic mylonites. **(a)** BSE image of the K-feldspar + biotite tails in strain shadows between two plagioclase porphyroclasts. It is interesting to note the occurrence of myrmekites in K-feldspar at the centre of the bridging structure. **(b)** BSE image of two K-feldspar porphyroclasts in the ultramylonitic matrix, mantled by plagioclase + quartz aggregates. **(c)** BSE image of the ultramylonitic matrix. Note the occurrence of oriented biotite flakes and K.feldspar grains nucleated at dilatant sites in dismembering quartz layer. **(d)** K-feldspar nucleates at triple junction and dilatant grain boundaries in quartz layers inside the ultramylonitic matrix.

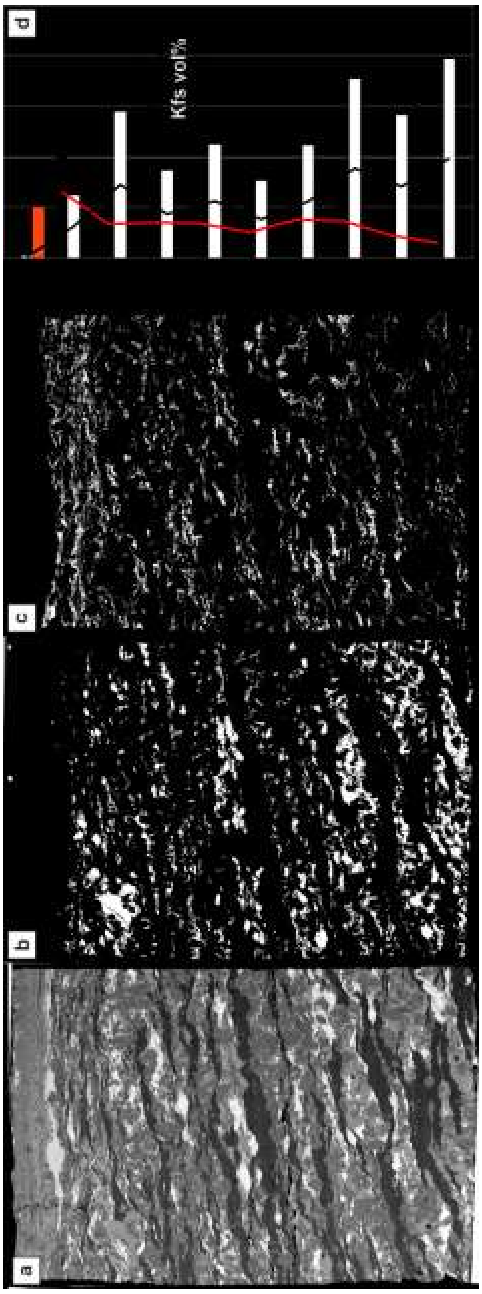

Figure 3. Phase distribution along the strain gradient of tonalitic mylonites. (a) Mosaic of BSE images of the analysed mylonite thin section. (b) Binary map of the distribution of K-feldspar along the strain gradient. (c) Binary map showing the distribution of fine-grained aggregates resulting from mineral reaction (myrmekite and symplectite formation). This can be considered as the volume percentage of plagioclase + quartz aggregates after myrmekite. (d) Bar diagram showing the relative variation in volume percentage of K-feldspar (white bars) and myrmekite (black bars).

3.4. EBSD analyses and myrmekite microstructures

Selected microstructures of the tonalitic mylonite have been analysed to characterize the processes of: (i) myrmekite nucleation; (ii) myrmekite shearing and the transition to plagioclase + quartz aggregates; (iii) deformation mechanisms in pure-quartz layers; (iv) deformation mechanisms and behaviour of feldspar porphyroclasts during shearing.

We have analysed the phase spatial distribution of plagioclase and quartz in both pristine myrmekite and sheared plagioclase + quartz aggregates to define their deviation from random distribution, either towards a clustered- or an anticlustered distribution (Kruse and Stünitz, 1999, Menegon et al., 2013; Heilbronner and Barrett, 2014). The spatial distributions of phases in deformed bimodal aggregates is usually interpreted in terms of the dominant deformation mechanism (e.g. Kruse and Stünitz, 1999; Menegon et al., 2013). Phase spatial distribution analysis compares the cumulative lengths of phase boundaries (boundaries that separate two grains of a different phase) and of grain boundaries (boundaries that separate two grains of the same phase) in a bimodal aggregate with those expected for a random distribution of the two phases. We have considered three types of boundaries: (i) plagioclase – plagioclase grain boundaries; (ii) quartz – quartz grain boundaries; and (iii) plagioclase – quartz grain boundaries. Analyses have been performed on pristine myrmekite and on sheared plagioclase + quartz aggregates.

Pristine myrmekite

Incipient myrmekite have systematic microstructural characteristics: (i) myrmekite usually mantle the whole K-feldspar grains but are preferentially developed along grain boundaries parallel to the mylonitic foliation (Figs. 1e,f,g,h); (ii) myrmekite are mainly composed by lobe-shaped plagioclase + quartz aggregates protruding into the host K-feldspar (Figs. 4 and 5); (iii) each lobe is usually composed of a single crystal of plagioclase, 20 to 50 μm in grain size, embedding small (up to 3 μm) vermicular quartz grains (indicated by white arrows in Figs. 4a-5a); (iv) the spacing between the quartz grains/vermicules is about 2 μm.

EBSD analysis has firstly focussed on the crystallographic relationship between K-feldspar host grains and myrmekitic phases. We observe that: (i) in some cases (e.g. Fig. 4), there is a perfect overlap between crystallographic planes ({100}, {010} and {001}) of parent K-feldspar (Fig. 4b) and myrmekitic plagioclase (Fig. 4c) grains. Plagioclase grains show significant internal distortion (Figs. SOM1e-f). (ii) There is no crystallographic relationship between parent K-feldspar and myrmekitic quartz and between myrmekitic plagioclase and myrmekitic quartz. However, the quartz vermicules within single crystals of myrmekitic plagioclase usually have similar crystallographic orientation (Fig. SOM2a). Dauphiné twins are occasionally observed in quartz grains along with internal quartz grain distortion (Figs. SOM1a-b; scattered misorientations of ~0.5° magnitude).

Sheared quartz and plagioclase aggregates: recrystallized and sheared myrmekite

Plagioclase + quartz aggregates are observed to originate from myrmekite developed around K-feldspar to form foliation-parallel polyphase layers. The aggregates are mainly composed of plagioclase and relatively minor amount of quartz. K-feldspar and biotite occasionally occur in negligible amounts. Pristine myrmekite and sheared aggregates display the same phase ratio, usually around 18 vol% of quartz.

Fig. 6 report the results from phase spatial distribution analyses for both pristine myrmekite and sheared plagioclase + quartz aggregates. Phase and grain boundaries cumulative length are plotted against surface area fraction of quartz boundaries (quartz – quartz grain + phase boundaries). Results show that: (i)the surface area fraction of quartz ranges between 0.55 and 0.75; (ii) quartz – quartz grain boundaries occur with a probability lower than that of a binomial random distribution; (iii) plagioclase – plagioclase grain boundaries occur with higher probability than that expected for binomial random distribution (i.e. it shows an ordered – anticlustered distribution); (iii) plagioclase – quartz phase boundaries occur with higher probability that that expected for random distribution of phases (i.e. the aggregates shows an ordered – anticlustered distribution).

Quartz grains in sheared plagioclase + quartz aggregates are scattered and isolated, usually occurring as single grains surrounded by plagioclase grains. Quartz displays: (i) very small grain size (about 3 µm) in the incipient un-exploited myrmekite (Figs. 7a-b), (ii) small grain size (~5 µm) in the sheared plagioclase + quartz aggregate (Fig. 7c); (iii) coarser grain size (>10µm) in strain shadows, or where quartz grains coalesce to form aggregates composed of several (>3) grains (Fig. 7d). They show sub-rounded to polygonal equant shapes (mode of aspect ratios $1.5<AR<1.75$) showing a weak SPO at low angle to the mylonitic foliation (Fig. 7e). Quartz grains are observed at triple/quadruple junctions between plagioclase grains, and occasionally they form 2-3 grains aggregates elongated normal to the foliation (e.g. Fig.4a). Pole figures do not show any preferred crystallographic orientations (close to uniform distribution, Fig. 5b). Low angle misorientation axis distributions show high density close to the X kinematic direction and are preferentially oriented parallel to the c-axis and rhomb crystal directions (Fig. 5c). In general, high misorientation angle boundaries are observed in greater number than low-angle ones. The misorientation axes for high misorientation are quite randomly distributed in crystal coordinates, even though a weak grouping is observed close to the centre of the pole figure in sample coordinates. Correlated misorientation angle distribution for quartz show two maxima with different strengths (Fig. 5d): (i) the strongest maximum occurs at around 60°; (ii) a weak maximum occurs at low angle misorientations (<10°). Uncorrelated misorientation angle distribution is very close to the random-pair theoretical distribution for quartz.

Local misorientation maps (Figs. SOM1a-b) for quartz grains in the sheared aggregate suggest that small quartz grains are the most distorted (mean internal distortion of 0.5°). Major misorientations are organized close to low/high-angle misorientation boundaries occurring in quartz grains. Coarser quartz grains usually show a more homogeneous internal distortion.

Plagioclase grains are mainly polygonal with straight boundaries. Plagioclase shows: (i) coarse grain size in incipient myrmekite (between 10 and 35 µm; Fig. 8a; e.g. coarse plagioclase grains in the incipient myrmekite in Fig. 5); (ii) homogeneous smaller grain size (about 7 µm) in plagioclase + quartz aggregates (Figs. 8b-d), (iii) grain shapes ranges from almost equant to elongated (mode of aspect ratios 1.75<AR<2) defining an inclined SPO almost parallel to the local mylonitic foliation (e.g. Fig.8e for sheared myrmekite reported in Fig. 5). Pole figures show a uniform distribution of crystallographic axes (Fig. 5e). Low angle misorientation boundaries are very rare inside plagioclase grains of the aggregate, even though they show a grouping of points close to [001] and [201] crystal directions (with the tendency to form a girdle between these two directions, Fig. 5f). These axes both plot close to X kinematic direction. High angle misorientation axis are evenly distributed in both crystal and sample coordinates. Misorientation angle distributions for plagioclase are very close to the random-pair theoretical distribution (Fig. 5f). Correlated misorientation distribution shows two weak peaks at very low angles (<5-10°) angles and close to 180° (Fig. 5g). In addition, correlated misorientations for angle lower than 70° occurs with slightly higher frequency than the random-pair theoretical distribution. Albite-twin is weakly developed inside new grains (weak peak close to 180° of misorientation).

Local misorientation maps (Figs. SOM1e-f) show that maximum misorientations and distortion of plagioclase grains are concentrated along high misorientation angle boundaries. However, the internal portion of plagioclase grains shows highly scattered blue/green colours, evidence of an heterogeneous distortion inside grains. This can be inferred also from the peak of the misorientation histogram related to plagioclase local misorientation map, whose maximum (~0.5°) occurs at higher angle than that of quartz (<0.5°).

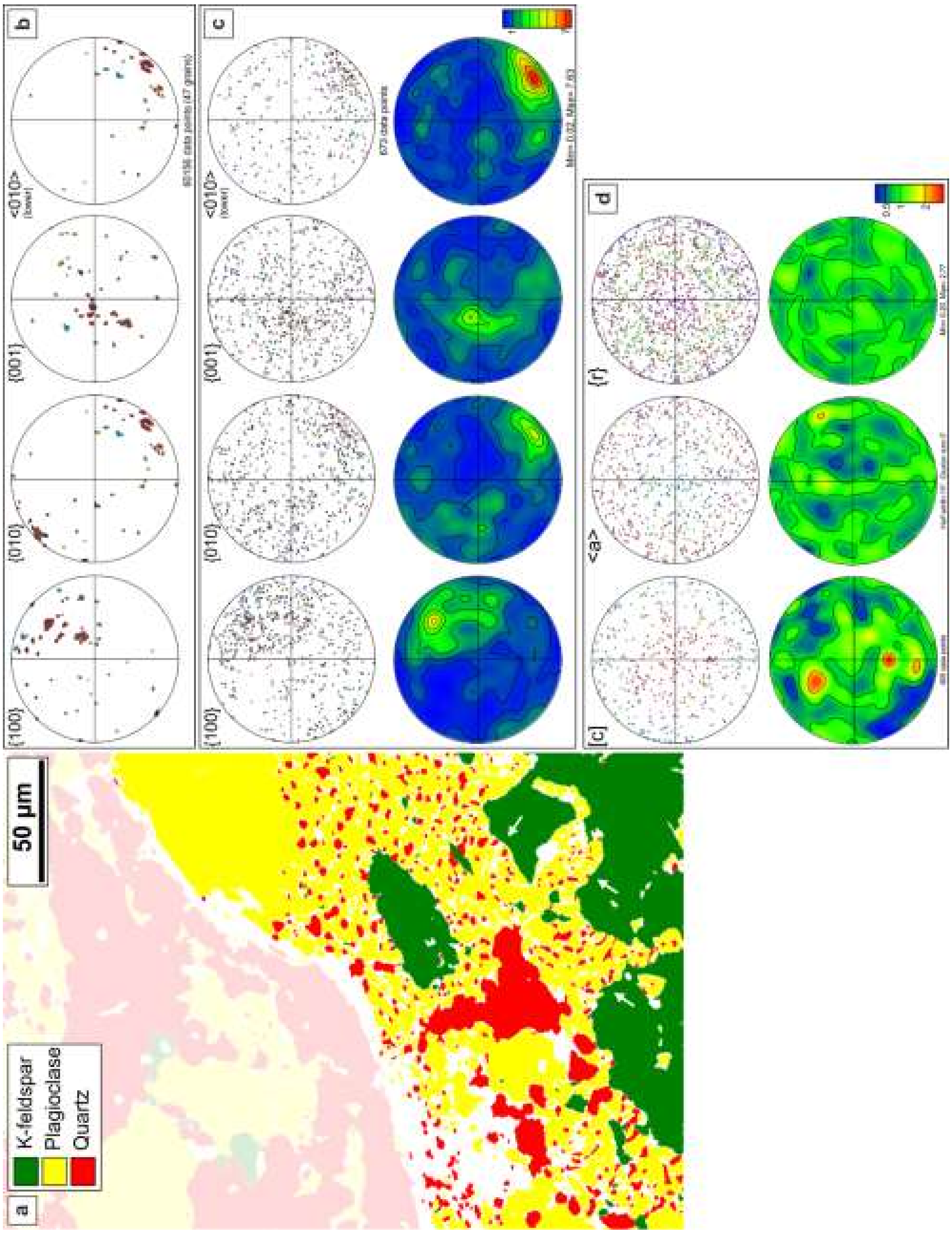

Figure 4. EBSD orientation data and mapping on incipient myrmekite and sheared plagioclase + quartz aggregate. **(a)** Phase map obtained from EBSD orientation mapping. **(b)** Pole figures for K-feldspar reporting low-Miller-indices crystal elements. **(c)** Pole figures for plagioclase reporting low-Miller-indices crystal elements. **(d)** Pole figures for quartz reporting low-Miller-indices crystal elements.

Figure 5. EBSD orientation data and mapping on incipient myrmekite and sheared plagioclase + quartz aggregate. **(a)** Phase map obtained from EBSD orientation mapping with highlighted areas where grain size analyses and phase distribution analyses have been performed. **(b)** Pole figures for quartz reporting low-Miller-indices crystal elements. **(c)** Misorientation axis distributions for quartz in sample (upper row) and crystal (lower raw) coordinate system. **(d)** Misorientation angle distribution for quartz. **(e)** Pole figures for plagioclase reporting low-Miller-indices crystal elements. **(f)** Misorientation axis distributions for plagioclase in sample (upper row) and crystal (lower raw) coordinate system. **(g)** Misorientation angle distribution for plagioclase.

Figure 5

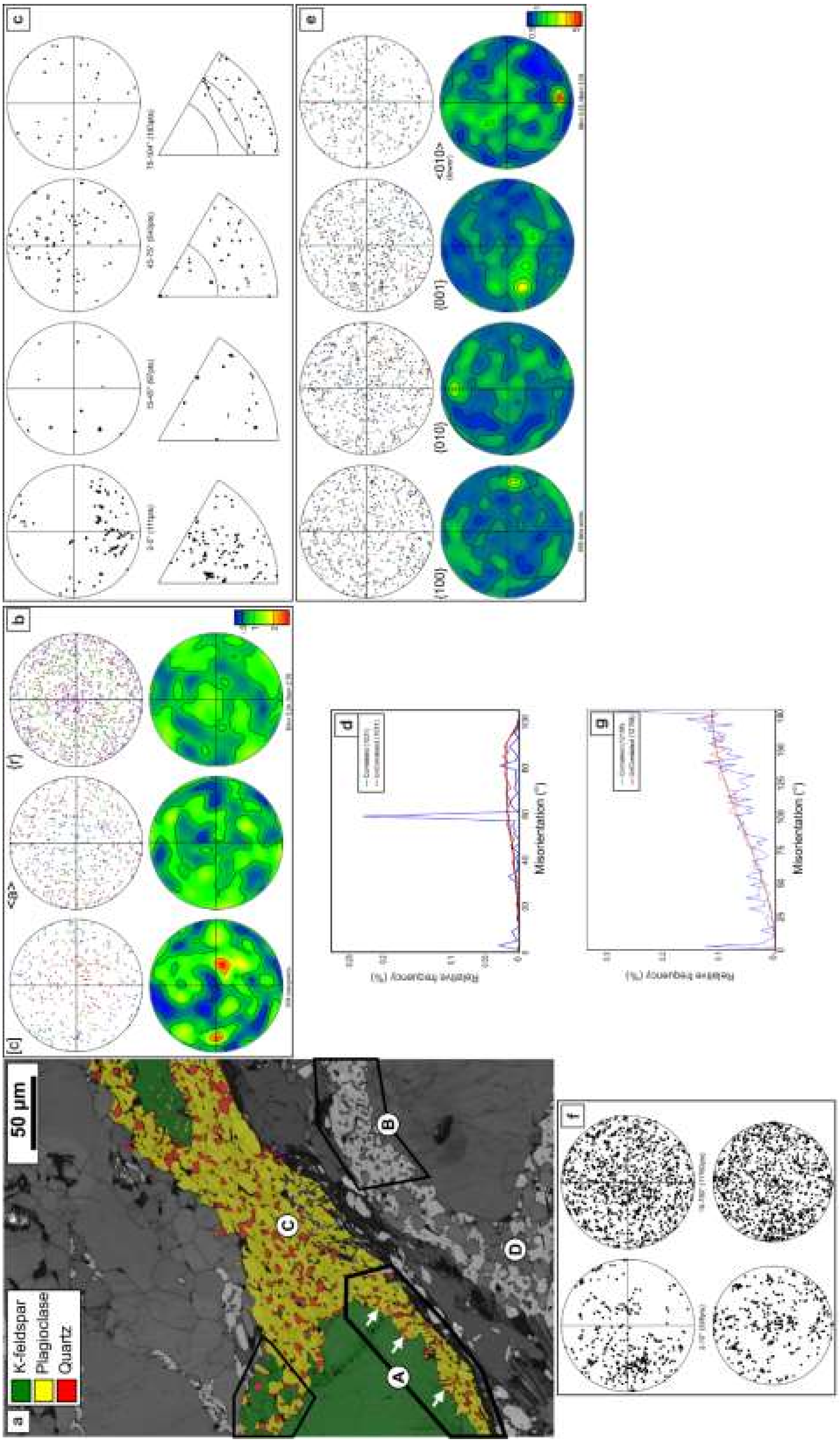
a
K-feldspar
Plagioclase
Quartz
50 µm
A
B
C
D
b
[c]
<a>
{r'}
c
d
Misorientation (°)
Relative frequency (%)
e
{100}
{010}
{001}
<010>
f
g
Misorientation (°)
Relative frequency (%)

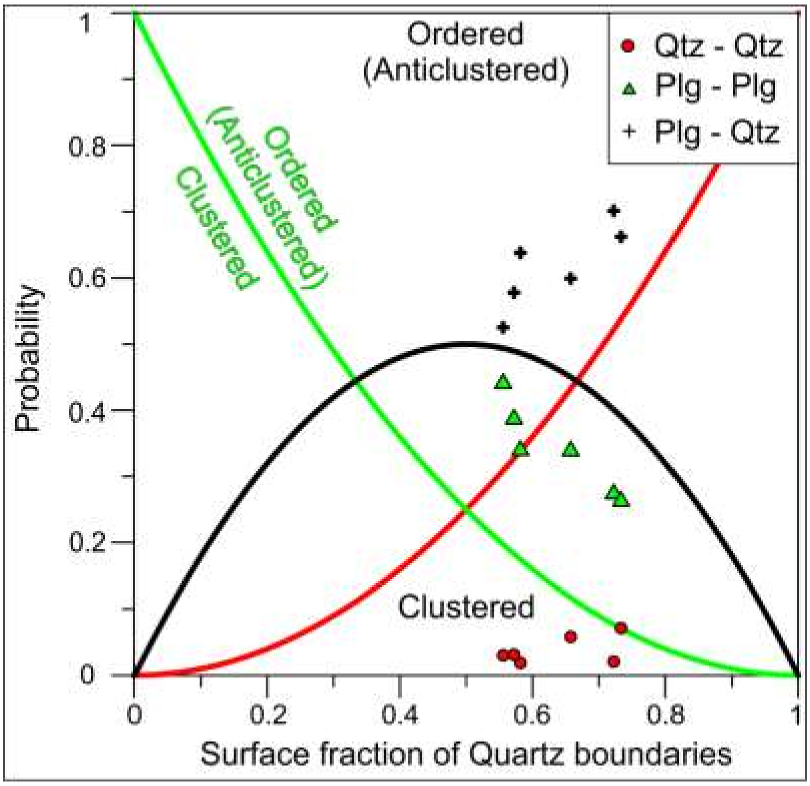

Figure 6. Phase- and grain-boundary fraction for plagioclase + quartz aggregates. Continuous curves represent the theoretical probability of phase- and grain-boundary fraction as a function of quartz content expected for a random distribution in a two-phase aggregate

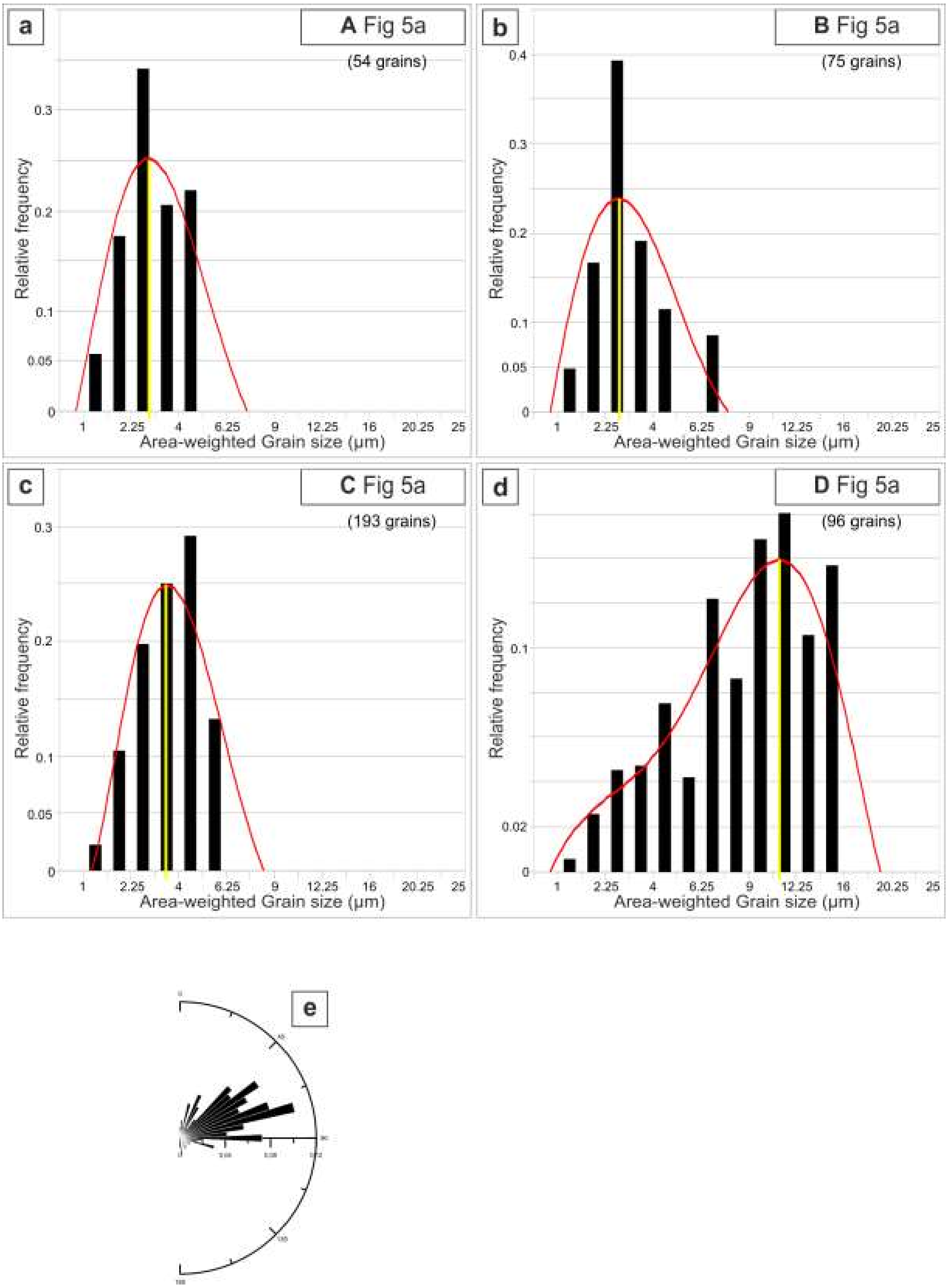

Figure 7. Area-weighted grain size distributions and SPO for quartz. **(a)** Grain size distribution for quartz in incipient myrmekite A in Fig. 5a. **(b)** Grain size distribution for quartz in incipient myrmekite B in Fig. 5a. **(c)** Grain size distribution for quartz in sheared plagioclase + quartz aggregate C in Fig. 5a. **(d)** Grain size distribution for quartz in sheared plagioclase + quartz aggregate D in Fig. 5a. **(e)** Rose diagram showing the orientation of major axis of quartz grains, defining a weak SPO.

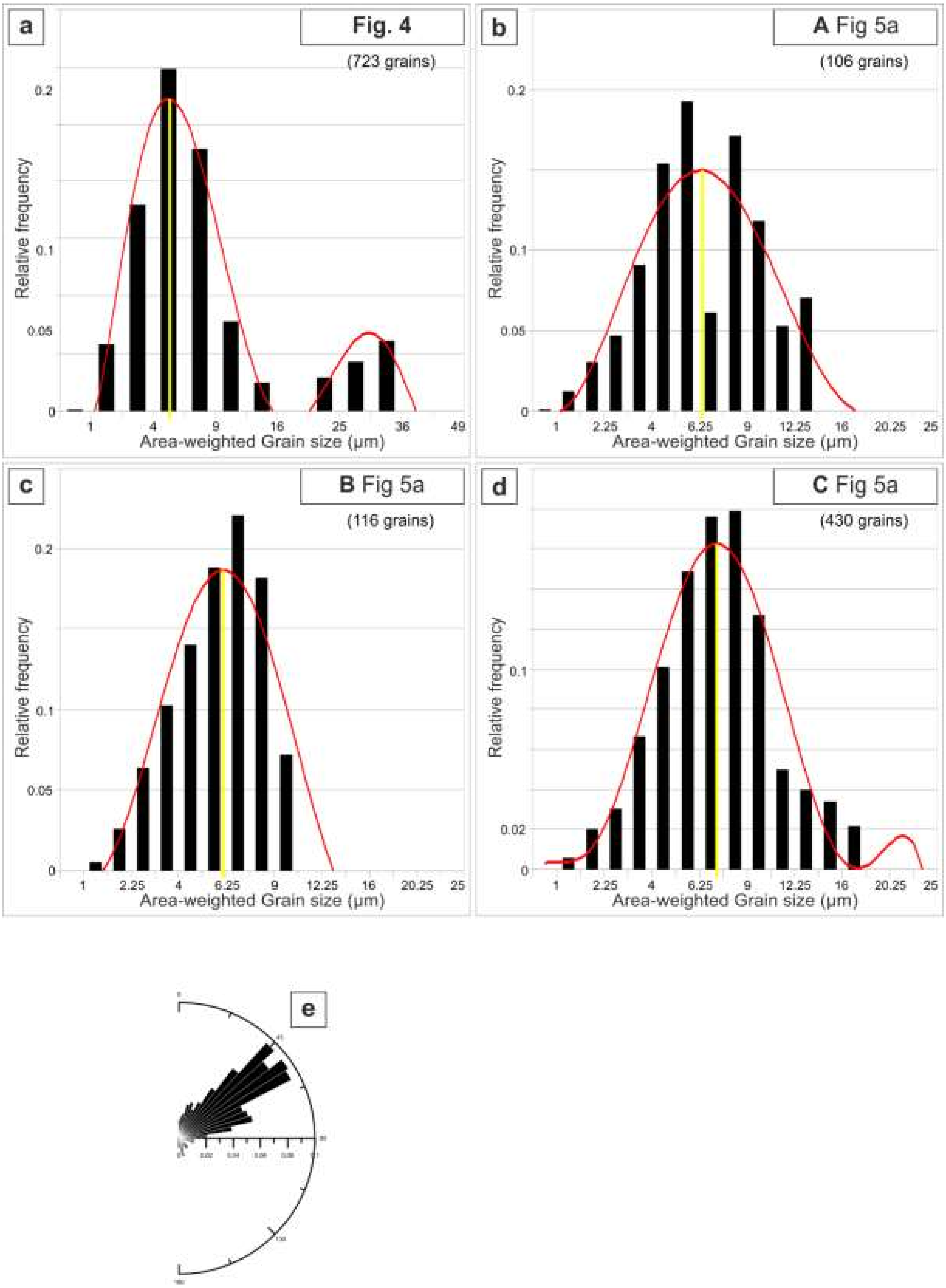

Figure 8. Area-weighted grain size distributions and SPO for plagioclase. **(a)** Grain size distribution for plagioclase in myrmekite of Fig. 4. **(b)** Grain size distribution for plagioclase in incipient myrmekite A in Fig. 5a. **(c)** Grain size distribution for plagioclase in incipient myrmekite B in Fig. 5a. **(d)** Grain size distribution for plagioclase in sheared plagioclase + quartz aggregate C in Fig. 5a. **(e)** Rose diagram showing the orientation of major axis of plagioclase grains, defining a weak SPO.

Quartz layers along foliation

Quartz layers along the foliation are mainly composed of quartz grains (Fig. 9a) showing a bimodal grain size distribution (Fig. 9b) with two maxima roughly around 35 μm and 100 μm. Quartz grains are elongated showing a well-developed shape preferred orientation (SPO), consistent with the mylonitic sense of shear. Dauphiné twin boundaries (red boundaries in Fig. 9a) are widespread but they do not show any particular geometric arrangement. Some twin boundaries are curved and irregular, amoeboid in shape.

Quartz show a c-axis CPO that define an asymmetric Type-I girdle roughly normal to the local mylonitic foliation (Fig. 9c). C-axis pole figure shows a stronger maximum close to the centre of the pole figure. No significant preferred orientations have been observed for the other crystallographic axes. Subgrains are well developed inside coarser (~100 μm) grains. Subgrain size is comparable to the size of finer (recrystallized) grains lacking subgrains.

Misorientation angle distribution (Fig. 9d) shows two peaks at very low angle misorientations (<10°) and around 60° for correlated misorientations. Un-correlated misorientation angle distribution is close to the random-pair distribution. Misorientation axis distribution for low angle misorientation (<10°) shows a wide maximum close to [c] and <π−π'> directions in crystal coordinates; instead, they are preferentially oriented slightly off-set from the Y-kinematic direction in sample coordinates (Fig. 9e). High angle misorientation axes distributions do not show any clear or systematic pattern, but the clear maximum close to c-axis direction, related to Dauphiné twinning. Local misorientation maps (Figs. SOM1a-b) show that misorientation and distortion of quartz grains are mainly organized along low/high misorientation boundaries, enclosing almost strain-free quartz subgrains/grains.

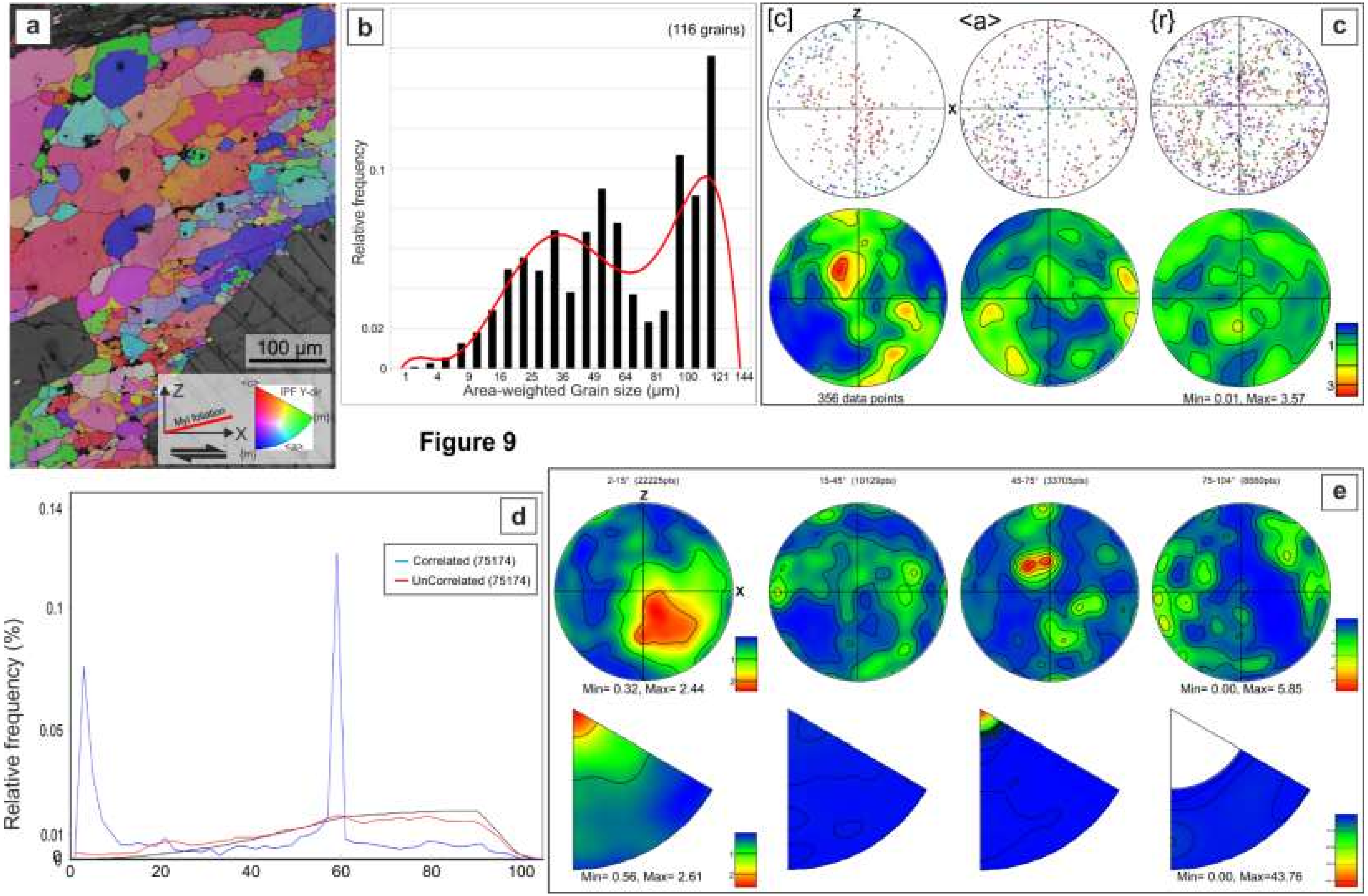
a
100 µm
Z
X
Myl foliation
IFF Y-dir
(m)
b
(116 grains)
Relative frequency
0.1
0.02
0
1
4
9
16
25
36
49
64
81
100
121
144
Area-weighted Grain size (µm)
[c]
<a>
{r}
c
z
x
356 data points
1
3
Min= 0.01, Max= 3.57
d
0.14
0.1
0.05
0.01
0
Relative frequency (%)
0
20
40
60
80
100
Correlated (75174)
UnCorrelated (75174)
e
2-15° (22225pts)
15-45° (10129pts)
45-75° (33705pts)
75-104° (8550pts)
Z
X
Min= 0.32, Max= 2.44
Min= 0.00, Max= 5.85
Min= 0.56, Max= 2.61
Min= 0.00, Max=43.76

Figure 9

Figure 9. EBSD orientation data and mapping for pure quartz layers. **(a)** Orientation map color coded according to the inverse pole figure for Y-direction reported in the lower right corner. **(b)** Area-weighted grain size distribution for pure quartz layer. **(c)** Pole figures for quartz [c], <a> and {r} crystallographic elements. **(d)** Misorientation angle distribution for quartz. **(e)** Misorientation axis distributions in sample (upper row) and crystal (lower raw) coordinate system.

Plagioclase porphyroclasts

Plagioclase porphyroclasts show very weak or absent internal distortion (no undulose extinction, polygonization or extinction domains). The dominant feature is the Albite-twins with the twinning plane coinciding with the (100) crystallographic plane of plagioclase (Fig. SOM3) that involves a rotation of 180° around <010>. Some straight (very, <5°) low angle grain boundaries are observed (both parallel and normal to the twin traces) in addition to scattered (and probably erroneous) point-like low angle boundaries. These low angle boundaries are preferentially oriented parallel to [001] crystal direction of both twins, close to X kinematic direction. Porphyroclast boundaries are irregular but sharp and they do not show any polygonization or subgrain formation.

K-feldspar porphyroclasts

K-feldspar porphyroclasts embedded and separated by plagioclase + quartz aggregates (sheared myrmekite) show slightly different crystallographic orientations. They show elongated and flattened shape parallel to the mylonitic foliation. Porphyroclasts show very low internal deformation and rare low angle grain boundaries. Misorientation angle/axis distributions show therefore scattered peaks/points different for each porphyroclast and without any clear pattern. Local misorientation maps (Figs. SOM1c-d) for K-feldspar porphyroclasts show that distortion increases toward the contact with myrmekite.

Sometimes, K-feldspar show a noisy microtexture where two individual crystal are compenetrated at small scale. This seems to follow a twinning law with twinning axis almost parallel to <001> and twinning plane parallel to {010} (possible Carlsbad-law twinning) and can explain the peculiar microstructure of some K-feldspar porphyroclasts.

K-feldspar in strain shadows

K-feldspar tails composed of single grains have been found at the tips of asymmetric σ-type porphyroclasts of both plagioclase (Figs. 5, SOM1c-d) and K-feldspar (Fig. 5) especially when these porphyroclasts are embedded in pure-quartz layers (Fig. 4a). (i) When K-feldspar tails occurs at tips of K-feldspar porphyroclasts, they show an orientation similar to the porphyroclast crystallographic orientation (Fig. 5). Misorientation axes related to subgrain/grain boundaries are preferentially oriented parallel to [001], in turn oriented at intermediate directions between Z and Y kinematic axes. Misorientation angle distribution shows mainly low-angle (<25°) misorientations (even though the number of data is very small). These grains show a heterogeneous internal distortion larger than that of the parent K-feldspar. (ii) K-feldspar grain may occur at the tip of plagioclase porphyroclasts (Figs 4 and SOM1c-d). In many cases we have observed a complete coincidence between low-Miller indices crystal planes and directions of adjacent K-feldspar and plagioclase grains (i.e. {100}, {010}, {001} and <100>, <010>, <001>).

(iii) In some cases, small K-feldspar grains form isolated aggregates in plagioclase + quartz aggregates around porphyroclasts (e.g. Fig.5). Grain size is comparable with that of the surrounding plagioclase + quartz aggregate (about 7 µm). The analysed K-feldspar aggregate shows a significant CPO for <010> and {010}. Instead, poles to {001} and {100} show a girdle distribution, almost parallel to the local mylonitic foliation, and smeared along the periphery of the pole figure, respectively. The maximum concentration of <010> crystal direction falls close to the Y-kinematic axis. In addition, nearby K-feldspar porphyroclasts show the same orientation of <010> crystal direction. Misorientation axis distributions show scattered clusters related to the few low-angle boundaries, and an uniform distribution for high-angle boundaries for feldspar. Misorientation angle distributions display scattered maxima along the profile for both uncorrelated and correlated misorientation. However, uncorrelated misorientations occurs with higher frequency than random-pair theoretical distribution for misorientation angles <60°. Local misorientation maps (Fig. SOM1c-

d) show that these grains are mainly strain-free (distortion are preferentially organized along low/high misorientation angle boundaries).

3.5. Discussion

Crystallographic relationship between K-feldspar and myrmekitic phases

Previous analyses on the crystallographic relationships between parent K-feldspar and myrmekitic plagioclase + quartz suggest that reaction products mimic the texture of neighbour phases rather than sharing crystallographic elements with the parent K-feldspar in both magmatic and metamorphic myrmekite (Hibbard, 1979; Stel and Breedveld, 1990; Abart et al., 2014). In general, growth processes, exsolution and neoblastesis should be usually controlled crystallographically due to interphase surficial energy (e.g. perthite formation in K-feldspar, Pryer and Robin, 1996): the new configuration of materials with different/similar structure tend to minimize the interfacial energy (e.g. Wirth and Voll, 1987; McNamara et al., 2012).

Results from EBSD analyses suggest a perfect overlap between primary crystallographic planes ({100},{010},{001}) of K-feldspar and plagioclase in pristine non-sheared myrmekite. Therefore, myrmekitic plagioclase seems to substitute parent K-feldspar maintaining the crystal structure (already qualitatively suggested by Hibbard, 1979, 1981; Wirth and Voll, 1987; Stel and Breedveld, 1990). A similar epitaxial relation, in turn, has been observed also when K-feldspar growth close to plagioclase porphyroclasts (e.g. Fig. SOM3). Previously identified crystallographic relationship between exsolving feldspars (perthites development along Murchison plane (601), e.g. Dowty, 1980; Lee et al., 1995) cannot be clearly discern in our case.

K-feldspar – plagioclase substitution may lead to relative epitaxial strain in both phases due to difference in crystal lattices and symmetry groups (as could be inferred from mean internal distortion of myrmekitic plagioclase grains, Fig. SOM1). However, lattice distortion in myrmekitic plagioclase can be relaxed considering the negative volume variation related to myrmekite forming reaction (Wirth and Voll, 1987).

Quartz vermicules that occurs inside the same plagioclase single grain show similar crystallographic orientations, as already reported by Abart et al. (2014) analysing magmatic myrmekite. The fabric inheritance relationships between pre-existing plagioclase (Abart et al., 2014) and quartz (Stel and Breedveld, 1990) crystals in direct contact with K-feldspar where myrmekite forms, are difficult to observe or identify in our maps. Most of the time, quartz does not show any systematic relationship with the neighbouring pre-existent quartz grains.

Deformation mechanisms during shearing of plagioclase + quartz aggregates

In the following, microstructural features are discussed and compared in order to define the dominant deformation mechanisms during shearing of plagioclase + quartz aggregates.

The development of a CPO is usually related to the occurrence of deformation mechanisms aided by dislocation creep (Schmid and Casey, 1986). Both quartz and plagioclase CPOs in sheared aggregates are very weak. In addition, the rare occurrence of low angle misorientations, the lack of a regular pattern in misorientation axis distribution and the similarities with random-pair distribution for misorientation angle show that dislocation creep processes related to the activity of slip systems and dislocations are lacking in both quartz and plagioclase (e.g. Wheeler et al., 2001). Therefore, subgrain rotation recrystallization seems to be unlikely in both plagioclase and quartz in plagioclase + quartz aggregates. However, this can be related to the mutual hindrance that each phase operates on the development of the other phase CPO (e.g. Herweg and Berger, 2004; Cross et al., 2017).

Microstructures and texture in the sheared plagioclase + quartz aggregates show that: (i) quartz and plagioclase grains are polygonal, equant to slightly elongated (AR<2); (ii) aligned grain boundaries (over several grain diameter) and triple/quadruple-junctions occur (e.g. Miranda et al. 2016); (iii) CPO for both phases are very weak or close to uniform; (iv) misorientation axis distributions almost resemble uniform distributions (Wheeler et al., 2001; Lapworth et al., 2002); (v) plagioclase and quartz show an anticlustered spatial distribution (e.g. Menegon et al., 2013); (vi) misorientation angle distribution for plagioclase show that high-angle misorientations occurs with more probability than random theoretical distribution (as in Bestmann and Prior, 2003; Miranda et al.,2016); (vii) grain sizes are very small in both in quartz and plagioclase. All these evidence suggest the occurrence of diffusion creep processes aided by grain boundary sliding (GBS) (White, 1977; Stünitz and Fitz Gerald, 1993; Jiang et al., 2000; Bestmann and Prior, 2003; Kilian et al., 2011; Menegon et al., 2013; Miranda et al., 2016). The SPO displayed by plagioclase grains inside the aggregate can further suggest the occurrence of non-rotational diffusion-assisted GBS (Tullis and Yund, 1991; Lapworth et al.,2002). The occurrence of quartz grains at triple/quadruple junctions and forming grain aggregates arranged normal to the mylonitic foliation suggest high mobility and a strong component of dissolution-precipitation mechanisms during quartz deformation (Behrmann and Mainprice, 1987).

Quartz show a clear and systematic trend in grain sizes that can be related to the microstructural site where it occurs. From un-exploited myrmekite to evolved sheared aggregates there is a net increase in grain size from 3 µm to 10 µm (compare Figs. 5a-5d). This is observed especially when quartz forms monophase aggregates, where phase pinning is avoided, and Ostwald ripening and grain growth might be favoured (Karato, 2002; Hiraga et al., 2013; Platt, 2015). Plagioclase grain size is almost constant from unexploited myrmekite to evolved sheared aggregates. However, initial coarse (>10µm) myrmekitic plagioclase grains can be dismembered during flow and shearing by rigid body rotation (that usually takes place during GBS) to reach the stable grain size of the sheared aggregate.

Spatial distribution of phases (in bimodal phase aggregate) is usually assumed to be the result of the process of formation of the aggregate (Kruse and Stünitz, 1999). Dislocation creep processes usually lead to monomineralic aggregates and do not allow the formation of poly-phase/mineralic aggregates and lead to the formation of perfectly clustered distributions (Heilbronner and Barrett, 2014). Phase mixing and polymineralic aggregates are usually promoted by diffusion-assisted creep aided by GBS: these processes usually lead to perfectly ordered (anticlustered) spatial distributions (Kilian et al., 2011; Menegon et al., 2013) that in turn inhibits grain growth and stabilizes grain size, hindering the efficiency of dynamic recrystallization processes and self-sustaining the activity of diffusion-aided GBS (e.g. Herweg and Berger, 2004; Czaplińska et al., 2015).

In our case, anticlustered phase spatial distribution is one of the microstructural evidence suggesting the occurrence of diffusion-assisted GBS. Phase spatial distribution is similar in both unexploited myrmekite and plagioclase + quartz aggregates (Fig. 8). The different surface fractions might be related either to difference in grain sizes or phase volume proportions (Kruse and Stünitz, 1999). However, if the anticlustered phase distribution is related to deformation processes in plagioclase + quartz aggregates, this is not the case in un-exploited myrmekite: phase spatial distribution in unexploited myrmekite is a microstructural characteristic inherited from heterogeneous nucleation during mineral reaction (Wirth and Voll, 1987). Therefore, myrmekite formation "pre-arrange" the anticlustered spatial distribution observed in sheared aggregates, and it promotes the activation of diffusion-assisted GBS. The occurrence of GBS alone in two-phase aggregates have been demonstrated to contribute to phase aggregation rather than phase mixing with increasing strain (Hiraga et al., 2013), explaining the formation of mono-phase quartz aggregates (e.g. Figs. 4a and 5a – zone D), in which grain growth is no more inhibited by phase pinning.

K-feldspar grain aggregates in strain shadows

K-feldspar grains have a strong CPO for <010> axes: given the lack of low misorientation angle boundaries and characteristic patterns in misorientation axis/angle distribution, this might be interpreted as a growth feature and/or an inherited CPO. The <010> axis of the nearby K-feldspar grain shows the same orientation, suggesting a possible inheritance relationship between the two. The smearing of other crystallographic axes along the pole figure periphery may be interpreted as the occurrence of rigid body rotation during shearing inside the plagioclase + quartz aggregates. A similar preferred orientation of <010> axes parallel to Y have already been observed in K-feldspar porphyroclasts in mylonites by Czaplińska et al. (2015) and have been related to dislocation creep processes ((010)[001] slip system).

Reaction softening mechanisms in Rieserferner tonalitic mylonites

In the Rieserferner pluton, strain softening is mainly obtained through metamorphic reactions likely involving (local) mass transfer. The two main mineral reactions are:

(i) myrmekite forming reaction (Becke, 1908; Simpson and Wintsch, 1989):

$$\textbf{\textit{(a)}}\ 1.25\ \mathrm{Kfs} + 0.75\ \mathrm{Na}^{+} + 0.25\ \mathrm{Ca}^{2+} = (\mathrm{Ab}_{75})\ \mathrm{Plg} + 1.25\ \mathrm{K}^{+} + \mathrm{SiO}_2$$

(ii) plagioclase + sphene + biotite/(secondary white mica) symplectite forming reaction (Johnson et al., 2008):

$$\textbf{\textit{(b)}}\ \mathrm{Bt}_{\mathrm{I}} + \mathrm{Plg}_{\mathrm{I}} = \mathrm{Sph} + \mathrm{Pl}_{\mathrm{II}} + \mathrm{Bt}_{\mathrm{II}}$$

This reaction is of secondary relevance as strain softening process compared to myrmekite formation. Symplectite formation is promoted on plagioclase – biotite phase boundaries parallel to the foliation, and therefore normal to the likely direction of principal shortening inferred from mylonite sense of shear.

Several microstructural features suggest that myrmekite forming reaction occurs during solid-state conditions: (i) myrmekite develop synkinematically around sheared K-feldspar porphyroclast; (ii) myrmekite overprint magmatic fabric; (iii) quartz vermicules spacing (~2 µm) suggests temperature of formation <580°C (Wirth and Voll, 1987; Menegon et al., 2006). Reaction ***(a)*** implies a negative volume variation of about 8-10% depending on the composition of the myrmekitic plagioclase (e.g. Wirth and Voll, 1987; Simpson and Wintsch, 1989; Hompson and Rarnseyer, 1990; Menegon et al., 2006). This volume change may have some relevant implication for the strain geometry of the shear zone (shear zone with change in volume; Ramsay, 1980) given the relative high amount of plagioclase + quartz sheared layers in the mylonite (up to 13 vol%, Fig. 3).

Reaction ***(a)*** implies also an incoming flux of fluids rich in Na and Ca toward the site of myrmekite formation. In the Rieserferner shear zones these fluids may come from the epidote vein (Ca-Al-Si bearing) on which shear zone nucleates. Fluid expulsion from “high-pressure” weaker mylonitic core (Mancktelow, 2002) related to plagioclase, K-feldspar, biotite and epidote recrystallization might enhance and trigger further metamorphic reactions in the surrounding host rock leading to the widening of the shear zone and (Means, 1995; Goncalves et al., 2016; Finch et al., 2016).

The volume percentage of quartz (18 vol%) is constant between unexploited myrmekite and sheared plagioclase + quartz aggregates (cfr. quartz amount in data plotted in Fig.6), and it is coherent with the observed composition – quartz volume amount relationship defined by previous authors (Becke, 1908; Simpson and Wintsch,1986; Abart et al.,2014). suggest that at least during pristine stages of shearing after myrmekite formation, the net mass transfer is close to zero and the deforming system behaves as a “closed system”.

The evidence for fluid-mediated local mass transfer processes and diffusion is also given by the precipitation of quartz, feldspar and biotite aggregates in sites of low stress/strains and the occurrence of “beard” structures (intrfingered growth of biotite and feldspar at the tip of plagioclase porphyroclasts, Fig. 1e; e.g. Johnson et al., 2008). K-feldspar precipitation is promoted by reaction (a) occurring in the opposite sense to myrmekite formation triggered by positive volume changes (Behrmann and Mainprice, 1987; Simpson and Wintsch, 1989). In the ultramylonite, diffusion processes are highlighted by the nucleation of K-feldspar and oriented biotite grains at dilatant sites and triple junction between quartz grains (e.g. Kilian et al., 2011) probably related also to the occurrence of grain boundary sliding and cavitation processes (Fusseis et al., 2016; Menegon et al., 2016).

Deformation mechanism in pure-quartz layers

Microstructures and strong textures of pure quartz layers suggest the occurrence of dislocation creep processes during deformation of pure quartz layers (e.g. Fliervoet et al., 1997). The occurrence of crystallographically controlled low angle misorientation axes, preferentially oriented parallel to the Y-kinematic (vorticity) axis suggest the occurrence of dislocation creep processes and in particular of subgrain rotation (SGR) recrystallization in pure quartz layers. The occurrence of misorientation axes close to [c] and [π–π'] directions almost aligned with Y-kinematic direction suggests the preferential activation of {m}<a> and {r-z}<a> slip systems (e.g. Ceccato et al., 2017).

The grain size range is similar to that expected for SGR at these conditions (Stipp et al., 2002a,b). The bimodal grain size distribution observed here is probably due to the location of the EBSD map close to a plagioclase porphyroclast that may have brought some stress concentration and grain size variation.

Strain partitioning between quartz and plagioclase + quartz layers

Mylonitic foliation in the RFP tonalitic mylonites is mainly composed of alternating pure quartz layers, plagioclase + quartz layers and recrystallized plagioclase + biotite layers. We have seen that each of these layers is characterized by a different dominant deformation mechanism. In particular we have described the occurrence of grain-size insensitive creep processes (dislocation creep) in pure quartz layers, and grain size sensitive (diffusion assisted GBS) in plagioclase + quartz aggregates. These two mechanisms have a different rheology (power-law vs. linear viscous) and therefore they might accommodate strain at different rates (e.g. Behrmann and Mainprice, 1987).

The rheology of the polyphase aggregate is controlled by the rheology of the finer-grained phase (quartz in our case, Platt, 2015). In particular, deformation might be controlled by the diffusion rates of quartz in the weaker plagioclase + quartz aggregates (similar to the model presented by Behrmann and Mainprice, 1987).

3.6. Conclusions

In the RFP Stage 3 mylonites and ultramylonites strain weakening is mainly obtained through reaction-softening processes. The dominant grain size reduction mechanisms is the development of myrmekite (plagioclase + quartz symplectites) at the expense of former magmatic K-feldspar. Myrmekite formation is triggered by crystal strain and stress concentration in K-feldspar grains. Pseudomorphic replacement relations have been inferred from the coincidence between myrmekitic plagioclase and parent K-feldspar grain crystal lattices. Shearing of myrmekite lead to development of fine grained plagioclase + quartz aggregates (7 µm and 4 µm in grain size, respectively) that show ordered (anticlustered) spatial distribution and well-defined shape preferred orientation; quartz usually occurs at triple- and quadruple-junction between plagioclase grains. Both plagioclase and quartz show weak CPOs and almost uniform misorientation angle distributions. Plagioclase + quartz microstructural features suggest that the dominant deformation mechanism is diffusion-assisted Grain Boundary Sliding. Myrmekite formation promote the activation of grain size sensitive creep processes in two ways: (i) myrmekite formation lead to a strong grain size reduction (up to 2 order of magnitude) resulting in very fine-grained aggregates where diffusion creep processes are dominant; (ii) myrmekite microstructure prearrange the aggregate to an "anticlustered" spatial distribution of phases. Strong grain size reduction and switch to dominant grain-size sensitive creep mechanisms lead to strong weakening and strain localization in plagioclase + quartz layers. Diffusion-accommodated GBS and myrmekite formation, in addition, induced phase mixing, promoting in turn the development of ultramylonites.

Acknowledgements

Raul Carampin (UniPd) and Andrea Risplendente (UniMi) are warmly thanked for the help during EMPA data acquisition and analyses. Leonardo Tauro (UniPd) is warmly thanked for its work and assistance during sample and thin section preparation and fundamental assistance during SEM analyses. LM thanks FP7 Marie Curie Career Integration Grant «Evolution of Continental Strength from Rifting to Collision - A Journey through the Wilson Cycle” PCIG13-GA-2013-618289 and the help of the Electronic Microscopy Centre staff at University of Plymouth.

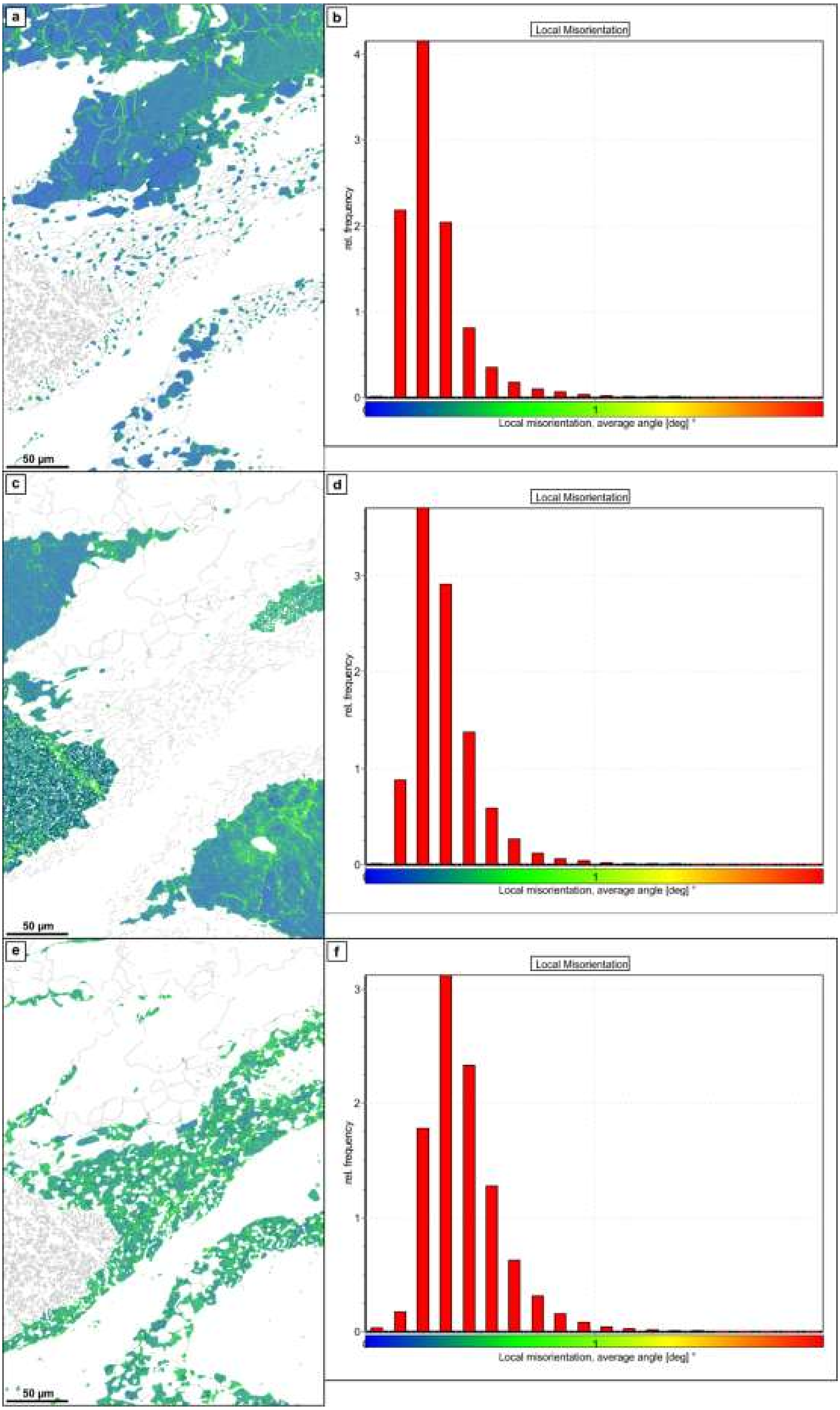
a
50 µm
b
Local Misorientation
rel. frequency
0
1
2
3
4
1
Local misorientation, average angle [deg] °
c
50 µm
d
Local Misorientation
rel. frequency
0
1
2
3
1
Local misorientation, average angle [deg] °
e
50 µm
f
Local Misorientation
rel. frequency
0
1
2
3
1
Local misorientation, average angle [deg] °

Figure SOM1

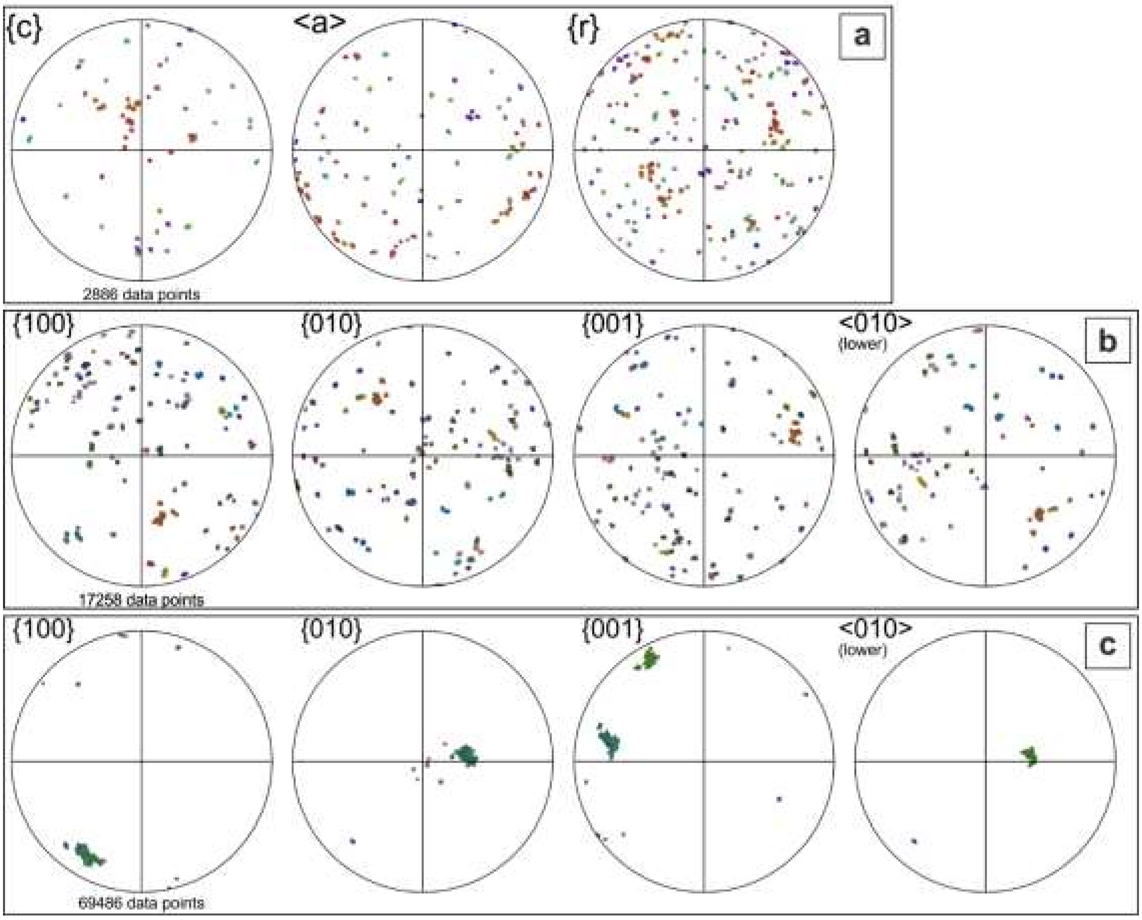

Figure SOM2. Crystallographic orientation for incipient myrmekite A of Fig. 5. **(a)** Pole figures for quartz reporting low-Miller-indices crystal elements. **(b)** Pole figures for plagioclase reporting low-Miller-indices crystal elements. **(c)** Pole figures for K-feldspar reporting low-Miller-indices crystal elements.

Figure SOM1. Local misorientation maps for EBSD map reported in Fig. 5. **(a)** Local misorientation map for quartz with grain boundaries. **(b)** Bar diagram showing the relative frequency (normalized to 100) of the average misorientation between each neighbouring pixel in quartz. **(c)** Local misorientation map for K-feldspar with grain boundaries. **(d)** Bar diagram showing the relative frequency (normalized to 100) of the average misorientation between each neighbouring pixel in K-feldspar. **(e)** Local misorientation map for plagioclase with grain boundaries. **(f)** Bar diagram showing the relative frequency (normalized to 100) of the average misorientation between each neighbouring pixel in plagioclase.

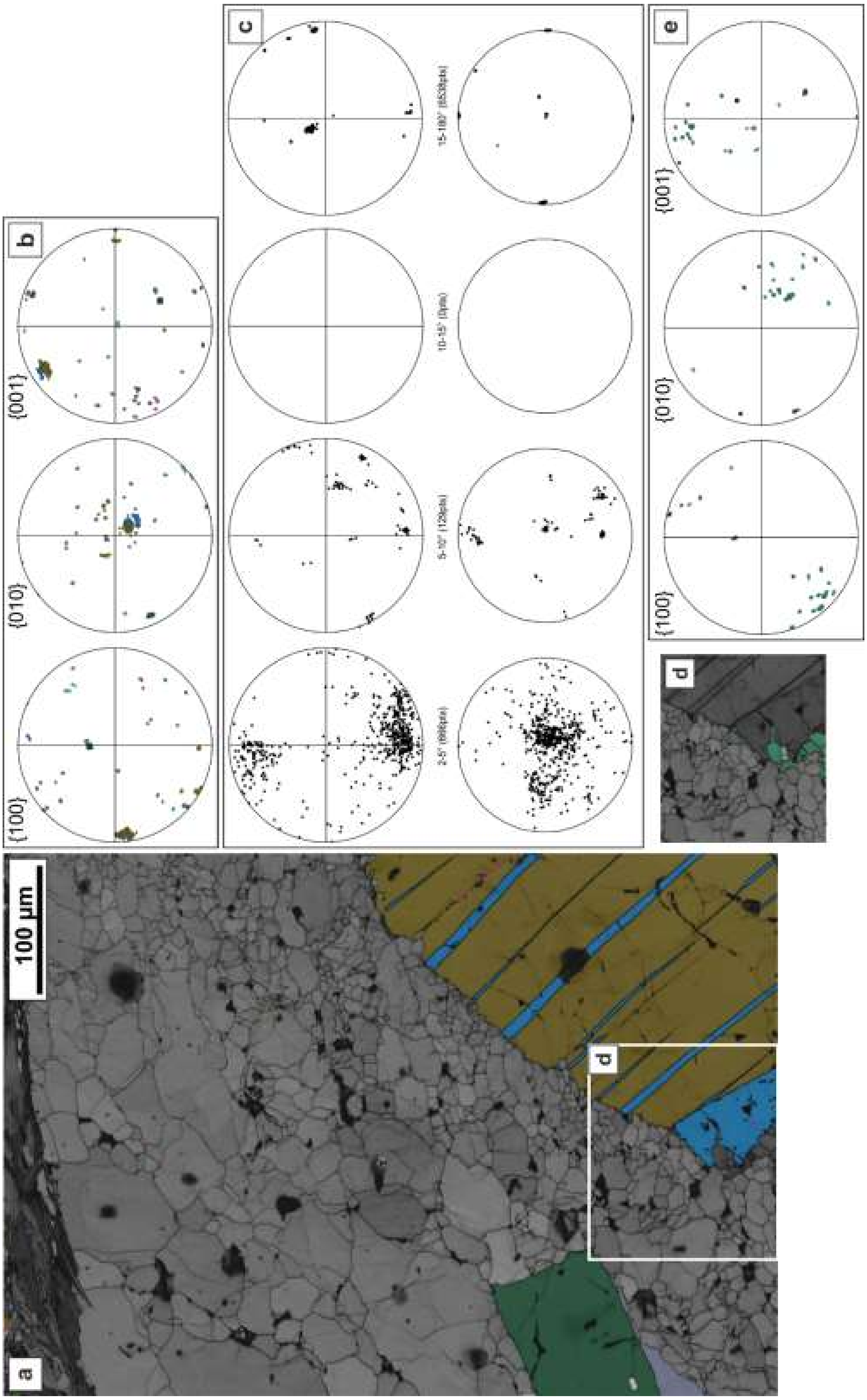

Figure SOM3. Plagioclase porphyroclast crystallographic orientation and K-feldspar. **(a)** Orientation map of plagioclase colour coded according to Euler angles colour of Channel5. **(b)** Pole figures for plagioclase reporting low-Miller-indices crystal elements. **(c)** Misorientation axis distributions for plagioclase in sample (upper row) and crystal (lower raw) coordinate system. **(d)** Orientation map of K-feldspar colour coded according to Euler angles colour of Channel5. **(e)** Pole figures for K-feldspar reporting low-Miller-indices crystal elements.

Chapter 4

Deformation conditions of localized ductile shear zones during deformation *stage 3*

Alberto Ceccato[1], Philippe Goncalves[2], Giorgio Pennacchioni[1]

[1] Department of Geosciences, University of Padova, Via Gradenigo 6, I-35131 Padova, Italy

[2] Laboratoire Chrono-environnement, CNRS e Universit_e de Bourgogne-Franche-Comt_e, 16 route de Gray, 25030 Besançon, France

Abstract

In this chapter 1 present thermodynamic modelling results that were obtained computing phase diagram sections with Perple_X (Connolly, 2005) based on new microstructural and microchemical data on the deformation Stage 3 localized tonalitic ultramylonites and mylonitic quartz veins described in previous Chapters. These ductile shear zones exploited pre-existent epidote- and quartz-rich veins. Thermodynamic modelling was aimed to define the temperature and fluid conditions under which deformation Stage 3 occurred. T-M_{H2O} and P-T pseudosections calculated for the chemical systems NaCaKFMASHO and MnNaCaKFMASHO yield the following results: (i) the epidote-veining event in the RFP likely occurred at temperatures between 520°C and 490°C at water-saturated conditions; (ii) the main deformation phase likely occurred at 460±40°C, lasting probably during pluton cooling down to 350°C at slightly under-saturated water-conditions. During this temperature evolution, pressure conditions remained fixed around 0.35±0.5 GPa. The characteristic microstructural and textural evolution of quartz veins, and the activation of weakening processes, as myrmekite shearing and the activation of grain-size sensitive creep, in the RFP likely occurred at 400-

450°C.

4.1. Introduction

Localized ductile deformation in cooling plutons occurs during a very short time span, during which the temperature conditions are suitable for the activation of crystal plastic processes. The duration of this “temperature-time window” usually depends on the pluton emplacement depth, the geothermal gradient and the temperature contrast with the country rock.

Microstructural and textural evolution of localized ductile shear zones similar to those observed in the RFP have been described also from other plutons and geological environments (e.g. Pennacchioni, 2005; Menegon et al., 2008; Pennacchioni and Zucchi, 2013).

Deriving accurate P-T conditions of deformation in granitoid rocks, under amphibolite to greenschist facies, is a challenging task, given their simple mineralogy (namely quartz, feldspars and biotite) and large number of chemical components (TiMnNaCaKFMASHO) that result in high variance assemblages with large P-T stability fields. Application of conventional geothermobarometry techniques, based on ion exchange and net-transfer reactions, is also very limited. Ductile deformation microstructures and microstructural evolution developed by dislocation creep processes are mainly temperature dependent (Hirth and Tullis, 1992), and many previous authors have tried to define the deformation conditions comparing deformation mechanisms, microstructures and crystallographic preferred orientations (CPOs) occurring in naturally deformed rocks to experimental deformation results of quartz-rich rocks (e.g. Stipp et al., 2002a; see Law, 2014 for a review). In granitoid and pure-quartz rocks deformed at middle-to-upper crustal conditions, a fundamental textural feature commonly adopted as deformation thermometer is the occurrence of Y-max c-axis quartz CPOs, usually related to Amphibolite-facies conditions (Stipp et al., 2002b; Pennacchioni et al., 2006, 2010; Menegon et al., 2008; Pennacchioni and Zucchi, 2013; Guastoni et al., 2014). An accurate estimation of temperature conditions during deformation is also fundamental for the application of rheological flow laws to natural cases, and to quantitatively describe the behaviour of rocks during deformation at natural geological conditions. As we have seen in Chapter 2, quartz microstructures and CPOs are mainly strain-dependent, rather than temperature-dependent (e.g.

Kilian et al., 2017) which therefore prevent the application of deformation mechanisms as a reliable and accurate geothermometers.

However, only in the last few years, robust petrological modelling has been applied on granitoid rocks, with the aim to define metamorphic conditions during solid-state deformation (e.g. Stipp et al., 2002b). In particular, the calculation of phase diagrams through thermodynamic modelling resulted to be a useful and accurate tool for the definition of metamorphic conditions during solid-state deformation of granitoid rocks (e.g. Oliot et al., 2010; Goncalves et al., 2012, 2016).

In this chapter, new microstructural and microchemical data from the ductile shear zones outcropping in the RFP have been used to quantify the P-T conditions of deformations. Phase diagram sections have been computed with Perple_X 6.7.5 (Connolly, 2005). The main focus of the chapter is to model part of the retrograde cooling path of the pluton and to define the exact temperature (-pressure-fluid) conditions during which crystal plastic processes described in the previous Chapters occur.

This chapter is part of a larger project of work, developed in collaboration with Prof. Philippe Goncalves (Université Franche-Comté), that aim to define metamorphic conditions during the development of ductile shear zones with similar microstructural evolution outcropping in the Adamello, Bergell, Rieserferner and Sierra Nevada (California) granitoid plutons (e.g. Pennacchioni, 2005; Pennacchioni et al., 2010; Pennacchioni and Zucchi, 2013, Ceccato et al., 2017).

4.2. Analysed shear zones

The ductile shear zones analysed here belong to the deformation Stage 3, the second stage of ductile shearing localized on joints and veins: localized shearing along shallowly E-dipping quartz- and epidote-rich veins led to progressive mylonitization and to the formation of homogeneous and heterogeneous ductile shear zones, respectively.

Two of the different compositions of ultramylonites reported in Table 1 have been selected for thermodynamic modelling: (i) thick homogeneous ultramylonite (Sample: Umyl(x)) and (ii) ultramylonitic layer including deformed epidote vein (Sample: 10.019A).

4.3 Sample preparation and methods

Selected samples of tonalitic mylonites localized along epidote-rich veins have been collected on the field. Sample were then prepared for powder analyses by crushing with WiDia (WC) mills. Bulk chemical XRF analyses were performed at the Università degli Studi di Padova with a WDS Philips PW2400 equipped with 3kW Rh X-ray tube. Fe_2O_3-FeO content have been determined through titration. Mineralogical composition and (semiquantitative) mineral proportions were obtained from XRPD analyses performed at the IGG-CNR Padova with PanAnalytical X'Pert PRO diffractometer. Microchemical analyses were performed with EMP at: (i) CNR-IGG laboratories at the Department of Geosciences in Padua, with a CAMECA SX50; (ii) Electron Microprobe Laboratory at the Università degli Studi di Milano with a Jeol 8200 Super Probe. Image analyses were performed with ImageJ software and FABRIC software suite (Heilbronner and Barrett, 2014).

Thermodynamic modelling was performed using Perple_X 6.7.5 (Connolly, 2005). In addition to pressure, temperature, and bulk composition, another fundamental parameter controlling shear zone mineralogical, chemical and microstructural evolution is the amount of fluids (water) available during deformation (e.g. Finch et al., 2016). Here, we assume that fluids consist in pure water such as the water activity is equal to 1. Before computing P-T sections, T-M_{H2O} pseudosections were computed in order to define if deformation occurred at water-saturated or undersaturated conditions. P-T pseudosections were then computed using fluid molar amounts (water) obtained from previous T-M_{H2O} pseudosections.

The thermodynamic database for pure end-members used in these models is from Holland and Powell (2011). The following solid solution models have been used: Pl(h), Kfs, Bi(W), Ep(HP11), Mica(W), Gt(W), Chl(W), Ctd(W), St(W), Opx(W). Modal amounts and iso-composition curves (isopleths) have been extracted from T-M and P-T pseudosections. Modal proportion and chemical compositions of solid solutions have been defined as follows: (i) albite component of Pl(h) model, Ab= Na/(Na+Ca); (ii) Mg# of Bi(W): Mg/(Mg+Fe^{2+}) in molar proportions; Ti, Fe^{3+} and Mn components of biotite were neglected.; (iii) epidote end-member ($Ca_2Al_2Fe^{3+}$) content of clinozoisite-epidote solid solution Ep(HP11) is calculated as XEp following the definitions of Franz and Liebscher (2004); this ratio is directly comparable to the results from thermodynamic models given in Fe^{3+} in atoms per formula unit (a.p.f.u.) (calculated over 12.5 O); (v) molar fractions of grossular, spessartine, almandine of garnet as XSps, XGr and XAlm components of Gt(W) solid solution.

The chemical system used for these model is the NaCaKFMASHO system. This system allows us to analyse the compositional variation of principal phases of our paragenesis (feldspars and biotite). Ferric iron (Fe^{3+}) has been included to consider the occurrence of epidote-clinozoisite solid solution members. Although Mn is negligible amounts and is therefore not taken into account, further modelling has seen the implementation of Mn into the chemical system (MnNaCaKFMASHO) to explore its effect of garnet stabilization (Spear, 1993). Even though Ti would have been useful for temperature estimates based on biotite chemistry and the stabilization of sphene, it was omitted from our model calculation, mostly because Ti incorporation in biotite at low-temperature (<500°C) is still poorly understood (Siron, pers. comm.)

4.4. Microstructures

Chemical and mineralogical composition of the analysed samples are reported in Tables 1 and 2. Microstructure of the ultramylonitic matrix is shown in Fig. 1. Chemical data are plotted in Figs. 2-4. Pseudosections result of thermodynamic modelling are reported in Figs 5-9.

Magmatic protolith and epidote vein (sample Host 16.078)

The magmatic assemblage of the RFP granodiorite consists of: quartz Qtz_I + plagioclase Pl_I + K-feldspar Kfs_I + biotite Bt_I + allanite/epidote + hornblende + apatite + sphene; chlorite, calcite, white mica are common alteration products. Plagioclase (Pl_I) shows a labradoritic to andesine composition (Fig. 2a) and it is usually zoned (commonly rhythmically) with a variable composition from An_{58} to An_{32} (Fig. 2b). K-feldspar (Kfs_I) has an Ab rich composition (Or_{93} – Ab_7) on average (Fig. 2a). Feldspars infilling magmatic fractures (see Chapter 1) have the same composition of magmatic feldspars (Plg2 of Fig. 1a, 2a). Biotite ($Bt_{I;}$ Mg#~0.43; $0.1<Ti$ (a.p.f.u.) <0.35) is observed either as single mm-size crystals or surrounding and embedding plagioclase glomeroclasts.

Epidote-rich veins are mainly composed by a granular aggregate of clinozoisite (XEp=0.43-0.52; Fe^{3+}=0.4-0.5 (a.p.f.u.)) + biotite + allanite (Fig. 1b). Some grains show a relevant percentage of an unidentified end-member, probably due to allanite and to the high content of REE.

Mylonitic granodiorite (sample Proto 16.078)

Shear zone developed exploiting epidote-rich veins are characterized by the development of a sigmoidal foliation in the host tonalite. Foliation development in the host granitoid is aided by: (i) recrystallization of quartz and biotite; (ii) myrmekite (plagioclase + quartz symplectite, Simpson and Wintsch, 1989) formation at the expense of K-feldspar; e.g. Fig. 1a Chapter 3; Menegon et al., 2006) and (iii) syn-kynematic symplectite formation between biotite and plagioclase (plagioclase + sphene + secondary muscovite; e.g. Fig. 1b Chapter 3; Pennacchioni et al., 2006; Johnson et al., 2008). Foliation is therefore defined by the alternation of: (i) pure quartz layers derived from the recrystallization and stretching of former magmatic quartz; (ii) plagioclase ($An_{26}Ab_{74}Or_{<1}$) + quartz + K-feldspar layers derived from the shearing of myrmekite; (iii) sphene + plagioclase ($An_{29}Ab_{71}Or_{<1}$) + recrystallized biotite (0.42<Mg#<0.49; 0.02<Ti (a.p.f.u.)<0.17) layers.

With increasing shearing, K-feldspar (Kfs_I) progressively disappears; newly formed Kfs_{II} (Or_{96}) is found in strain shadows and bridging between plagioclase porphyroclasts (e.g. Fig. 2a, Chapter 3). White mica commonly occurs close to plagioclase + sphene symplectites and along the boundaries of biotite-fish grains.

Ultramylonite (samples Umyl(x), 10.019A, Umyl 16.078)

Ultramylonites are characterized by a fine-grained (about 30 µm) homogeneous matrix, whose mineral paragenesis consists of: quartz Qtz_{II} + plagioclase Pl_{II} ($An_{24}Ab_{76}Or_{<1}$) + biotite Bt_{II} (0.105<Ti (a.p.f.u.) <0.177; 0.42<Mg#<0.50) + epidote Ep_{II} (XEp=0.39-0.56; Fe^{3+}=0.4-0.55 (a.p.f.u.); Fig. 3a) + K-feldspar Kfs_{II} ($Or_{96}Ab_4$) + Sphene Sph + Apatite Ap (Figs. 1c-1f). Recrystallized plagioclase does not show any particular texture (zoning or growth rim of different composition), i.e. no albite (XAb>90) neocrystallization have been observed. The matrix envelops several rounded plagioclase and K-feldspar porphyroclasts that survive up to very high strains (γ>10). K-feldspar is usually observed in strain shadows and in dilatant triple junction in quartz layers along with oriented biotite lamellae (e.g. Kilian et al., 2011) (Fig. 1e, Figs. 2a-d Chapter 3).

Epidote occurs in coarse grains (>40 µm) with either straight boundaries probably mimicking crystal facets, or irregular convoluted boundaries showing mineral inclusions (Figs. 1a-1f). Sometimes, epidote show some pinning and windowing microstructures when in contact with the biotite of the mylonitic foliation. No significant zoning or growth texture have been identified.

In some cases, white mica (Si~6.4 a.p.f.u.; Mg#=0.56; Fig. 3b) is observed in significant amounts in the ultramylonitic matrix (pseudomorphing biotite lamellae; Figs. 1d-1f).

Garnet (Alm_{35-48} Grs_{23-40} Sps_{20-27} Pyr_{0-4}; Fig. 3c) is sometimes observed in the ultramylonitic matrix as small (40-100 µm) euhedral zoned crystals (Figs. 1d-1f, 3d, 4a-d). Zoning trend is characterized by a general increase in Ca and Mn content from garnet core to rim at the expense of Fe content (Figs. 3c-d, 4d). Garnet rims have common compositions (Alm_{35-36} Grs_{35-37} Sps_{24-27} Pyr_{1-2}, Fig. 3c).

The former epidote-rich vein is still observed along the ultramylonitic layer, in the form of large boudins and foliated lenses with S-C' fabric.

The stable ultramylonitic paragenesis includes at least: $Qtz_{II} + Pl_{II} + Kfs_{II} + Bt_{II}$. The main differences between analysed samples is the occurrence of epidote, white mica and garnet. In sample Umyl(x), garnet and white mica have not been observed, whereas epidote occur as small, rare and scattered angular fragments (Figs. 1c-1e). In sample 10.019A, epidote, garnet and white mica are omnipresent (Figs. 1d-1f).

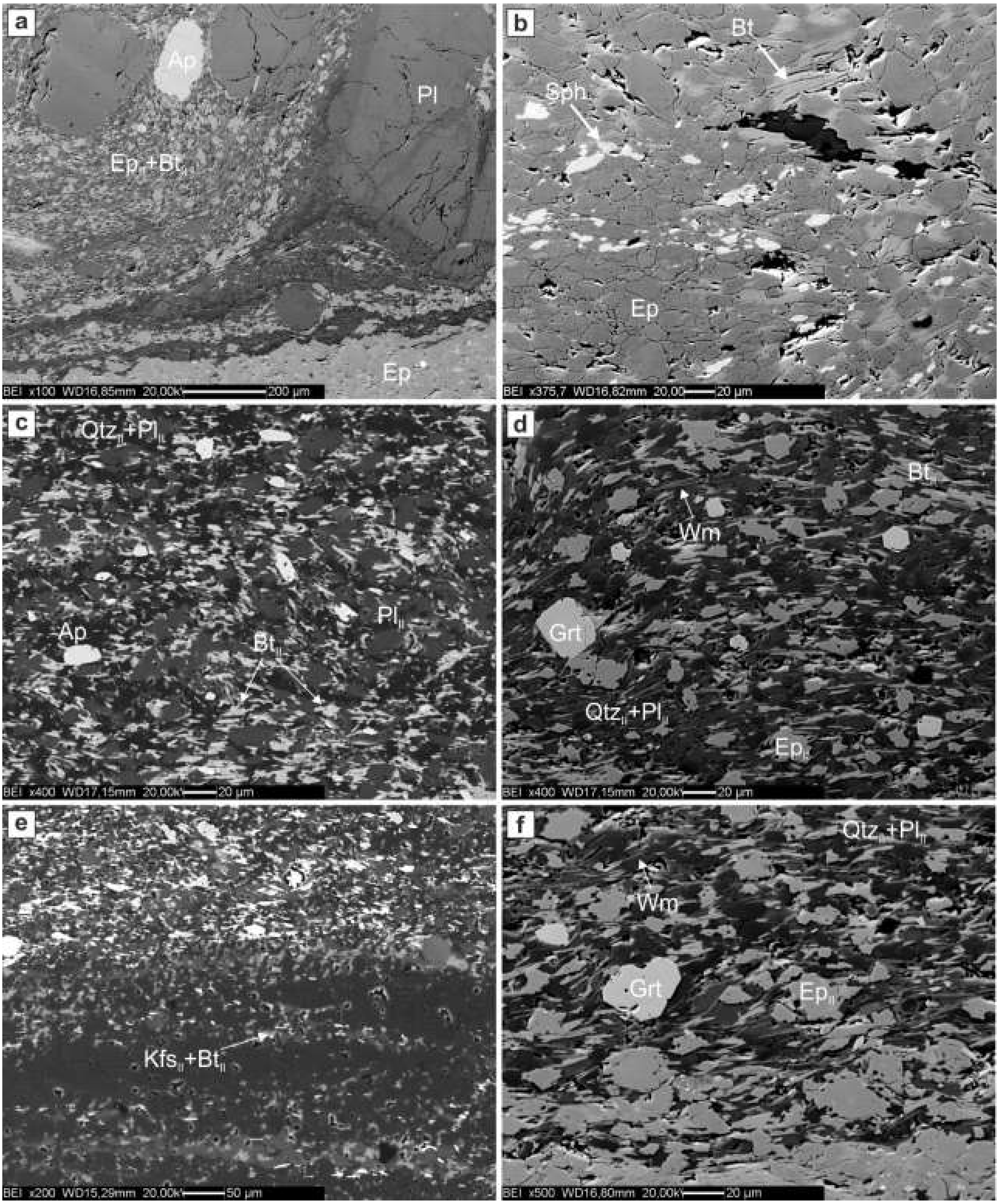

Figure 1. Microstructures of tonalite mylonites and ultramylonites. (a) Fine-grained ultramylonitic matrix and sheared epidote vein (bottom), hosting several feldspar and apatite porphyroclasts. (b) Microstructure of the granular aggregate forming the (sheared) epidote vein. (c) Homogeneous ultramylonitic matrix including recrystallized Qtz + Pl_{II} + Bt +Kfs and Ap (sample Umyl(x)). (d) Ultramylonitic matrix of sample 10.019A showing the occurrence of euhedral post-kinematic garnets and white mica pseudomorphing biotite. (e) Quartz layers alternating with ultramylonitic matrix in sample Umyl(x). Note the nucleation of K-feldspar and oriented biotite grains at dilatant triple junction between quartz grains. (f) Microstructures of (recrystallized?) epidote in the ultramylonitic matrix (sample 10.019A). Note the different grain shapes and grain boundary morphology of epidote: (i) coarser grains usually show anhedral, subrounded shapes with lobate boundaries ; (ii) smaller grains show straight grain boundaries (resembling crystal facets) or parallel to the mylonitic foliation (limited by biotite grains).

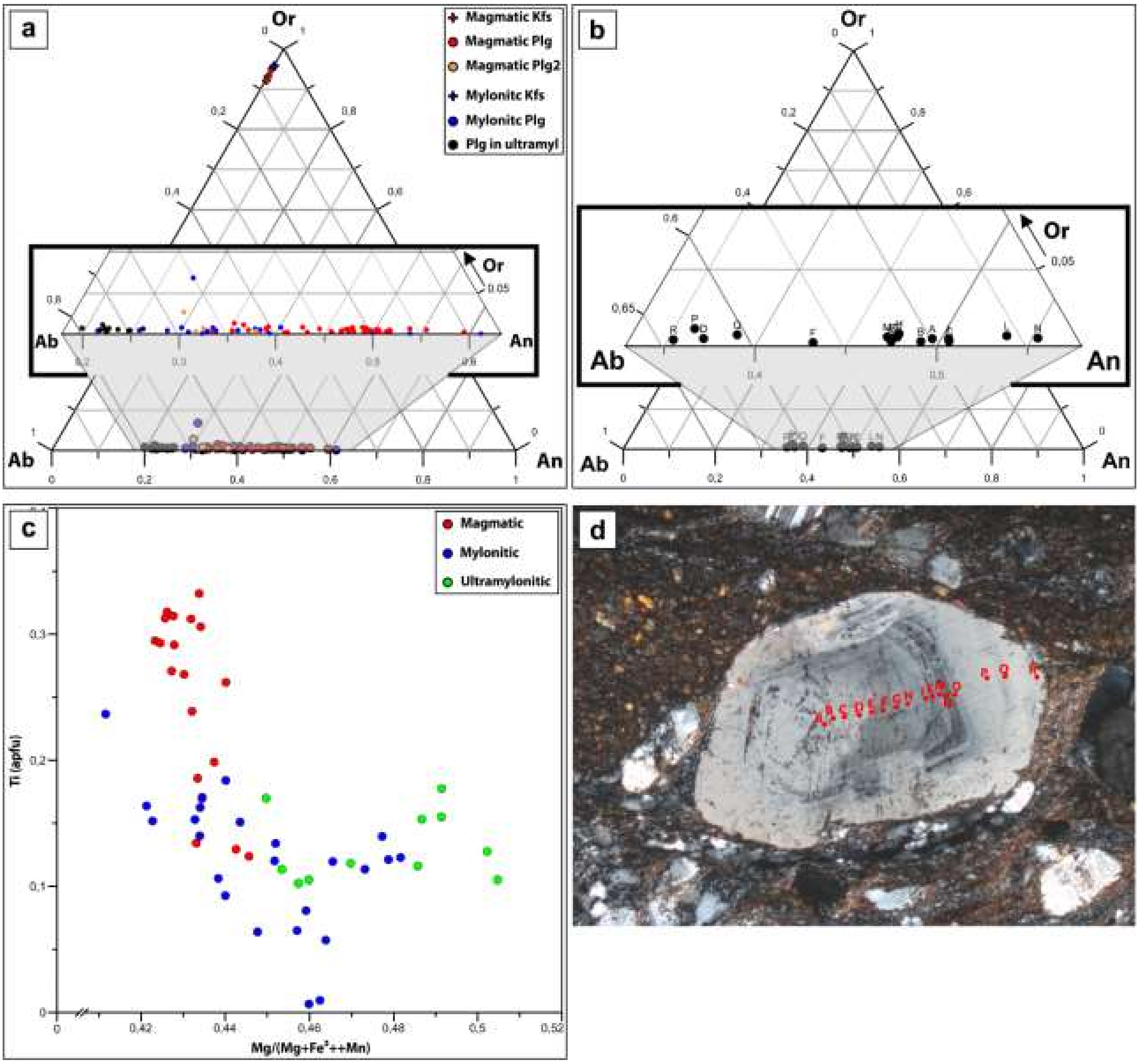

Figure 2. Chemical composition diagrams for feldspars and biotite. (a) Ternary diagram showing compositional range of magmatic and mylonitic feldspars. Note the enrichment in XAb from magmatic to mylonitic feldspars. (b) Ternary diagram showing the compositional variation in zoned magmatic plagioclase of (d). (c) Ti vs Mg# variation diagram showing the compositional differences between magmatic and mylonitic biotite. (d) Optical micrograph of the analysed zoned plagioclase.

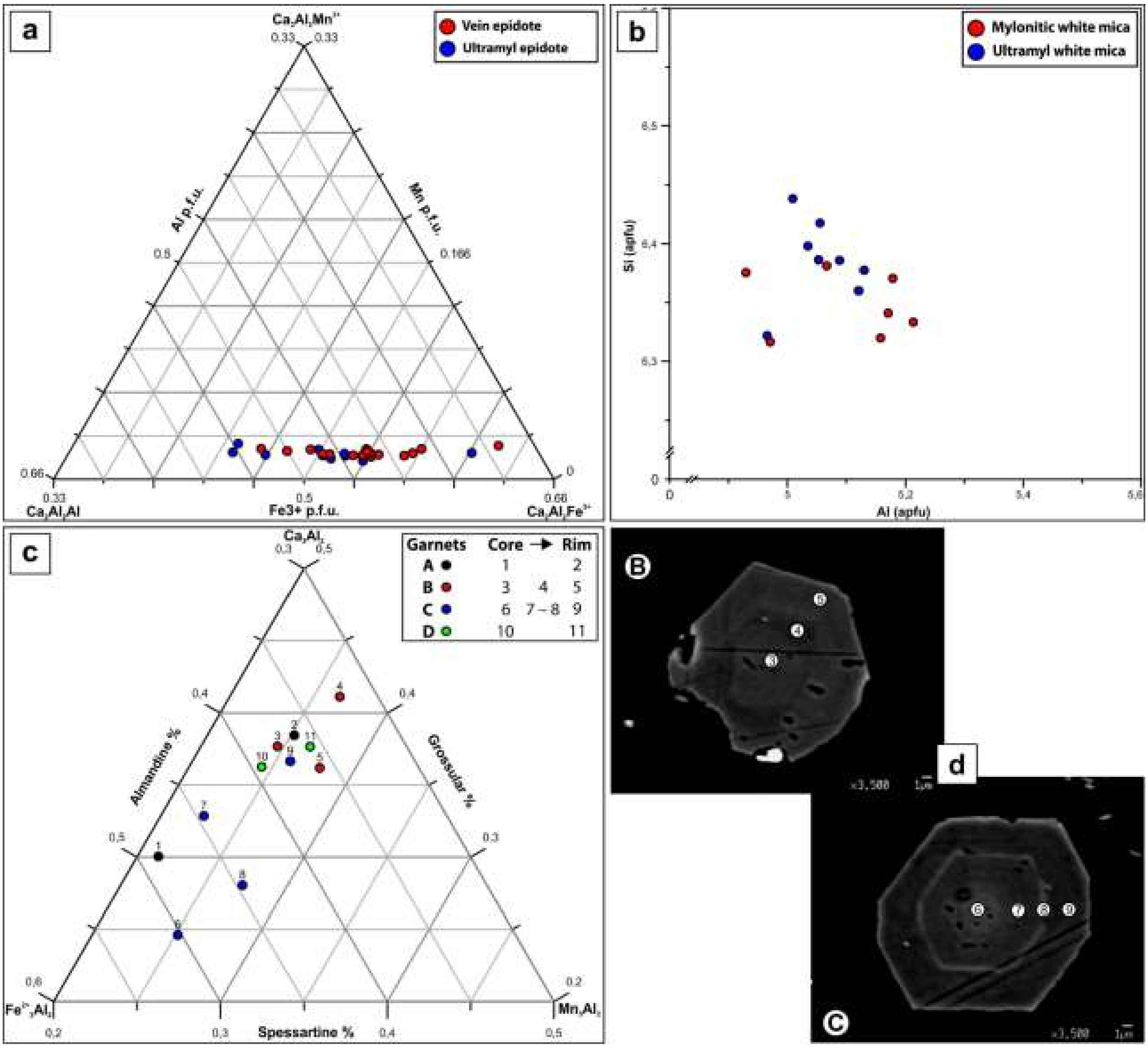

Figure 3. Chemical compositional diagrams for epidote, white mica and garnet. (a) Ternary diagram for epidote composition. The epidote series end-members are: Clinozoisite Ca_2Al_3; Epidote $Ca_2Al_2Fe^{3+}$; Piemontite $Ca_2Al_2Mn^{3+}$. Vein crystals are on average slightly richer in Epidote component with respect to ultramylonitic epidote. (b) Si vs Al variation diagram for white mica. Ultramylonitic white mica show. (c) Ternary diagram for garnet composition in which the relative proportion between almandine, grossular and spessartine end-members are plotted. Each analysed garnet is represented by a different colour and capital letter. Note the common composition of garnet rims. (d) SEM-BSE images of analysed garnets B and C, showing the compositional zoning and position of point analyses reported in (c).

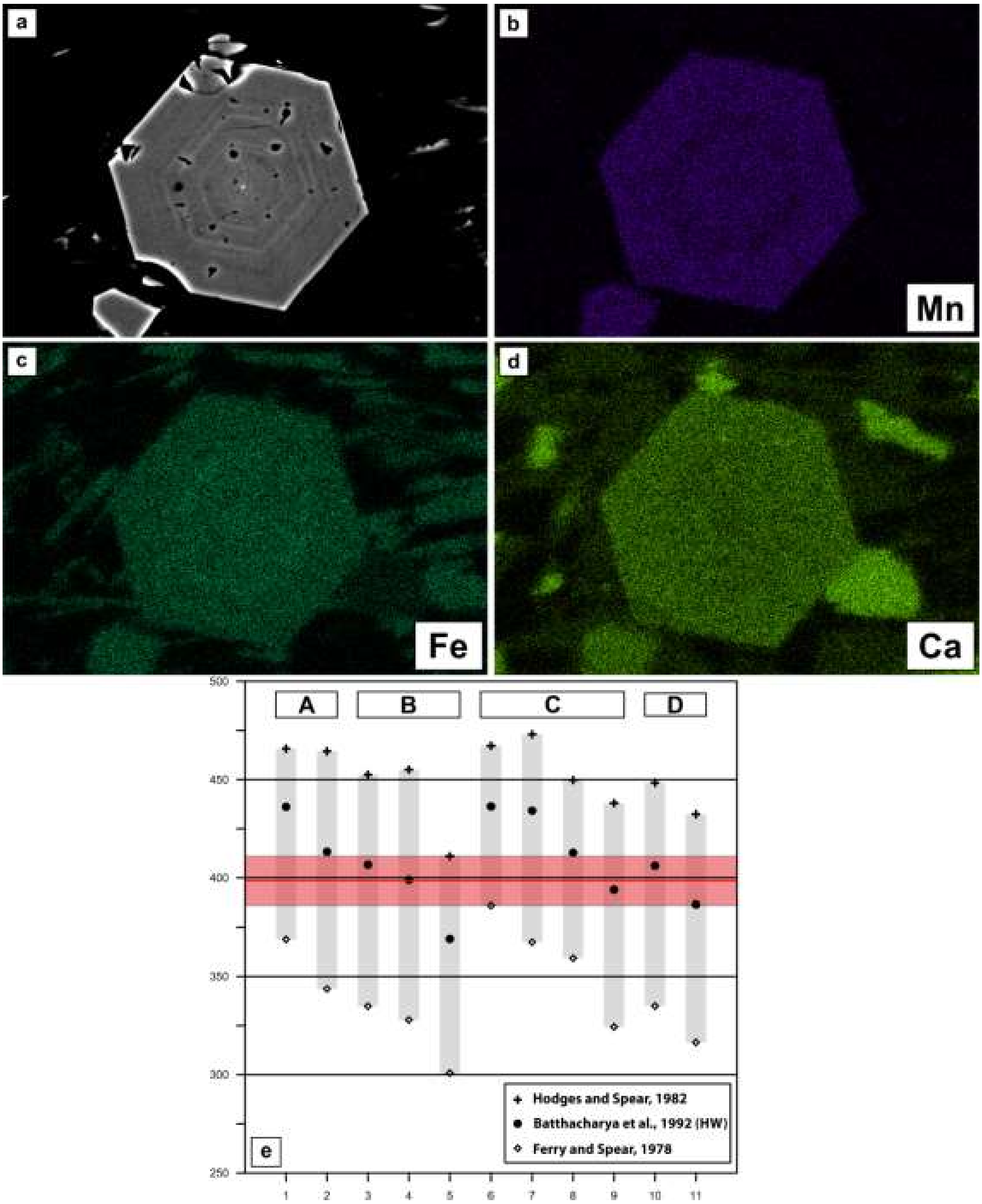

Figure 4. BSE-EDS compositional maps of zoned garnets and relative geothermometric data from garnet-biotite geothermometer. (a) SEM-BSE image showing the thin rhythmical compositional zoning of a selected garnet. (b-d) EDS intensity mapping for selected elements: (b) Mn; (c) Fe; (d) Ca. Note the slightly enrichment in Ca toward garnet rims. (e) Diagram reporting the results from garnet-biotite geothermometry. Grey boxes represent the temperature range including results from different geothermometer calibration. Point result for thermometer calibration giving maximum, mean and minimum results are reported. Capital letters indicate the analysed garnet; numbers indicate the sequence of point analyses. Number and letters are the same of Fig. 3c-d. Red box indicates the range of common temperatures between different samples. Note the common decreasing temperature trend described in each garnet

.

4.5 Qualitative inferences on temperature and pressure conditions

Deformation temperature can be qualitatively inferred from field and microstructural constraints. The development of mylonitic quartz and epidote vein during deformation Stage 3 follows deformation Stage 2 structures, probably developed at submagmatic stage (T>600°C), and predate the occurrence of Stage 4 brittle-ductile faults (developed around 300°C). The occurrence of oligoclase (XAn>0.20) as stable plagioclase composition and the lack of albite during mylonitic recrystallization suggests the development at temperatures around 450-500°C (above the peristerite miscibility gap; e.g. Maruyama et al., 1982). The stability of biotite during recrystallization and the lack of retrograde phases, such as chlorite, are other evidence for mid- to high-temperature conditions during deformation. Syn-kinematic myrmekite development suggest temperatures >500°C (e.g. Menegon et al., 2006, and reference therein). The occurrence of syn- to post-kinematic plagioclase + sphene symplectites suggests temperatures close to 475 ± 50°C (Johnson et al., 2008). All these qualitative constraints limit the temperature window of formation to 550 to 350°C (lower Amphibolite to upper Greenschists facies).

For T-M pseudosections, pressure heve been kept fixed to 0.3 GPa: This is a reliable minimum value for pressure conditions during deformation, assuming that after pluton emplacement at 0.41 GPa (15km, Tajčmanová et al., 2009; Cesare et al., 2010) exhumation was limited to less than 4 km (as inferred from very low ~1 mm* year^{-1}exhumation rates defined by Steenken et al., 2002 for the RFP region).

4.6 Results from garnet-biotite geothermometry

Garnet-biotite geothermometer based on Fe-Mg ion exchange has been applied to our ultramylonites. All the composition of the zoned garnets have been compared to the average biotite composition in the ultramylonite. Geothermometric calculations have been performed with the aid of an Excel spreadsheet made available by Dave Water on his webpage (grt-bt.xls; https://www.earth.ox.ac.uk/~davewa/pt/th_tools.html). This spreadsheet allows to compare the results of different calibration for the garnet-biotite geothermometer (references can be found in the above-mentioned webpage). Results are shown in Fig. 4e. Two are the main interesting results for our purpose: (i) resulting temperatures are invariably included between 473 and 300 °C at a reference pressure of 0.3 GPa; (ii) the overlap between temperature ranges of the different samples occurs at 398 ± 15°C; (iii) garnet zoning qualitatively reflect garnet growth at decreasing temperatures.

4.7 Results of thermodynamic modelling for NaCaKFMASH systems

Samples Umyl(x) and 10.019A best represent the average chemical and mineralogical compositions observed for the RFP Stage 3 ductile shear zones. Even though the compositions of 16.078 sample set are quite similar to the other, the occurrence of huge amount of white mica (see Table 1), probably related to the following deformation Stage 4 (see Chapter 2), dissuaded us to use those composition for thermodynamic modelling.

Metamorphic reactions (or phase assemblage boundaries) that lead to the disappearance/stabilization of a mineral phase (e.g. plagioclase-out, biotite-in reaction) during pluton cooling (retrograde) path are labelled with small boxes reporting the caption (phase-name)-out/-in.

Pseudosections and results from thermodynamics modelling are reported in Figs. 5-8. In general, both T-M and P-T pseudosections show multivariant fields (variance V from 2 to 6) characterized by slightly different mineral monotonous paragenesis, among which is difficult to choose which one really represents the observed ultramylonitic paragenesis. Therefore, mineral chemistry (isopleths) and modal amounts of different index phases (biotite, plagioclase, epidote, garnet) have been adopted to better constrain water molar amounts and pressure-temperature conditions of deformation. In addition, for the interpretation of pseudosections of sample 10.019A (Figs. 5C-d, 6c-d, 7d,e,f, 8d,e,f), we have to consider that, above the temperature of epidote stability, i.e. before the formation of the epidote vein, the composition of this system does not make any sense from the geological point of view in the Rieserferner pluton system.

T-M_{H2O} pseudosections

The main feature of T-M pseudosections is the presence of the H_2O saturation curve (blue solid line in Figs. 5a-c,7a-d, 8a-d) that separate water-undersaturated (low-temperature, low M_{H2O})from water-saturated (high-temperature, high M_{H2O}) domains where the H_2O component is expressed as a free H_2O-rich phase. The saturation curve describes an inversely proportional relationship between temperature and the molar amount of water required to saturate the assemblage. Above the H_2O-

saturation line, mineral assemblages and phase boundaries are only temperature-dependent. In contrast, in the undersaturated domains, mineral assemblages (chemistry and modes) are strongly dependent on whether water content or temperature. The occurrence of many multivariant fields in the undersaturated-domain shows the high sensitiveness of mineral parageneses to the amount of water.

In both analysed samples, in the NaCaKFMASHO system, the high-temperature and water-saturated assemblage consists in the usual magmatic assemblage Bt + Pl + Kfs + Q ± Grt depending on the bulk composition. With decreasing temperature, under water-saturated conditions, the main change in mineralogy correspond to the appearance of chlorite, epidote/zoisite, albite ± white mica coupled with the breakdown of Kfs, Bt and Pl. These changes in mineralogy lead to the formation at low temperature (< 400°C) of mineral assemblages typical of the Greenschist facies (Chl + Ep + Zo + Ab). The temperature of the in- and out-reaction is very sensitive to the bulk rock composition (Fig. 5). Under greenschist facies conditions (T ~ 350-400°C), in the simplified NaCaKFMASHO system, water undersaturation has a major influence on phase relations. A subtle undersaturation induces the appearance of plagioclase and biotite. With increasing loss of water, chlorite breaks down to produce garnet and finally epidote disappears. The resulting greenschist assemblage would consist of Grt + Pl + Ab + Bt + Q ± Ep.

Sample Umyl(x)

Biotite and plagioclase compositions were used to better constrain the fluid conditions during deformation: (i) biotite Mg# varies between 0.24 to 0.56 below the saturation line; (ii) Albite content of plagioclase increases with decreasing temperature up to 65% at 430°C. Biotite and plagioclase are no more stable at T<420°C and water content M>0.074-0.092 (Fig. 5a). Chlorite and epidote are stable below T=500°C and T=450°C (Fig. 5a), respectively; their modal amount increases with increasing water content up to 10%. The molar amount of H_2O of 0.036 mol quantified in the L.O.I. of XRF analyses is a reliable value that we have used for further P-T pseudosection modelling, given that (Fig. 5b): (i) compositional fields of biotite Mg# and albite content of plagioclase overlap in a small field between 0.025 and 0.038 mol at T close to 420°C; (ii) Opx (unlikely phase) does not occur (M>0.033 mol); (iii) the occurrence of Chl is limited to a few percentages (<2%; below the analytical error of XRPD or image analysis quantifications; M<0.039 mol); (iv) Zoisite does not occur; (v) the composition of epidote contains a significant amount of Ep (up to Fe^{3+}=0.5 a.p.f.u.), not so far from the observed composition. To conclude, the selected amount of water for the P-T pseudosection (M=0.036 mol) corresponds to water under-saturated conditions under upper greenschist facies conditions.

Sample 10.019A

Preliminary results have shown the stability of monoclinic pyroxenes and amphibole over the whole range of conditions. Given the unlikely occurrence of these phases in our system, for further modelling Cpx (Clino-pyroxene) and Camph (Clino-Amphibole) have been excluded. T-M pseudosection for sample 10.019A is characterized by (Fig. 5c): (i) epidote stability below 527°C with a composition comparable to that measured; (ii) biotite Mg# varies between 0.75 and 0.3 below the saturation line; (iii) plagioclase display compositions richer in Ab than previous models (XAb=0.67) that are displayed close to 440°C and higher pressure; (iv) plagioclase and biotite are no more stable below 440°C and M>0.1 mol; (v) chlorite is stable above M>0.074 mol and below 440°C. For a molar amount of H_2O of 0.074 mol (similar to that obtained from L.O.I., 0.083 mol), we can see that (Fig. 5d): (i) the compositions of vein epidote (Fe^{3+}=0.40-0.55 a.p.f.u.), biotite Mg# (0.48-0.42) and plagioclase overlap in a region with large variability of water content but limited temperature. However, molar amounts of H_2O above the saturation line would lead with decreasing temperature to the development of large amounts of chlorite and to the destabilization of plagioclase and biotite. Therefore, water molar amounts lower than the maximum value at water undersaturated conditions are preferred. (ii) Chlorite occurs in limited amounts (<3wt%) (M<0.088 mol).

The intersection between biotite, plagioclase and epidote isopleths and the lack/occurrence of index phases suggest that deformation occurred at conditions near to water saturation, but still undersaturated, in both samples. Important to note is the sensitiveness of epidote stability and biotite composition (Mg#) to the amount of water in the system.

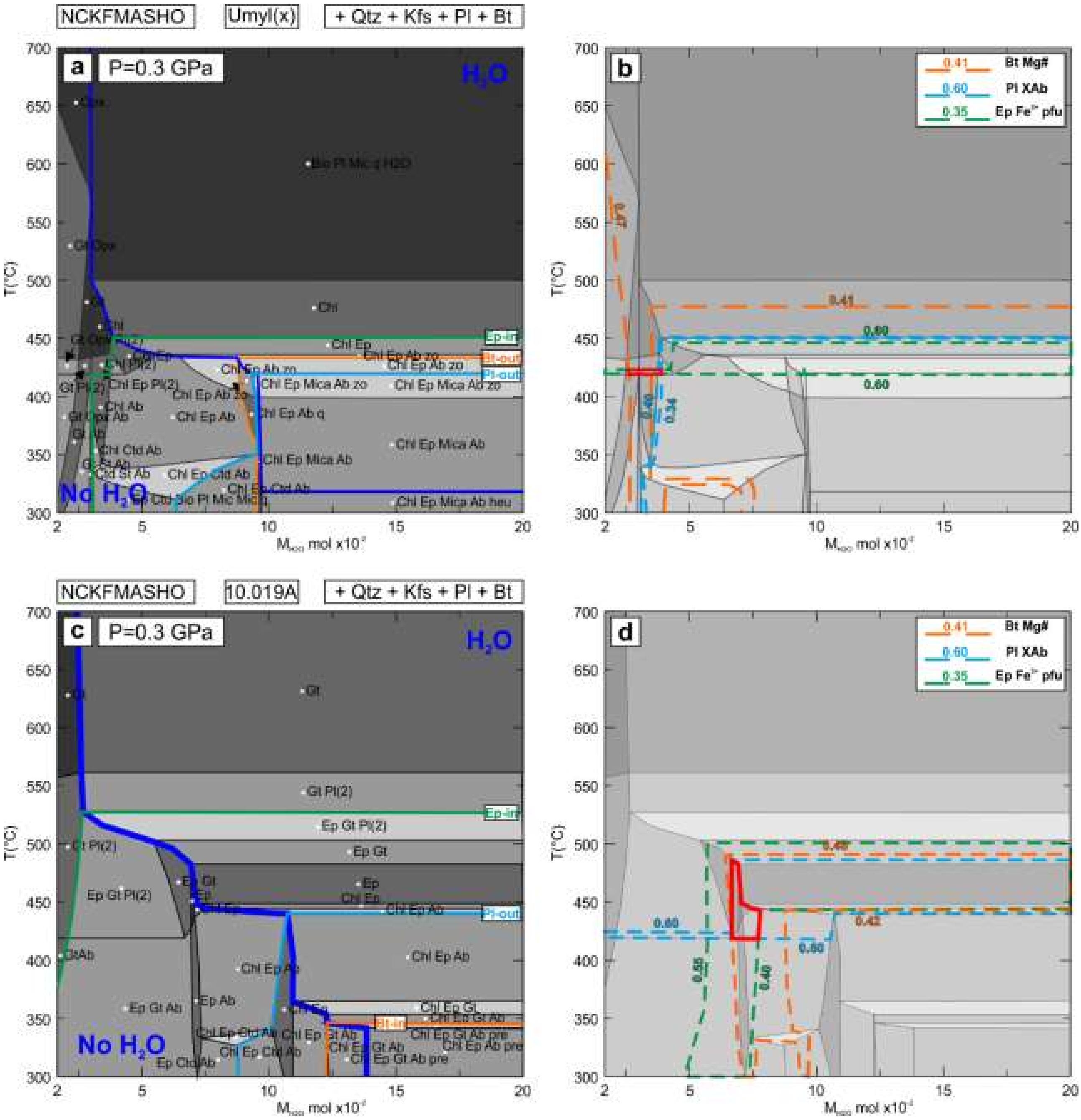

Figure 5. T-M_{H2O} pseudosections for NaCaKFMASHO system for samples Umyl(x) and 10.019A. (a) T-M_{H2O} pseudosection calculated at 0.3 GPa for sample Umyl(x). Water saturation curve is shown as thick blue line. Epidote-, plagioclase- and biotite-in reaction are reported. (b) T-M_{H2O} pseudosection calculated at 0.3 GPa for sample Umyl(x). Compositional ranges for biotite, plagioclase and epidote are reported in dashed lines (orange, blue and green, respectively). Thick bold red line indicates the intersection field between compositional ranges of different phases (see text for explanation). (c) T-M_{H2O} pseudosection calculated at 0.3 GPa for sample 10.019A. Water saturation curve is shown as thick blue line. Epidote-, plagioclase- and biotite-in reaction are reported. (d) T-M_{H2O} pseudosection calculated at 0.3 GPa for sample 10.019A. Compositional ranges for biotite, plagioclase and epidote are reported in dashed lines (orange, blue and green, respectively). Thick bold red line indicates the intersection field between compositional ranges of different phases (see text for explanation).

P-T pseudosection

P-T pseudosections are characterized by mainly temperature-dependent multivariance fields. The high temperature side is characterized by the occurrence of a free-fluid phase, as it could be expected in the former magmatic assemblage. With decreasing temperature, chlorite, albite and epidote are produced. Negligible amounts of staurolite, chloritoid and kyanite occur at T<350°C and P>0.3 GPa.

Sample Umyl(x) at 0.036 mol H_2O

P-T pseudosection for sample Umyl(x) is characterized by the following features (Figs.6a-b): (i) biotite Mg# is almost constant all over the P-T conditions, increasing at low temperature or high pressure conditions; (ii) chlorite is stable below 520°C but its amount is negligible (always lower than 1 wt%); (iii) plagioclase composition reach its maximum (XAb=0.61) close to 420°C. (iv) pure albite occurs at temperature lower than 420°C. Therefore, Bt + Pl + Kfs + Q ± Chl ultramylonitic paragenesis is likely stable at temperatures between 420 and 480°C.

Sample 10.019A at 0.074mol

We can observe that (Figs. 6c-d): (i) epidote stability occurs below 530°C on average (observed at 0.3 GPa) (ii) the modelled composition and modal amount (26%) of epidote is similar to that observed in the sample; (iii) biotite Mg# is almost constant over a large P-T field; (iv) plagioclase show andesine composition (up to XAb=0.67). Its albite richest composition is observed at 450°C between 0.32 and 0.4 GPa; (v) chlorite is stable below 440°C at 0.3 GPa.

Compositional fields of different phases overlap: (i) biotite Mg#, plagioclase (XAb>60) and vein epidote composition show a large overlapping field (red field); (ii) Considering a more strict compositional constrain for plagioclase, i.e. using the Ab richest composition obtained from calculation, the overlap between plagioclase, biotite and epidote composition occur over a strict range of temperature and pressures: 450°C<T<470°C and 0.32<P<0.4 GPa consistent with the temperature estimations derived from sample Umyl(x) (Fig. 6b-d).

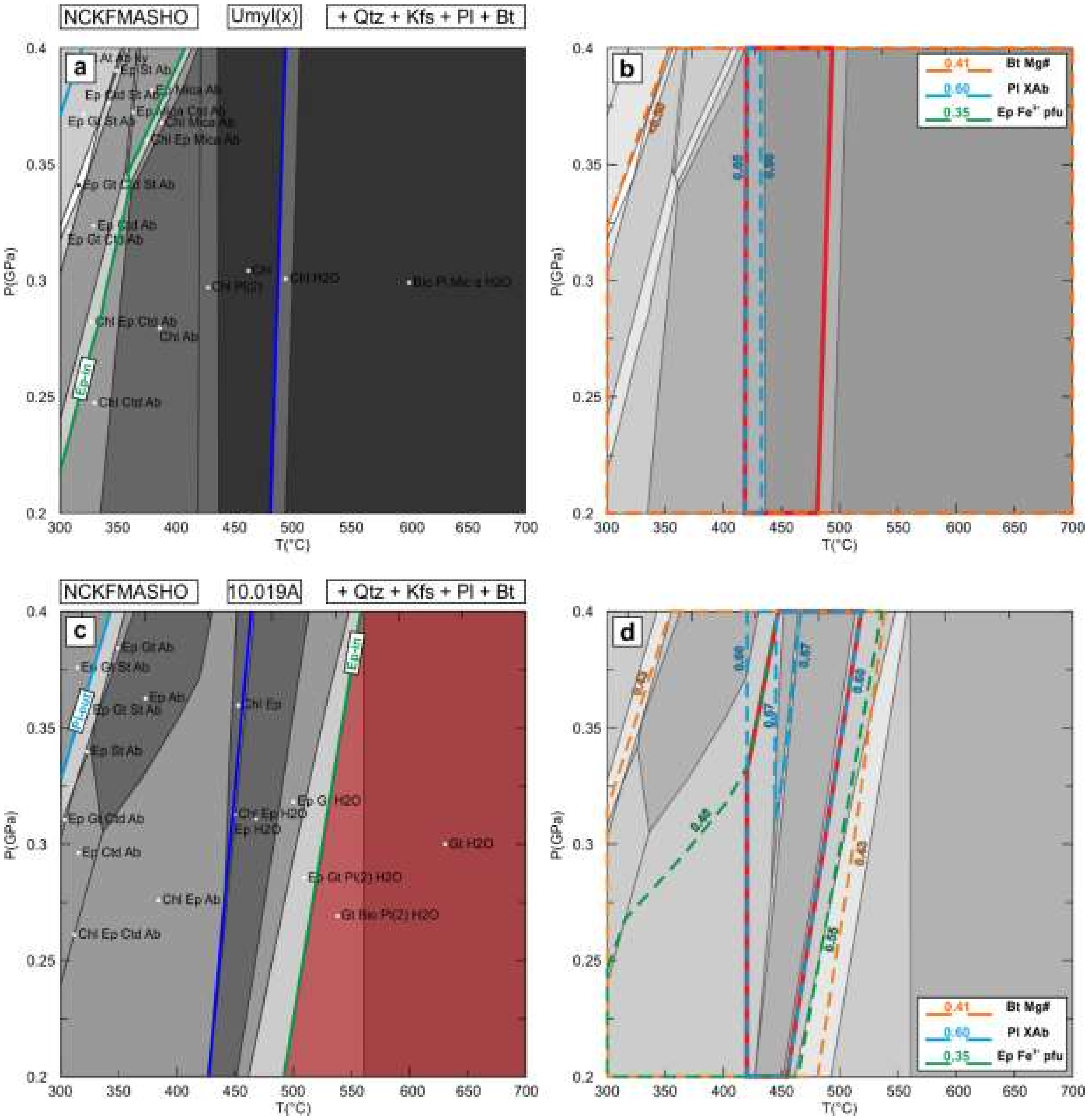

Figure 6. P-T pseudosections for NaCaKFMASHO system for samples Umyl(x) and 10.019A. (a) P-T pseudosection calculated at 0.036 mol H_2O for sample Umyl(x). Water saturation curve is shown as thick blue line. (b) P-T pseudosection calculated at 0.036 mol H_2O for sample Umyl(x). Compositional range limits for biotite and plagioclase are reported as dashed lines (orange and blue, respectively). Thick bold red line indicates the intersection field between compositional ranges of different phases (see text for explanation). (c) P-T pseudosection calculated at 0.076 mol H_2O for sample 10.019A. Water saturation curve is shown as thick blue line. (d) P-T pseudosection calculated at 0.076 mol H_2O for sample 10.019A. Compositional range limtis for biotite, plagioclase and epidote are reported as dashed lines (orange, blue and green, respectively). Thick bold red line indicates the intersection field between compositional ranges of different phases (see text for explanation). The transparent red field indicates the P-T conditions under which epidote is not stable, and therefore, the chemical system does not reflect a real composition of RFP rocks (see text for explanation).

4.8 Results of thermodynamic modelling for MnNaCaKFMASHO systems

The occurrence of garnets in the NaCaKFMASHO chemical system must be taken with regards, given that Mn is not considered (Spear, 1993). To further investigate the occurrence of garnet in some parageneses, further thermodynamic modelling on the same sample set have been performed including Mn in the chemical system, resulting in the system MnNaCaKFMASHO (Figs. 7-8). Introduction of Mn induces the stabilization of garnet all over the investigated P-T conditions, even if in negligible amounts (<2 wt%). In our case, the introduction of Mn in the chemical system does not affect significantly the stability conditions defined before for the ultramylonite paragenesis in both samples (Figs. 7c-f, 8c-f).

MnNaCaKFMASHO T-M pseudosection

In sample Umyl(x), **t**he observed garnet composition is stable at T<380°C and 0.033<M<0.088 mol (Figs. 7a-b). In Sample 10.019A, garnet with the measured compositions is stable at low temperatures T<370°C and 0.07<M<0.102 mol (Figs. 7d-e).

MnNaCaKFMASHO P-T pseudosection

In sample Umyl(x), the measured composition of garnet is observed in a limited P-T field centred at T=380°C and P=0.34GPa (Figs. 8a-b). In sample 10.019A, measured garnet composition would be stable between 300 and 380 °C for a pressure range of 0.25 to 0.4 GPa.

These estimated P-T, based only on garnet composition, are significantly lower in temperature than the ultramylonite paragenesis field (~350-380°C vs 420-480°C; Fig. 8c). These would suggest that garnet grew during the cooling path after the development of the ultramylonite. At these conditions (i.e. ~350°C - 0.3 GPa) garnet would be in equilibrium with Chl + Ab + Ep ± White mica (+ Qtz + Kfs + Pl + Bt). The assemblages where garnet and biotite are stable together also includes, with decreasing temperature: (i) Chl + Ab; (ii) Chl + Ep + Ab; (iii) Chl + Ep + Mica + Ab; (iv) Ep + Mica + Ab in addition to the ultramylonite paragenesis. However, albite is never observed in our assemblage, epidote shows low XEp (<0.4), and white mica shows low phenigitic content (Si a.p.f.u.<3) with respect to the measured compositions.

Figure 7. T-M_{H2O} pseudosections for MnNaCaKFMASHO system for samples Umyl(x) and 10.019A. (a-d) T-M_{H2O} pseudosection calculated at 0.3 GPa for sample Umyl(x)/10.019A. Water saturation curve is shown as thick blue line. Epidote-, plagioclase- and biotite-in reaction are reported. (b-e) T-M_{H2O} pseudosection calculated at 0.3 GPa for sample Umyl(x)/10.019A. Compositional range limits for almandine, spessartine and grossular garnet components are reported as dashed lines (orange, blue and green, respectively). (c-f) T-M_{H2O} pseudosection calculated at 0.3 GPa for sample Umyl(x)/10.019A. Compositional range limits for biotite, plagioclase and epidote are reported as dashed lines (orange, blue and green, respectively). Thick bold red line indicates the intersection field between compositional ranges of different phases (see text for explanation).

Figure 8. P-T pseudosections for MnNaCaKFMASHO system for samples Umyl(x) and 10.019A. (a-d) T-M_{H2O} pseudosection calculated at 0.036 and 0.074 mol H_2O, respectively for sample Umyl(x)/10.019A. Water saturation curve is shown as thick blue line. Epidote-, plagioclase- and biotite-in reaction are reported. (b-e) P-T pseudosection calculated at 0.036 and 0.074 mol H_2O, respectively for sample Umyl(x)/10.019A. Compositional range limits for almandine, spessartine and grossular garnet components are reported as dashed lines (orange, blue and green, respectively). (c-f) P-T pseudosection calculated at 0.036 and 0.074 mol H_2O, respectively for sample Umyl(x)/10.019A. Compositional range limits for biotite, plagioclase and epidote are reported as dashed lines (orange, blue and green, respectively). Thick bold red line indicates the intersection field between compositional ranges of different phases (see text for explanation).

Figure 7

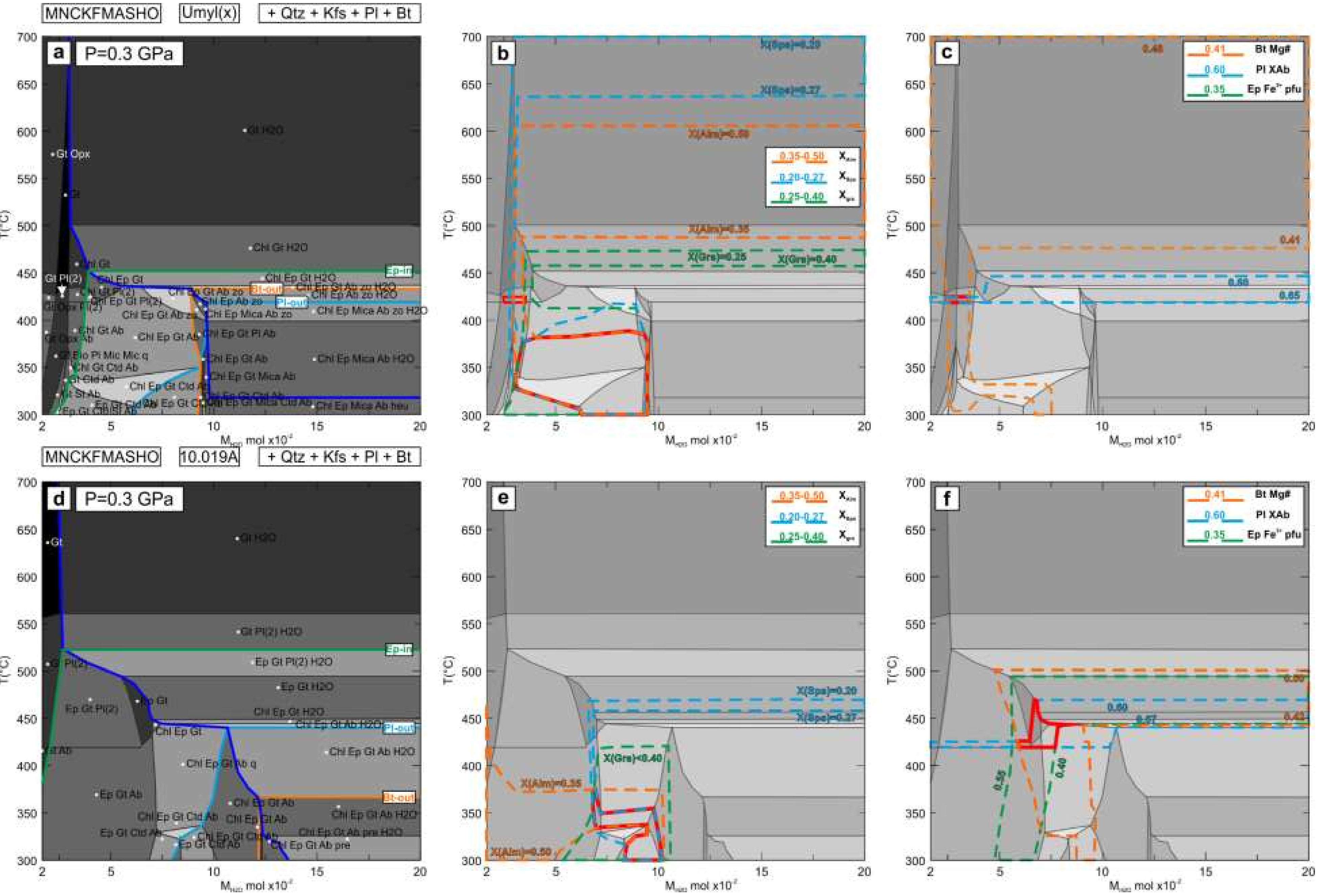
MNCKFMASHO
Umyl(x)
+ Qtz + Kfs + Pl + Bt
a
P=0.3 GPa
b
c
MNCKFMASHO
10.019A
+ Qtz + Kfs + Pl + Bt
d
P=0.3 GPa
e
f
T(°C)
M$_{H2O}$ mol x10^{-2}
Gt Opx
Gt
Gt H2O
Chl Gt H2O
Chl Gt
Gt Pl(2)
Chl Ep Gt
Chl Ep Gt H2O
Ep-in
Bt-out
Pl-out
Chl Ep Gt Ab zo
Chl Ep Gt Ab zo H2O
Chl Ep Ab zo H2O
Chl Ep Ab zo
Chl Ep Mica Ab zo
Chl Ep Mica Ab zo H2O
Chl Ep Gt Pl(2)
Chl Ep Gt Ab zo
Chl Gt Ab
Chl Ep Gt Ab
Chl Ep Gt Pl Ab
Chl Ep Gt Ab
Chl Ep Mica Ab H2O
Chl Gt Ctd Ab
Gt Ctd Ab
Chl Ep Gt Ctd Ab
Chl Ep Gt Mica Ab
Gt St Ab
Chl Ep Mica Ab heu
Gt Opx Pl(2)
Gt Opx Ab
Ep Gt Ctd Ab
Ep Gt Chl St Ab
Chl Ep Gt Mica Ctd Ab
X(Sps)=0.20
X(Sps)=0.27
X(Alm)=0.50
X(Alm)=0.35
X(Grs)=0.25
X(Grs)=0.40
0.35-0.50 X$_{Alm}$
0.20-0.27 X$_{Sps}$
0.25-0.40 X$_{grs}$
0.41 Bt Mg#
0.60 Pl XAb
0.35 Ep Fe^{3+} pfu
0.48
0.41
0.60
0.65
Gt H2O
Gt Pl(2) H2O
Ep Gt Pl(2) H2O
Ep Gt H2O
Gt Pl(2)
Ep Gt Pl(2)
Ep Gt
Chl Ep Gt H2O
Chl Ep Gt Ab H2O
Chl Ep Gt
Chl Ep Gt Ab H2O
Chl Ep Gt Ab q
Gt Ab
Ep Gt Ab
Chl Ep Gt Ab
Chl Ep Gt Ctd Ab
Chl Ep Gt Ab
Chl Ep Gt Ab H2O
Ep Gt Ctd Ab
Chl Ep Gt Ctd Ab
Chl Ep Gt Ab pre H2O
Ep Gt Ctd Ab
Chl Ep Gt Ab pre
X(Grs)<0.40
X(Alm)=0.35
X(Alm)=0.50
0.50
0.60
0.67
0.42
0.55
0.40
2
5
10
15
20
300
350
400
450
500
550
600
650
700

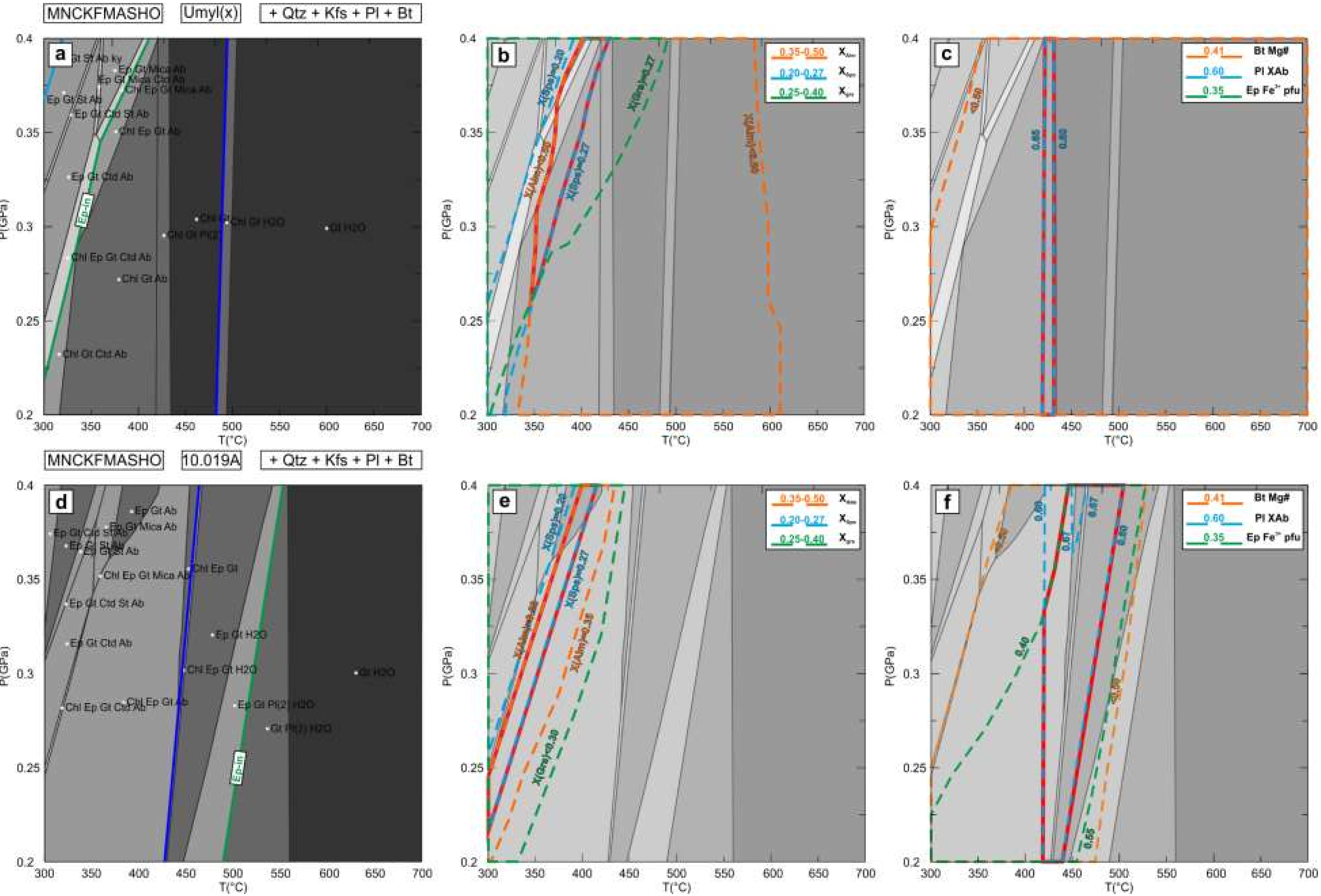
MNCKFMASHO
Umyl(x)
+ Qtz + Kfs + Pl + Bt
a
b
c
MNCKFMASHO
10.019A
+ Qtz + Kfs + Pl + Bt
d
e
f
P(GPa)
T(°C)
0.4
0.35
0.3
0.25
0.2
300
350
400
450
500
550
600
650
700
St St Ab ky
Ep Gt Mica Ab
Ep Gt Mica Ctd Ab
Chl Ep Gt Mica Ab
Ep Gt St Ab
Ep Gt Ctd St Ab
Chl Ep Gt Ab
Ep Gt Ctd Ab
Ep-in
Chl Gt
Chl Gt H2O
Chl Gt Pl(2)
Gt H2O
Chl Ep Gt Ctd Ab
Chl Gt Ab
Chl Gt Ctd Ab
0.35-0.50 X_Alm
0.20-0.27 X_Sps
0.25-0.40 X_Grs
X(Sps)=0.20
X(Alm)=0.50
X(Sps)=0.27
X(Grs)=0.27
X(Alm)<0.50
0.41 Bt Mg#
0.60 Pl XAb
0.35 Ep Fe3+ pfu
0.50
0.85
0.80
Ep Gt Ab
Ep Gt Ctd St Ab
Ep Gt Mica Ab
Ep Gt St Ab
Chl Ep Gt
Chl Ep Gt Mica Ab
Ep Gt H2O
Chl Ep Gt H2O
Chl Ep Gt Ab
Ep Gt Pl(2) H2O
Gt Pl(2) H2O
X(Alm)=0.50
X(Alm)=0.35
X(Grs)<0.30
0.40
0.87
0.55

Figure 6

4.9 Discussion

Assemblages and P-T conditions of deformation

The stable ultramylonitic paragenesis includes at least: $Qtz_{II} + Pl_{II} + Kfs_{II} + Bt_{II}$.

Plagioclase seems to have escaped the peristerite miscibility gap during re-equilibration (XAb<0.80), in accordance with the lack of a coexisting pure-albite plagioclase (e.g. Maruyama et al., 1982; Oliot et al., 2010). Epidote have not been inserted as certain phase of the paragenesis because we don't know its behaviour during deformation. Apparently, all the observed epidote in ultramylonites comes from the disaggregation and weak recrystallization (through a non-defined deformation mechanism) of the former vein epidote. No growth rims or zoning have been identified in small epidote grains. Therefore, re-equilibration of vein epidote to deformation conditions (assuming that conditions changed between vein formation and deformation) might not have occurred. Chlorite has been found in negligible amounts through XRPD analysis on our samples, but it is rarely observed in thin section.

Late post-kinematic garnet and white mica growth

Garnet and white mica microstructures clearly suggest that their occurrence might be related to post-kinematic growth and, therefore, they might be not in equilibrium with the synkinematic ultramylonite paragenesis. This is confirmed by their occurrence in assemblages developed at lower temperatures with respect to the above defined deformation conditions.

Garnet microstructures suggest that phase nucleation and growth occurred during the waning stages of deformation localized on ultramylonites. Limited water content is suggested by other microstructural features of garnets: (i) their occurrence in large number but small crystals suggests that a great number of phase nuclei were present but diffusion processes (aided by the occurrence of fluids) and mass transfer were active only at local scale; (ii) garnet zoning again suggest that phase growth occurred at limited mass transfer conditions and low element mobility. If zoning result from different availability of elements in the surroundings of garnet nuclei, this might have some effect on the interpretation of garnet-biotite geothermometry (e.g. Hoinkes, 1986). In any case, geothermometry suggests decreasing temperature conditions during (static) phase growth. Therefore, garnet nucleation and growth sign the end point of localized ductile deformation on ultramylonites. The lack of pure albite and the inconsistency between measured and observed white mica composition make difficult to explain exactly the occurrence of garnet alone.

Even though garnet has been observed only in sample 10.019A, we have analysed the circumstances of its possible occurrence also in sample Umyl(x).

Vein formation, deformation and reactivation conditions

Integrating data from field, microstructural data and thermodynamic models we can define not only the deformation conditions during ultramylonite development, but also explain other microstructural features. In sample 10.019A, the stability of epidote and biotite compositions alone, at high temperature and water saturated conditions may represent the epidote vein formation, probably occurred in a temperature range between 527°C and 493°C at a minimum pressure of 0.3 GPa (Fig 9).

The overlap between biotite, plagioclase and epidote compositional ranges/isopleths defines the P-T conditions of deformation at 457 ± 40°C at 0.35 ± 0.05 GPa at slightly under-saturated water conditions (Fig 9). If we consider the maximum XAb (~0.67) of plagioclase obtained from thermodynamic models of sample 10.019A, deformation occurred in a strict P-T field at 457 ± 10°C and 0.38 ± 0.013 GPa.

Post-kinematic garnets may have nucleated during the latest stages of deformation, occurred at temperatures between 415°C and 352°C and 0.35 ± 0.05 GPa (Fig 9). These results are also consistent with the cooling trend described by garnet-biotite geothermometry during garnet growth.

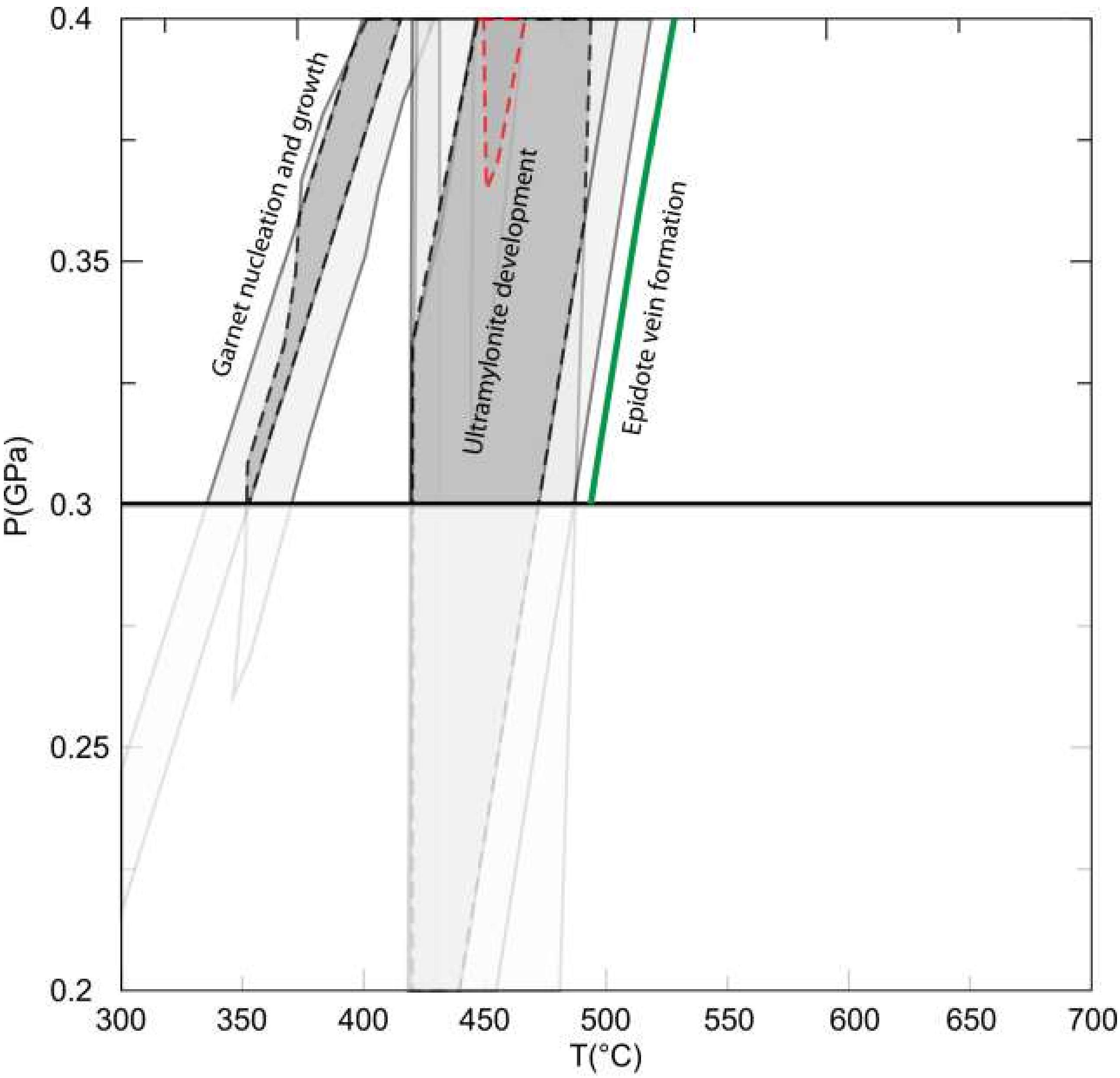

Figure 9

Figure 9. P-T diagram showing the inferred P-T conditions of deformation, vein formation and garnet nucleation. Grey, dashed fields represent the conditions defined by overlapping compositional fields.

Processes affecting results interpretation.

Possible differences in compositions and phase stability may be explained in different ways:

(1) The role of myrmekite on the control of amount and composition of quartz and feldspars

The mineralogical changes and metamorphic reaction related to myrmekite formation (e.g. Cesare et al., 2002) are not easy to identify in our models. In many cases, K-feldspar is reported to be chemically stable but myrmekite develop triggered by deformation (e.g Simpson and Wintsch, 1989; Menegon et al., 2006). This fact has three main consequences that might be relevant for the interpretation of our results: (i) the amount of K-feldspar predicted by the model will be always higher than that observed; (ii) the amount of quartz and plagioclase predicted by the model will be always lower than that observed; (iii) myrmekite formation, neoblastesis and diffusion-assisted creep during plagioclase deformation re-equilibrate the composition of one-single-phase plagioclase.

In particular, myrmekite development, lead to an increase in plagioclase and quartz content of about 0.8*Kfs and 0.2*Kfs, respectively, according to the following reaction (Simpson and Wintsch, 1989)

$$1.25\ \text{Kfs} + 0.75\ \text{Na}^{+} + 0.25\ \text{Ca}^{2+} = (\text{Ab}_{75})\ \text{Plg} + 1.25\ \text{K}^{+} + \text{SiO}_2$$

.

(2) Undersaturation and dispersal of fluids due to recrystallization

All the P-T phase diagrams have been computed assuming constant water content. However, grain size reduction due to recrystallization and deformation mechanisms in general have been demonstrated to cause fluid dispersion due to increasing grain surface area (Pennacchioni and Cesare, 1997; Mancktelow and Pennacchioni, 2004). Water expulsion during weakening and ultramylonite formation is a common process (e.g. Mancktelow, 2002; Finch et al., 2016). Small variation in water content (in the order of 0.1wt%) might have strong influence on the stabilization and composition of water-bearing mineral phases (cfr. biotite Mg#, epidote). Nominally anhydrous minerals, instead, may be less sensitive to water changes and therefore may preserve the original chemical signature obtained during deformation at equilibrium conditions.

(3) Thermodynamic modelling of retrograde path

It is worth noting that during retrograde paths, real metamorphic reactions and phase assemblages may suffer from reduced reaction kinetics and “reverse-overstepping” (downward shift of the effective temperature at which reaction occurs). Metamorphic reaction and phase assemblages calculated by thermodynamic modelling may therefore represent a sort of high-temperature limit for their occurrence. Under this light, the occurrence of metastable phases and/or assemblages is favoured.

Deformation mechanisms and rheology of ductile shear zones in the RFP

As we have seen in previous chapters, tonalitic and quartz mylonites in the RFP nucleated exploiting epidote- and quartz-rich veins. Localization and weakening in these structures are related to different deformation and grain size reduction processes. Quartz veins are a-priori weaker than the surrounding host granitoid, they localize and accommodate ductile strain through the activation of dominant SGR recrystallization. Weakening in tonalite mylonites and ultramylonites is triggered by the activation of grain-size sensitive processes, such as diffusion-accommodated GBS, during shearing of plagioclase + quartz aggregates. Temperature ranges during which these deformation processes occur are coherent with many other studies (e.g. Stöckhert et al., 1999; Stipp et al., 2002a,b). Cooling from 520 to ~400°C in the RFP occurred in less than 2 Myrs (Steenken et al., 2002; Wagner et al., 2006). Assuming that the observed throw across *stage 3* shear zones occurred during this temperature-time window, we can infer the strain rate at which deformation was accommodated. However, a reliable quantification of throw across *stage 3* shear zones in the RFP is very difficult in many cases, due to outcrop exposure or lack of displaced markers (see *Chapter 2*). Where observed, throws are always smaller than 1 m. A reliable throw range could be 10-50 cm. Considering the shear zone thickness in the order of several mm to cm, the inferred shear strain γ ranges between 10 and 100.

This range of shear strain values accommodated over the above-described temperature-time window of 2 Myrs implies bulk strain rates in the order of 10^{-12}-10^{-13} s^{-1}.

4.10 Conclusions

Tonalitic mylonites develops during deformation Stage 3 exploiting precursor epidote- and quartz-rich veins. The ultramylonitic paragenesis includes: quartz + plagioclase + biotite + epidote + K-feldspar ± sphene ± apatite ± garnet ± white mica ± chlorite. Thermodynamic modelling with Perple_X were calculated to define the temperature-fluid conditions at which this paragenesis develop. T-M_{H2O} and P-T pseudosections calculated for the chemical systems NaCaKFMASHO yield the following results: (i) the epidote-veining event in the RFP likely occurred at temperatures between 520°C and 490°C at water-saturated conditions; (ii) the main deformation phase likely occurred at 460 ± 40°C at slightly under-saturated water-conditions. During this temperature evolution, pressure conditions remained fixed around 0.35 ± 0.05 GPa given the limited amount of exhumation during first phases of pluton cooling. In addition, T-M_{H2O} and P-T pseudosections were calculated for the chemical systems MnNaCaKFMASHO, to analyse the occurrence of post-kinematic garnet in some samples. Garnet develops at lower temperature conditions with respect to the synkinematic ultramylonite paragenesis, at around 380 ± 30°C and 0.35 ± 0.05 GPa. Grain size reduction and weakening processes described in the previous Chapters for quartz and tonalite ultramylonites likely occurred in the temperature window between 520 and 350°C. The RFP cooled through this temperature range in less than 2 Myrs, according to published thermal cooling models. Strain rates, therefore, are limited in the range between $10^{-12} – 10^{-13}$ s^{-1}.

Acknowledgements

Leonardo Tauro (UniPd) is warmly thanked for its work and assistance during sample and thin section preparation and fundamental assistance during SEM analyses. Andrea Risplendente (UniMi) and Raul Carampin (IGG-CNR Padova) are thanked for the unvaluable help during EMPA data acquisition. Federico Zorzi (UniPd) and Daria Pasqual (UniPd) are thanked for their work in the acquisition of XRPD and XRF data. Silvio Ferrero (UniPotsdam) and Patrick O'Brien (UniPotsdam) are thanked for fruitful discussions about garnet growth and zoning.

%Ox	**Host 16.078**	**Proto 16.078**	**Umyl 16.078**	**10.019A**	**Umyl(x)**	**16.363**	**16.121A**
SiO_2	66,13	65,8800	65,96	52,82	66,17	74,59	76,10
TiO_2	0,51	0,5200	0,55	0,82	0,53	0,10	0,04
Al_2O_3	16,67	16,9700	16,82	21,55	16,88	14,46	14,00
FeO	3,92	3,9300	4,18	3,92	3,81	0,92	0,41
Fe_2O_3	0,03	0,0500	0,05	2,64	0,09	0,06	0,02
MnO	0,09	0,0900	0,09	0,19	0,09	0,04	0,01
MgO	1,68	1,6700	1,80	1,94	1,62	0,31	0,10
CaO	4,30	4,4000	4,03	10,91	4,24	2,26	1,76
Na_2O	3,11	3,2200	2,97	2,46	3,55	3,07	2,86
K_2O	2,28	2,1900	2,54	2,08	2,56	4,45	5,28
P_2O_5	0,15	0,1500	0,16	0,22	0,16	0,03	0,01
Tot	98,87	99,07	99,15	99,55	99,70	100,29	100,59
L.O.I.	0,98	1,13	1,22	1,51	0,73	0,27	0,28
ppm							
S	*17*	*24*	*20*	*<10*	*<10*	*<10*	*<10*
Sc	6	<5	<5	<5	7	7	<5
V	28	20	34	62	30	14	<5
Cr	18	15	15	28	14	<6	<6
Co	65	120	82	80	196	84	89
Ni	5	5	4	6	5	<3	<3
Cu	28	24	19	25	15	16	35
Zn	81	71	73	87	67	17	5
Ga	27	26	26	63	27	22	20
Rb	128	110	113	132	116	130	140
Sr	313	332	322	472	315	151	138
Y	19	15	16	51	15	44	28
Zr	135	133	134	205	134	60	47
Nb	10	8	8	20	7	8	11
Ba	509	645	477	180	457	120	98
La	37	23	34	45	28	<10	<10
Ce	64	54	73	94	89	18	25
Nd	29	<10	21	58	29	18	27
Pb	45	46	46	66	45	102	109
Th	7	5	8	11	9	<3	<3
U	7	7	7	26	12	28	<3

vol%	**Modal amounts from XRPD Rietveld refinement**						
Qtz	41	43	44	20	44	54	49
Olig	33	31	16	39	42	20	30
Andes	9	-	23	-	-	-	-
Kfs	5	-	-	2	5	19	18
Bt	5	7	5	12	5	4	2
Ep	-	-	1	26	3	-	-
Ms	5	17	11	-	-	-	-
Chl	2	1	-	1	-	2	1
Ap	<1	-	-	-	-	-	-
Sph	-	-	-	-	1	-	-
Cc	-	1	-	-	-	-	-

Table 1. Results from XRF and XRPD analyses. 16.078 sample set have been collected along a strain gradient from proto- to ultramylonitic tonalite. Sample 10.019A and Umyl(x) compositions have been used for thermodynamic modelling with Perple_X. Sample 16.363 and 16.121A are undeformed and sheared aplite, respectively.

	Magmatic Pl		Pl$_{II}$/Intergrowth		Pl$_{II}$/Ultramyl		Magmatic Kfs		Kfs Ultramyl	
	Average	Std Dev	Average	Std Dev	Average	Std Dev	Average	Std Dev	Average	Std Dev
	N= 41		N= 22		N= 10		N= 9		N= 3	
Oxigens	8.00		8.00				8.00			
SiO_2	56.16	1.97	60.62	10.05	62.99	1.06	64.98	0.22	64.61	0.05
TiO_2	0.01	0.01	0.01	0.01	0.03	0.04	0.00	0.00	0.02	0.03
Al_2O_3	26.17	1.39	23.47	6.17	23.19	0.64	18.40	0.25	18.46	0.25
FeO	0.04	0.03	0.06	0.04	0.22	0.08	0.05	0.05	0.21	0.01
MnO	0.01	0.02	0.01	0.02	0.01	0.01	0.01	0.01	0.00	0.00
MgO	0.00	0.01	0.01	0.01	0.02	0.03	0.00	0.01	0.02	0.01
CaO	9.27	1.64	7.54	2.84	4.77	0.41	0.01	0.02	0.02	0.01
Na_2O	6.42	0.91	6.56	2.04	8.83	0.25	0.68	0.13	0.45	0.01
K_2O	0.12	0.07	0.08	0.04	0.13	0.04	15.44	0.35	15.94	0.14
Cr_2O_3	0.02	0.02	0.02	0.02	0.01	0.01	0.03	0.03	0.00	0.00
Fe_2O_3 (Calc)	0.05	0.04	0.06	0.04	0.24	0.09	0.05	0.05	0.24	0.01
Totale	98.23	0.72	98.38	0.66	100.22	0.48	99.60	0.51	99.75	0.17
H2O calc.	-	-	-	-	-	-	-	-	-	-
Totale	-	-	-	-	-	-	-	-	-	-
Si	2.57	0.08	2.72	0.34	2.78	0.04	3.00	0.01	2.99	0.01
Ti	0.00	0.00	0.00	0.00	0.00	0.00	0.00	0.00	0.00	0.00
Al	1.41	0.08	1.26	0.34	1.21	0.04	1.00	0.01	1.01	0.01
Cr	0.00	0.00	0.00	0.00	0.00	0.00	0.00	0.00	0.00	0.00
Fe^{2+}	0.00	0.00	0.00	0.00	0.01	0.00	0.00	0.00	0.01	0.00
Fe^{3+}	0.00	0.00	0.00	0.00	0.01	0.00	0.00	0.00	0.01	0.00
Mn	0.00	0.00	0.00	0.00	0.00	0.00	0.00	0.00	0.00	0.00
Mg	0.00	0.00	0.00	0.00	0.00	0.00	0.00	0.00	0.00	0.00
Ca	0.45	0.08	0.37	0.14	0.23	0.02	0.00	0.00	0.00	0.00
Na	0.57	0.08	0.58	0.18	0.76	0.02	0.06	0.01	0.04	0.00
K	0.01	0.00	0.00	0.00	0.01	0.00	0.91	0.02	0.94	0.01
Totale	5.01	0.01	4.94	0.24	4.99	0.02	4.98	0.01	4.99	0.01
Sito Z	3.98	0.01	3.99	0.01	4.01	0.01	4.01	0.00	4.01	0.00
Sito X	1.03	0.01	0.95	0.25	0.99	0.02	0.97	0.01	0.98	0.01
Ab %	55.22	7.79	61.01	9.85	76.47	1.79	6.24	1.23	4.10	0.03
An %	44.11	7.84	38.20	10.16	22.80	1.86	0.06	0.12	0.10	0.07
Or %	0.67	0.42	0.79	1.38	0.73	0.22	93.69	1.30	95.81	0.05

	Magmatic Bt		Bt$_{II}$/Intergrowth		Bt$_{II}$ Ultramyl		Ms$_{II}$ Ultramyl		Ms$_{II}$	
	Average	Std Dev	Average	Std Dev	Average	Std Dev	Average	Std Dev	Average	Std Dev
	N= 19.00		N= 24.00		N= 11		N= 8		N= 7	
Oxigens	22.00		22.00		22.00		22.00		22	
SiO_2	36.74	0.37	36.65	0.66	37.08	0.47	48.50	0.36	46.67	0.93
TiO_2	2.18	0.62	1.04	0.46	1.15	0.24	0.34	0.09	0.48	0.55
Al_2O_3	17.28	0.58	17.90	0.41	18.32	0.51	32.59	0.34	31.80	0.80
FeO	20.57	0.45	20.29	0.76	18.50	0.69	2.73	0.54	2.21	0.45
MnO	0.48	0.07	0.49	0.08	0.37	0.05	0.07	0.06	0.06	0.03
MgO	8.99	0.26	9.52	0.50	9.68	0.49	2.00	0.23	1.62	0.16
CaO	0.08	0.09	0.21	0.19	0.13	0.06	0.07	0.03	0.05	0.04
Na_2O	0.09	0.15	0.08	0.08	0.04	0.03	0.17	0.04	0.19	0.03
K_2O	9.31	0.39	8.94	0.57	9.44	0.21	10.01	0.11	10.79	0.13
Cr_2O_3	0.02	0.04	0.02	0.02	0.01	0.02	0.01	0.01	0.02	0.03
Fe_2O_3 (Calc)										
Totale	95.77	0.83	95.12	1.03	94.72	0.78	96.49	0.59	93.89	1.37
H2O calc.	3.94	0.04	3.93	0.05	3.94	0.03	4.55	0.02	4.41	0.07
Totale	99.71	0.86	99.05	1.08	98.67	0.81	101.04	0.60	98.30	1.44
Si	5.59	0.03	5.60	0.05	5.64	0.06	6.39	0.04	6.35	0.03
Ti	0.25	0.07	0.12	0.05	0.13	0.03	0.03	0.01	0.05	0.06
Al	3.10	0.09	3.22	0.06	3.28	0.07	5.06	0.06	5.10	0.11
Cr	0.00	0.00	0.00	0.00	0.00	0.00	0.00	0.00	0.00	0.00
Fe^{2+}	2.62	0.06	2.59	0.11	2.35	0.09	0.30	0.06	0.25	0.05
Fe^{3+}	-	-	-	-	-	-	-	-	-	-
Mn	0.06	0.01	0.06	0.01	0.05	0.01	0.01	0.01	0.01	0.00
Mg	2.04	0.06	2.17	0.11	2.19	0.11	0.39	0.04	0.33	0.03
Ca	0.01	0.02	0.03	0.03	0.02	0.01	0.01	0.00	0.01	0.01
Na	0.03	0.04	0.02	0.02	0.01	0.01	0.04	0.01	0.05	0.01
K	1.81	0.07	1.74	0.10	1.83	0.04	1.68	0.02	1.87	0.04
Totale	15.52	0.05	15.56	0.06	15.51	0.05	13.91	0.04	14.01	0.03
Al IV	2.41	0.03	2.40	0.05	2.36	0.06	1.61	0.04	1.65	0.03
Al VI	0.69	0.09	0.82	0.07	0.92	0.07	3.44	0.07	3.45	0.11
Sito O	5.67	0.06	5.76	0.08	5.65	0.03	4.18	0.04	4.08	0.03
Sito A	1.85	0.04	1.80	0.09	1.86	0.03	1.73	0.02	1.93	0.04
Mg#	0.44	0.01	0.46	0.02	0.48	0.02	0.57	0.02	0.57	0.05

	Epidote			Garnet		Sphene		Hornblende	
	Average	Std Dev		Average	Std Dev	Average	Std Dev	Average	Std Dev
	N= 27			N= 11		N= 4		N= 7	
Oxigens	12.5			12		5		23	
SiO2	38.39	0.59		38.14	0.39	30.03	0.10	45.87	0.46
TiO2	0.17	0.15		0.26	0.31	37.38	0.69	0.78	0.11
Al2O3	27.28	0.65		21.58	0.24	2.33	0.49	9.23	0.43
FeO	7.15	0.56		17.50	2.29	0.42	0.17	18.81	0.18
MnO	0.27	0.04		10.83	0.93	0.06	0.07	0.77	0.06
MgO	0.12	0.28		0.65	0.18	0.00	0.01	9.40	0.22
CaO	23.62	0.78		11.74	1.84	28.88	0.21	11.71	0.23
Na2O	0.01	0.01		0.01	0.01	0.01	0.01	0.97	0.17
K2O	0.12	0.28		0.02	0.01	0.04	0.04	0.90	0.09
Cr2O3	-	-		0.01	0.02	0.02	0.04	0.02	0.02
Totale	97.14	1.01		100.75	0.35	99.19	0.28	98.46	0.31
Si	3.00	0.02		3.01	0.02	0.99	0.00	6.86	0.06
Ti	0.01	0.01		0.02	0.02	0.93	0.02	0.09	0.01
Al	2.51	0.04		2.01	0.02	0.09	0.02	1.63	0.08
Cr	-	-		0.00	0.00	0.00	0.00	0.00	0.00
Fe3+	0.47	0.04		-	-	-	-	-	-
Fe2+	-	-		1.15	0.16	0.01	0.00	2.35	0.02
Mn	0.02	0.00		0.72	0.06	0.00	0.00	0.10	0.01
Mg	0.01	0.03		0.08	0.02	0.00	0.00	2.10	0.05
Ca	1.98	0.07		0.99	0.15	1.02	0.00	1.88	0.04
Na	0.00	0.00		0.00	0.00	0.00	0.00	0.28	0.05
K	0.01	0.03		0.00	0.00	0.00	0.00	0.17	0.02
Totale				7.98	0.01	3.04	0.01	15.46	0.04
Xcz (Perple_X)	0.84	0.01	**Sito O**	3.01	0.01				
Xep (Perple_X)	0.16	0.01	**Sito T**	2.02	0.01				
Xpm (Perple_X	0.01	0.00	**Sito A**	2.95	0.02				
			Py	2.60	0.73				
Xcz (F&L,'04)	0.47	0.08	**Al**	39.20	5.37				
Xep (F&L,'04)	0.48	0.04	**Sp**	24.56	2.03				
			Grs	33.64	5.09				

Table 2. Average composition of magmatic and ultramylonitic phases.

Conclusions

In this thesis we have described the structural evolution of the Rieserferner pluton, analysing the processes and conditions at which deformation occurs.

The Rieserferner pluton have recorded a ductile-to-brittle deformation sequence during its cooling and exhumation, reflecting the complex tectonic and geodynamic processes that occurred in the Eastern Alps during Oligocene and Miocene. During Oligocene cooling, three different generation of discrete and localized ductile shear zones developed at decreasing temperatures, whose kinematics analysis suggested a switch in the regional stress field from N290° shortening dominated to N350° shortening direction related to the switch in dominant geodynamic process from N-S convergent margins and slab breakoff, to initial exhumation and tectonic unroofing of the central Eastern Alps. Miocene exhumation of the Rieserferner pluton developed under constant transpressive field, dominated by N-S shortening and E-W extension, reflected in the development of brittle strike-slip faults with different orientations.

Ductile shear zone nucleation processes have been investigated in more detail integrating structural analyses at different scales.

Ductile shear zone nucleates on pre-existing structural discontinuities and compositional heterogeneities, such as brittle joints, veins and dykes (Mancktelow and Pennacchioni, 2005; Pennacchioni and Mancktelow, 2007) during the whole deformation history during pluton cooling (from 700°C down to 300°C). Shear zone geometry depends on the competence contrast (i.e. compositional contrast) between the exploited precursor and the host rock: heterogeneous shear zones develop exploiting “stiff” discontinuities (such as epidote veins, joints), whereas homogeneous shear zones develop in weak layers (such as quartz veins and aplitic dykes).

In particular, we have focused our attention on the processes that control the development of localized shear zones during deformation *stage 3*, during which quartz and epidote veins have been exploited as site for the nucleation of homogeneous and heterogeneous shear zones, respectively.

Localization occurs because part of the deforming medium (the rock) is weaker than its surroundings.

Quartz veins shows a characteristic microstructural evolution with increasing strain, that is a quite common evolution occurring at upper greenschist to lower amphibolite facies conditions in many other geological settings. Quartz veins are inherently weaker than the surrounding rock, and therefore localization leads to the development of homogeneous shear zones (Platt et al., 2015). Strain accommodation lead to increasing mylonitization and SGR recrystallization of the quartz vein crystals. Mylonitization of coarse grained quartz veins resulted in a complex evolution with increasing strain, mainly controlled by the initially different crystallographic orientations of the vein crystals, reflecting the mechanical anisotropy and the different strain behaviour of crystals wth different orientation during shearing. Crystals suitably oriented for the activation of {m}<a> slip system, the most efficient slip system at *stage 3* deformation conditions, stretched to form high aspect ratio ribbons without strong recrystallization. Crystals with different orientation underwent early hardening and recrystallized along conjugate sets of crystallographically-controlled µSZs.

Heterogeneous shear zones nucleated exploiting *stage 3* epidote veins. Strain localized along the boundaries of the epidote vein, leading to the mylonitization of the host granitoid. Host rock mylonitization is aided by several weakening and grain size reduction mechanisms, such as dynamic recrystallization and metamorphic reactions. The dominant grain size reduction mechanisms is the development of myrmekite (plagioclase + quartz symplectites) at the expense of former magmatic K-feldspar. Myrmekite formation is triggered by crystal strain and stress concentration in K-feldspar grains. Pseudomorphic replacement relations have been inferred from the coincidence between myrmekitic plagioclase and parent K-feldspar grain crystal lattices. Strong grain size reduction and microstructural characters of myrmekite promoted the increasing role of grain-size sensitive creep processes, such as diffusion-assisted grain boundary sliding. Diffusion assisted creep processes promoted also phase mixing and the formation of ultramylonitic layers along sheared epidote vein, leading to strong weakening of the rock and extreme strain localization.

Microstructures and deformation mechanisms characterising *stage 3* localized ductile shear zones likely developed at 460 ± 40°C and 0.35 ± 0.05GPa. Epidote vein formation occurred at temperatures close to 500°C, and ultramylonite development likely persisted during cooling down to 350°C. Deformation occurred at conditions close to water saturation.

The RFP cooled through this temperature range in less than 2 Myrs, according to published thermal cooling models. Strain rates, therefore, are limited in the range between $10^{-12} – 10^{-13}$ s^{-1}.

Quartz paleopiezometry on quartz veins during recrystallization yield differential stress values ranging between 60 MPa (for maximum incipient recrystallization grain size of 20 µm) and 117 MPa (for minimum observed grain size during ultramylonite recrystallization) (Stipp et al., 2003; Cross, et al. 2017). Assuming that the ultramylonitic microstructure represents a steady-state microstructure, the differential stress at which ultramylonites underwent was around 120 MPa at 450°C and 0.35 GPa. According to the flow law of Hirth et al. (2001) for quartz recrystallization during dislocation creep at 450°C (water fugacity of 97 MPa calculated after Sterner and Pitzer, 1994, at 0.35 GPa and 450°C) ultramylonites developed at strain rate as large as 10^{-11} s^{-1}.

Recrystallizing pure quartz layers along tonalite mylonite foliation, instead suggest differential stresses of about 20-50 MPa (calculated for 35 and 100 µm grain size) and strain rates in the order of 10^{-13}-10^{-14} s^{-1}. In plagioclase + quartz deforming aggregates, the switch in dominant deformation mechanism from dislocation to diffusion creep decreased the bulk aggregate strength. Bulk strength of a polyphase aggregate is controlled by the rheology of the weaker phase (Platt, 2015; quartz in our case), that might be controlled in turn by the diffusivity of the phase (Behrmann and Mainprice, 1987). Therefore, a strong strain partitioning between quartz layers and plagioclase + quartz aggregates is expected. If we assume that (i) deformation occurred under constant differential stress, and (ii) the dominant rate controlling mechanisms during shearing of tonalitic mylonites is diffusion creep, a differential stress of about 50 MPa would induce larger strain rates localized in the plagioclase + quartz aggregates and ultramylonites. Strain rates are probably close to 10-^{12} s^{-1}, as retrieved from time-temperature relationships. However, recrystallized quartz veins deformed along granitoid ultramylonites are often found as very elongated lens-shaped boudins, suggesting that quartz is still stronger than the ultramylonitic layer. Therefore, strain rates inside ultramylonites may be as high as 10^{-11} s^{-1}.

In the dislocation creep field, granite bulk strength is larger than monomineralic quartz aggregates, showing instead almost the same strength in the diffusion creep dominated field (Platt, 2015). Therefore, deformation is localized in quartz veins because during dislocation creep, quartz + feldspar + biotite aggregates (granitoid rocks) are stronger than pure quartz aggregates (veins) of several orders of magnitude. When diffusion creep is activated after the development of myrmekite, quartz and granite have more or less the same strength. Given that dislocation creep is dominant in quartz inside granitoid mylonites, whereas mylonitic-ultramylonitic aggregates are dominated by diffusion creep, strain localizes in mylonite/ultramylonite layers.

References

- Abart, R., Heuser, D., Habler, G., 2014. Mechanisms of myrmekite formation: case study from the Weinsberg granite, Moldanubian zone, Upper Austria. Contributions to Mineralogy and Petrology 168, 1074.
- Becke, F., 1908, Über myrmekit: Mineralogie und Pétrographie Mitteilungen, v. 27, p. 377-390.
- Behrmann, J. H., and Mainprice, D., 1987. Deformation mechanisms in a high-temperature quartz-feldspar mylonite: evidence for superplastic flow in the lower continental crust. Tectonophysics, 140, 297-305.
- Bellieni, G., 1978. Caratteri geochimici del massiccio granodioritico tonalitico delle Vedrette di Ries (Rieserferner) - Alto Adige Orientale. Rendiconti della Società Italiana di Mineralogia e Petrologia 34, 527-548.
- Bellieni, G., Fioretti, A. M., Marzoli, A., and Visonà, D., 2010. Permo–Paleogene magmatism in the eastern Alps. Rendiconti Lincei 21, 51-71.
- Bellieni, G., Peccerillo, A., and Poli, G., 1981. The Vedrette di Ries (Rieserferner) plutonic complex: petrological and geochemical data bearing on its genesis. Contributions to Mineralogy and Petrology 78(2), 145-156.
- Berger, A., Herwegh, M., Schwarz, J. O., and Putlitz, B., 2011. Quantitative analysis of crystal/grain sizes and their distributions in 2D and 3D. Journal of Structural Geology 33, 1751-1763.
- Bertrand, A., Rosenberg, C., and Garcia, S., 2015. Fault slip analysis and late exhumation of the Tauern Window, Eastern Alps. Tectonophysics 649, 1-17.
- Bestmann, M., and Prior, D.J., 2003. Intragranular dynamic recrystallization in naturally deformed calcite marble: diffusion accommodated grain boundary sliding as a result of

subgrain rotation recrystallization. Journal of Structural Geology 25, 1597-1613.

- Bestmann, M., Pennacchioni, G., 2015. Ti distribution in quartz across a heterogeneous shear zone within a granodiorite: The effect of deformation mechanism and strain on Ti resetting. Lithos 227, 37-56, doi:10.1016/j.lithos.2015.03.009.
- Borsi, S., Del Moro, A., Sassi, F. P., and Zirpoli, G., 1979. On the age of the Vedrette di Ries (Rieserferner) massif and its geodynamic significance. Geologische Rundschau 68, 41-60.
- Bouchez, J.-L., 1977. Plastic deformation of quartzites at low temperature in an area of natural strain gradient. Tectonophysics 39, 25-50, doi:10.1016/0040-1951(77)90086-5.
- Ceccato, A., Pennacchioni, G., Menegon, L., and Bestmann, M., 2017. Crystallographic control and texture inheritance during mylonitization of coarse grained quartz veins. Lithos.
- Cesare, B., 1994. Hercynite as the product of staurolite decomposition in the contact aureole of Vedrette di Ries, eastern Alps, Italy. Contributions to Mineralogy and Petrology 116, 239-246.
- Cesare, B., and Hollister, L. S., 1995. Andalusite□bearing veins at Vedrette di Ries (eastern Alps, Italy): fluid phase composition based on fluid inclusions. Journal of Metamorphic Geology 13, 687-700.
- Cesare, B., Marchesi, C., and Connolly, J. A. D., 2002. Growth of myrmekite coronas by contact metamorphism of granitic mylonites in the aureole of Cima di Vila, Eastern Alps, Italy. Journal of Metamorphic Geology 20, 203-213.
- Cesare, B., Mazzoli, C., Sassi, R., Spiess, R., and Sassi, F. P., 2010. Beauty and complexity of metamorphism: case studies from the frontal part of the Adria microplate. Rendiconti Lincei 21, 73-94.
- Ciancaleoni, L., and Marquer, D., 2006. Syn□extension leucogranite deformation during

convergence in the Eastern Central Alps: example of the Novate intrusion.Terra Nova18, 170-180.

- Ciancaleoni, L., and Marquer, D., 2008. Late Oligocene to early Miocene lateral extrusion at the eastern border of the Lepontine dome of the central Alps (Bergell and Insubric areas, eastern central Alps). Tectonics 27.
- Connolly, J. A., 2005. Computation of phase equilibria by linear programming: a tool for geodynamic modeling and its application to subduction zone decarbonation. Earth and Planetary Science Letters 236, 524-541.
- Cross, A. J., Hirth, G., Prior, D. J., 2017. Effects of secondary phases on crystallographic preferred orientations in mylonites. Geology.
- Czaplińska, D., Piazolo, S., Zibra, I., 2015. The influence of phase and grain size distribution on the dynamics of strain localization in polymineralic rocks. Journal of Structural Geology 72, 15-32.
- Dal Piaz, G., 1934. Studi Geologici sull'Alto Adige Orientale e regioni limitrofe. Mem. Ist. Geol. Univ. Padova.
- Davies, J. H., and von Blanckenburg, F., 1995. Slab breakoff: a model of lithosphere detachment and its test in the magmatism and deformation of collisional orogens. Earth and Planetary Science Letters 129, 85-102.
- De Bresser, J., Ter Heege, J., and Spiers, C., 2001. Grain size reduction by dynamic recrystallization: can it result in major rheological weakening?. International Journal of Earth Sciences 90, 28-45.
- Dell'Angelo, L. N., Tullis, J., 1996. Textural and mechanical evolution with progressive strain in experimentally deformed aplite. Tectonophysics 256, 57-82.
- Dempsey, E. D., Holdsworth, R. E., Imber, J., Bistacchi, A., and Di Toro, G., 2014. A geological explanation for intraplate earthquake clustering complexity: The zeolite-bearing fault/fracture networks in the Adamello Massif (Southern Italian Alps). Journal of

Structural Geology 66, 58-74.

- Derez, T., Pennock, G., Drury, M., and Sintubin, M., 2015. Low-temperature intracrystalline deformation microstructures in quartz. Journal of Structural Geology 71, 3-23.
- Di Toro, G., and Pennacchioni, G.. 2004. Superheated friction-induced melts in zoned pseudotachylytes within the Adamello tonalites (Italian Southern Alps). Journal of Structural Geology 26(, 1783-1801.
- Di Vincenzo, G., Pennacchioni, G., Ceccato, A., … , in preparation.
- Dowty, E., 1980. Synneusis reconsidered. Contributions to Mineralogy and Petrology 74, 75-84.
- Finch, M. A., Weinberg, R. F., and Hunter, N. J., 2016. Water loss and the origin of thick ultramylonites. Geology 44, 599-602.
- Fitz Gerald, J., and Stünitz, H., 1993. Deformation of granitoids at low metamorphic grade. I: Reactions and grain size reduction. Tectonophysics 221, 269-297.
- Fliervoet, T. F., White, S. H., Drury, M. R., 1997. Evidence for dominant grain-boundary sliding deformation in greenschist-and amphibolite-grade polymineralic ultramylonites from the Redbank Deformed Zone, Central Australia. Journal of Structural Geology 19, 1495-1520.
- Franz, G., and Liebscher, A., 2004. Physical and Chemical Properties of the Epidote Minerals–An Introduction–. Reviews in mineralogy and geochemistry 56, 1-81.
- Frisch, W., Dunkl, I., and Kuhlemann, J., 2000. Post-collisional orogen-parallel large-scale extension in the Eastern Alps. Tectonophysics 327, 239-265.
- Fusseis, F., Regenauer-Lieb, K., Liu, J., Hough, R. M.,, De Carlo, F., 2009. Creep cavitation can establish a dynamic granular fluid pump in ductile shear zones. Nature 459, 974.
- Gapais, D., and Barbarin, B., 1986. Quartz fabric transition in a cooling syntectonic

granite (Hermitage Massif, France). Tectonophysics 125, 357-370.

- Genser, J., and Neubauer, F., 1989. Low angle normal faults at the eastern margin of the Tauern window (Eastern Alps). Mitteilungen der Österreichischen Geologischen Gesellschaft 81 (1988), 233-243.
- Gleason, G. C., Tullis, J., Heidelbach, F., 1993. The role of dynamic recrystallization in the development of lattice preferred orientations in experimentally deformed quartz aggregates. Journal of Structural Geology 15, 1145-1168.
- Gleason, G.C., Tullis, J., 1995. A flow law for dislocation creep of quartz aggregates determined with the molten-salt cell. Tectonophysics 247, 1-23.
- Goncalves, P., Oliot, E., Marquer, D., and Connolly, J. A. D., 2012. Role of chemical processes on shear zone formation: an example from the Grimsel metagranodiorite (Aar massif, Central Alps). Journal of Metamorphic Geology 30, 703-722.
- Goncalves, P., Poilvet, J. C., Oliot, E., Trap, P., and Marquer, D., 2016. How does shear zone nucleate? An example from the Suretta nappe (Swiss Eastern Alps). Journal of Structural Geology 86, 166-180.
- Guastoni, A., Pennacchioni, G., Pozzi, G., Fioretti, A. M., and Walter, J. M., 2014. Tertiary pegmatite dikes of the Central Alps. The Canadian Mineralogist 52, 191-219.
- Halfpenny, A., Prior, D. J., Wheeler, J., 2012. Electron backscatter diffraction analysis to determine the mechanisms that operated during dynamic recrystallisation of quartz-rich rocks. Journal of Structural Geology 36, 2-15.
- Handy, M. R., 1994. Flow laws for rocks containing two non-linear viscous phases: a phenomenological approach. Journal of Structural Geology 16, 287-301.
- Handy, M. R., Babist, J., Wagner, R., Rosenberg, C., and Konrad, M., 2005. Decoupling and its relation to strain partitioning in continental lithosphere: insight from the Periadriatic fault system (European Alps). Geological Society, London, Special

Publications 243, 249-276.

- Harlov, D. E., Wirth, R., 2000. K-feldspar–quartz and K-feldspar–plagioclase phase boundary interactions in garnet–orthopyroxene gneiss's from the Val Strona di Omegna, Ivrea–Verbano Zone, northern Italy. Contributions to Mineralogy and Petrology 140, 148-162.
- Heilbronner, R. P., Pauli, C., 1993. Integrated spatial and orientation analysis of quartz c-axes by computer-aided microscopy. Journal of Structural Geology 15, 369-382.
- Heilbronner, R., and Barrett, S., 2014.Image analysis in earth sciences: microstructures and textures of earth materials. Springer Science & Business Media.
- Heilbronner, R., Kilian, R., 2017. The grain size(s) of Black Hills Quartzite deformed in the dislocation creep regime. Solid Earth Discussion, doi:10.5194/se-2017-30
- Heilbronner, R., Tullis, J., 2006. Evolution of c axis pole figures and grain size during dynamic recrystallization: Results from experimentally sheared quartzite, Journal of Geophysical Research 111, B10202, doi:10.1029/ 2005JB004194.
- Henry, B., 1975. Microtectonique et anisotropie de susceptibilite magnetique du massif tonalitique des riesenferner—vedrette di ries (frontiere italo-autrichienne). Tectonophysics 27, 155-165.
- Herwegh, M., & Berger, A., 2004. Deformation mechanisms in second-phase affected microstructures and their energy balance. Journal of structural geology 26, 1483-1498.
- Hibbard, M. J., 1979. Myrmekite as a marker between preaqueous and postaqueous phase saturation in granitic systems. Geological Society of America Bulletin 90, 1047-1062.
- Hibbard, M. J., 1981. The magma mixing origin of mantled feldspars. Contributions to Mineralogy and Petrology 76, 158-170.
- Hiraga, T., Miyazaki, T., Yoshida, H.,, Zimmerman, M. E., 2013. Comparison of

microstructures in superplastically deformed synthetic materials and natural mylonites: Mineral aggregation via grain boundary sliding. Geology 41, 959-962.

- Hirth, G., and Tullis, J., 1992. Dislocation creep regimes in quartz aggregates. Journal of Structural Geology 14, 145-159.
- Hirth, G., Teyssier, C., Dunlap, W.J., 2001. An evaluation of quartzite flow laws based on comparisons between experimentally and naturally deformed rocks. International Journal of Earth Sciences 90, 77-87, doi:10.1007/s005310000152
- Hobbs, B.E., 1968. Recrystallization of single crystals of quartz. Tectonophysics 6, 353-401.
- Hoinkes, G., 1986. Effect of grossular-content in garnet on the partitioning of Fe and Mg between garnet and biotite. Contributions to Mineralogy and Petrology 92, 393-399.
- Holland, T. J. B., and Powell, R., 2011. An improved and extended internally consistent thermodynamic dataset for phases of petrological interest, involving a new equation of state for solids. Journal of Metamorphic Geology 29, 333-383.
- Hutton, D. H., 1988. Granite emplacement mechanisms and tectonic controls: inferences from deformation studies. Earth and Environmental Science Transactions of the Royal Society of Edinburgh 79, 245-255.
- Jiang, Z., Prior, D. J., Wheeler, J., 2000. Albite crystallographic preferred orientation and grain misorientation distribution in a low-grade mylonite: implications for granular flow. Journal of Structural Geology 22, 1663-1674.
- Johnson, S. E., Marsh, J. H., Vernon, R. H., 2008. From tonalite to mylonite: coupled mechanical and chemical processes in foliation development and strain localization. J. Virtual Explor 30.
- Karato, S. I., 2012. Deformation of earth materials: an introduction to the rheology of solid earth. Cambridge University Press.

- Kilian, R. and Heilbronner, R., 2017. Texture analysis of experimentally deformed Black Hills Quartzite. Solid Earth Discuss., doi:10.5194/se-2017-44.
- Kilian, R., Heilbronner, R., Stünitz, H., 2011. Quartz grain size reduction in a granitoid rock and the transition from dislocation to diffusion creep. Journal of Structural Geology 33, 1265-1284, doi:10.1016/j.jsg.2011.05.004
- Kjøll, H.J., Viola, G., Menegon, L., Sørensen, B.E., 2015. Brittle–viscous deformation of vein quartz under fluid-rich low greenschist facies conditions. Solid Earth 7, 213-257.
- Kruhl, J. H., 1996. Prism□and basal□plane parallel subgrain boundaries in quartz: A microstructural geothermobarometer. Journal of metamorphic Geology 14, 581-589.
- Kruse, R., and Stünitz, H., 1999. Deformation mechanisms and phase distribution in mafic high-temperature mylonites from the Jotun Nappe, southern Norway. Tectonophysics 303, 223-249.
- Lapworth, T., Wheeler, J., Prior, D. J., 2002. The deformation of plagioclase investigated using electron backscatter diffraction crystallographic preferred orientation data. Journal of Structural Geology 24, 387-399.
- Law, R. D., 2014. Deformation thermometry based on quartz c-axis fabrics and recrystallization microstructures: A review. Journal of Structural Geology 66, 129-161.
- Lee, M. R., Waldron, K. A., Parsons, I. 1995. Exsolution and alteration microtextures in alkali feldspar phenocrysts from the Shap granite. Mineralogical Magazine 59, 63-78.
- Linner, M., Habler, G., and Grasemann, B., 2009. Switch of kinematics in the Austroalpine basement between the Defereggen-Antholz-Vals (DAV) and the Pustertal-Gailtal fault. In 9th Workshop on Alpine Geological Studies Cogne/Italy (Vol. 16, p. 18).
- Lloyd, G. E., 2004. Microstructural evolution in a mylonitic quartz simple shear zone: the significant roles of dauphine twinning and misorientation. Geological Society of London, Special Publications 224, 39-61.

- Lloyd, G. E., Law, R. D., Mainprice, D., Wheeler, J., 1992. Microstructural and crystal fabric evolution during shear zone formation. Journal of Structural Geology 14, 1079-1100.
- Luan, F.C., Paterson, M.S. ,1992. Preparation and deformation of synthetic aggregates of quartz. Journal of Geophysical Research 97, 301-320.
- Luth, S. W., and Willingshofer, E., 2008. Mapping of the post-collisional cooling history of the Eastern Alps. In Orogenic Processes in the Alpine Collision Zone (pp. S207-S223). Birkhäuser Basel.
- Mager, D., 1985. Geologische und petrographische Untersuchungen am Südrand des Rieserferner-Plutons (Südtirol): unter Berücksichtigung des Intrusionsmechanismus. Unpublished PhD thesis.
- Mainprice, D., Bouchez, J. L., Blumenfeld, P., and Tubià, J. M., 1986. Dominant c slip in naturally deformed quartz: implications for dramatic plastic softening at high temperature. Geology 14, 819-822.
- Mancktelow, N. S., 2002. Finite-element modelling of shear zone development in viscoelastic materials and its implications for localisation of partial melting. Journal of Structural Geology 24, 1045-1053.
- Mancktelow, N. S., and Pennacchioni, G., 2004. The influence of grain boundary fluids on the microstructure of quartz-feldspar mylonites. Journal of Structural Geology 26, 47-69.
- Mancktelow, N. S., and Pennacchioni, G., 2013. Late magmatic healed fractures in granitoids and their influence on subsequent solid-state deformation. Journal of Structural Geology 57, 81-96.
- Mancktelow, N. S., Stöckli, D. F., Grollimund, B., Müller, W., Fügenschuh, B., Viola, G., ... and Villa, I. M., 2001. The DAV and Periadriatic fault systems in the Eastern Alps south

of the Tauern window. International Journal of Earth Sciences 90, 593-622.

- Mancktelow, N.S., 1981. Strain variation between quartz grains of different crystallographic orientation in a naturally deformed metasiltstone. Tectonophysics 78, 73-84.
- Mancktelow, N.S., Pennacchioni, G., 2005. The control of precursor brittle fracture and fluid–rock interaction on the development of single and paired ductile shear zones. Journal of Structural Geology 27, 645-661.
- Mancktelow, N.S., Pennacchioni, G., 2010. Why calcite can be stronger than quartz. Journal of Geophysical Research 115, B01402, doi:10.1029/2009JB006526.
- Martin, S., Prosser, G., and Morten, L., 1993. Tectono-magmatic evolution of sheeted plutonic bodies along the north Giudicarie line (northern Italy). Geologische Rundschau 82, 51-66.
- Maruyama, S., Liou, J. G., and Suzuki, K., 1982. The peristerite gap in low-grade metamorphic rocks. Contributions to Mineralogy and Petrology 81, 268-276.
- Mazzoli, C., Peruzzo, L., and Sassi, R., 1993. An Austroalpine mylonite complex at the southern boundary of the Tauern Window: crystallization-deformation relationships in the Cima Dura-Durrek Complex. IGCP International Geological Correlation Program No. 276, Newsletter 6, 22-25.
- Means, W. D., 1995. Shear zones and rock history. Tectonophysics 247, 157-160.
- Menegon, L., Fusseis, F., Stünitz, H., Xiao, X., 2015. Creep cavitation bands control porosity and fluid flow in lower crustal shear zones.Geology 43, 227-230.
- Menegon, L., Pennacchioni, G., 2010. Local shear zone pattern and bulk deformation in the Gran Paradiso metagranite (NW Italian Alps). International Journal of Earth Sciences 99, 1805-1825, doi:10.1007/s00531-009-0485-6

- Menegon, L., Pennacchioni, G., and Stünitz, H., 2006. Nucleation and growth of myrmekite during ductile shear deformation in metagranites. Journal of Metamorphic Geology 24, 553-568.
- Menegon, L., Pennacchioni, G., Heilbronner, R., and Pittarello, L., 2008. Evolution of quartz microstructure and c-axis crystallographic preferred orientation within ductilely deformed granitoids (Arolla unit, Western Alps). Journal of Structural Geology 30, 1332-1347.
- Menegon, L., Pennacchioni, G., Spiess, R., 2008. Dissolution-precipitation creep of K-feldspar in mid-crustal granite mylonites. Journal of Structural Geology 30, 565-579.
- Menegon, L., Piazolo, S., Pennacchioni, G., 2011. The effect of Dauphiné twinning on plastic strain in quartz. Contributions to Mineralogy and Petrology 161, 635-652.
- Menegon, L., Stünitz, H., Nasipuri, P., Heilbronner, R., Svahnberg, H., 2013. Transition from fracturing to viscous flow in granulite facies perthitic feldspar (Lofoten, Norway). Journal of Structural Geology 48, 95-112.
- Miranda, E. A., Hirth, G., John, B. E., 2016. Microstructural evidence for the transition from dislocation creep to dislocation-accommodated grain boundary sliding in naturally deformed plagioclase. Journal of Structural Geology 92, 30-45.
- Morales, L. F., Mainprice, D., Lloyd, G. E., Law, R. D., 2011. Crystal fabric development and slip systems in a quartz mylonite: an approach via transmission electron microscopy and viscoplastic self-consistent modelling. Geological Society of London, Special Publications 360, 151-174.
- Müller, D. G. D., Stumpfl, E. F., and Taylor, W. R., 1992. Shoshonitic and alkaline lamprophyres with elevated Au and PGE concentrations from the Kreuzeck Mountains, Eastern Alps, Austria. Mineralogy and Petrology 46, 23-42.
- Müller, W., Mancktelow, N. S., and Meier, M., 2000. Rb–Sr microchrons of synkinematic

mica in mylonites: an example from the DAV fault of the Eastern Alps. Earth and Planetary Science Letters 180, 385-397.

- Muto, J., Hirth, G., Heilbronner, R., Tullis, J., 2011. Plastic anisotropy and fabric evolution in sheared and recrystallized quartz single crystals. Journal of Geophysical Research 116, B02206, doi:10.1029/2010JB007891
- Neumann, B., 2000. Texture development of recrystallised quartz polycrystals unravelled by orientation and misorientation characteristics. Journal of Structural Geology 22, 1695-1711.
- Nishikawa, O., and Takeshita, T., 2000. Progressive lattice misorientation and microstructural development in quartz veins deformed under subgreenschist conditions. Journal of Structural Geology, 22, 259-276.
- Oliot, E., Goncalves, P., and Marquer, D., 2010. Role of plagioclase and reaction softening in a metagranite shear zone at mid‐crustal conditions (Gotthard Massif, Swiss Central Alps). Journal of Metamorphic Geology 28, 849-871.
- Passchier, C. W., and Trouw, R. A. J., 2005. Microtectonics, 366 pp.
- Pauli, C., Schmid, S. M., Heilbronner, R. P., 1996. Fabric domains in quartz mylonites: localized three dimensional analysis of microstructure and texture. Journal of Structural Geology 18, 1183-1203.
- Pennacchioni, G., 2005. Control of the geometry of precursor brittle structures on the type of ductile shear zone in the Adamello tonalites, Southern Alps (Italy). Journal of Structural Geology 27, 627-644.
- Pennacchioni, G., and Cesare, B., 1997. Ductile‐brittle transition in pre‐Alpine amphibolite facies mylonites during evolution from water‐present to water‐deficient conditions (Mont Mary nappe, Italian Western Alps). Journal of Metamorphic Geology 15, 777-791.

- Pennacchioni, G., and Mancktelow, N. S., 2007. Nucleation and initial growth of a shear zone network within compositionally and structurally heterogeneous granitoids under amphibolite facies conditions. Journal of Structural Geology 29, 1757-1780.
- Pennacchioni, G., and Mancktelow, N. S., 2013. Initiation and growth of strike-slip faults within intact metagranitoid (Neves area, eastern Alps, Italy). Geological Society of America Bulletin 125, 1468-1483.
- Pennacchioni, G., and Zucchi, E., 2013. High temperature fracturing and ductile deformation during cooling of a pluton: The Lake Edison granodiorite (Sierra Nevada batholith, California). Journal of Structural Geology 50, 54-81.
- Pennacchioni, G., Di Toro, G., Brack, P., Menegon, L., and Villa, I. M., 2006. Brittle–ductile–brittle deformation during cooling of tonalite (Adamello, Southern Italian Alps). Tectonophysics 427, 171-197.
- Pennacchioni, G., Di Toro, G., Mancktelow, N.S., 2001. Strain-insensitive preferred orientation of porphyroclasts in Mont Mary mylonites. Journal of Structural Geology 23, 1281-1298, doi: 10.1016/S0191-8141(00)00189-9
- Pennacchioni, G., Menegon, L., Leiss, B., Nestola, F., and Bromiley, G., 2010. Development of crystallographic preferred orientation and microstructure during plastic deformation of natural coarse□grained quartz veins. Journal of Geophysical Research: Solid Earth 115.
- Piazolo, S., Montagnat, M., Blackford, J.R., 2008. Sub-structure characterization of experimentally and naturally deformed ice using cryo-EBSD. Journal of Microscopy 230, 509-519.
- Platt, J. P., Behrmann, J. H., Cunningham, P. C., Dewey, J. F., Helman, M., Parish, M., Shepley, M. G., Wallis, S., and Western, P. J., 1989. Kinematics of the Alpine arc and the motion history of Adria. Nature 337, 158-161.

- Pomella, H., Klötzli, U., Scholger, R., Stipp, M., and Fügenschuh, B., 2011. The Northern Giudicarie and the Meran-Mauls fault (Alps, Northern Italy) in the light of new paleomagnetic and geochronological data from boudinaged Eo-/Oligocene tonalites. International Journal of Earth Sciences 100, 1827-1850.
- Price, N. A., Song, W. J., Johnson, S. E., Gerbi, C. C., Beane, R. J., West, D. P., 2016. Recrystallization fabrics of sheared quartz veins with a strong pre-existing crystallographic preferred orientation from a seismogenic shear zone. Tectonophysics 682, 214-236.
- Prior, D. J., Wheeler, J., Peruzzo, L., Spiess, R., Storey, C., 2002. Some garnet microstructures: an illustration of the potential of orientation maps and misorientation analysis in microstructural studies. Journal of Structural Geology 24, 999-1011.
- Prochaska, W., (1981). Eigene Ganggesteine der Riesenfernerintrusion mit neuen radiometrischen Altersdaten. Gesellschaft der Geologie und Bergbaustudenten in Österreich: 161-171.
- Prosser, G., 1998. Strike□slip movements and thrusting along a transpressive fault zone: The North Giudicarie line (Insubric line, northern Italy).Tectonics 17, 921-937.
- Pryer, L. L., Robin, P. Y., 1996. Differential stress control on the growth and orientation of flame perthite: a palaeostress-direction indicator. Journal of Structural Geology 18, 1151-1166.
- Rahl, J. M., Skemer, P., 2016. Microstructural evolution and rheology of quartz in a mid-crustal shear zone. Tectonophysics 680, 129-139.
- Ramsay, J. G., 1980. Shear zone geometry: a review. Journal of structural geology 2, 83-99.
- Ranalli, G., 2000. Rheology of the crust and its role in tectonic reactivation. Journal of Geodynamics 30, 3–15.

- Ratschbacher, L., Frisch, W., Linzer, H. G., and Merle, O., 1991. Lateral extrusion in the Eastern Alps, part 2: structural analysis. Tectonics 10, 257-271.
- Ratschbacher, L., Frisch, W., Neubauer, F., Schmid, S. M., and Neugebauer, J., 1989. Extension in compressional orogenic belts: the eastern Alps. Geology 17, 404-407.
- Riley, P., and Tikoff, B., 2010. Tabular fracture clusters: Dynamic fracturing produced by volatile expulsion, Sierra Nevada Batholith, California. Journal of Structural Geology 32, 1488-1499.
- Rogowitz, A., White, J. C., Grasemann, B., 2016. Strain localization in ultramylonitic marbles by simultaneous activation of dislocation motion and grain boundary sliding (Syros, Greece). Solid Earth 7, 355-366, doi:10.5194/se-7-355-2016
- Romer, R. L., and Siegesmund, S., 2003. Why allanite may swindle about its true age. Contributions to Mineralogy and Petrology 146, 297-307.
- Rosenberg, C., 2004. Shear zones and magma ascent: a model based on a review of the Tertiary magmatism in the Alps. Tectonics 23, TC3002, doi:10.1029/2003TC001526
- Scharf, A., Handy, M. R., Favaro, S., Schmid, S. M., and Bertrand, A., 2013. Modes of orogen-parallel stretching and extensional exhumation in response to microplate indentation and roll-back subduction (Tauern Window, Eastern Alps). International journal of earth sciences 102, 1627-1654.
- Scheuvens, D., and Mann, A., 2004. Syn-and postintrusive deformation at the northern margin of the Rieserferner plutonic complex (Eastern Alps): strain partitioning during emplacement and cooling of granitoids. Zeitschrift der Deutschen Geologischen Gesellschaft 497-517.
- Schmid, S. M., and Casey, M., 1986. Complete fabric analysis of some commonly observed quartz c□axis patterns. Mineral and rock deformation: laboratory studies: the Paterson Volume, 263-286.

- Schneider, S., Hammerschmidt, K., and Rosenberg, C. L., 2013. Dating the longevity of ductile shear zones: Insight from 40 Ar/39 Ar in situ analyses. Earth and Planetary Science Letters 369, 43-58.
- Schulz, B., 1994. Microstructural evolution of metapelites from the Austroalpine basement north of Staller Sattel during pre-Alpine and Alpine deformation and metamorphism (Eastern Tyrol, Austria). Jahrb Geol BA Wien 137, 197-212.
- Schulz, B., Steenken, A., and Siegesmund, S., 2008. Geodynamic evolution of an Alpine terrane—the Austroalpine basement to the south of the Tauern Window as a part of the Adriatic Plate (eastern Alps). Geological Society, London, Special Publications 298, 5-44.
- Simpson, C., Wintsch, R. P., 1989. Evidence for deformation□induced K□feldspar replacement by myrmekite. Journal of Metamorphic Geology 7, 261-275.
- Spear, F. S., 1993. Metamorphic Phase Equilibria and Pressure–Temperature–Time Paths. Mineralogical Society of America, Washington, DC, pp. 353–354.
- Steenken, A., Siegesmund, S., and Heinrichs, T., 2000. The emplacement of the Rieserferner Pluton (Eastern Alps, Tyrol): constraints from field observations, magnetic fabrics and microstructures. Journal of Structural Geology 22, 1855-1873.
- Steenken, A., Siegesmund, S., Heinrichs, T., and Fügenschuh, B., 2002. Cooling and exhumation of the Rieserferner Pluton (Eastern Alps, Italy/Austria). International Journal of Earth Sciences 91, 799-817.
- Stel, H., Breedveld, M., 1990. Crystallographic orientation patterns of myrmekitic quartz: a fabric memory in quartz ribbon-bearing gneisses. Journal of structural geology 12, 19-28.
- Stipp, M., Fügenschuh, B., Gromet, L. P., Stünitz, H., and Schmid, S. M., 2004. Contemporaneous plutonism and strike□slip faulting: A case study from the Tonale fault zone north of the Adamello pluton (Italian Alps). Tectonics 23.
- Stipp, M., Kunze, K., 2008. Dynamic recrystallization near the brittle-plastic transition in

naturally and experimentally deformed quartz aggregates. Tectonophysics 448, 77-97.

- Stipp, M., Stünitz, H., Heilbronner, R., and Schmid, S. M., 2002a. Dynamic recrystallization of quartz: correlation between natural and experimental conditions. Geological Society, London, Special Publications 200, 171-190.
- Stipp, M., Stünitz, H., Heilbronner, R., and Schmid, S. M., 2002b. The eastern Tonale fault zone: a ‘natural laboratory’for crystal plastic deformation of quartz over a temperature range from 250 to 700 °C. Journal of Structural Geology 24, 1861-1884. doi:10.1016/S0191-8141(02)00035-4.
- Stipp, M., Tullis, J., 2003. The recrystallized grain size piezometer for quartz. Geophysical Research Letters 30, 2088, doi:10.1029/2003GL018444, 2003
- Stöckhert, B., Brix, M. R., Kleinschrodt, R., Hurford, A. J., and Wirth, R., 1999. Thermochronometry and microstructures of quartz—a comparison with experimental flow laws and predictions on the temperature of the brittle–plastic transition. Journal of Structural Geology 21, 351-369.
- Stünitz, H., Fitz Gerald, J. F., 1993. Deformation of granitoids at low metamorphic grade. II: Granular flow in albite-rich mylonites. Tectonophysics 221, 299-324.
- Stünitz, H., Gerald, J. F., Tullis, J., 2003. Dislocation generation, slip systems, and dynamic recrystallization in experimentally deformed plagioclase single crystals. Tectonophysics 372, 215-233.
- Tajčmanová, L., Connolly, J. A. D., and Cesare, B., 2009. A thermodynamic model for titanium and ferric iron solution in biotite. Journal of Metamorphic Geology 27, 153-165.
- ten Grotenhuis, S.M., Passchier, C.W., Bons, P.D., 2002. The influence of strain localisation on the rotation behaviour of rigid objects in experimental shear zones. Journal of Structural Geology 24, 485-499.
- Toy, V.G., Prior, D.J., Norris, R.J., 2008. Quartz fabrics in the Alpine Fault mylonites:

Influence of pre-existing preferred orientations on fabric development during progressive uplift. Journal of Structural Geology 30, 602-621, doi:10.1016/j.jsg.2008.01.001.

- Trepmann, C. A., Stöckhert, B., and Chakraborty, S., 2004. Oligocene trondhjemitic dykes in the Austroalpine basement of the Pfunderer Berge, Südtirol-level of emplacement and metamorphic overprint. European journal of mineralogy 16, 641-659.
- Trepmann, C.A., Hsu, C., Hentschel, F., Döhler, K., Schneider, C., Wichmann, V., 2017. Recrystallization of quartz after low-temperature plasticity – The record of stress relaxation below the seismogenic zone. Journal of Structural Geology, 95, 77-92.
- Trepmann, C.A., Stöckhert, B., Dorner, D., Moghadam, R. H., Küster, M., Röller, K., 2007. Simulating coseismic deformation of quartz in the middle crust and fabric evolution during postseismic stress relaxation – an experimental study. Tectonophysics, 442, 83-104.
- Tsurumi, J., Hosonuma, H., Kanagawa, K., 2003. Strain localization due to a positive feedback of deformation and myrmekite-forming reaction in granite and aplite mylonites along the Hatagawa Shear Zone of NE Japan. Journal of Structural Geology 25, 557-574.
- Tullis, J., &and Yund, R. A., 1991. Diffusion creep in feldspar aggregates: experimental evidence. Journal of Structural Geology 13, 987-1000.
- Tullis, J., 1977. Preferred orientation of quartz produced by slip during plane strain. Tectonophysics 39, 87-102.
- Tullis, J., Christie, J., Griggs, D., 1973. Microstructures and preferred orientations of experimentally deformed quartzites. Geological Society of America Bulletin 84, 297-314.
- van Daalen, M., Heilbronner, R., Kunze, K., 1999. Orientation analysis of localized shear deformation in quartz fibres at the brittle–ductile transition. Tectonophysics 303, 83-107.
- Vernon, R. H., 1991. Questions about myrmekite in deformed rocks. Journal of Structural

Geology 13, 979-985.

- Vernooij, M.G., 2005. Dynamic recrystallisation and microfabric development in single crystals of quartz during experimental deformation (Doctoral dissertation, Diss., Naturwissenschaften, Eidgenössische Technische Hochschule ETH Zürich, Nr. 16050, 2005).
- Vernooij, M.G., Kunze, K., den Brok, B., 2006a. 'Brittle' shear zones in experimentally deformed quartz single crystals. Journal of Structural Geology 28, 1292-1306.
- Vernooij, M.G., den Brok, B., Kunze, K., 2006b. Development of crystallographic preferred orientations by nucleation and growth of new grains in experimentally deformed quartz single crystals. Tectonophysics 427, 35-53.
- Viola, G., Mancktelow, N. S., and Seward, D., 2001. Late Oligocene□Neogene evolution of Europe□Adria collision: New structural and geochronological evidence from the Giudicarie fault system (Italian Eastern Alps). Tectonics 20, 999-1020.
- Vollbrecht, A., Stipp, M., Olesen, N. Ø., 1999. Crystallographic orientation of microcracks in quartz and inferred deformation processes: a study on gneisses from the German Continental Deep Drilling Project (KTB). Tectonophysics 303, 279-297.
- von Blanckenburg, F., and Davies, J. H., 1995. Slab breakoff: a model for syncollisional magmatism and tectonics in the Alps. Tectonics 14, 120-131.
- Wagner, R., Rosenberg, C. L., Handy, M. R., Möbus, C., and Albertz, M., 2006. Fracture-driven intrusion and upwelling of a mid-crustal pluton fed from a transpressive shear zone—The Rieserferner Pluton (Eastern Alps). Geological Society of America Bulletin 118, 219-237.
- Wheeler, J., Prior, D., Jiang, Z., Spiess, R., Trimby, P., 2001. The petrological significance of misorientations between grains. Contributions to Mineralogy and Petrology 141, 109-124.

- White, S., 1977. Geological significance of recovery and recrystallization processes in quartz. Tectonophysics 39, 143-170.
- Wirth, R., and Voll, G., 1987. Cellular intergrowth between quartz and sodium-rich plagioclase (myrmekite)—an analogue of discontinuous precipitation in metal alloys. Journal of Materials Science 22, 1913-1918.
- Wölfler, A., Rabitsch, R., Fritz, H., Gaich, H., Kurz, W., and Reiter, A., 2008. Deformation partitioning within a sinistral transpression zone along the southwestern margin of the Tauern Window (eastern Alps). Geological Society, London, Special Publications 299, 211-230.
- Xiao, X., Wirth, R., Dresen, G., 2002. Diffusion creep of anorthite□quartz aggregates. Journal of Geophysical Research: Solid Earth 107(B11).